NITRIDATION BEHAVIOUR

AND

INTERFACE STRUCTURES OF Ni-Ti-N Alloys

By

GEORGE C. SAVVA, M.A.Sc.

A thesis

Submitted to the School of Graduate Studies

in Partial Fulfilment of the Requirements

for the Degree

Doctor of Philosophy

McMaster University

NITRIDATION BEHAVIOUR

AND

INTERFACE STRUCTURES OF Ni-Ti-N ALLOYS

DOCTOR OF PHILOSOPHY (1995) McMASTER UNIVERSITY

(Materials Science and Engineering) Hamilton, Ontario

Title: Nitridation and Interface Structures of Ni-Ti-N Alloys

Author: George C. Savva M.A.Sc., B.A.Sc (University of Toronto)

Supervisors: Professors G.C. Weatherly and J.S. Kirkaldy

Number of Pages: xix, 218

ABSTRACT

A two part study was conducted on the nitridation behaviour of dilute Ni-Ti alloys, and on the orientation relationships (OR)s and interfacial structures between TiN and Ni. Beginning with the Fickian relationships first proposed by Kirkaldy (1969) to describe internal sulphidation and assuming a solubility product of the form K=BC, these equations were combined to yield for the metal solute:

$$\frac{\partial B}{\partial t}=[D_B+\frac{KD_C}{B^2}]\frac{\partial^2 B}{\partial x^2}$$

This second order differential equation shows that the concentration profile of the metal solute, B, is dependent not only on the diffusivity of the metal, D_B, but also on the solubility product K and on the gas diffusivity D_C. Two limiting cases were identified from the previous equation. The first which depends only on the metal diffusivity, D_B, corresponds to Wagner's (1952) error function solution for the superficial oxidation of alloys dilute in B. The second limiting case (D_B=0) corresponds to Wagner's (1959) oxygen controlled internal oxidation as proven analytically by Ohriner and Morral (1979). A criterion describing the transition from internal to external nitridation (oxidation) was deduced from the previous equation as:

$$\frac{KD_C}{B_I^2 D_B} < 0.1$$

where B_I is the interfacial composition of the metal solute.

A finite difference algorithm was presented based on these ideas. A comprehensive test of this approach showed that it could generate the well known analytical solutions of Wagner's two limiting conditions. It was also shown that provided the solubility product K is small, Ohriner and Morral's (1979) analytical solution is valid even for an alloy not saturated in the gas phase (i.e. the composition need not be confined to the solvus of the ternary isotherm). As well as reproducing these analytical solutions, the model was successfully tested against the experimental work of Swisher (1968) and Kirkaldy (1969). A detailed investigation was conducted on the concentration profiles of Ti in Ni as a consequence of either internal nitridation or superficial nitridation using Energy Dispersive X-Ray (EDX) analysis. It was found that the program always generated the correct shapes of the diffusion profiles as well the transition to external nitridation in the Ni-Ti-N system. Based on the measured interfacial composition of the interface, first time determinations of both KD_N and D_{Ti} values were obtained between 800°C and 1020°C. The diffusivity of Ti in Ni is similar to other substitution solutes in Ni and can be expressed as:

$$D_{Ti}=0.07 \exp(-320000/RT)\ m^2/s \quad (900°C\text{-}1020°C)$$

where R is the universal gas constant 8.314 J/mole-K

A solubility product calculation of TiN in Ni showed values between 1.4×10^{-6} and 5×10^{-8} $[w/o]^2$ (between1020°C and 800°C respectively). Using this data a diffusivity of N in Ni was obtained which compares favourably to other interstitial diffusivity data in Ni and γFe. The upper bound value for the diffusivity of N in dilute Ni-Ti alloys can be expressed as:

$$D_N = 0.0003 \exp(-17000/RT) \ m^2/s \ (900°C\text{-}1020°C)$$

Stoichiometric TiN was the only precipitated phase found between 800°C-1020°C in this work. A first time investigation of the interfacial structure between TiN and Ni was conducted using transmission electron microscopy (TEM). It was determined that at least five different orientation relationships between TiN and Ni exist. All these ORs had relatively small near coincidence site lattice (CSL) relationships. The planar Σ value of Ni (σ_{Ni}) with respect to the Ti sublattice were all found to be under 50. No correlation was found between the size of the CSL unit cell and the frequency of observation of a particular OR. In only two cases were misfit dislocations observed. Both O-lattice and plane matching theory made correct predictions as to the misfit dislocation configurations. In both cases one predominate set of dislocations was calculated. It was not possible, however, to unambiguously identify the Burgers vector.

The habit planes were dominated by {010}TiN indicating that this was an important factor in selecting the morphology and orientation relationships of these particles. This plane coincided both with a primary O-lattice plane and, as already noted, with a planar CSL relationship. These factors probably all play a role in the selection of these orientation relationships and habit planes in the Ni/TiN system.

Acknowledgements

I would like to thank my supervisors Dr. J.S. Kirkaldy and Dr. G.C. Weatherly for their guidance and support throughout this study. Their insights and intuition have rarely failed to contribute in a positive manner to this endeavour.

In addition, I would like to express my sincere appreciation to the many research fellows and technicians who have also contributed immeasurably to this work. I would like to thank, Bruce Collier for helpful advice on furnace design, Mike Palme for his excellent glass blowing services, Jim Garrett for help with alloy preparation, W. Gong for X-ray diffraction services, Dr. A. Perovic and Dr. M. Prikryl for EELS analysis, Andy Duft for Auger analysis, Jim McAndrew for the XFS service, Martin Van Oosten for the N, C and O gas analysis, Tom Bryner and Chris Butcher for their helpful advice on metallography, Ed McCaffery for the many computers repairs, John Hudak for help with the SEM which made the EDX analysis portion of this work possible, and lastly Fred Pearson for maintenance and training on the CM-12 transmission electron microscope which permitted the interfacial characterization portion of this work to be completed.

Valuable discussions with Dr. J.D. Embury, Dr. J. Morral and Dr. J.P. Hirth are also gratefully acknowledged.

The financial support of NSERC and the department of Materials Science and Engineering is greatly appreciated.

Finally, I would like to thank my wife Irene (the most pleasant outcome of my stay at McMaster). This work would not have been possible without her.

Table of Contents:

List of Figures:

List of Tables:

Chapter 1

Introduction:

A two part study of the nitriding behaviour of Ni- Ti alloys and on the interface structure between TiN and Ni was conducted. In the first part the evolution of the TiN microstructure in Ni and the transition that occurs from internal nitridation to superficial nitridation was investigated for a series of Ni- Ti alloys ranging in composition from 0.1 to 5 w/o Ti, between 800°C and 1020°C. In the study of internal nitridation (or oxidation), the results are often analyzed in terms of Wagner's (1959) parabolic solutions. In one limiting case these strictly apply to a negligible metal solute diffusivity (D_B) and a negligible solubility product (K). In the other limiting case where diffusion of the metal solute is significant, a constant distribution of particles representing a local average in excess of the original alloy content is predicted. In a number of systems, such as the one investigated in this study, neither of these limiting solutions may be valid. Furthermore the transition to a superficial scale cannot be adequately explained in the framework of Wagner's models. Finite difference computer algorithms have been written by Christ et. al. (1989) and Bongartz et. al. (1986) to deal with a non-zero solubility product. However, a general approach accounting for counter diffusion of the metal solute which can subsume a transition to an external oxide or nitride has not been undertaken prior to

this investigation.

The excess volume change associated with internal precipitation reactions has also recently garnered some attention (Gurusway and co-workers 1986), (Rubly and Douglass, 1991), (Mackert et. al. 1983), (Yi and co-workers 1994). The reason being that if a large volume mismatch exists between the precipitating phase and the solvent, the rate determining step may become the removal of the solvent towards internal or surface sinks. Solvent removal as controlled by pipe diffusion along dislocations has been postulated as rate limiting in the oxidation of Ag- In alloys (Gurusway and co-workers 1986). In a more recent study of Ni-Al- Si alloys, the mechanism of solvent removal was suggested to change from Nabarro- Herring creep to pipe diffusion as the Si content increased (Yi et. al. 1994).

The second part of this work examines for the first time the morphology, orientation relationships, and interface dislocation structures of TiN in Ni. Unlike interfaces made by hot pressing together the ceramic and metallic components, interfaces produced by internal nitridation or oxidation are governed by nucleation and growth. Nucleation of TiN in Ni should select low energy interfaces, free of defects due to processing. A study of these interfaces is important from both a theoretical and an industrial point of view, the latter given the appearance of TiN/metal or TiN/semiconductor interfaces in many industrial applications. Some examples of the

utilization of TiN/metal interfaces are:

1/ TiN is used both for precipitation hardening, and for austenite (γFe) grain size control during hot rolling of alloy steels. Ni/TiN makes an ideal model system for γFe/TiN due to the similarity in lattice parameter and identical crystal structure in the two systems and does not possess the observational complications attendant upon the fcc-bcc transformation in Fe.

2/ TiN is used in cermets to reinforce Ni- based alloys.

3/ TiN is used as a hard coating in the aerospace industry and as a diffusion barrier coating in the electronics industry. In these applications TiN is usually deposited by one of any number of vapour deposition techniques. Defects in these systems are important in that they may become short circuit diffusion paths, or facilitate reduced adherence to the substrate.

In chapter 2 of this thesis the established ideas of internal oxidation are briefly reviewed. The less well known development due to Kirkaldy (1969)(1971) along with the analytical modifications by LaFlamme and Morral (1978), and Ohriner and Morral (1979) are used as a starting point to analyze both internal oxidation and the transition to external oxidation. A finite difference (FD) program based upon these ideas

is presented and compared with previous experimental and theoretical work.

Geometrical models of interface structures are also reviewed in chapter 2. Primary and secondary O-lattice theory, near Coincidence Site Lattice theory (CSL) and plane matching theory are presented. It will be demonstrated that many types of metal/ceramic interfaces have coincidence-site-lattice relationships.

Chapters 3 and 4 will describe the experimental procedures and experimental results respectively. Scanning Electron Microscopy (SEM) and Energy Dispersive X-ray (EDX) analysis were used to measure the diffusion profiles of the metal solute. These profiles are compared with predictions from the finite difference algorithm. Transmission electron microscopy (TEM) both in bright field and in weak beam dark field was used to study the interfacial structure between TiN and Ni. Chapters 5 and 6 present the discussion and conclusion portions of this document, respectively. The diffusion results are analyzed with respect to the proposed finite difference model while the interfacial structures are analyzed in terms of the theories presented in chapter 2. Good closure was obtained between theory and experiment in the case of the nitridation studies. Although the interface exhibited structures that could be described well by near CSL relationships, O-lattice theory, and Plane Matching theory, no one theory could account for the number of observed orientation relationships. Recommendations for future work are presented in Chapter 7.

Chapter 2

Literature Review:

2.1: Internal Oxidation:

When a noble metal A alloyed with B, is placed in an atmosphere containing a reactive gas C, the gas may dissolve in the alloy to a concentration in excess of the solubility product K and precipitate as BC. If the gas is oxygen then the process is commonly known as internal oxidation (Rapp 1965), (Swisher 1971). Alternatively a compact BC phase may form on the surface of the material or a combination of the two phenomena may occur. A schematic diagram of these two extremes is shown in Figure 2.1.1. The depth of the internal oxide front ξ is given by Wagner (1959) as

$$\xi^2 = \frac{2D_C X_C^s}{X_B^o \nu} t \qquad (2.1.1)$$

where D_C is the diffusivity of the gas species, t is time, ν is the stoichiometric ratio of the gas to the metal atoms in the precipitate, X_C^S is the gas solubility in the alloy (atom fraction) and X_B^o is the original metal solute content (atom fraction). The concentration profiles of metal and gas are shown schematically in Figure 2.1.2. Precipitation is

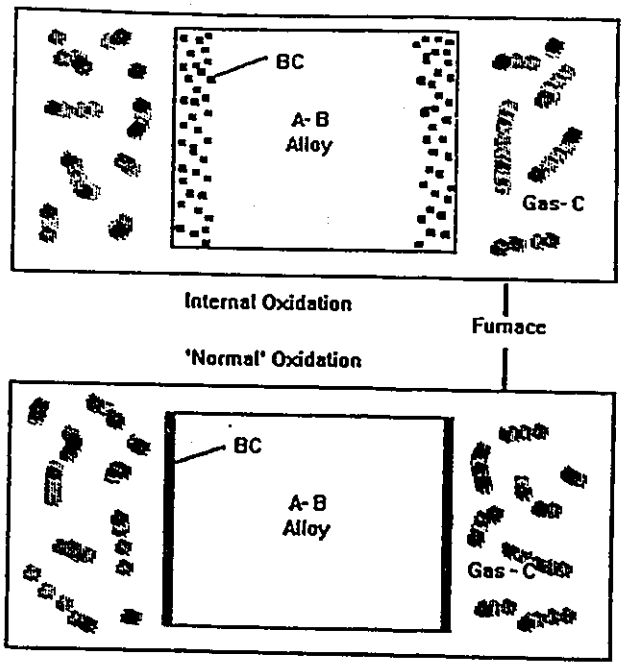

Figure 2.1.1: Schematic Diagram of a) internal oxidation b) superficial oxidation.

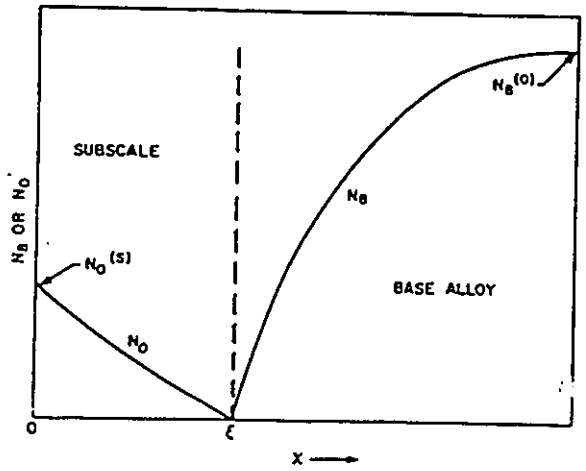

Figure 2.1.2: Schematic diagram of diffusion profiles of the gas species (O) and the metal solute (B) during internal oxidation.. Swisher (1971)

conjectured only to occur at the subscale/metal interface at $x=\xi$. This has the consequence that when metal solute counter diffusion is significant a uniform distribution of precipitates is predicted (Wagner 1959), (Swisher 1971).

The virtual path concept (Kirkaldy and Brown 1964), (Dalvi and Coates, 1972) on the ternary phase isotherm is useful in understanding the possible reactions between B and C. These are shown in Figure 2.1.3 for four different diffusion paths. The dog-leg portion of the diffusion paths is predicated upon the on- diagonal diffusivity relation $D_{CC}>>D_{BB}$(where CC and BB represent the gas and metal respectively). Paths II and III imply supersaturation, leading through an instability to the appearance of a non-planar interface or internal precipitates, the volumetric mix being qualitatively determined by the penetration of the virtual path into the two phase field. The evolution of morphology as the alloy content is increased is: I- stable γ + gas: II- γ with internal precipitates: III- superficial scale + γ + internal precipitates: IV- superficial scale + γ.

Kirkaldy (1969)(1971) constructed a pair of Fickian second order differential equations describing the counter diffusion of the gas and metal, the precipitation effect being represented by a sink or source term controlled by the solute solubility product of Figure 2.1.3. For equimolar compounds like BC, Kirkaldy's relationships are:

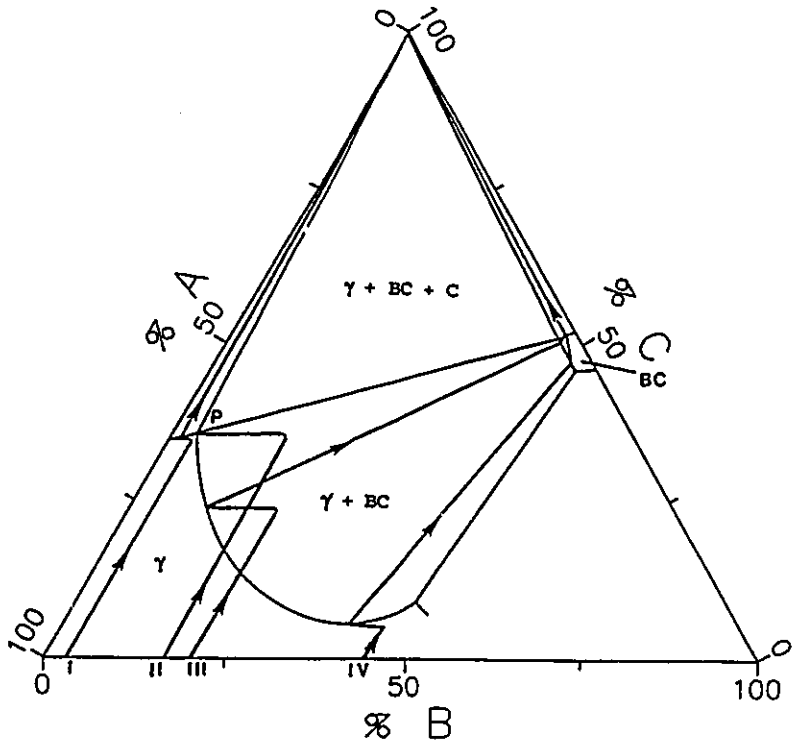

Figure 2.1.3: Virtual paths on ternary isotherm: I- γ + gas: II- internal oxidation III- mixed internal/ external oxidation IV- superficial oxidation.

$$-\frac{\partial p}{\partial t} = -D_C \frac{\partial^2 C}{\partial x^2} + \frac{\partial C}{\partial t} \qquad (2.1.2)$$

$$-\frac{\partial p}{\partial t} = -D_B \frac{\partial^2 B}{\partial x^2} + \frac{\partial B}{\partial t} \qquad (2.1.3)$$

where D_B, D_C are the diffusivity of the metal solute and gas respectively, p is the number of moles of precipitate per unit volume, C is the concentration of solute gas species (moles per unit volume) and B is the concentration of solute metal species (moles per unit volume). For large precipitate fractions this would also require a diffusion blockage term of order $(1-V_p)$ where V_p is the volume fraction of precipitates (Kirkaldy 1971).

Kirkaldy (1969) succeeded in predicting the distribution of MnS particles in Fe produced within a MnS/Fe diffusion couple similar to Path III of Figure 2.1.3. Assuming a linear solubility product (i.e. B = -mC + constant, where the slope |-m| was considered to be large) he was able to couple and then integrate Equation 2.1.2 or 2.1.3 to obtain Equation 2.1.4, which described the approximate distribution of these particles.

$$p(x,t)=\frac{D_C-D_B}{D_B}C(I)\,erfc\left(\frac{\frac{x}{\sqrt{t}}}{2\sqrt{D_B}}\right) \qquad (2.1.4)$$

where C(I) is the scale/ alloy interface composition

This approximation clearly represents a nonuniform distribution of particles in the subscale which may represent a local average over the original alloy content. For relatively dilute solutions one is justified as with equations 2.1.2 and 2.1.3 in neglecting ternary interactions, although these interactions (through Wagner interaction coefficients), may otherwise have a significant effect on the solubility product (Zou and Kirkaldy, 1990). Equation 2.1.4 has its limitations since the solubility product has been assumed to be small. Furthermore it cannot be used directly to solve for the distribution of particles under purely internal oxidation conditions, i.e. when $D_B \rightarrow 0$.

When Equations 2.1.2 and 2.1.3 are equated and coupled with a solubility product of the form K=BC and higher order derivative terms are neglected one obtains for the gas species:

$$\frac{\partial C}{\partial t} = D_B \frac{\partial^2 C}{\partial x^2}\left[\frac{K+C^2\,\phi}{C^2+K}\right] \qquad (2.1.5)$$

where $\phi = D_c/D_B$.

Assuming with Ohriner and Morral (1979), $K >> C^2$ and $D_B=0$, their equation

for C is recovered

$$\frac{\partial C}{\partial t} = \frac{D_C}{K} C^2 \frac{\partial^2 C}{\partial x^2} \qquad (2.1.6)$$

In a similar way the concentration of B can be determined as

$$\frac{\partial B}{\partial t} = D_B \frac{\partial^2 B}{\partial x^2} \left[\frac{B^2 + K\phi}{B^2 + K}\right] \qquad (2.1.7)$$

Assuming with Ohriner and Morral (1979) that $B^2 >> K$ but removing the restriction of $D_B = 0$, one obtains for B

$$\frac{\partial B}{\partial t} = \left[D_B + \frac{KD_C}{B^2}\right] \frac{\partial^2 B}{\partial x^2} \qquad (2.1.8)$$

From Equation 2.1.8, it can be seen that the metal solute diffusion profile will be invariant for constant KD_C. Therefore measurement of the metal diffusion profile will yield KD_C values as opposed to individual values of K or D_C. This is analogous to Wagner's limiting case solution (Equation 2.1.1) for oxygen diffusion controlled internal oxidation. In this case the depth of the internal oxidation front is invariant with constant $(X^S D_C)^{1/2}$, so that only the product $X^S D_C$ can be determined from an internal oxidation experiment. Furthermore if $(KD_C/B_I^2)/D_B < 0.1$, where B_I is the interfacial composition of

B, the terms in equation 2.1.8 dependant on the gas diffusivity will become negligible and external oxidation will result. This limiting condition has an error function solution for the solute B (Wagner 1952), characteristic of superficial oxidation of an A-B alloy where B is dilute and much more reactive than A

$$B=B_I+(B^O-B_I)erf[\frac{x}{2(D_Bt)^{\frac{1}{2}}}] \qquad (2.1.9)$$

where B^o is the original alloy content. This unique analysis through equation 2.1.8 is a precise way to view the transition from internal to external oxidation as opposed to a criterion based upon a critical blocking fraction of precipitates (Wagner 1965) (Rapp 1961). Equation 2.1.8 shows that for a varying interfacial composition there is an adjustable balance between the inward diffusion of the gas species and the outward diffusion of the solute which favours a superficial scale. This balance becomes unstable at some critical mole fraction. Therefore knowing D_B, D_C, and K, estimates can be made of B_I. This value sets a lower bound for the alloy concentration (B^o) needed to achieve external oxidation. Guan and Smeltzer (1994)(1994a) (1994b), based on a knowledge of the rate constant k_s for oxidation, have also looked at criteria for precipitation of a second solute underneath a pre-existing oxide layer, based on the earlier work of Wagner (1968).

2.1.2: Solvent Removal:

Although the displacement of solvent atoms in the form of 'nodules' on the surface of internally oxidized samples was observed by Darken in 1961, it was not until Mackert et. al. (1983) suggested that Nabarro-Herring creep could be the mechanism for removing solvent to the surface that debate began as to the actual rate determining step in internal oxidation. Since then Gurusway and co-workers (1986) and Yi and co-workers (1994) performed a series of experiments in an attempt to determine the mechanism for this behaviour. The experiments involved measuring the weight gain of samples during oxidation as a function of time^{½} and temperature and converting this information to activation energy data. A strict interpretation of Equation 2.1.1, would imply that the measured activation energy must be equal to the activation energy for oxygen diffusion. In contradiction to this the activation energy was found to be higher than for interstitial solute diffusion. Activation energies were calculated from models of pipe diffusion (i.e. along dislocation cores) as well as for Nabarro- Herring creep. Comparisons to the experimental results suggested that dislocation pipe diffusion was the operative mechanism in Ag- In alloys (Gurusway et. al. 1986), while the mechanism was found to change from Nabarro-Herring creep to pipe diffusion as the Si content increased in Ni-Al-Si alloys (Yi et. al. 1994). These results have important implications since they cast doubt on numerous determinations of gas diffusivities using internal oxidation.

2.1.3: Finite Difference Approach

The concentration of the gas, metal and precipitate can be solved directly by a finite difference approach. The algorithm adopted in this work is shown in Figure 2.1.4. The essential feature of the program is that it uses the finite difference form of Fick's Second Law (Press et. al. 1992). For example the gas species concentration is written for C(Δt) as:

$$C(J)' = D_C \frac{\Delta t}{(\Delta x)^2}(C(J+1)-2C(J)+C(J-1)) + C(J) \qquad (2.1.10)$$

where C(J)′ is the composition at position J at time t+Δt, C(J) is the composition at position J at time t and Δx, Δt are increments of position and time respectively. The computational stability of Equation 2.1.10 requires that

$$2D_C \frac{\Delta t}{\Delta x^2} \leq 1 \qquad (2.1.11)$$

The program first sets the semi - infinite boundary conditions. The gas species is sequentially allowed to diffuse into the material. At each point a check is made of the solubility product. If it is exceeded the number of moles of solute and gas which are consumed as well as the number of moles of the precipitate phase created are calculated. The concentration of gas and solute are confined to the phase boundary by

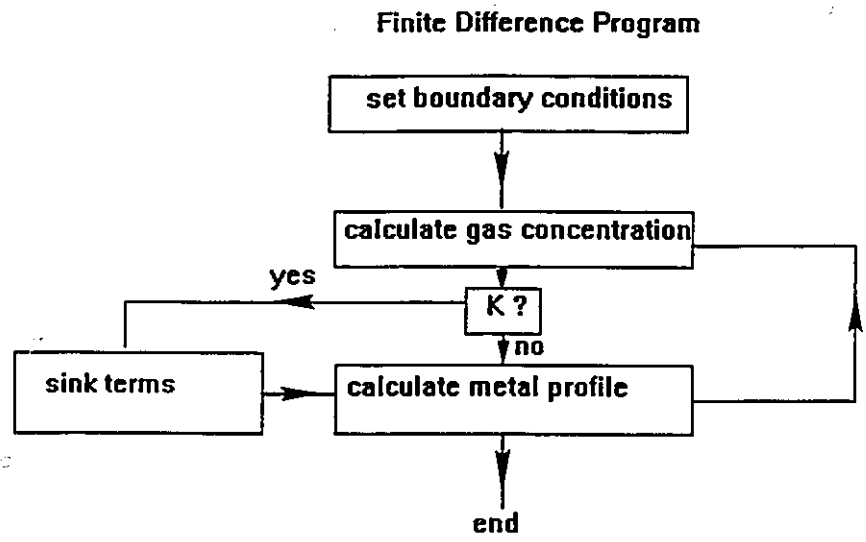

Figure 2.1.4: Computer algorithm for finite difference program.

the solubility product. Effectively the program creates and collapses the virtual diffusion path with each iteration in Δt. The mass balance is carried out in the following manner for the reaction:

$$[B] + x[C] = BC_x \qquad (2.1.12)$$

The conservation of mass requires that $1/x(C^o-C')=(B^o-B')= \delta m_{BCx}$ where C^o and B^o are the known gas and metal composition respectively in moles/cm^3, C′ and B′ are the unknown gas and metal composition in moles/cm^3, and δm_{BCx} is the number of moles of precipitate formed (moles/cm^3). This, coupled to the appropriate solubility product, $BC^x= K$, allows for the solution of the mass balance, and the resulting concentration of both the gas and solute species. The counter diffusion of the metal solute species is then calculated by another finite difference scheme. The program ends after performing the required number of iterations (typically 10^6 for the experimental times chosen). This direct solution for the mass balance is similar to the one used by Zou and Kirkaldy (1991) in their study of carbonitride precipitation in steel. This approach has the advantage that the mass balance is explicitly performed in each iteration. Some of the pitfalls of integrating Equation 2.1.2 or 2.1.3 directly to obtain the distribution of particles have been discussed by Buchmayr and Kirkaldy (1991).

The input parameters required are: the diffusivity of the solute and the gas,

the solubility product K, the original solute concentration, the gas or solute concentration at (or near) the interface and the Wagner interaction coefficients if necessary or available. The full program includes the blocking terms ($1-V_p$), which accounts for the reduced areas for diffusion as precipitates form.

Although the simplest type of internal oxidation reaction, one solute reacting with one gas species, was examined, additional species may be readily incorporated into the finite difference algorithm.

2.1.4: Test of Program:

Ohriner and Morral (1979) found an analytical solution for the amount of precipitate in the subscale based on Equation 2.1.6, with the restrictive condition that the solute is immobile in the alloy ($D_B=0$). Their results for the distribution of particles is shown in Figure 2.1.5 for a gas saturated alloy. As can be observed the distribution of particles will depend on the solubility product. They recognized that the case of a low solubility product $\alpha=1$ (where $\alpha=1-K/C^S B^O$ and C^S is the surface concentration of gas) corresponds to Wagner's case for oxygen controlled internal oxidation (Equation 2.1.1).

The computer generated results for the same experimental conditions with a gas saturated and unsaturated alloy are shown in Figures 2.1.6a and 2.1.6b respectively. The

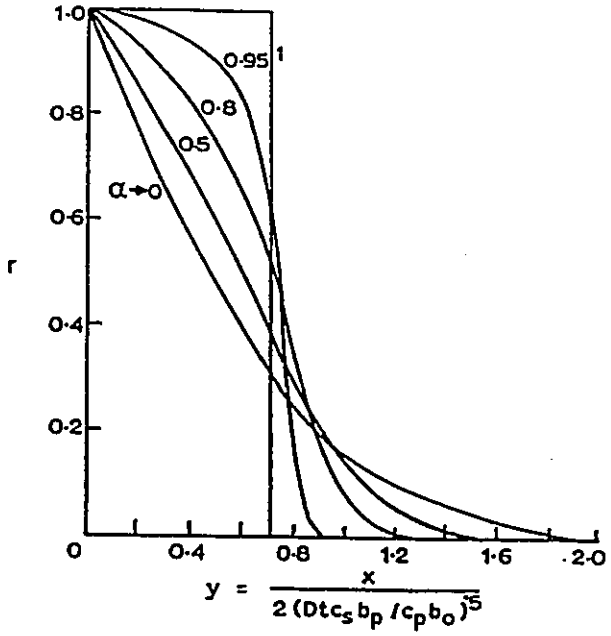

Figure 2.1.5: Normalized precipitate volume fraction as a function of reduced distance. After Ohriner and Morral (1979)

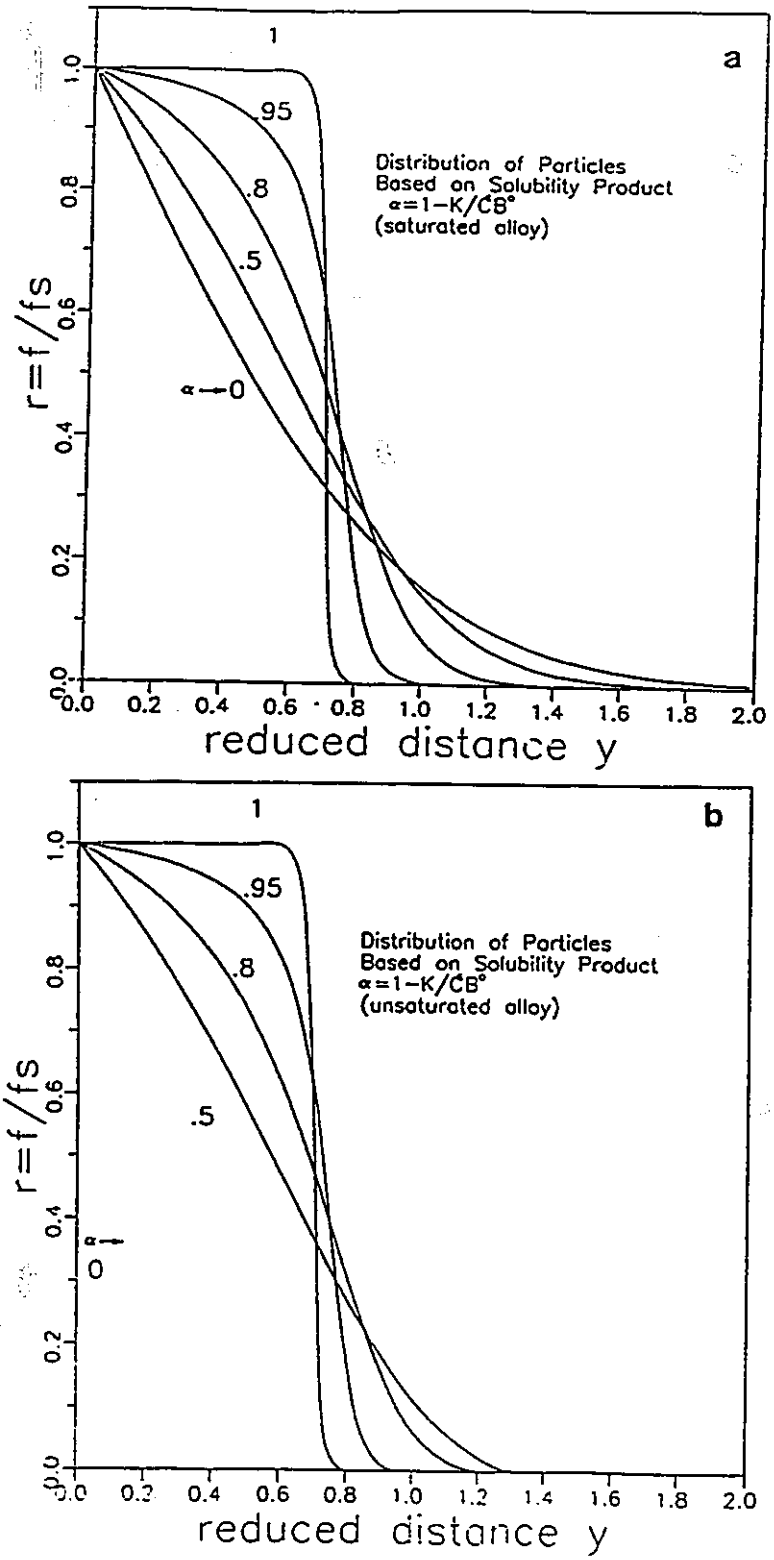

Figure 2.1.6: The Finite Difference Algorithm Results after Ohriner and Morral's analysis a) saturated b) unsaturated alloy

agreement with the gas saturated case of Ohriner and Morral (1978) is excellent (Figure 2.1.5a). The unsaturated alloy was found to behave like the saturated one at a low solubility product (i.e. α=1), but as the solubility product increased (i.e. α<1) it becomes difficult to saturate the alloy. Hence only surface particles are found as $\alpha \rightarrow 0$, in these materials (Figure 2.1.5b). An important point to note is that even when an alloy is not saturated with gas, Wagner's solution (Equation 2.1.1) still applies for a low solubility product K.

The results of Swisher (1968) for the internal sulphidation of Fe-Ti provides a good test of the theory since the diffusivity of Ti (Moll and Oglivie 1957) and S (Hoshino and Ataki 1970) in γFe have been measured independently and the solubility product and boundary conditions can be determined directly from Swisher's experimental data. A comparison is made between the measured concentration profile of Ti and that calculated using the finite difference program in Figure 2.1.7 for both TiS_2 and TiS formation (the composition of the sulphide phase was not analyzed). The agreement between the calculated and experimental Ti profile is excellent for TiS formation, suggesting strongly that this was the precipitated phase in this system.

The distribution of MnS particles in Fe, formed from an Fe/MnS diffusion couple was calculated using Equation 2.1.6 (Kirkaldy, 1969) and compared with the finite

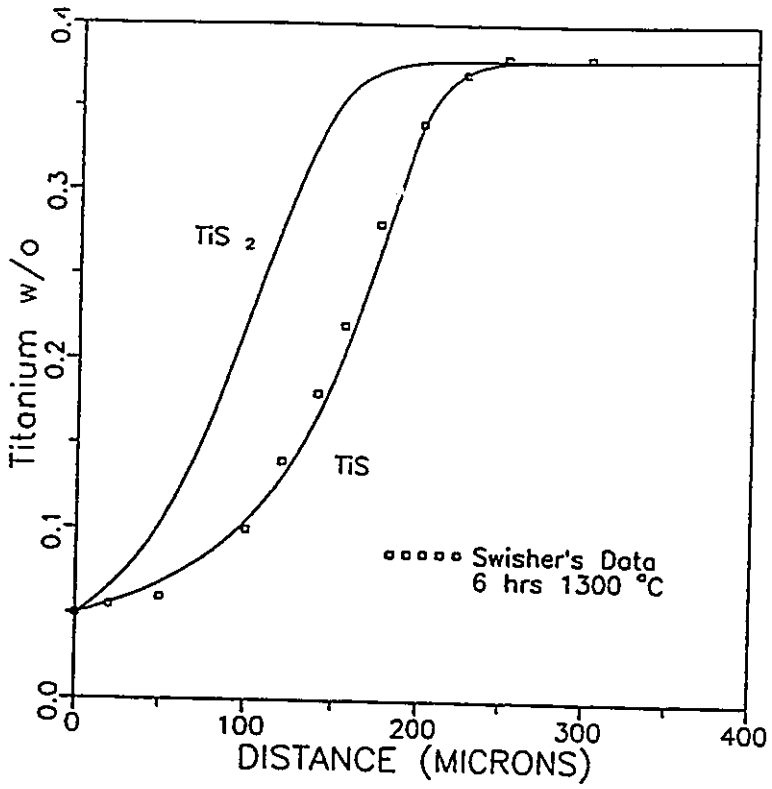

Figure 2.1.7: Algorithm results for TiS and TiS_2 formation in Fe. Experimental points after Swisher (1968)

difference results in Figure 2.1.8 for differing Δx and Δt. Good agreement is obtained between the two solutions for the distribution of MnS in the subscale at all values of Δt and Δx. A surface artifact is noted as a function of step size Δx. The smaller the step size the greater is the apparent surface concentration, but at the same time the results are unaffected in the interior of the alloy. Larger step sizes tend to 'average out' surface concentrations. There is no effect of step size on the concentration profile of Mn.

The program's ability to deal with ternary interactions is assessed in Figure 2.1.9. A variation of Darken's (1948) classic experiment is recreated. A gradient in Si provides the driving force for C diffusion through a strong ternary interaction between Si and C. The results are compared with the analytical solution (Kirkaldy 1957) for this exact case. The diffusional cross term D_{CB} was obtained from (Kirkaldy and Purdy 1969) as

$$D_{CB}=X_C\varepsilon_{CB}D_{CC} \qquad (2.1.13)$$

where X_C is the mole fraction of the gas , ε_{CB} is the Wagner interaction parameter and D_{CC} is the on-diagonal diffusivity of the gas C. An average value of X_C and therefore D_{CB} was assumed for the purposes of calculation. Once again excellent agreement was obtained between the numerical and analytical approach.

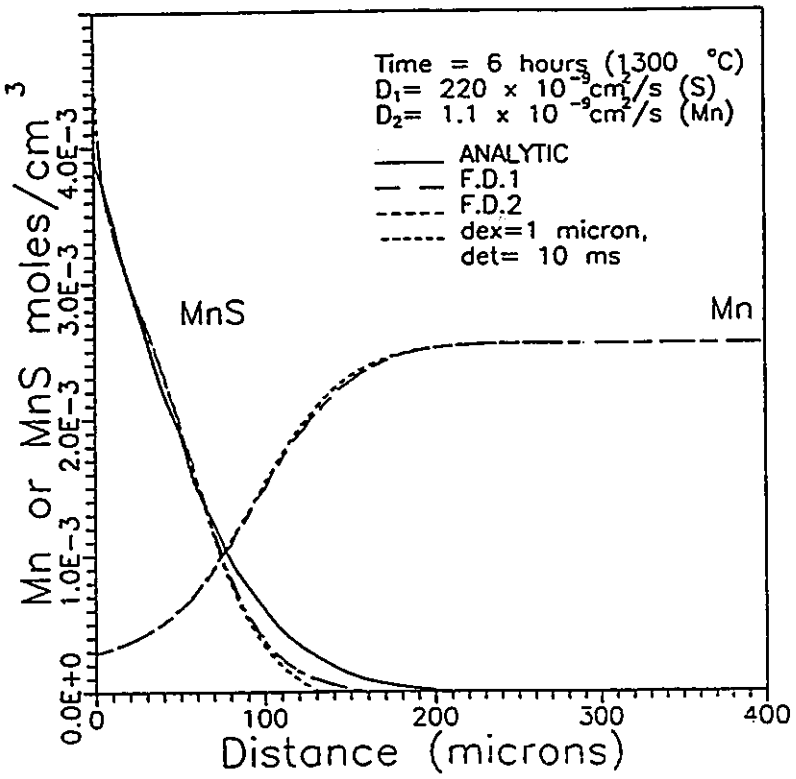

Figure 2.1.8: Mn profile and MnS distribution after 6 hours at 1050°C. Solid line is based on equation 2.1.4. The dashed lines are for these exact conditions using differing Δx and Δt values.

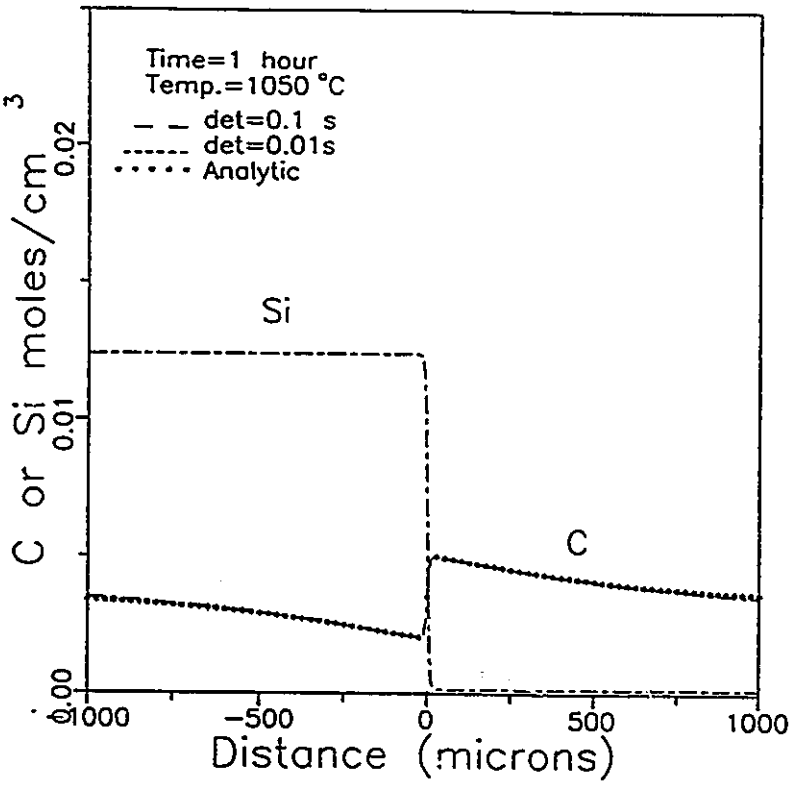

Figure 2.1.9: The computer generated results for C diffusion under a Si concentration gradient. Dashed lines are the computer generated results for varying Δt. The asterisks are from Kirkaldy's (1957) solution for this exact case.

Finally a sensitivity analysis was performed as a verification of both the finite difference approach and the theoretical developments outlined in the previous section. Two main predictions were made there. The first was that the diffusion profile of the metal solute should be invariant with constant KD_C. The second was that the diffusion profile of the metal solute will approach an error function if $(KD_C/B_I^2)/D_B<0.1$. These conclusions are in agreement with calculations, shown in Figure 2.1.10 for various combinations of KD_C, keeping B_I and D_B constant. The negative deviation from error function behaviour with increasing $(KD_C/B_I^2)/D_B$ is a consequence of greater internal precipitation. It should be realized that by changing D_B the shapes of the profiles will change substantially.

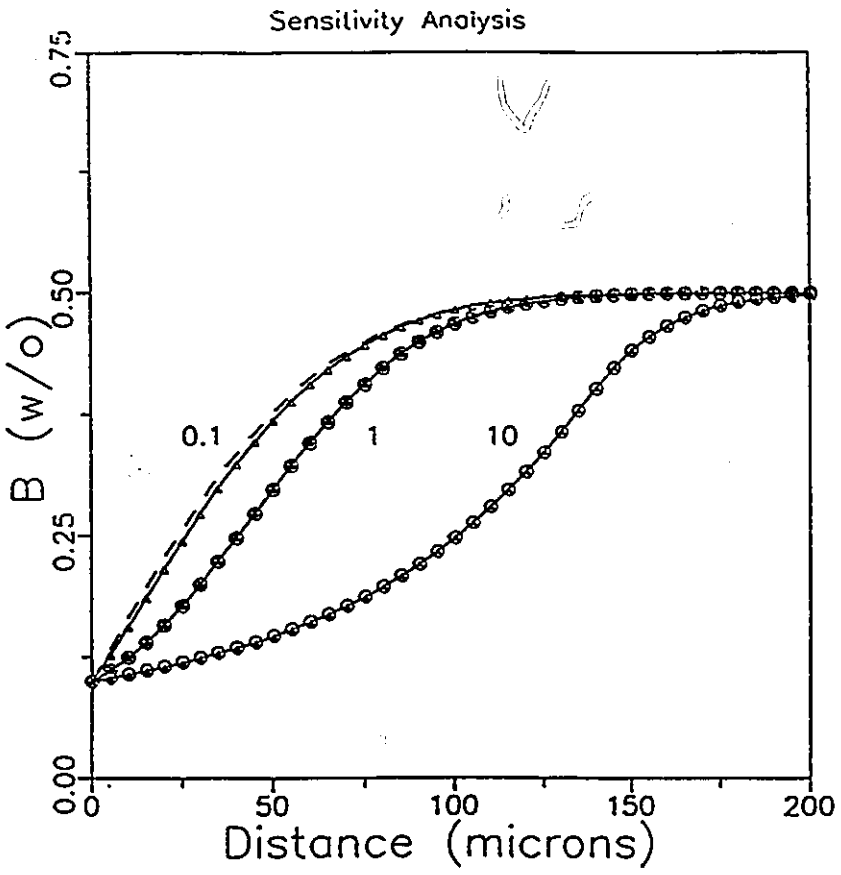

Figure 2.1.10: Sensitivity analysis pertaining to internal precipitation effects. Each profile represents a constant value of $(KD_C/B_I^2)/D_B$ for constant B_I and D_B. The points on each curve represent differing order of magnitude values of K or D_C, but still maintaining the product KD_C constant. The dashed line represents the error function solution for external oxidation (equation 2.1.9) which is approached by the $(KD_C/B_I^2)/D_B$ =0.1 curve. With increasing $(KD_C/B_I^2)/D_B$ the profiles are increasingly deflected from the error function solution due to internal precipitation.

2.2 Geometrical Models of Interface Structures.

Introduction:

One of the simplest and most general approaches to the understanding of interface structure is a geometrical one. In this chapter the commonality of dislocation models, O-Lattice theory, coincidence site lattice (CSL) theory and plane matching theory of interfaces will be outlined. Examples of interphase boundary structures (particularly of metal/ceramic systems) will be considered at the end of this section.

2.2.1: Dislocation Models:

Prior to 1940 a grain boundary was envisioned as an amorphous layer separating the two crystals adjacent to it. At this time Bragg and Burgers (1940) proposed a model for low angle grain boundaries. This model regarded the two crystals as juxtaposing in such a manner that the misfit between them was locally accommodated by an array of dislocations forming an interface. This is illustrated in Figure 2.2.1. for a low angle tilt boundary. (A pure tilt boundary is one in which the rotation axis is in the plane of the interface. A pure twist boundary has the rotation axis normal to the interface). The dislocation spacing, D, is given by

$$D=b/(2\sin\theta/2)\approx b/\theta \qquad (2.2.1)$$

where b is the lattice parameter (which is also the Burgers vector of the edge dislocation in this case) and θ is the angle of rotation. The energy (E) of such an array of dislocations was first determined by Read and Shockley (1950), with the result that

$$E=\tau_o\theta(A_o-\ln\theta) \qquad (2.2.2)$$

where

$$\tau_o=Gb/4\pi(1-\sigma) \qquad (2.2.3)$$

and

$$A_o=1+\ln(b/2\pi r_o) \qquad (2.2.4)$$

A_o is regarded a constant which is material dependent and found to be around 0.23 for some metals (Brooks 1952), r_o is some arbitrary cut off distance which accounts for the core energy of the dislocation, G is the shear modulus and σ is the Poisson ratio. The solution to this equation is shown by the solid line in Figure 2.2.2. There are several intractable problems to this approach. For example when $\theta\approx15°$, the spacing between dislocations is approximately 4a (where a is the lattice parameter). At this separation the core regions are considered to overlap, so that the superposition of single dislocation energies is no longer valid. In fact in many systems the energy is found to be

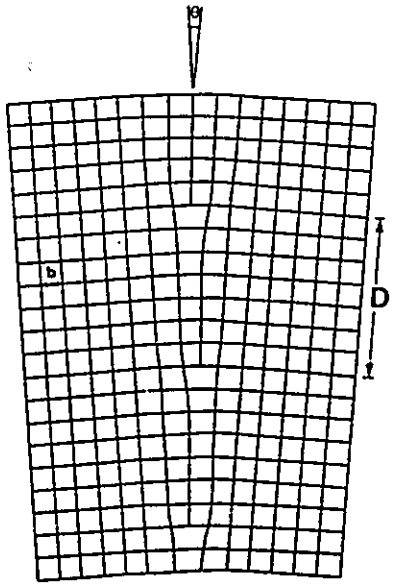

Figure 2.2.1: Schematic Diagram of a simple tilt boundary.
(Forwood and Clareborough 1991)

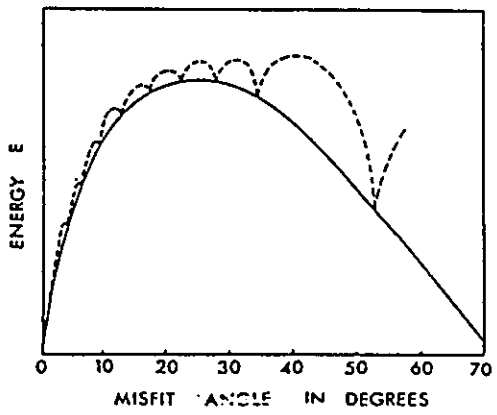

Figure 2.2.2: Energy of a simple tilt boundary. The solid line is the solution to Equation 2.2.2, while the dashed line is predicated by the hierarchial dislocation model. (Fletcher 1971)

independent of orientation beyond about 20°. Furthermore the energy plot should contain cusps and be symmetrical (the crystals are equivalent at rotations of 0° and 90°). In contrast, the calculation shows a maximum at about 30° and negative energies beyond 70°. Since dislocations must occur on atomic planes cusps should also appear when $\tan\theta=1/n$, where n is an integer. Deviations from these exact angles are accompanied by an additional superimposed grid of 'second order' dislocations which increase the energy around each cusp (dashed line in Figure 2.2.2) (Read and Shockely 1950). Energy cusps will be further explored in the coincidence site lattice (CSL) theory.

Van der Merwe (1950)(1963) obtained the same functional form (Equation 2.2.2) for the energy of a misfit, tilt and twist boundary using a different approach. A sinusoidal potential was assumed for the inter-atomic interaction between the atoms and linear elasticity theory was used to calculate the strain energy on either side of the interface. The advantage of this approach is that it solves the energy of the core of the dislocation explicitly. The results of a calculation of energy versus misfit (δ) is shown in Figure 2.2.3, where the energy rapidly increases near zero misfit. Van der Merwe went on to show that below a critical thickness it was energetically favorable for the interface to remain coherent as opposed to forming dislocations. This has important implications for small elastically constrained crystals and in strained-layer semiconductor work.

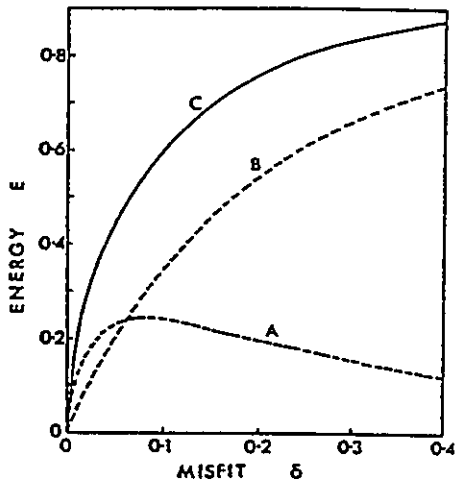

Figure 2.2.3: Interfacial energy versus misfit. Curve A shows the elastic strain energy in the two half crystals, curve B shows the misfit energy due to the sinusoidal potential at the interface and C is the total energy. (Fletcher 1971)

Frank (1950) developed a general treatment for the total Burgers vector content of a grain boundary. Since the energy of an interface scales with its Burgers vector content favorable interfaces should correspond to those that have the smallest total Burgers vector content. The geometrical formation of a boundary is shown in Figure 2.2.4. A square lattice is sectioned along A'A (Figure 2.2.4a), each section is then rotated by $\pm\theta/2$ (Figure 2.2.4b) about a unit vector **u** through O, normal to the plane of the figure. Both lattices are extended until they juxtapose at the original cut thus forming a grain boundary (Figure 2.2.4c) with unit normal v. A vector **x** is chosen in the boundary plane extending over several unit cells. The net Burgers vector intercepting **x** can be found in the following way, using the finish/start right hand (FS/RH) convention, with the closure failure being made in the perfect lattice. A Burgers circuit is started at **S** in Figure 2.2.4c, i.e. the end point of **x**, extends through lattice (+) to the origin and then returns through lattice (-) to the point F which is coincident with S. In the reference lattice (Figure 2.2.4d), the first part of the circuit **SO**, is represented by $\mathbf{S_+O}$ and the second part of the circuit **OF** is represented by $\mathbf{OF_-}$. There is a closure failure $\mathbf{F_-S_+=B}$ in the reference lattice and this defines the net Burgers vector of those dislocations which are intersected by the vector **x**. In general the vector **x** can make any angle with **u** and therefore.

$$\boldsymbol{B}=2\sin(\theta/2)(\boldsymbol{x}\wedge\boldsymbol{u}) \qquad (2.2.5)$$

and with respect to Figure 2.2.4e,

$$|\boldsymbol{B}|=|\boldsymbol{x}|2\sin(\theta/2)\sin\alpha \qquad (2.2.6)$$

This analysis can be generalized to any interface boundary (Bilby 1955) with reference to Figure 2.2.4d. The net Burgers vector is

$$\boldsymbol{B}=\boldsymbol{F\_S_+}=\boldsymbol{OS_+}-\boldsymbol{OF\_} \qquad (2.2.7)$$

If $\mathbf{R}_+$ is defined as the rotation $(\mathbf{u},+\theta/2)$ which transforms the reference lattice into (+), and $\mathbf{R}_-$ as the rotation $(\mathbf{u},-\theta/2)$ which transforms the reference lattice into (-), then

$$\begin{aligned}\boldsymbol{OS_+}&=\boldsymbol{R^{-1}_+x}\\ \boldsymbol{OF\_}&=\boldsymbol{R^{-1}\_x}\end{aligned} \qquad (2.2.8)$$

so that

$$\boldsymbol{B}=(\boldsymbol{R^{-1}_+}-\boldsymbol{R^{-1}\_})\boldsymbol{x} \qquad (2.2.9)$$

If lattice (+) is taken to be the reference lattice then

$$\boldsymbol{B}=(\boldsymbol{I}-\boldsymbol{R^{-1}})\boldsymbol{x} \qquad (2.2.10)$$

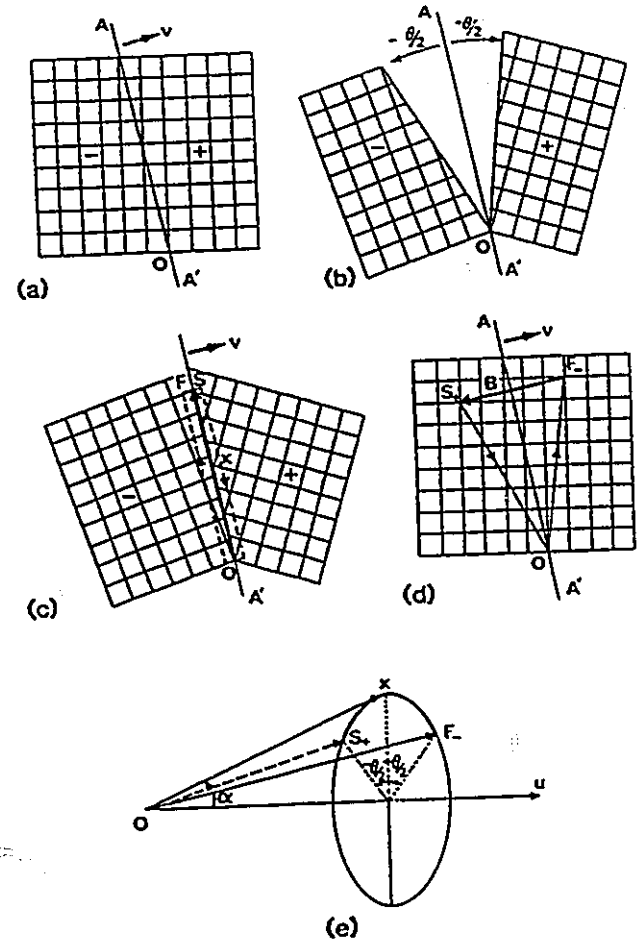

Figure 2.2.4: Schematic illustration of the derivation of the net Burgers vector **B** crossing a vector **x** in a planar grain boundary AA′ with unit normal ν. See text for details.(Forwood and Clareborough 1991)

where **R** is the rotation which transforms lattice (+) into lattice (-) and **I** is the identity matrix. This approach is easily generalized to any transformation **A** which transforms lattice (+) to lattice (-)

$$B=(I-A^{-1})x \qquad (2.2.11)$$

As will be shown in the next section this is equivalent to Bollman's O-Lattice approach.

2.2.2: O-Lattice Theory:

Instead of regarding the dislocations as being continuous, Bollman (1969) took the dislocations as being discrete lattice vectors. Since Bollman's procedure will be emphasized throughout this work, we will develop this procedure and give a sample calculation so that the reader may become familiar with the method. The two lattices, 1(+) and 2(-), are envisioned as having a common coordinate origin and allowed to interpenetrate and fill all of space. Analogous to Bilby's approach a transformation **A** can be defined relating the nearest neighbour atom positions of the two lattices near the origin

$$x^{(2)}=Ax^{(1)} \qquad (2.2.12)$$

where $\mathbf{x}^{(1)}$ and $\mathbf{x}^{(2)}$ are vectors of lattice 1 and 2 respectively. Bollman postulated that

there are certain equivalence classes of positions in the two lattices, which need not be atom positions, termed O- lattice points $\mathbf{X}^{(o)}$.

$$x^{(2)}(C^{(2)})=x^{(1)}(C^{(1)})+b_l=x^{(o)}(C) \qquad (2.2.13)$$

where the $C^{(2)}$ and $C^{(1)}$ refer to the equivalence class positions and $\mathbf{b}_l$ are the Burgers vector. Relating Equation 2.2.12 to Equation 2.2.13 yields

$$x^{(o)}=A^{-1}x^{(o)}+b_l \qquad (2.2.14)$$

and

$$b_l=(I-A^{-1})x^{(o)} \qquad (2.2.15)$$

Comparison of Equation 2.2.11 with 2.2.15, shows the similarity between Bilby's and Bollman's approach. The solution of the O-lattice is therefore

$$x^{(o)}=(I-A^{-1})^{-1}b_l \qquad (2.2.16)$$

or

$$x^{(o)}=T^{-1}b_l \qquad (2.2.16a)$$

where

$$T=(I-A^{-1}) \qquad (2.2.17)$$

The positions represented by the O-lattice points are therefore positions of best fit. The positions between the O-lattice points are consequently positions of worst fit and are idealized to collapse into cell walls. It is the intersection of the boundary with the cell walls that becomes the dislocation network. Once the boundary plane is chosen, lattice 1 and 2 are then allocated to their respective sides of the boundary. There are several problems with O-lattice theory. First, the choice of the transformation **A** may not be unique. Second, the regions of poor misfit may not collapse to form discrete dislocations. Finally, for interphase boundaries it is often not clear which of the two crystals should be used as lattice 1 and therefore which Burgers vectors should be used. Despite these uncertainties O-lattice theory has been successful in predicting dislocation structures in a number of systems particularily those of FCC/BCC interfaces (Bollman 1974).

An sample calculation will be given of a simple rotation about [001] of a unit cube lattice to illustrate the O-Lattice method. The transformation in this case is a rotation **R** given by

$$A=R=\begin{vmatrix}\cos\theta & -\sin\theta\\ \sin\theta & \cos\theta\end{vmatrix} \qquad (2.2.18)$$

$$T^{-1}=\begin{vmatrix}1/2 & (1/2)cotan(\theta/2)\\ -(1/2)cotan(\theta/2) & 1/2\end{vmatrix} \qquad (2.2.19)$$

If cotan(θ/2)=3 (this is also a CSL relationship), shown in Figure 2.2.5, the O-lattice becomes

$$X^{o}=\left|\begin{array}{cc|cc} 1/2 & 3/2 & 1 & 0 \\ -3/2 & 1/2 & 0 & 1 \end{array}\right| \qquad (2.2.20)$$

$$X^{o}=\left|\begin{array}{cc} 1/2 & 3/2 \\ -3/2 & 1/2 \end{array}\right| \qquad (2.2.21)$$

where the basis vectors of the O-lattice are represented by the columns of Equation 2.2.21. The columns of the identity matrix **I** in Equation 2.2.20 represent the Burgers vectors of the simple cubic lattice. Every other O-point 'O' is also a coincidence site 'C' position in this particular example (Figure 2.2.5). The O-lattice will be a point lattice for rank (**T**)= 3, a line lattice for rank (**T**)= 2 or a plane for rank (**T**)= 1. Because rank (**T**)= 2 in the preceding example, each 'O' or 'C' point depicted in Figure 2.2.5, represents a line in the [001] direction. The space between these O-lines is now envisioned as containing the cell walls and consequently the dislocation lines. In this example the spacing of the dislocations lines is approximately the same size as that of the unit cell. When this situation arises it is perhaps more realistic to consider the interface in terms of coincidence site lattice (CSL) theory.

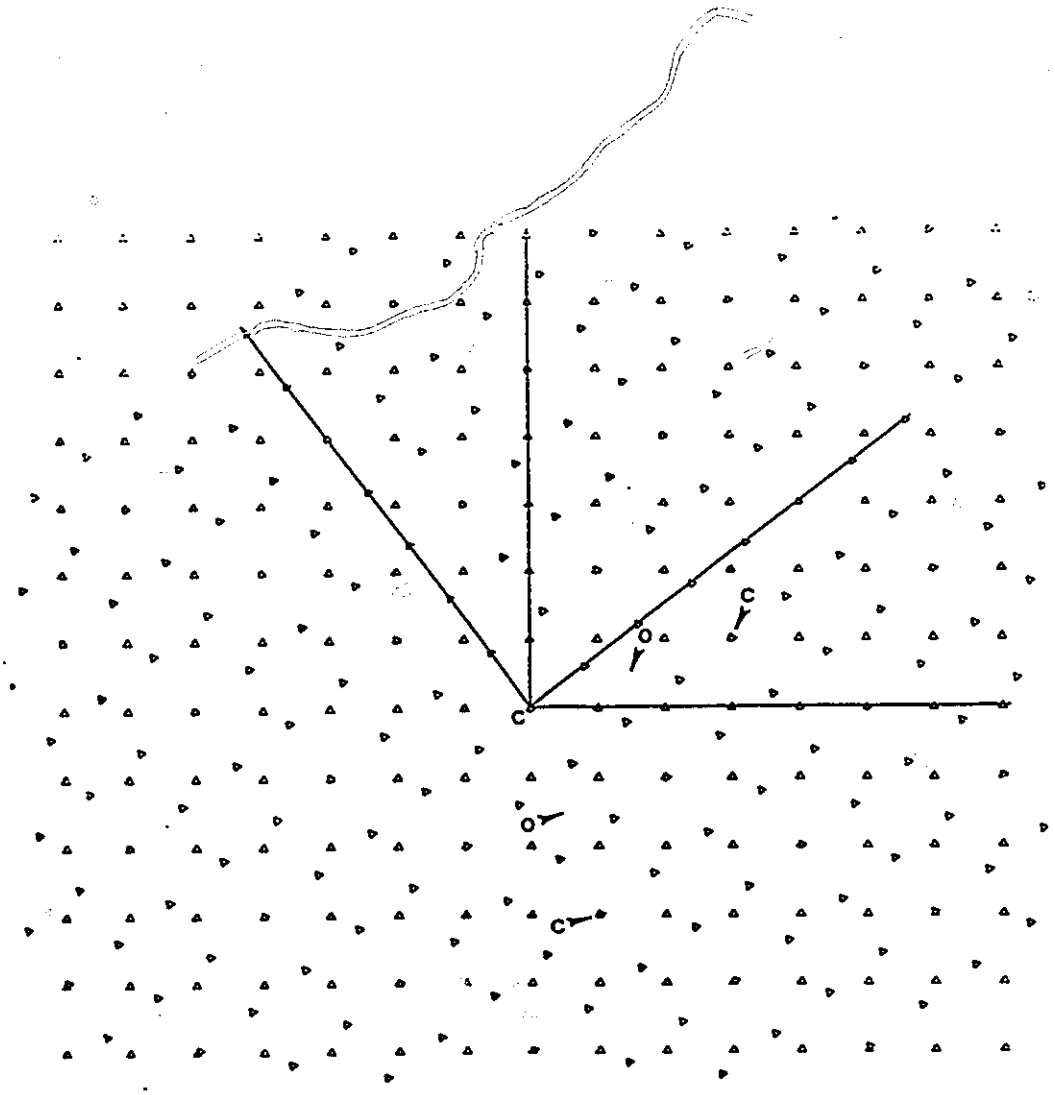

Figure 2.2.5: Two square lattices showing a rotation of 36.48°. The O- lattice points are indicated by 'O'. Every other O- point is also a coincidence lattice point 'C'.

2.2.3: Coincidence Site Lattices:

It was shown in the previous section (by way of example) that the CSL is a subset of the O-lattice. This is useful in that the O-lattice procedure may be used to determine CSL positions. In crystals of differing structure it is difficult to obtain exact coincidence between lattice points. The O-Lattice procedure can then be used to determine the configuration of the 'second order' or secondary dislocations which accommodate the misfit between near CSL points of the two crystals. The transformation A_{CSL} is this case is the one which maps the near CSL unit cell of lattice 1 (M_1) into the near CSL unit cell of lattice 2 (M_2). The translation vectors are the **DSC** (displacement shift complete) vectors. These vectors act as effective Burgers vectors and have the property that by displacing any one of the lattices by a **DSC** vector the complete near CSL pattern is recreated but shifted. The **DSC** vectors can consequently be of lower magnitude than the Burgers vector of the crystal. The reciprocity relationship states that the CSL in reciprocal space is the DSC lattice in real space and conversely the DSC lattice in reciprocal space is the CSL in real space (Grimmer 1974). The method of Bonnet and Durand (1975) can also be used to determine the DSC lattice. Consider the example shown in Figure 2.2.6, of the near coincidence cells M_1 and M_2 which have been separated into their respective DSC-1 and DSC-2 lattices (Balluffi, Brokman and King 1982). These DSC lattices can be determined in the following way. A transformation

A_{CSL} is defined such that

$$X^{M_2}=A_{CSL}X^{M_1} \tag{2.2.22}$$

and a new lattice 2′ is defined as

$$X^{2'}=A_{CSL}^{-1}X^{2} \tag{2.2.23}$$

As pointed out by Bonnet and Durand (1975) a DSC-1 lattice is formed by taking the difference (or sum) of the translation vectors of lattice 1 and 2′. A DSC-2 lattice can be defined in a similiar manner between lattice 1′ and lattice 2. The DSC-2 lattice can also be obtained from the DSC-1 lattice by applying the A transformation. This leads to an interpretation of interphase boundaries as a semicoherent boundary between the DSC-1 and DSC-2 lattices (Balluffi, Brokman and King 1982). The DSC lattice determined by these various means, however, may not be unique. For example Forwood and Clarebrough (1989) using image simulation techniques found for a fcc/bcc interphase boundary that the Burgers vectors were not the primitive basis vectors of the DSC lattice but a sum of multiples of the these vectors.

A sample calculation (Bollman 1982) will be shown for the secondary O-lattice between Al (fcc, a=4.04Å) and AlSb (ZnS-structure, a=6.13Å) forming a cube on

cube orientation relationship, with a (001) boundary plane. The structure of AlSb can be interpreted as two fcc lattices one of Al and the other of Sb displaced by [1/4,1/4,1/4]. The near CSL unit cells are identified from the fact that $3a_{Al} \approx 2a_{AlSb}$ and taking Al as lattice 1, with Al atoms taken to be the origin in both lattices. The CSL transformation is

$$A_{CSL} = \begin{vmatrix} 1.01155 & 0 & 0 \\ 0 & 1.01155 & 0 \\ 0 & 0 & 1.01155 \end{vmatrix} \qquad (2.2.24)$$

The equation for the secondary O-lattice becomes

$$X^{sec} = (I - A_{CSL}^{-1})^{-1} DSC \qquad (2.2.25)$$

Therefore

$$X^{sec} = \begin{vmatrix} 87.57 & 0 & 0 \\ 0 & 85.57 & 0 \\ 0 & 0 & 85.57 \end{vmatrix} \begin{vmatrix} 1.01 & 1.01 & 1.01 \\ -1.01 & 1.01 & 0 \\ 0 & 0 & 1.01 \end{vmatrix} \qquad (2.2.26)$$

The DSC-1 vectors are given by the columns of the second matrix in Equation 2.2.26 (i.e. b_1=[1.01 -1.01 0], b_2=[1.01 1.01 0] and b_3=[1.01 0 1.01]). These represent the difference vectors between the Al and the AlSb' ($a_{AlSb'}$= 6.06Å) lattice. The

secondary O-lattice is therefore.

$$X^{sec}=\begin{vmatrix} 88.45 & 88.45 & 88.45 \\ -88.45 & 88.45 & 0 \\ 0 & 0 & 88.45 \end{vmatrix} \qquad (2.2.27)$$

A diagonal square dislocation network of edge dislocations is predicted from Equation 2.2.27 and is shown in Figure 2.2.7 for a (001) boundary plane.

Measurements of boundary energy often show that the lowest energy boundaries are those having a large number of coincidence lattice points. The Σ designation is often used to descibe CSL boundaries and refers to the ratio of the volume of the CSL unit cell to the volume of the crystal unit cell. The grain-boundary energy of Al as a function of misorientation is shown in Figure 2.2.8, where sharp cusps can be observed at 'special' low Σ values (Otsuki and Mizuni 1986).

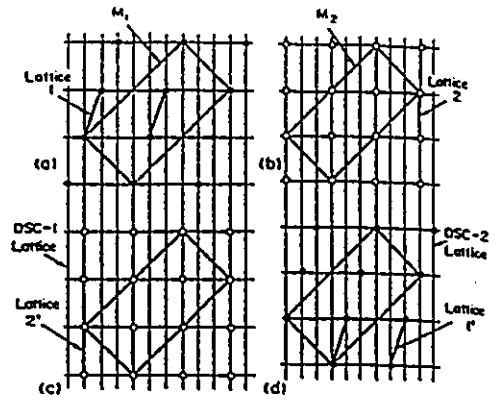

Figure 2.2.6: Formation of the DSC-1 and the DSC-2 lattice from M_1 and M_2 respectively. (Balluffi et. al. 1982)

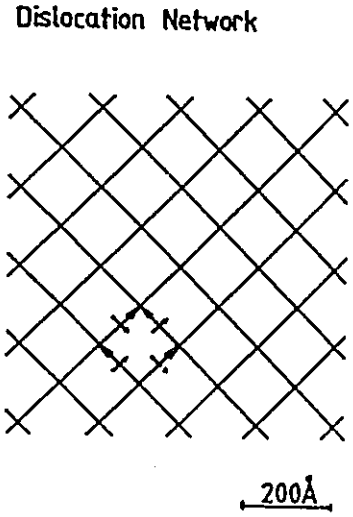

Figure 2.2.7: Predicted secondary dislocation structure of a (100) cube on cube interphase boundary between Al and AlSb. (Bollman 1982)

2.2.4: Plane Matching Theory:

Plane matching theory has been shown to be the one dimensional analogue of O-Lattice theory (Bollman 1974). Furthermore Balluffi and Schober (1972) have also suggested that plane matching theory can be interpeted as a limiting case of the CSL model in certain instances. In plane matching theory Pumphrey (1972) ascertained that crystallographic planes of low index may match particularly well across an interface. The misfit may be accommodated by 'plane matching dislocations' whose spacing and orientation are given by the Moiré spacing formulae (Equations 2.2.28 and 2.2.29). This is shown by the Moiré pattern in Figure 2.2.9, where the coarse set of fringes are interpreted as being dislocations. The spacing (D_M) and orientation ($\sin\rho$) of the dislocations are given by

$$D_M = \frac{s_1 s_2}{(s_1^2 + s_2^2 - 2 s_1 s_2 \cos\theta)^{1/2}} \qquad (2.2.28)$$

$$\sin\rho = \frac{s_1 \sin\theta}{(s_1^2 + s_2^2 - 2 s_1 s_2 \cos\theta)^{1/2}} \qquad (2.2.29)$$

where S_1 and S_2 are the projected spacings on the boundary plane and θ is the angle between them. ρ is the angle between S_1 and the dislocation. The Burgers vectors of these dislocations is given by the interplanar spacing of crystal 1. It is interesting to note that this result was anticipated by Hirsch et. al. (1964).

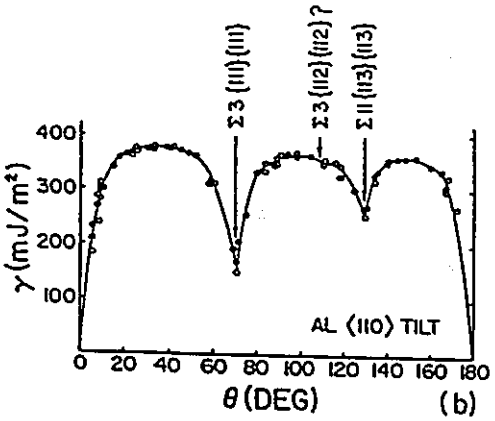

Figure 2.2.8: Grain boundary energy versus orientation for Al. (Otsuki and Mizuni 1986)

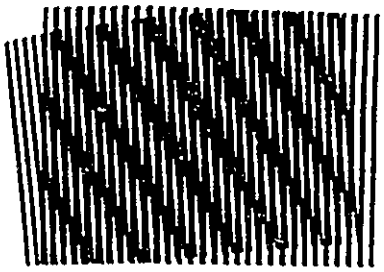

Figure 2.2.9: Moiré pattern showing plane matching dislocations. (Pumphrey 1972).

They noted that the Moiré fringe spacing ($D_M=d/\delta$) and the dislocations spacing given by Van der Merwe ($D_d=|b|/\delta$) would be identical if $|b|=d$, where d is the interplanar spacing. Finally it has been pointed out (Wolf 1985) that parallelism of low index planes may be a crucial criterion for the formation of low energy interfaces.

2.2.5: Examples of Interphase Boundaries:

i) Ceramic/Ceramic and Metal/Ceramic Interphase Boundaries:

a) MgO/CdO

The remainder of this review will focus on interphase structure and orientation relationships observed in ceramic/ceramic and metal/ceramic systems since these are closely related to this work. There is a set of experiments referred to as rotating crystallite experiments where a large number of ceramic or metal single crystal spheres (about 1 μm in diameter) are placed on an oriented ceramic substrate and annealed at a suitable temperature. If the temperature is high enough the particles may rotate into low energy positions which can be determined by X-ray diffraction or electron diffraction techniques. The distribution of cuboidal CdO particles bounded by {100} faces produced by a 'smoke technique' collected on a heated (100) MgO substrate are shown in Figure

2.2.10 as a function of orientation (H. Mykura and co-workers 1980). There is clearly a non-uniform distribution of particles as a function of orientation, with conspicuous gaps in the distribution of these particles. Schematic diagrams of the hypothetical atom positions for some of these orientations on (100) are shown in Figure 2.2.11 with respect to Figure 2.2.10. In Figure 2.2.11 the positions labeled 'C' are the near coincidence sites (between like ions) of the two interpenetrating lattices (these are also O-lattice points). The positions labeled 'A' refer to anti-coincidence points (coincidence between unlike charged ions) and are not O-lattice points. The areas between the 'C' points are envisioned as collapsing to form primary dislocation structures with a spacing in the order of the unit cell, suggesting that CSL theory may be more appropriate in this situation. A closer examination of these patterns is instructive. The schematic diagram for a misorientation of 7.5° corresponding to the first preferred orientation on (100)MgO is shown in Figure 2.2.11a. Figure 2.2.11b shows the 'forbidden' orientation at 10.5°, Figure 2.2.11c shows the pattern at 23° while Figure 2.2.11d corresponds to the forbidden orientation at 26.5°. Although small CSL units are observed at 10.5° and 26.5°, these orientation relationships were not observed. The reason is that these CSL relationships form a high density of 'anti-CSL' points, i.e. between triangles and squares in Figure 2.2.11. Furthermore there are no positions of anion coincidence (taking the cation as origin). The CSL corresponding to rotations of 7.5° and 23° have the symmetry of the NaCl structure with both anion and cation coincidence occuring in equal numbers. It would appear that interfaces of low energy try to preserve the symmetry of the original

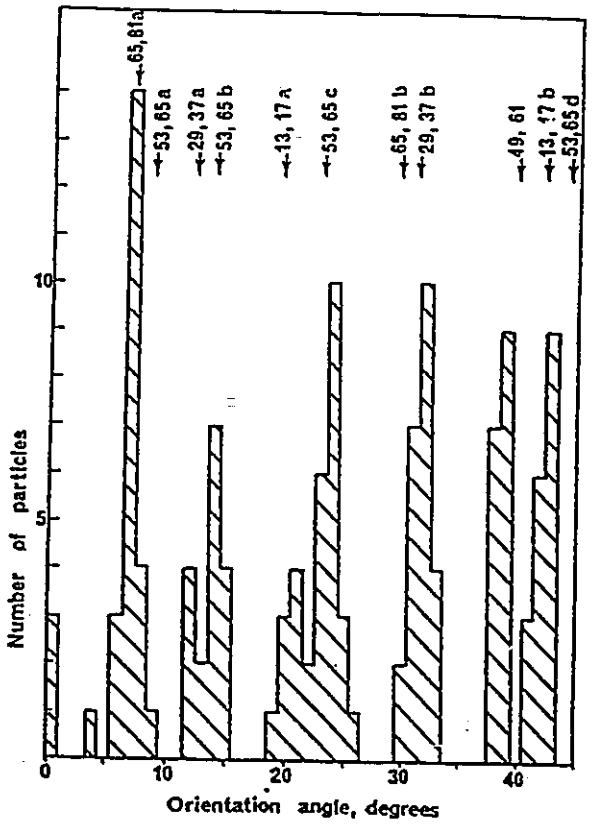

Figure 2.2.10: Number of particles versus orientation for CdO crystallites on (100)MgO. (Mykura et. al. 1980)

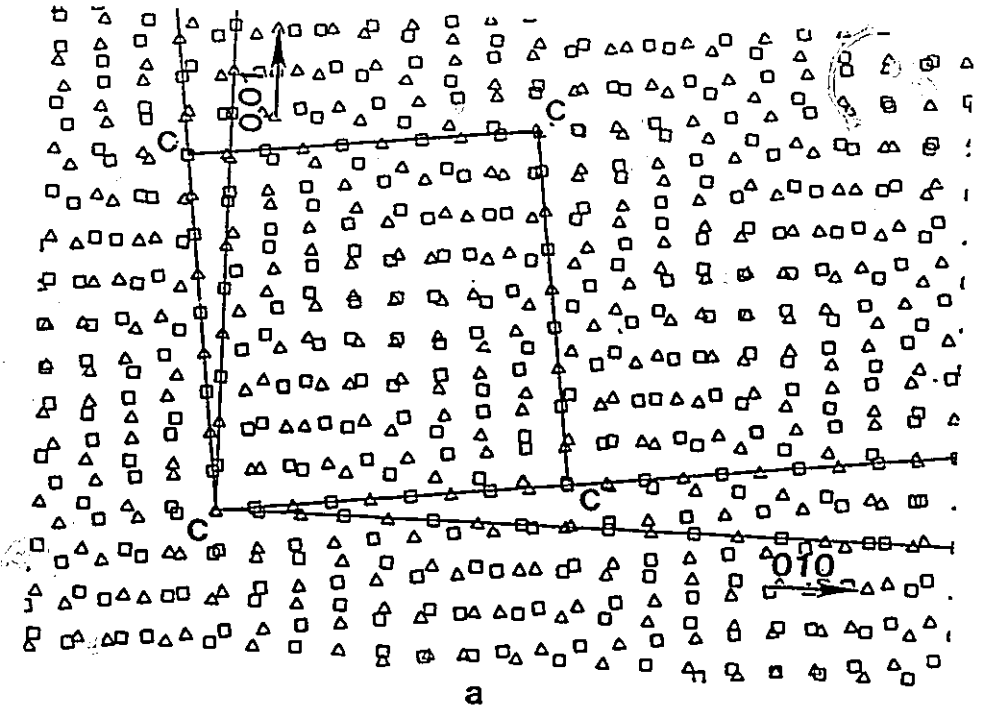

a

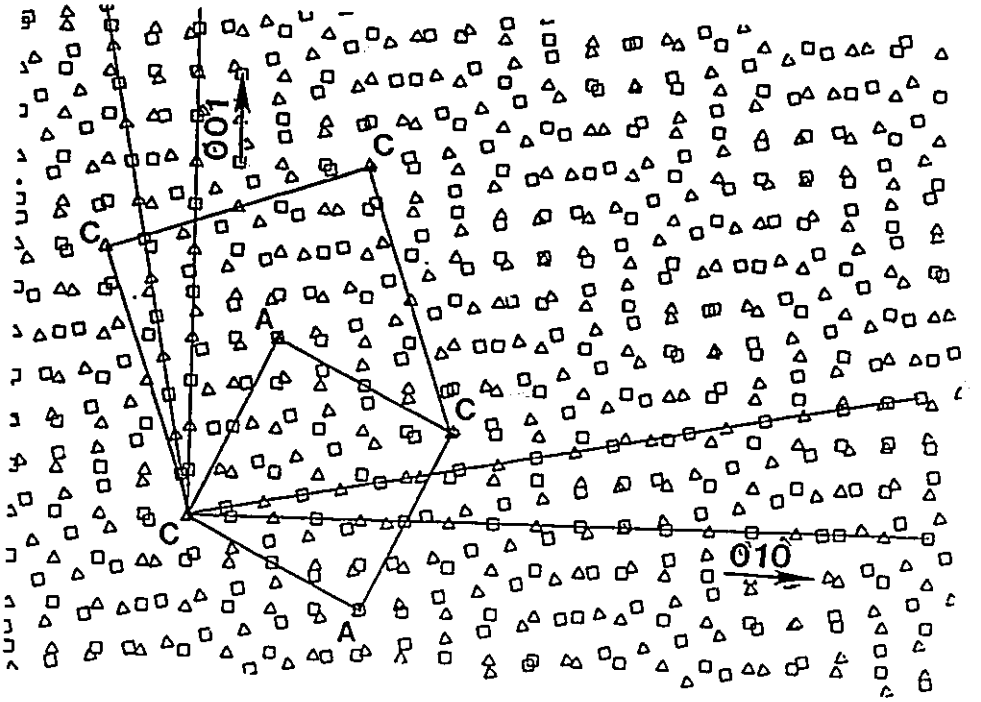

b

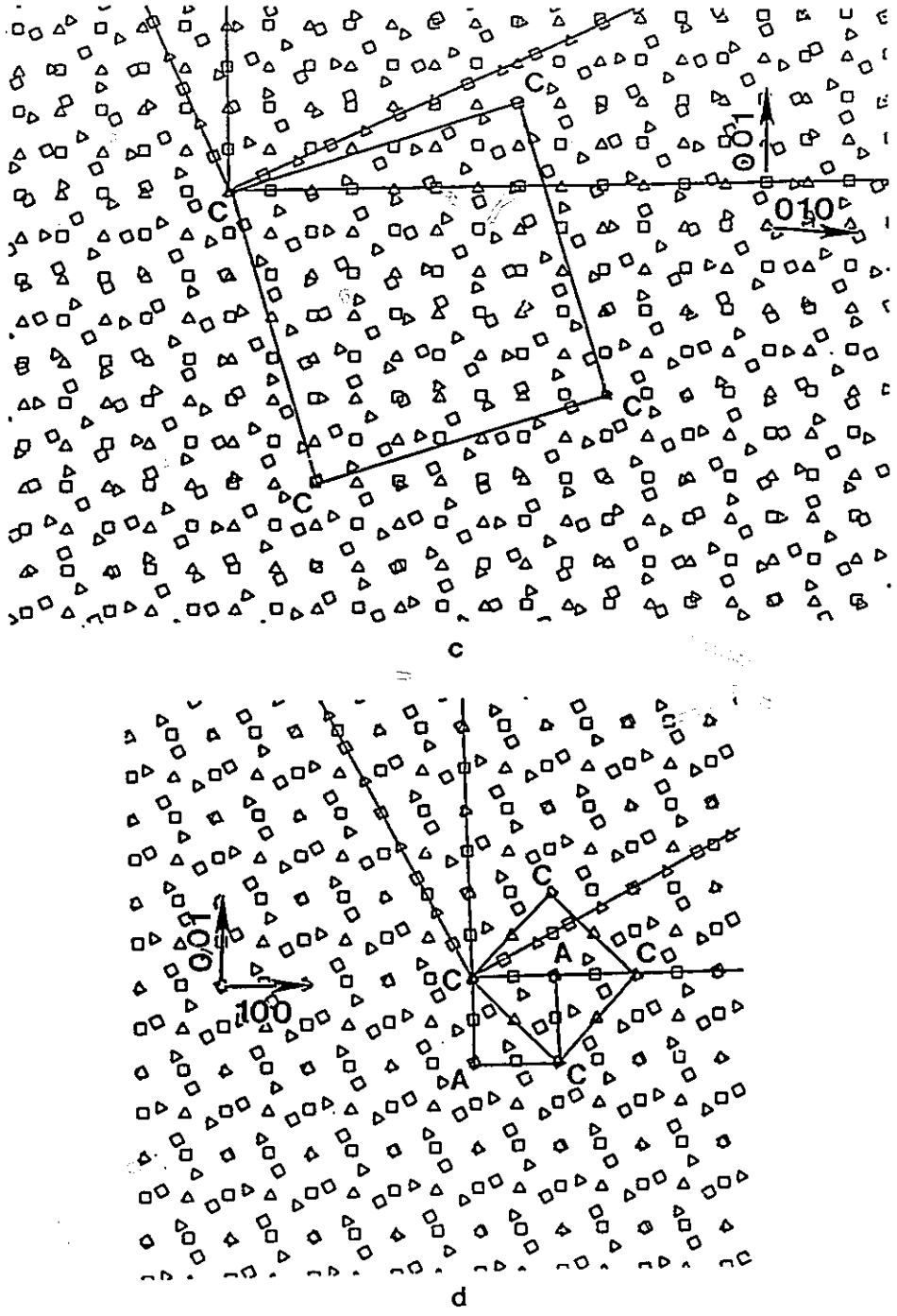

Figure 2.2.11: Schematic diagrams showing rotations of
a) 7.5°, b) 10.5°, c) 23°, and d) 26.5° in MgO/CdO. The triangles and squares are cation and anion positions respectively. C is a near coincidence site and A is a near 'anti'- coincidence site. Indices are with respect to CdO.

crystal as much as possible. The small peak (Figure 2.2.10) at a misorientation of 0° (known as the cube on cube orientation relationship) was also observed, despite the appearance of 'anti-CSL' sites between the CSL points (Figure 2.2.12). O-Lattice theory in this case predicts that the 'anti-coincidence' sites would correspond to the 'dislocated' regions at the interface. Although many of the peaks in distribution were CSL relationships, the Σ values for many of these orientation relationships (Figure 2.2.10) were in excess of 50, indicating that local minima in interphase boundary energy can be found with relatively high Σ values.

b) NiO/Pt System

In a study of hot pressed polycrystalline Pt to (100) NiO, Shiue and Sass (1991) found four different orientation relationships. These were 1/ $(001)_{Pt} \| (001)_{NiO}$ $[110]_{Pt} \| [110]_{NiO}$ (cube on cube); 2/ orientation relationship 1 with a 0.5° to 3° rotation about [001]; 3/ $(\bar{1}23)_{Pt} \| (001)_{NiO}$ with $[210]_{Pt}$ 12° away from $[\bar{1}10]_{NiO}$ and 4/$(\bar{1}14)_{Pt} \| (001)_{NiO}$ with $[110]_{Pt}$ 8° away from $[100]_{NiO}$. They were able to observe primary O-Lattice dislocations with high resolution electron microscopy. What was not stated in their work was that orientations 1,2,3,4 were also CSL relationships. Schematic diagrams of orientations 3 and 4 are shown in Figures 2.2.13a and 2.2.13b respectively. The CSL unit cell is taken between like cations. At the center of these

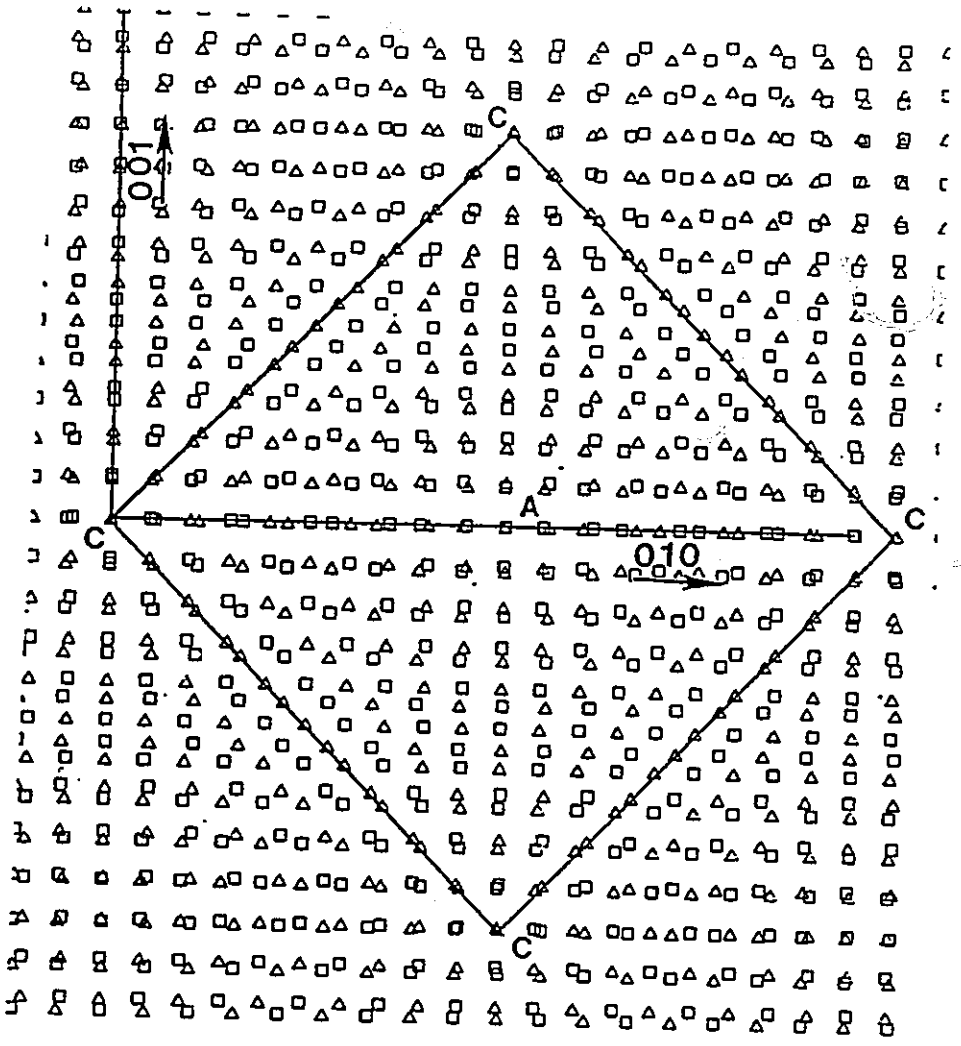

Figure 2.2.12: Cube on cube orientation relationship for MgO/CdO.

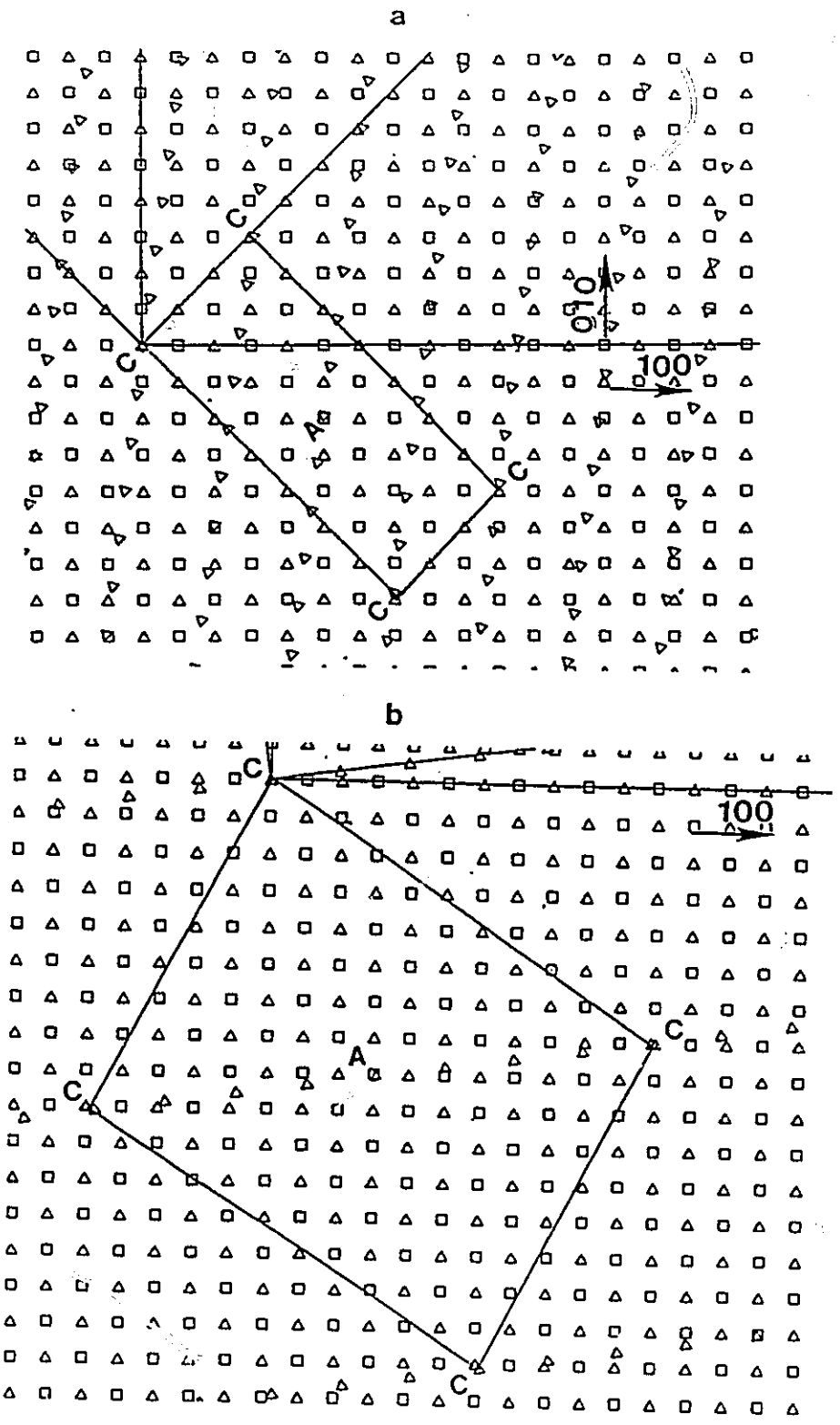

Figure 2.2.13: Schematic diagram of atom positions for a) orientation 3 and b) orientation 4 in NiO/Pt. See text for details. Indices are with respect to NiO.

CSL units is an 'anti-CSL' position, which does not appear to unduly increase the energy of these interfaces in contrast to many of the MgO/CdO interfaces. It is noteworthy that interfaces were produced with high index planes which would indicate that in these systems low energy interfaces need not always be composed of low index planes between the constituent crystals. In these cases, however, the interface might be expected to be stepped.

c) Cu/MgO and Pd/MgO

i) Rotating Cu Crystallites on MgO

In rotating crystallite experiments Fecht and Gleiter (1985) found only the cube on cube orientation relationship ($(001)_{Cu} \| (001)_{MgO}$ with $[110]_{Cu} \| [110]_{MgO}$) shown in Figure 2.2.14. This result has fuelled arguments (Sutton and Balluffi 1991) that low energy interfaces cannot be judged solely on a geometrical basis, since other near CSL relationships shown in Table 2.2.1 for Cu/MgO were not observed (Γ refers to the number of CSL points in the boundary plane per unit lattice parameter, ϵ refers to the maximum strain required to reach an exact CSL relationship, M and I refer to the metal and the

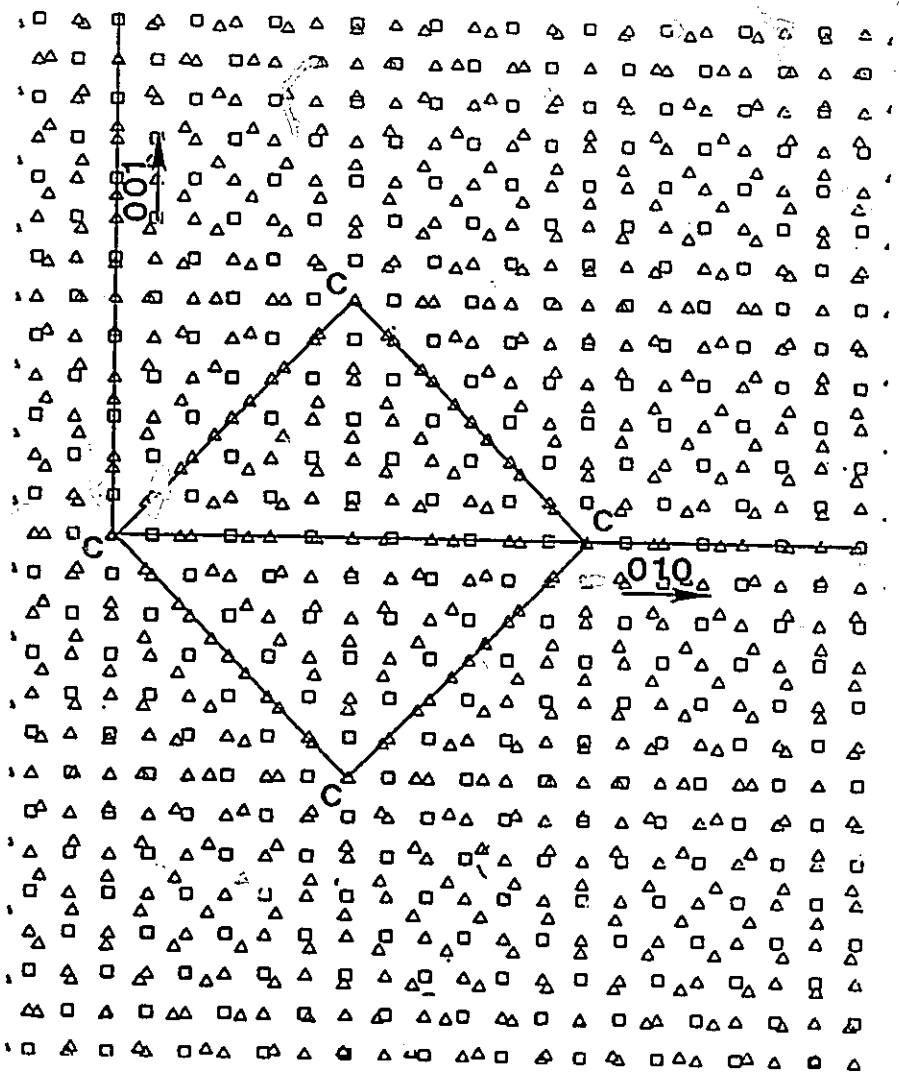

Figure 2.2.14: Cube on Cube orientation relationship for Cu/MgO.

oxide component respectively).

Table 2.2.1
Possible CSL Orientation Relationships in (100)Cu/(100)MgO

Orientation	maximum $\|\epsilon\|$%	$\Gamma(a_m^{-2})$	corrected $\|\epsilon\|$%
$<110>_M \| <100>_I$	1.3	0.08	1.1
$<710>_M \| <100>_I$	1.3	0.08	1.1
$<110>_M \| <110>_I$	0.3	0.04	0.06
$<100>_M \| <110>_I$	2.2	2	-
$<210>_M \| <310>_I$	2.2	0.2	-

Although Sutton and Bailuffi's argument is well justified in systems such as CdO/MgO, where strong chemical effects were noted to be important (i.e., interfaces with a large number of anti- CSL points per unit area were not observed), their argument for the Cu/MgO system is not entirely valid. There are a number of points which need to be addressed in Table 2.2.1. First, the strain needed to obtain the near CSL relationships has been recalculated in column 4. For example, the value of $|\epsilon|$ for the cube/cube CSL orientation relationship (6 MgO unit cells ≈ 7 Cu unit cells) is 0.06% not 0.3% as given in column 3 of Table 2.2.1. Of the five CSL relationships listed in Table 2.2.1 only three are unique: $<710>_M \| <100>_I$ is identical to $<210>_M \| <310>_I$ and $<110>_M \| <100>_I$ is identical to $<100>_M \| <110>_I$. The larger values of ϵ and Γ noted in Table 2.2.1 for these duplicate orientation relationships are other near coincidence cells

requiring greater strain. Although the absence of some of the near CSL relationships is intriguing, it would seem to indicate that strain plays an important role in rotating crystallite experiments. Since the strain energy scales with volume this should not be surprising. The CSL relationship observed was the one with the least strain although not the highest Γ. Furthermore discrepancies sometimes arise in different studies; e.g. orientation relationships not observed by one group (P. Chaudhari and H. Charbnau 1972) have been found by others (H. Mykura and co-workers 1980).

ii) Internal Oxidation/Reduction

Internal oxidation/reduction experiments are an excellent means of fabricating metal/ceramic interfaces because artifacts originating from the manufacturing process are avoided. The problem then is one of nucleation and growth. The critical nucleus size and shape is almost exclusively governed by capillarity and the system will select orientation relationships that minimize its interfacial energy. In an internal oxidation study of Cu-Mg and Pd-Mg, Lu and Cosandy (1992) observed three different types of interfaces with high resolution microscopy. The orientation relationships observed were of the cube on cube type with both (100) and (111) planes forming the bounding interfacial plane in Pd/MgO. A 60° rotation normal to (111) termed a twin configuration was also observed in Pd/MgO. Cu/MgO showed only the cube on cube orientation relationship bounded by (111) planes. Misfit dislocations spaced about 22 Å

apart were observed. In a similar study H. Jang et. al. (1993) using atom probe field ion and high resolution microscopy, determined that the terminating layer of (111) MgO produced by internal oxidation of Cu-Mg alloys was an oxygen layer related by a cube on cube orientation relationship to (111)Cu. Misfit dislocations were also observed with an average separation of 13 Å. In contrast to this in an internal reduction study of (CuMg)O the [010]MgO ‖ [112]Cu with (100)MgO ‖ $(11\bar{1})$Cu orientation relationship was observed (Backhaus-Ricoult and S.Hagège 1992). The small planar CSL unit cell for this orientation relationship is shown in Figure 2.2.15. It is not clear why the Cu/MgO system shows such complex behavior. In ionic (NaCl type) crystals the (111) plane is of high energy; it is therefore surprising that the cube/cube orientation relationship with (111) interfaces is observed. Recent high resolution electron microscopy results in the Ag/CdO system suggest that steps may also form at these interfaces exposing a terminating Cd metal layer (Chan and co-workers 1994). In addition it is not understood why Pd/MgO shows both (111) and (100) interfaces.

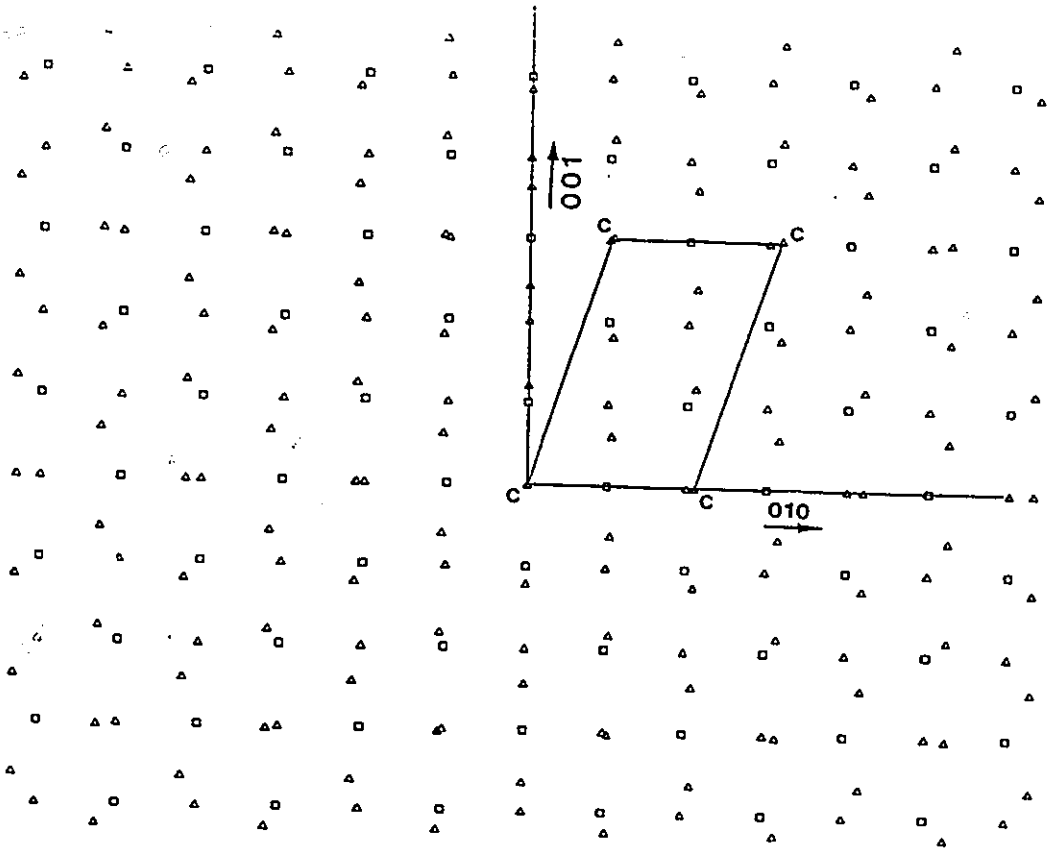

Figure 2.2.15: Near CSL relationship found in Cu/MgO with [112]Cu ‖ [010]MgO with $(1\bar{1}1)$Cu ‖ (100)MgO. Indices are with respect to MgO

2.3: Physical and Chemical Properties of the Ni-Ti-N:

The Ni-Ti-N system remains largely unexplored despite the growing interest in this system for cermets. The 1100°C isotherm due to Binder et. al. (1991) shown in Figure 2.3.1 is at present the only assessment of the Ni-Ti-N ternary. The Ni rich end of the diagram remains undefined. Ni is an FCC phase with a room temperature lattice parameter of 3.523 Å (Wriedt 1991). No nickel nitride phases have been produced from Ni and N_2 gas at any temperature. Ni_3N and Ni_4N have, however, been reported to form from the reaction of NH_3 and Ni below 600°C. Furthermore, little is known about the solubility of N in Ni other than that it is very low. Wriedt (1991) gives the solubility as 8±8 ppm (atom basis). The Ni-Ti system has a wide single phase region of up to 12 w/o Ti, as shown in Figure 2.3.2, at which point the intermetallic Ni_3Ti forms. The Ti-N system has been extensively investigated. Ohanti and Hillert (1990) summarize Gibbs free energy of formation data on TiN and Ti_2N. The phase diagram (Figure 2.3.3) shows a high solubility of N in Ti, with two nitride phases Ti_2N and TiN_x, where $0.3 \leq x \leq 1.1$. The lattice parameter of TiN as a function of composition is shown in Figure 2.3.4. Despite the appearance of Ti_2N below 1100° C, this nitride has never been observed in any of the Fe-Ti-N internal nitridation work (Kirkwood et. al. (1974), Wada and Pehlke (1985)). A summary of important data on TiN and Ni are shown in Table 2.3.1.

Table 2.3.1
Physical Properties of TiN and Ni

Properties	Ni	TiN
Crystal Structure	fcc (S.G.:Fm3m)	NaCl (S.G.:Fm3m)
Melting Temperature	1453°C	3290°C
Lattice Parameter RT	3.523 Å	4.241 Å
Thermal Expansion α	13 x 10^{-6} /°C	9.35 x 10^{-6} /°C (1)
Young's Modulus	214 GPa	599 GPa (2)
Density	8.9 g/cm^3	5.2 g/cm^3

(1) Toth (1971)

(2) Portnoi, Mukaseev, Gribkov, and Levinskii (1968)

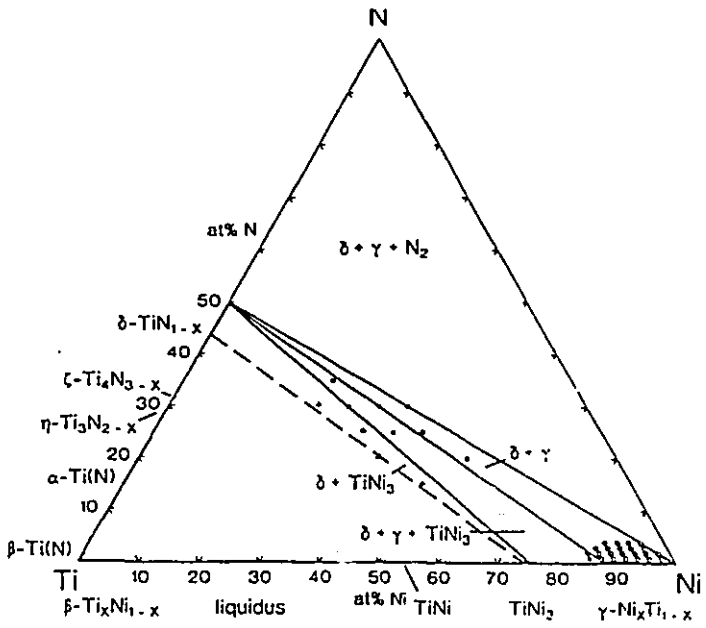

Figure 2.3.1: 1100° C isotherm of Ni-Ti-N phase diagram. (Binder et. al. 1991)

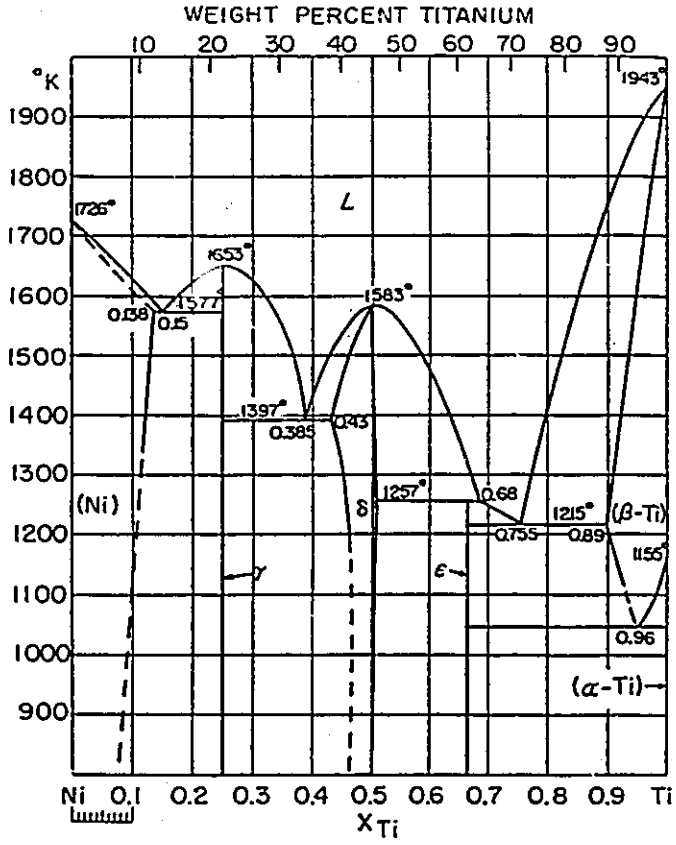

Figure 2.3.2: Ni- Ti phase diagram. (Hultgren et. al. 1973)

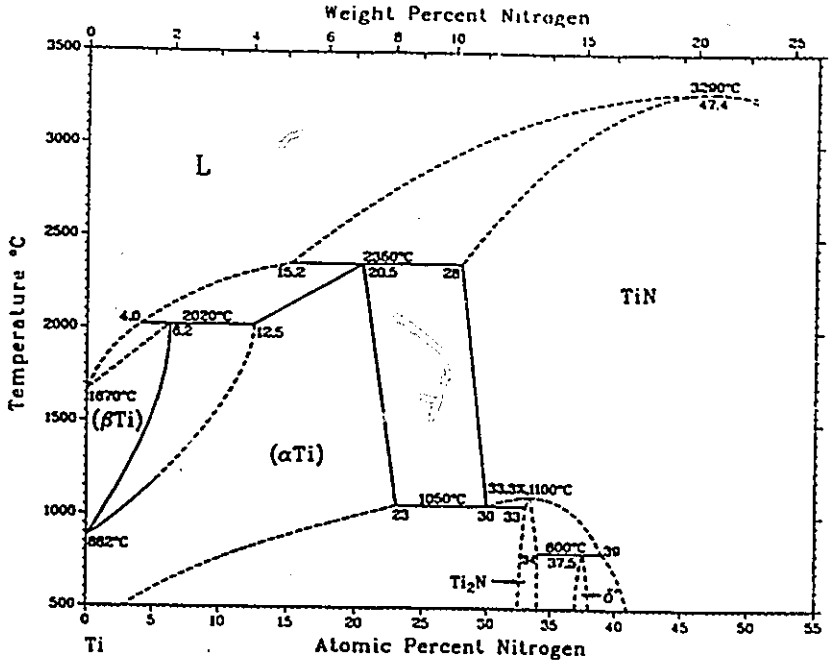

Figure 2.3.3: Ti-N phase diagram. (Wreidt and Murray 1987)

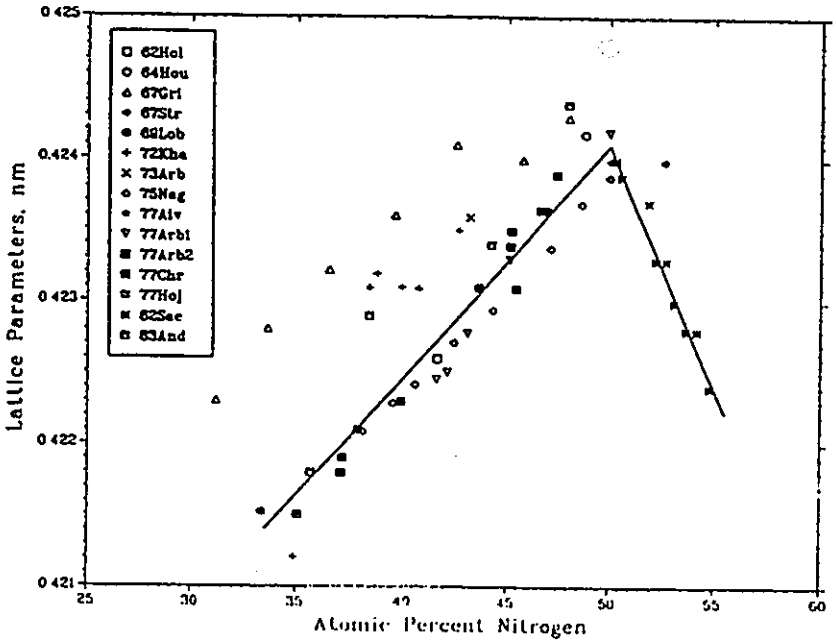

Figure 2.3.4: Lattice parameter of TiN_x versus composition. (Wriedt and Murray 1987)

Chapter 3

Experimental Procedure:

3.1: Diffusion Studies:

Ni (>99.95 % purity) and Ti (>99.5 % purity) were each vacuum arc melted under flowing high purity argon. Carbon analysis was performed using the Leco© combustion/ volumetric method while oxygen and nitrogen gas analysis were performed using the Leco© inert gas fusion method with infra-red detection of oxygen and thermal conductivity measurements for nitrogen determinations. The levels of these substances were below the detectability limit of these instruments i.e., 50 ppm for carbon, 2 ppm for oxygen and 1 ppm for nitrogen. The Ti and Ni were then melted together in the appropriate proportions and reweighed to check that there was no weight loss. They were cold-rolled to a thickness of about 2 mm, and annealed for 24 hours at 1020° C in argon. The alloys were nominally 0.1, 0.5, 1, 2, or 5 w/o Ti. XFS confirmed that there was no measurable loss of Ti. The major impurities in these samples were Fe, Al, and Co each at approximately 0.015 w/o. Experiments were performed at 800°C, 900°C, and 1020°C in nitrogen gas or an argon/ 25% nitrogen mixture with a flow rate of 250 cm^3/s at a total pressure slightly in excess of 1 atm. Experimental times of 48 or 96 hours were chosen

to yield easily determined penetration curves and also to ensure that transient effects associated with heating time could be neglected.

The nitriding furnace was of a horizontal design. The gas train consisted of Cu turnings at 375°C for oxygen removal, followed by anhydrous calcium sulphate for water removal, and sodium hydroxide- coated silica, for CO_2 removal. The main body of the quartz furnace tube had another oxygen getter consisting of steel wool in the temperature range of 400°C to 800°C, located near the hot zone. After an internal nitridation experiment the steel wool had a characteristic band of discolouration located in the 600°C temperature region. Assuming thermodynamic equilibrium, this corresponds to an oxygen partial pressure of 10^{-25} atmospheres which was calculated to be adequate to prevent the oxidation of TiN between 800°C and 1020°C. Before each experiment the system was evacuated by a mechanical rotary pump to 10^{-2} torr, and the system was then back-filled with argon or nitrogen. In this way the system could also be checked for leaks. The procedure was repeated three times. At this point the Cu getter furnace was turned on and the gas was allowed to purge the system for 36-48 hours before nitriding could begin.

Cross- sections of the nitrided specimens were cut, then plated with NiP for edge retention. Samples were ground and polished to at least 1μm diamond or 0.05μm colloidal silica and examined by Scanning Electron Microscopy (SEM). The

diffusion profiles were obtained with Energy Dispersive X- Ray Analysis (EDX) with each sample acting as its own standard. A detailed description of the methods and error analysis will be provided in Section 3.1.1. The sample surfaces were examined in the as-nitrided condition. The minimum detectable mass fraction of Ti in Ni was determined to be 0.05 w/o Ti for counting times in excess of 2250 seconds. Statistical counting errors were found to be ±10% for the high Ti alloys increasing to ±20% for lower Ti concentrations (99% confidence level).

3.1.1: Quantitative chemical analysis using EDX Analysis:

One of the aims of this project was to obtain reliable concentration profiles across the subscale. This section offers a detailed description of how this information was obtained. Some of this information is unique to the McMaster SEM facility. The intensity of a given X-ray peak depends not only on the concentration of that particular element but also in a very complicated way on the conditions used to obtain that information (Goldstein et. al. 1981). From this perspective great care was needed in setting up the identical operating conditions on the SEM as the subscale was traversed. An operating voltage of 20kV was found to be adequate for Ti and Ni. The specimens were ground as evenly as possible and a zero degree tilt was used on the specimen holder so that the working distance and take off angle (15°) did not change as spectra were collected from various parts of the sample. In this regard it is very important that the

working distance be set at the eucentric height.

Since the samples could act as their own standards, a ratio method (Goldstein et. al. 1981) was employed for quantification. In this method the concentration of Ti and Ni can be defined as:

$$\frac{C_{Ti}}{C_{Ni}} = K_{TiNi}\frac{I_{Ti}}{I_{Ni}} \qquad (3.1)$$

Since K_{TiNi} is determined from standards close in concentration to the quantities being measured, it can be regarded as constant. The concentrations can therefore be determined directly from equation 3.1 (under the identical operating conditions). The error in K_{TiNi} values was assessed at the 99% confidence level from all the experiments as ±3% i.e.

$$\%err. = \frac{t_{99}{}^{n-1}S_n}{\sqrt{n}K_{TiNi}} \times 100 \qquad (3.2)$$

where S is the standard deviation and t is the student t value for n readings at the 99% confidence level. A summary of the average K_{TiNi} values is presented in Figure 3.1 from all the experiments. The near constant value of K_{TiNi} over the entire composition range determined in this work is justification for neglect of the so-called ZAF corrections. The total error in each measurement, according to Williams (1984), is the error in K plus the statistical counting error given at the 99% confidence level as:

$$\%err.=\pm 2\frac{3\sqrt{N}}{N}\times 100 \qquad (3.3)$$

The large error produced in some of these measurements is a consequence of the fact that in many instances spectra were collected near the minimum detectable mass limit. This value was determined to be near 0.05 w/o Ti as noted by the spectra obtained from a 0.1 w/o Ti standard alloy (Figure 3.2). Note the long counting times (25 minutes live time) involved in collecting a statistically significant signal at these concentrations.

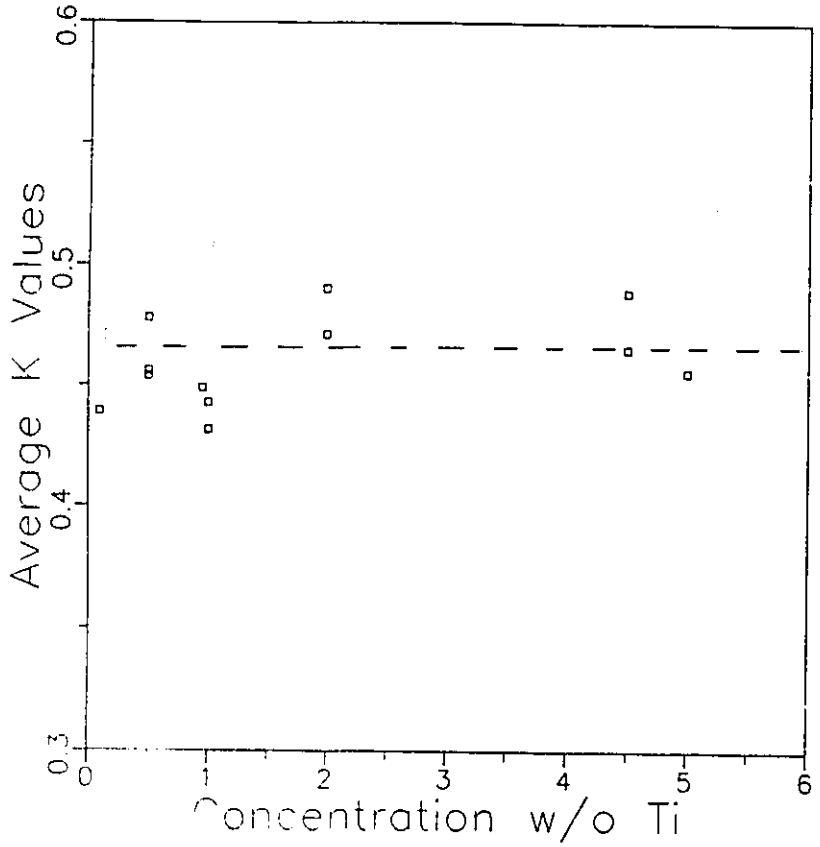

Figure 3.1: Summary of average K values determined from various experiments.

3.2: Electron Microscopy:

A Philips' CM12 TEM operating at 120 kV, equipped with a double tilt holder was used in this study. The sample preparation was essentially the same as in the previous section except that the 0.1 Ti w/o alloys were additionally cold rolled to a thickness between 300 and 400 μm to facilitate TEM foil preparation. These foils were once again annealed in Ar gas before nitriding. After nitriding, at 900°C or 1020°C, 3 mm discs were spark cut, ground to between 150 μm and 200 μm in thickness and electropolished at 0°C, with a voltage of 20 V in a solution of 10% sulphuric acid in methanol.

3.3: Additional Techniques:

In order to ascertain the composition and crystal structure of the precipitated phase a variety of other analytical techniques were employed. These were: 1/ Windowless EDX, 2/ Auger Spectroscopy, 3/ Electron Energy Loss Spectroscopy (EELS), and 4/ X-ray diffraction.

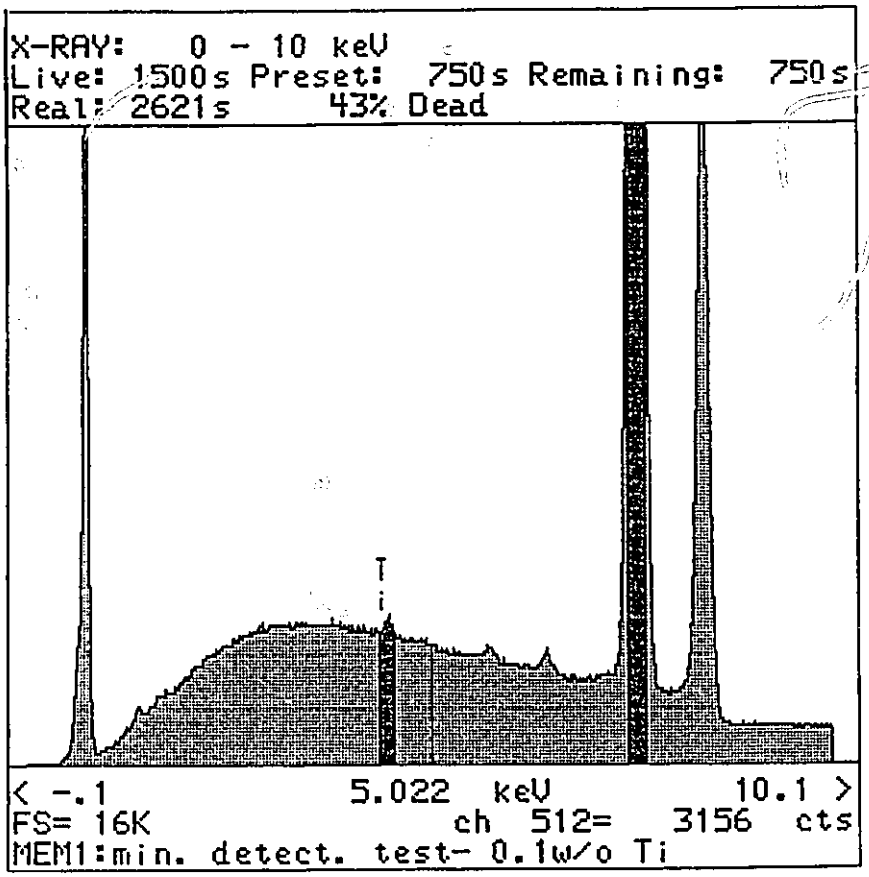

Figure 3.2: Typical spectra collected near the minimum detectable mass fraction.

Chapter 4
Experimental Results

4.1.1: Appearance of nitrided Ni-Ti alloys

The surface appearance of the samples nitrided at 900°C for 96 hours is shown in Figure 4.1.1 for alloys ranging in composition from 0.1 w/o Ti to 5 w/o Ti. The surface of the 0.1 w/o Ti (Figure 4.1.1a) has a reflective metallic appearance with a grain size of several millimetres. As the Ti concentration is increased from 0.5 w/o to 5 w/o Ti the appearance of these surfaces becomes increasingly gold-like in colour. A transition is marked by the 1 w/o Ti alloy, Figure 4.1.1c. Beyond this composition the underlying grain structure can no longer be observed. These surfaces are representative of the other experiments with some minor variations which will be addressed in the subsequent sections.

4.1.2: Auger and X-Ray Diffraction Studies

Auger spectroscopy was performed on some of the nitrided samples. An example from a 5 w/o Ti alloy nitrided at 1020°C for 48 hours is shown in Figure 4.1.2.

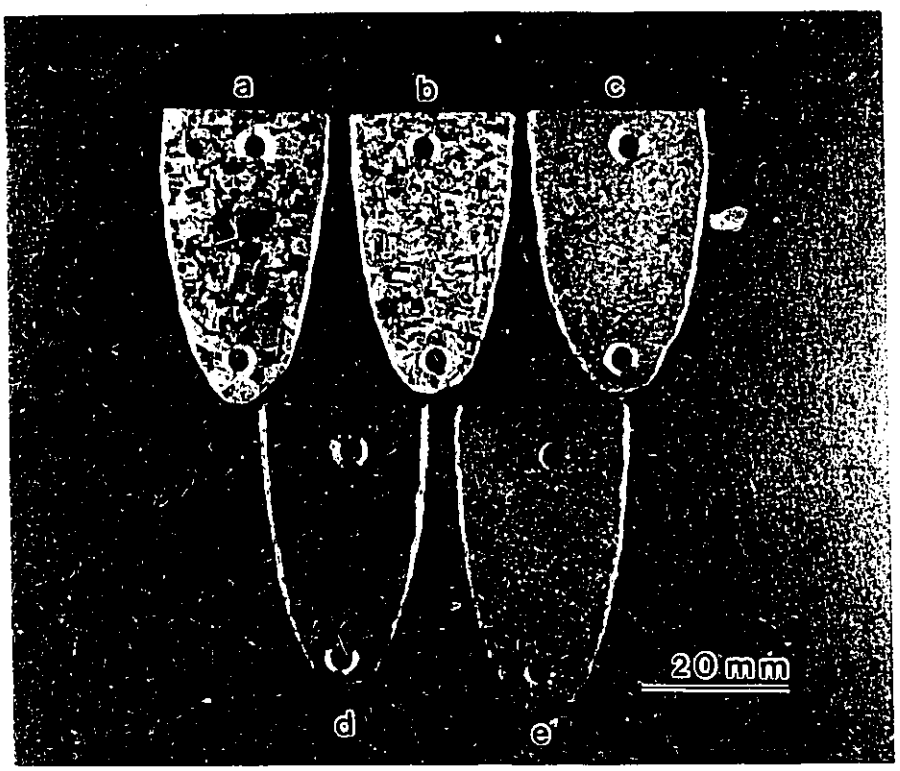

Figure 4.1.1: Surfaces of samples nitrided 96 hours at 900°C in 1 atmosphere nitrogen gas. a) 0.1 w/o Ti, b) 0.5 w/o Ti, c) 1 w/o Ti, d) 2 w/o Ti and e) 5 w/o Ti

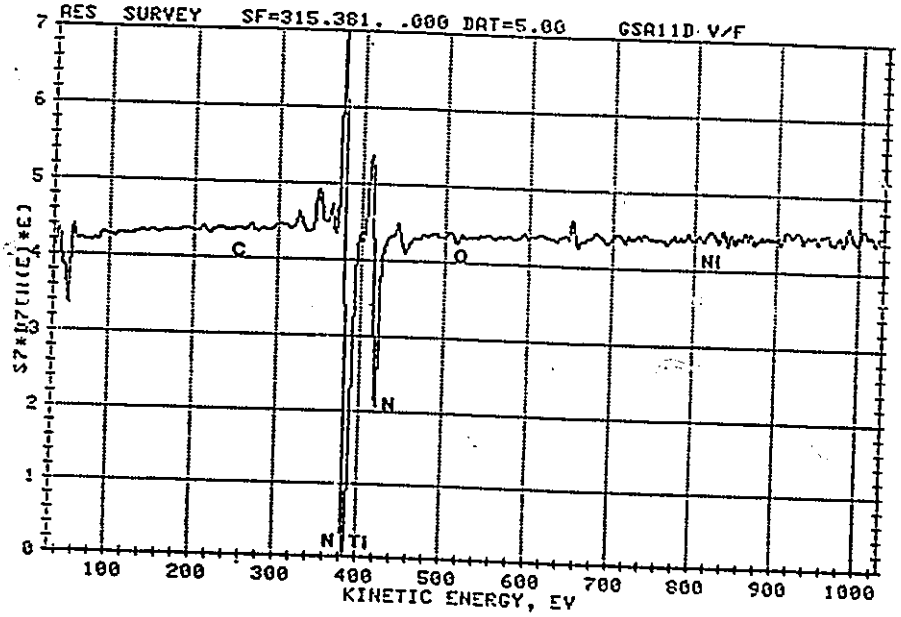

Figure 4.1.2: Auger spectroscopy result of a 5 w/o Ti alloy nitrided 48 hours at 1020°C. Nitrogen and titanium are the only constituent elements of these scales.

After sputtering to remove a carbon contamination film, only Ti and N were observed. X- ray diffraction was used to identify the nitride phase on all the high Ti alloys (Figure 4.1.3) nitrided between 800°C and 1020°C. TiN was the only observed phase (other than Ni) on all these surfaces. The peaks were shifted with respect to the TiN standard, and an accurate lattice parameter determination could not be obtained from these samples. This is shown in Figure 4.1.4, where extrapolations to $\sin^2\theta=1$ should yield values of the lattice parameter (Cullity 1978). Despite the large scatter in the experimental data, the TiN lattice parameter extrapolates to an apparent value of 4.25 Å ± .01. When the nitride was mechanically removed from the Ni substrate, the lattice parameter was determined to be: 4.2412 Å ±0.0003 Å in excellent agreement with stoichiometric TiN (Wreidt and Murray 1987). This indicates the presence of tensile residual stress on these surfaces.

4.1.3: Scanning Electron Microscopy:

The surfaces of the samples nitrided for 96 hours at a temperature of 1020°C are shown in Figures 4.1.5 to 4.1.8. The 0.1 w/o Ti alloy (Figure 4.1.5), shows a two phase surface consisting of angular TiN, as the dark contrast phase, and a thermally etched Ni substrate. The surface of a 0.5 w/o Ti alloy is shown in Figure 4.1.6. There are several noteworthy features; the light phase on the surface (Figure 4.1.6a) is Ni protruding from the surface, while the darker contrast is a two phase structure consisting

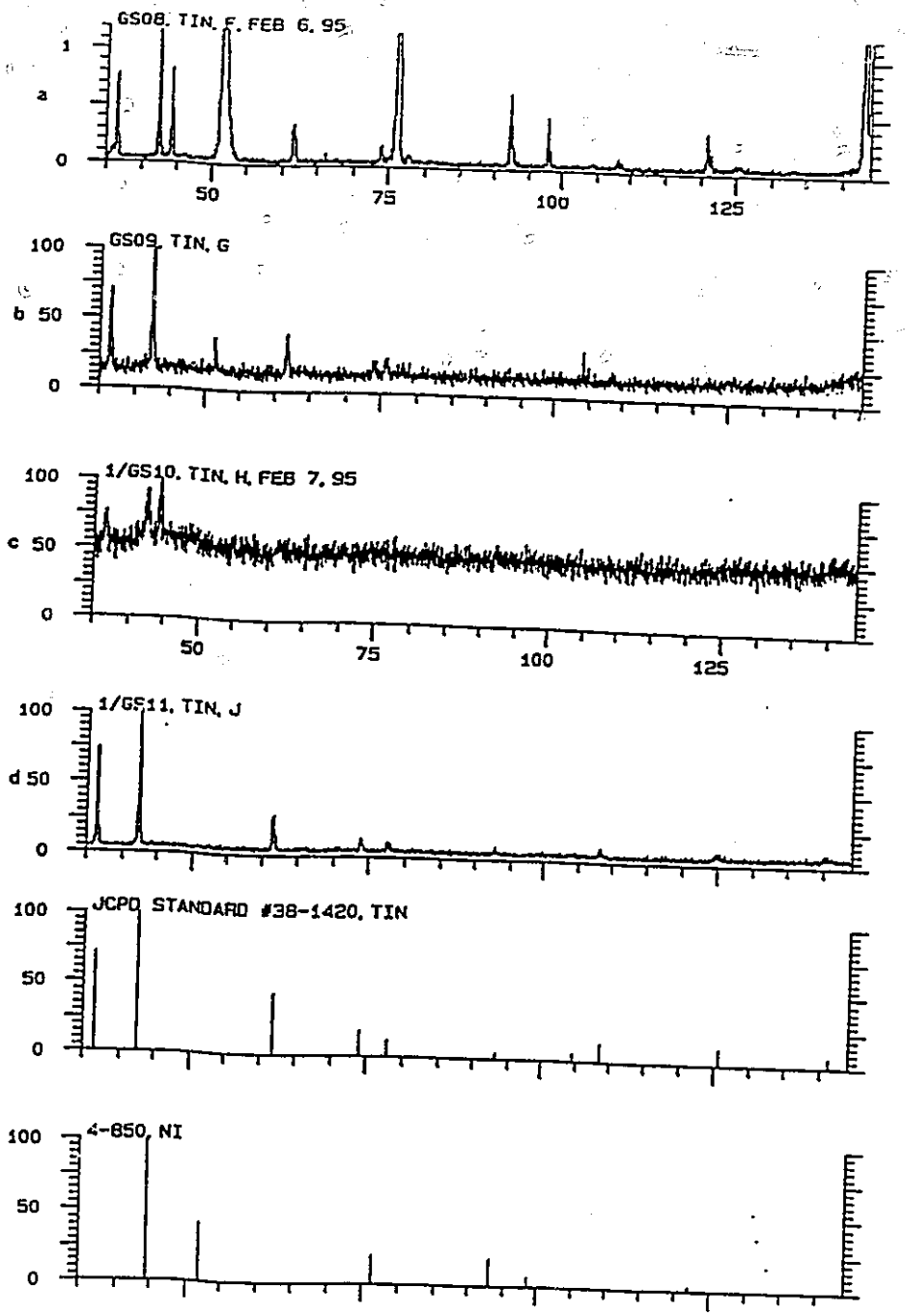

Figure 4.1.3: X-ray diffraction results for experiments performed at a) 1020°C b) 900°C c) 800°C and d) 1020°C at PN_2=0.25 atm. In all cases the scale is TiN. The TiN and Ni standard spectra are shown in the bottom of this figure.

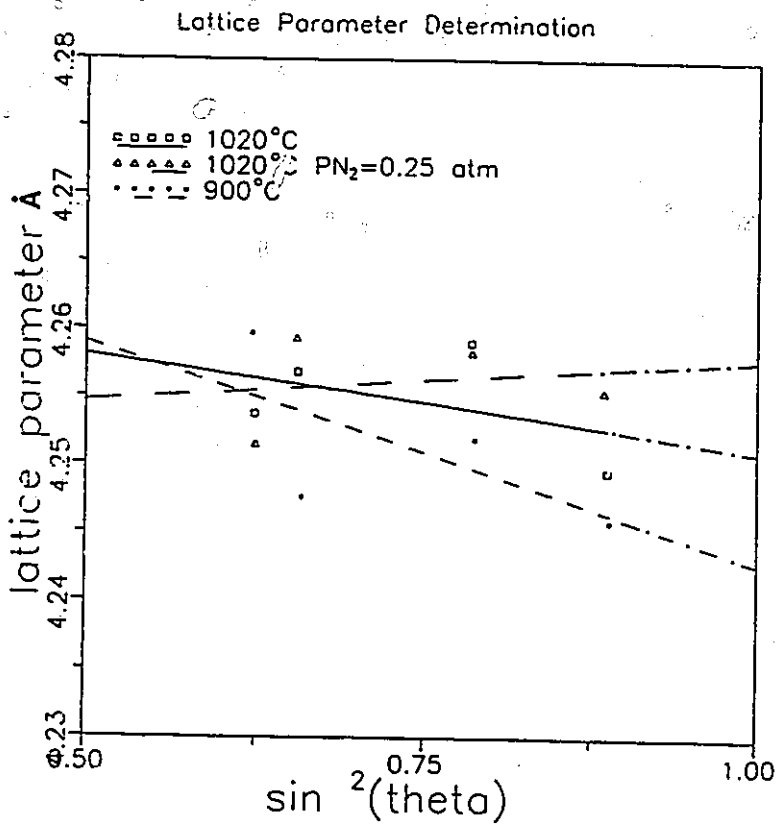

Figure 4.1.4: Graph of lattice parameter versus $\sin^2(\theta)$ for various experiments. The extrapolation of the data points to $\sin^2(\theta)=1$ show that these films are in an apparent state of tension.

of Ni with a high volume fraction of TiN. Furthermore, Ni nodules may be seen on the twin boundaries but not on the high angle grain boundaries. The high volume fraction of TiN particles is shown in Figure 4.1.6b, where once again the dark contrast phase is TiN. A 1 w/o Ti alloy is shown in Figure 4.1.7a; the density of Ni nodules varies from grain to grain. A higher magnification image of this surface is shown in Figure 4.1.7b. A continuous superficial scale is observed with Ni on top of it. This alloy marks the transition point to an exclusive external nitridation. As expected a continuous scale can be observed in the 2.2 w/o Ti with a concomitant diminished density of Ni nodules (Figure 4.1.8).

Cross- sections for some of these materials are shown in Figure 4.1.9. Both the 4.5 w/o Ti (Figure 4.1.9a) and 2.2 w/o Ti alloy (Figure 4.1.9b) show a continuous TiN scale on the surface. The subscale of the 0.5 w/o Ti alloy is shown in Figure 4.1.10. A decreasing volume fraction of particles from the surface towards the interior of the sample is noted in Figure 4.1.10a, with the particles penetrating to a depth of approximately 150μm into the sample (marked by the arrow in Figure 4.1.10a). A close inspection of the Ni cap (Figure 4.1.10b) shows the high density of TiN particles approximately 0.25μm in size below the original surface of the alloy. Windowless EDX confirmed that the particles are composed of Ti and N. Electron diffraction studies confirmed that they were TiN (see Chapter 4.2).

Figure 4.1.5: Surface micrograph of a 0.1 w/o Ti nitrided 96 hours, at 1020°C in 1 atmosphere nitrogen gas.

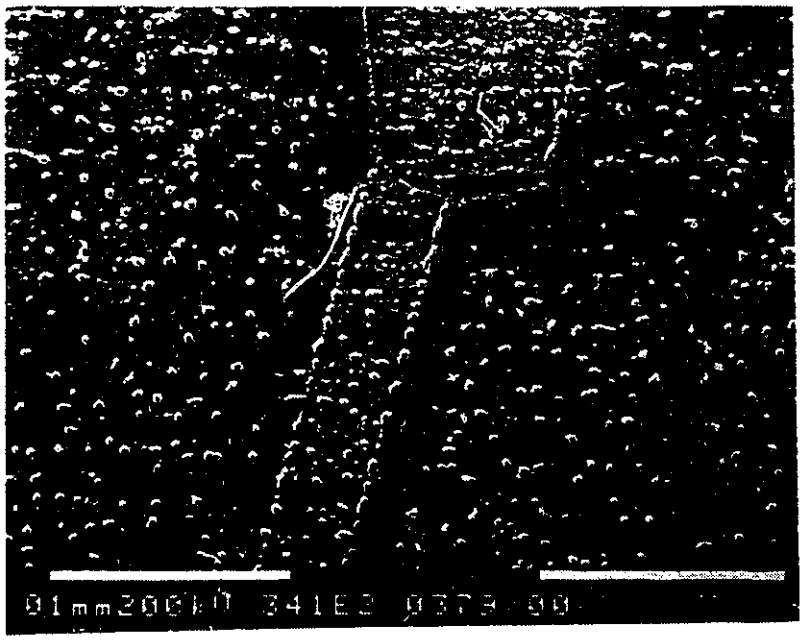

Figure 4.1.6: Surface micrograph of a 0.5 w/o Ti nitrided 96 hours, at 1020°C in 1 atmosphere nitrogen gas a) low magnification b) high magnification

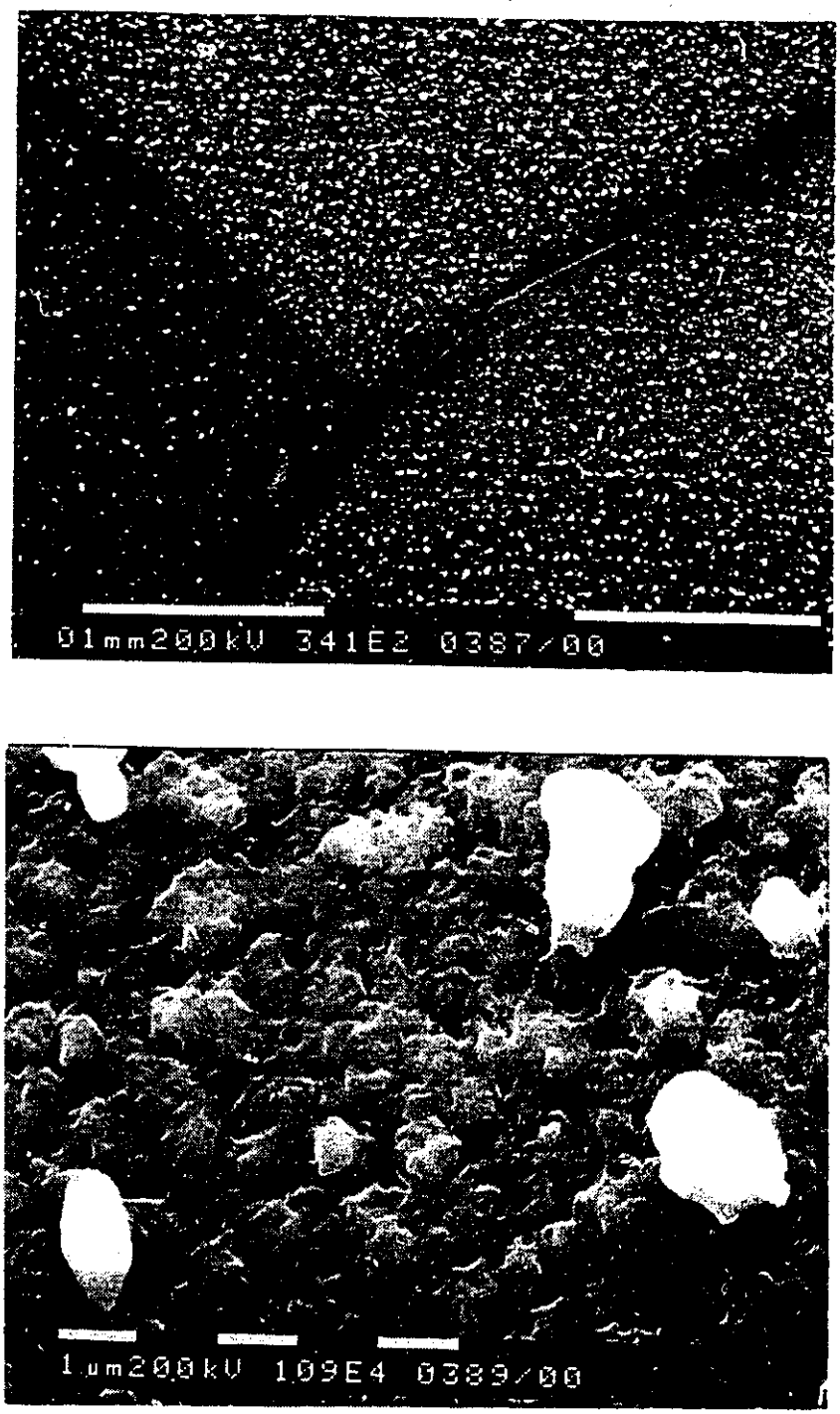

Figure 4.1.7: Surface micrograph of a 1 w/o Ti nitrided 96 hours, at 1020°C in 1 atmosphere nitrogen gas. a) low magnification b) high magnification

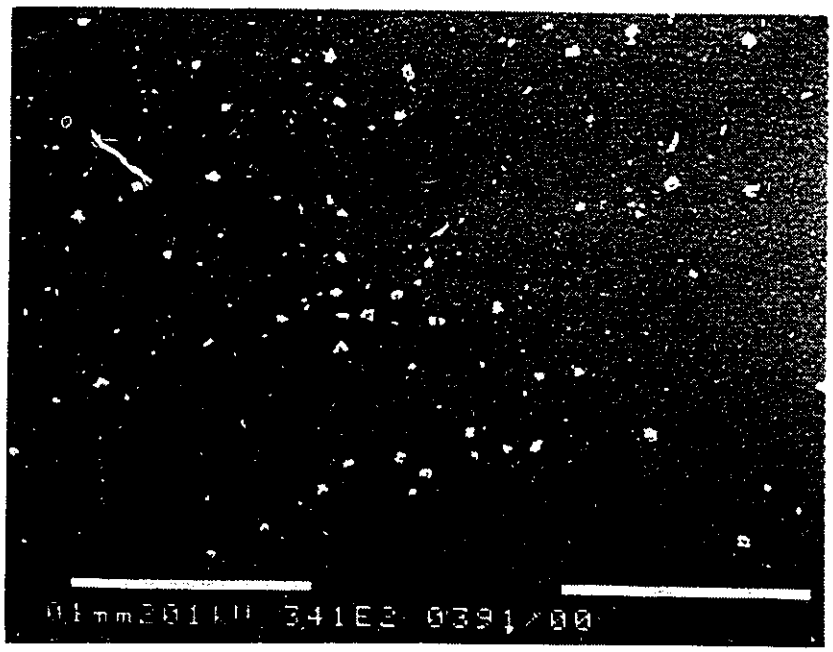

Figure 4.1.8: Surface micrograph of a 2.2 w/o Ti nitrided 96 hours, at 1020°C in 1 atmosphere nitrogen gas.

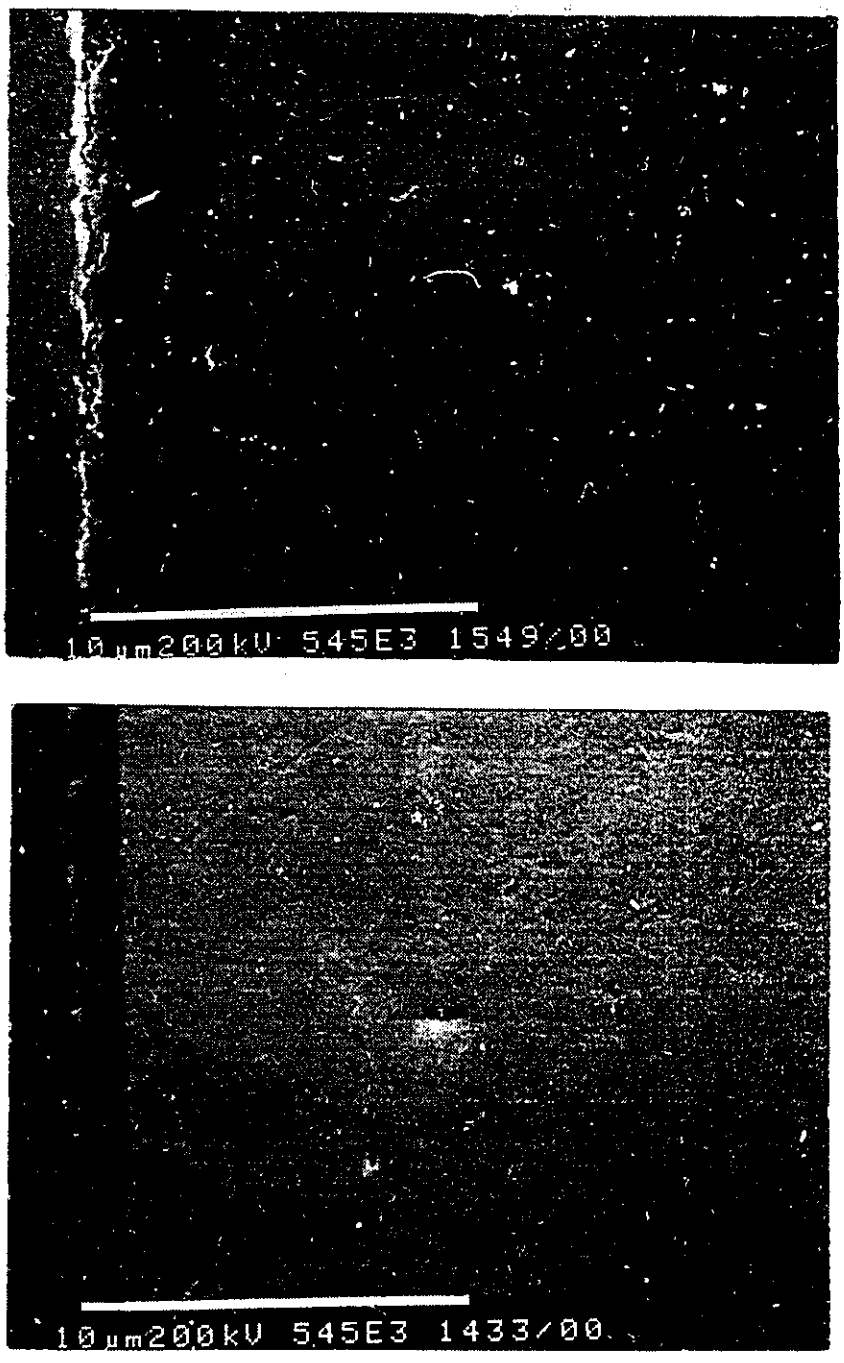

Figure 4.1.9: Cross sections of a) 4.5 w/o Ti alloy b) 2.2 w/o Ti alloy, showing a continuous TiN scale, nitrided 96 hours at 1020°C in 1 atmosphere nitrogen gas.

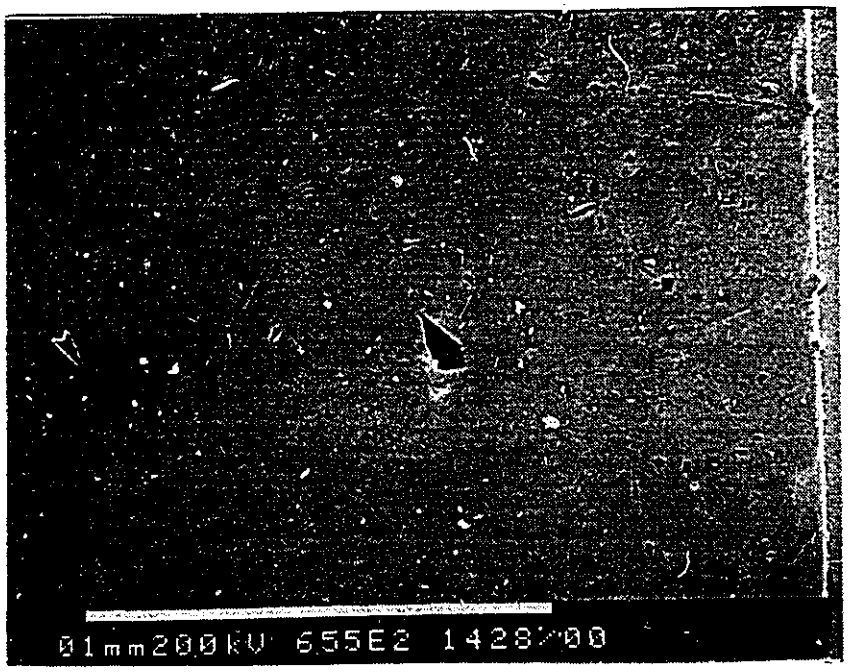

a

b

Figure 4.1.10: Cross sections of a 0.5 w/o Ti alloy: nitrided 96 hours at 1020°C in 1 atmosphere nitrogen gas. The large dark particle in the centre of Fig 4.1.10a is an artifact; the precipitation front extends to the arrow b) higher magnification image under 'Ni Cap'

The surfaces of some of the samples nitrided at 900°C are shown in Figure 4.1.11. The surface of a 0.1 w/o Ti alloy nitrided for 96 hours is shown in Figure 4.1.11a where a two phase surface is observed. An interesting section of a grain boundary showing a precipitate-free region can be observed. The morphology of the 0.5 w/o Ti is shown in Figure 4.1.11b. A two phase microstructure with a high volume percent of TiN is shown similar to the alloy nitrided at 1020°C. Thermally faceted Ni nodules can also be seen protruding from the surface. The surfaces of the 1 w/o and 2 w/o Ti alloys are shown in Figure 4.1.12a and 4.1.12b respectively. Once again the variability of Ni extrusion in the 1 w/o Ti alloy and the virtual disappearance of Ni from the surface in the 2 w/o Ti alloy can be seen.

The surfaces of some of the samples nitrided at 800°C for 96 hours are shown in Figure 4.1.13. The differences between these and the 1020°C experiment are the much smaller particle size at 800° C (compare Figure 4.1.13a with Figure 4.1.5a), and the greater anisotropy in the nitriding behaviour. Some grains in the 0.5 w/o Ti alloy (Figure 4.1.13b) show a superficial scale with little to no extrusion of N. A similar behaviour is noted in the 1 w/o Ti alloy (Figure 4.1.13c).

Cross sections for some of the 0.5 w/o Ti alloys are shown in Figure 4.1.14. Figure 4.1.14a shows a cross section of a O.5 w/o Ti alloy nitrided 48 hours at

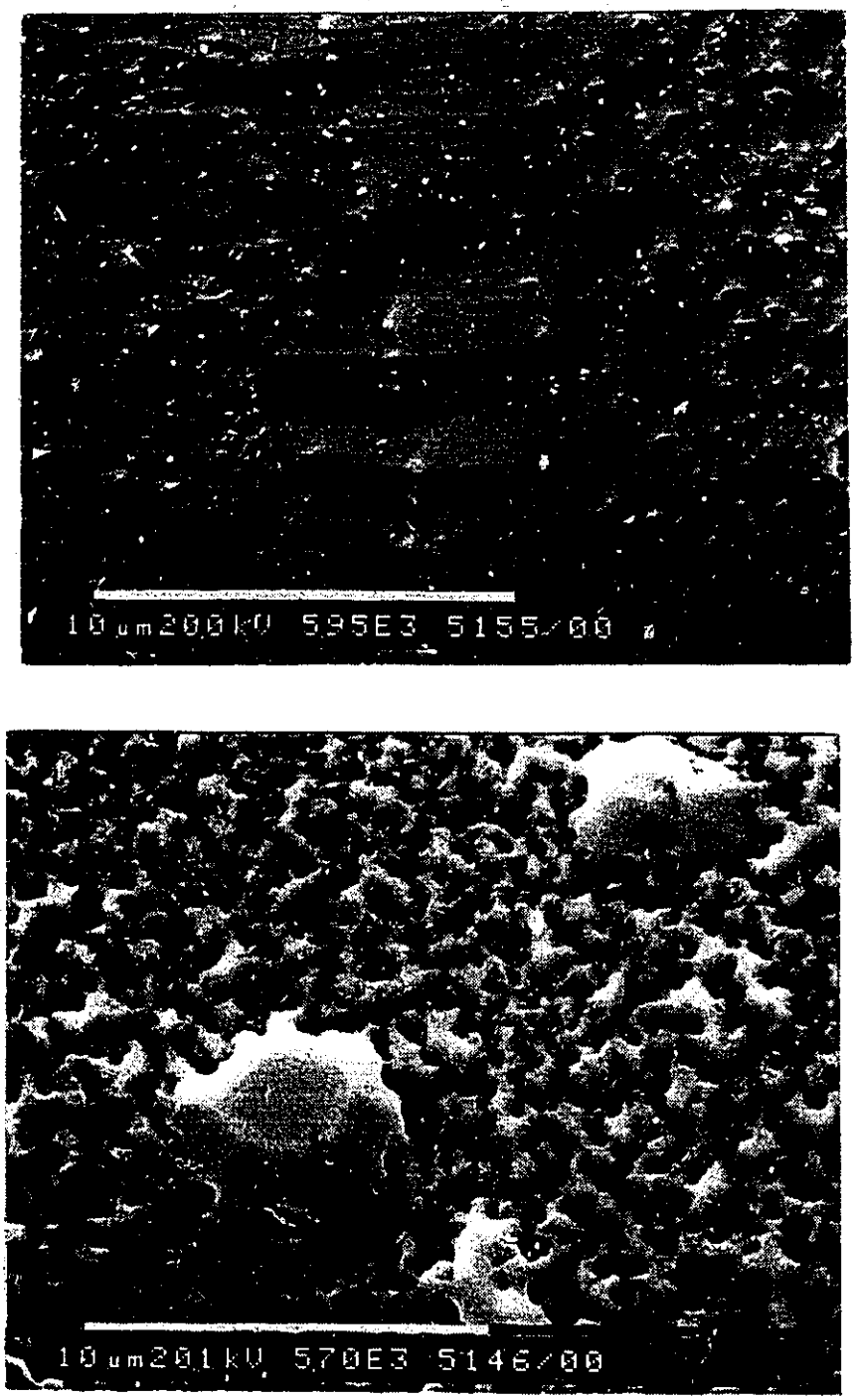

Figure 4.1.11: The surfaces of a) 0.1 w/o Ti alloy b) 0.5 w/o Ti alloy nitrided 96 hours at 900°C in 1 atmosphere nitrogen gas.

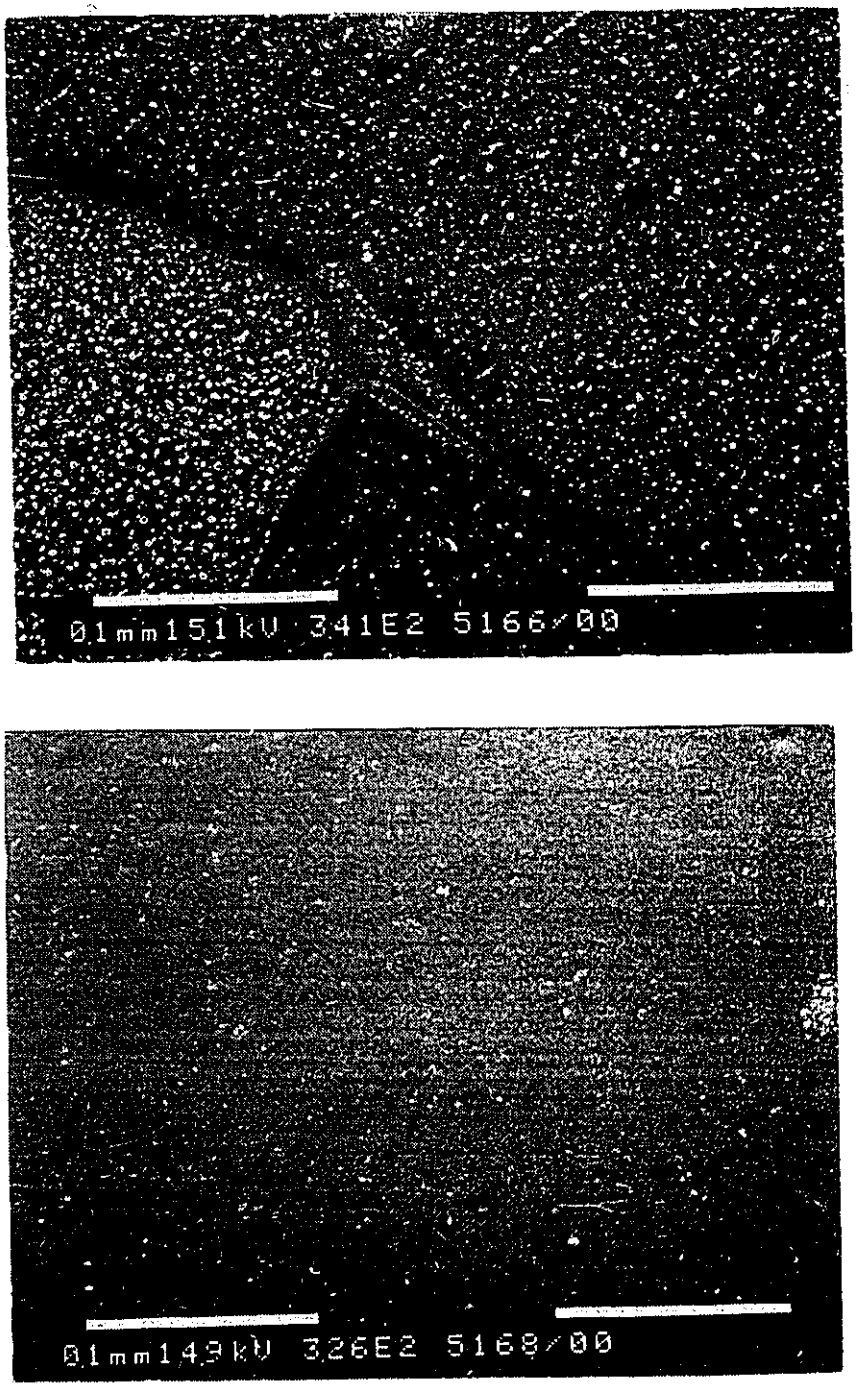

Figure 4.1.12: The surfaces of a) 1 w/o Ti alloy b) 2.2 w/o Ti alloy nitrided 96 hours at 900°C in 1 atmosphere nitrogen gas.

a

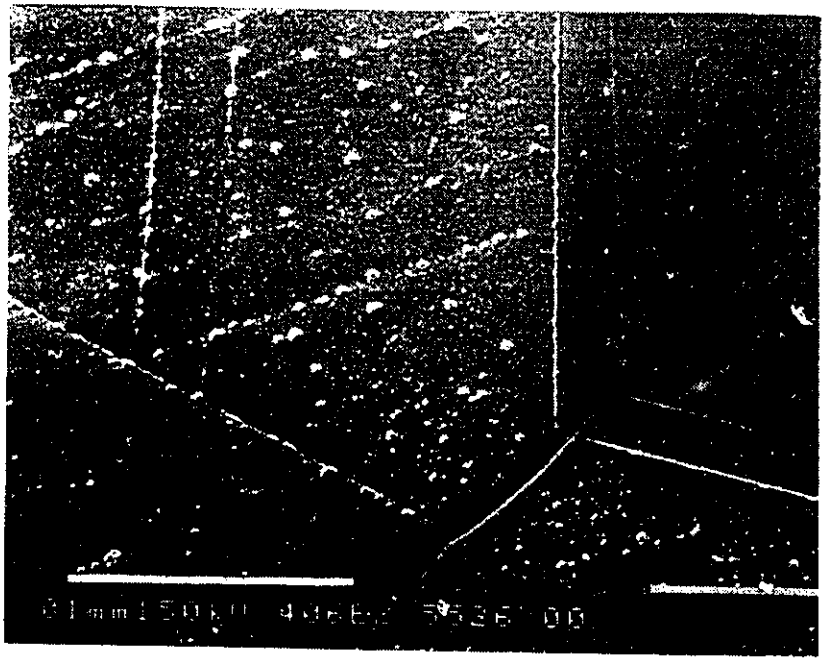

b

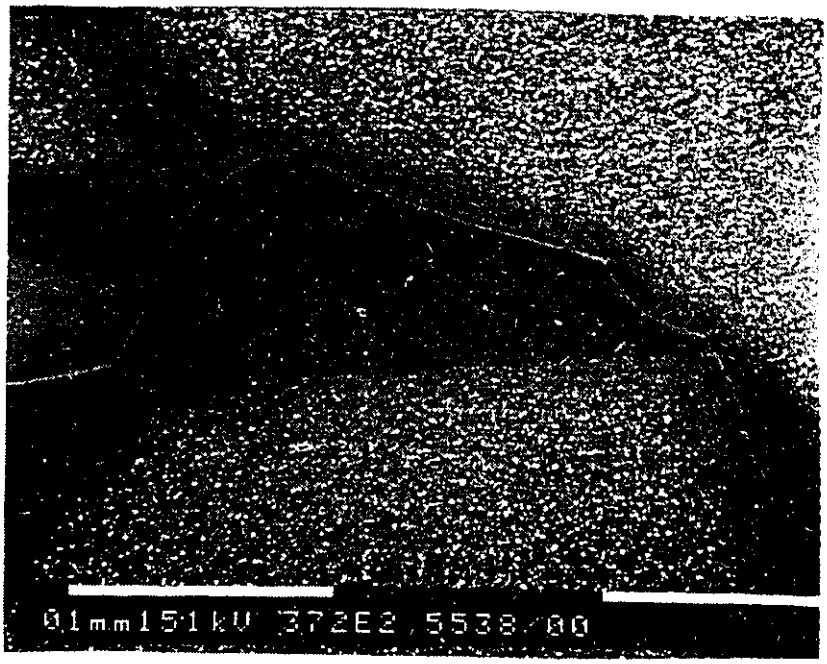

c

Figure 4.1.13: The surfaces of a) 0.1 w/o Ti alloy b) 0.5 w/o Ti alloy and c) a 1 w/o Ti, nitrided 96 hours at 800°C in 1 atmosphere nitrogen gas.

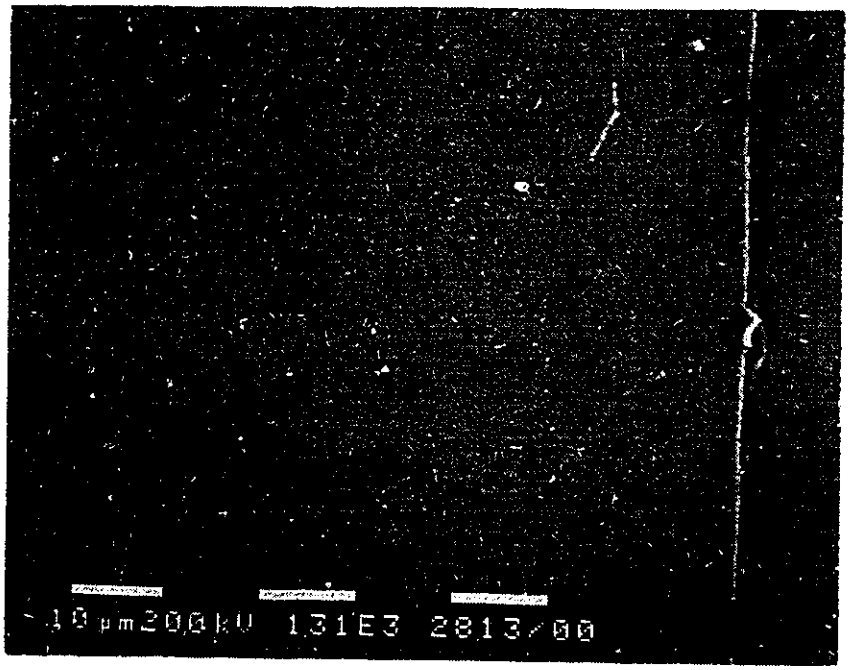

a

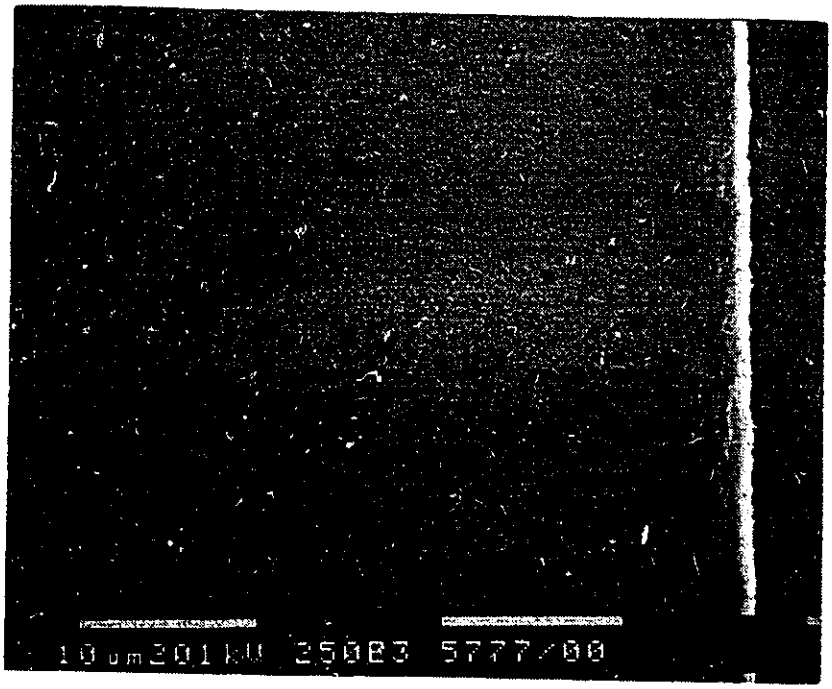

b

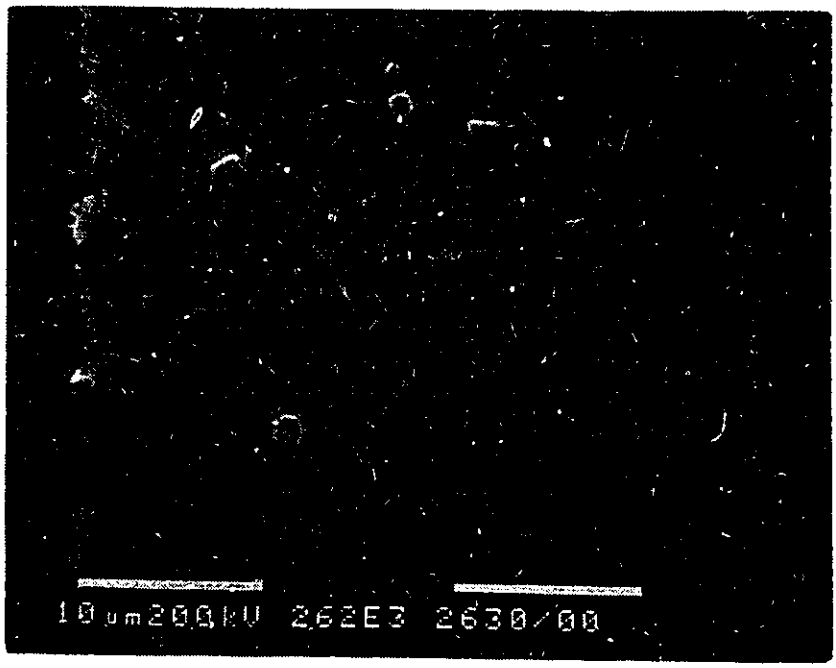

C

Figure 4.1.14: Cross sections of 0.5 w/o Ti alloys: a) nitrided 48 hours at 1020°C in 1 atmosphere nitrogen gas b) 96 hours at 900°C in 1 atmosphere nitrogen gas and c) 48 in 0.25 atmospheres nitrogen gas.

at a temperature of 1020°C. Figure 4.1.14b shows a cross section from a 0.5 w/o Ti nitrided 96 hours at 900°C, while Figure 4.1.14c shows the cross- section of a 0.5 w/o Ti alloy nitrided 48 hours with a partial pressure of 0.25 atmosphere nitrogen gas. No resolvable internal particles were observed in the samples nitrided at 800°C. The amount of internal precipitation (i.e. density and depth) in general decreased with decreasing temperature and partial pressure of nitrogen.

4.1.4: Comparison of Measured and Calculated Diffusion Profiles:

I: Introduction:

The procedure that was adopted for experimental closure was to use the diffusion profile from the highest Ti alloys and Equation 2.1.9, to determine the diffusivity of Ti in Ni. The 0.5 w/o Ti alloys were then used for the determination of KD_C values, both from the diffusion profile and the penetration curve of TiN into the alloy. Whenever possible an attempt was made to assess the predictive ability of the algorithm by using a minimum set of experiments to predict the bulk of the experimental outcomes. The computer program is listed in Appendix I.

II: Results:

The concentration of Ti as a function of distance for a 4.5 w/o Ti alloy nitrided at 1020°C for 96 hours is shown in Figure 4.1.15. This sample showed a continuous TiN scale as observed in Figure 4.1.14a. As discussed previously the solution of this concentration profile should approach an error function solution (provided that D_{Ti} is regarded as constant). This solution (Equation 2.1.9) is also plotted in Figure 4.1.15 along with the calculated diffusion profile from our finite difference algorithm. The agreement between the two solutions is excellent. A diffusivity of 5×10^{-15} m^2/s for Ti in Ni at 1020°C was determined by matching the experimental data to either solution.

Similar profiles are shown (Figure 4.1.16) for the 1 w/o Ti and 0.5 w/o Ti alloys nitrided 96 hours in 1 atmosphere nitrogen gas. The calculated profiles were obtained by fitting a value of $KD_C = 7 \times 10^{-17}$ $[w/o]^2$ m^2/s to our algorithm from the 0.5 w/o Ti alloy. The shape of the profile for the 1 w/o Ti alloy was correspondingly predicted. The calculated distribution of particles in the subscale is shown in Figure 4.1.17 for the 0.5 w/o Ti alloy. A high volume fraction of particles near the surface is predicted with a decreasing amount of TiN to about 120 μm, which bears a qualitative resemblance to observation (Figure 4.1.10a). The program cannot determine the amount of TiN at the surface since (as already discussed in Chapter 2.1.5) it depends on the step size used in the program.

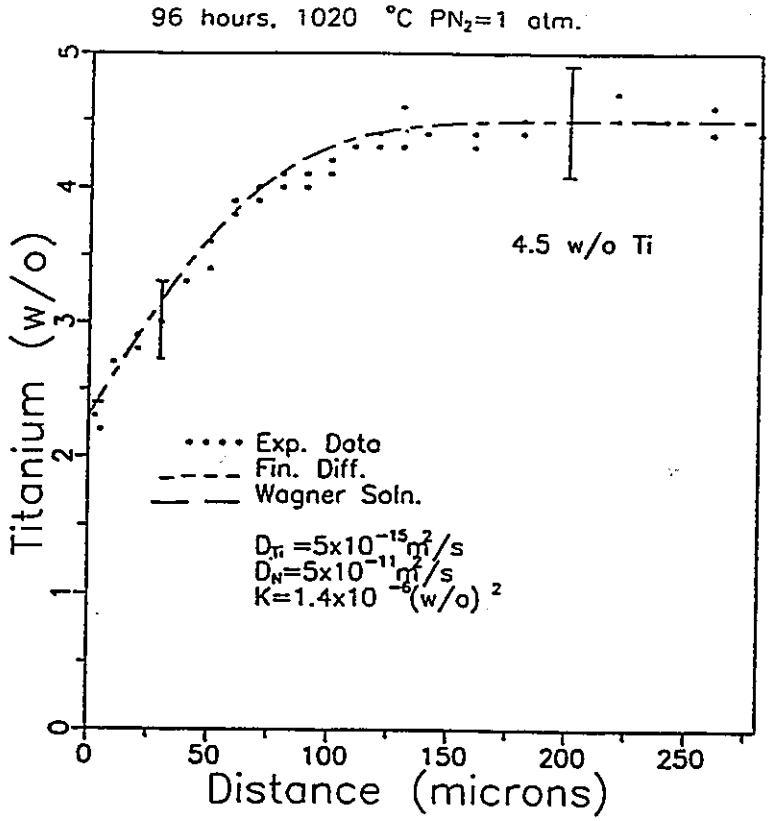

Figure 4.1.15: Measured concentration profile of Ti in a 4.5 w/o Ti alloy nitrided 96 hours at 1020°C in 1 atmosphere nitrogen gas. The results from Equation 2.1.9 (long dash) and the finite difference solution (short dash) are identical. Error bars represent statistical counting errors at the 99% confidence level.

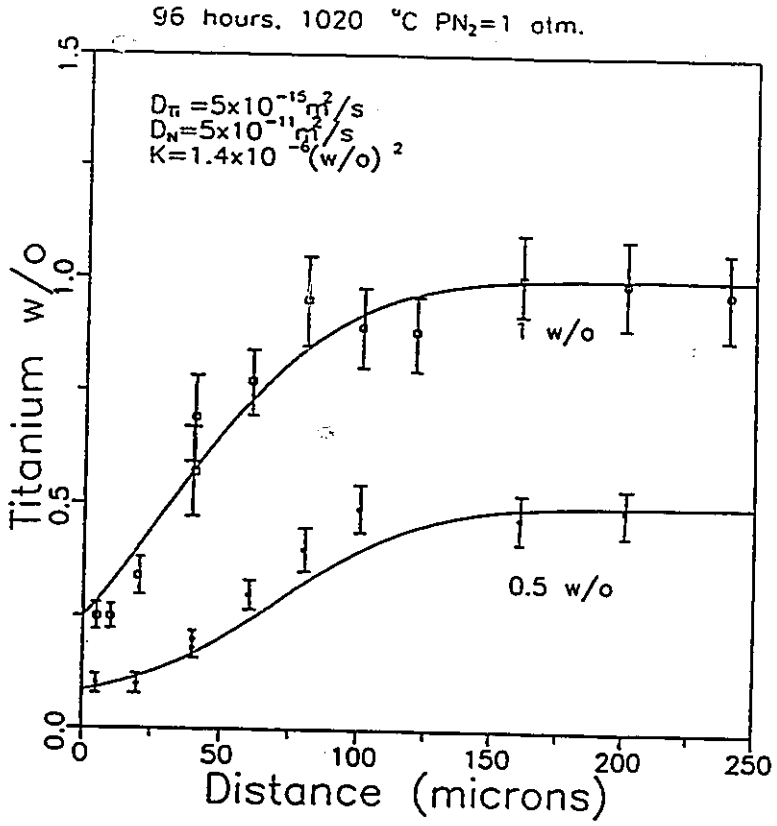

Figure 4.1.16: Measured profile of Ti in a 1 w/o Ti alloy and a 0.5 w/o Ti alloy nitrided 96 hours at 1020°C in 1 atmosphere nitrogen gas. The solid lines represent the finite difference calculation using a value of $KD_C = 7 \times 10^{-17}$ m²/s (w/o)², for the 0.5 and 1 w/o Ti alloy.

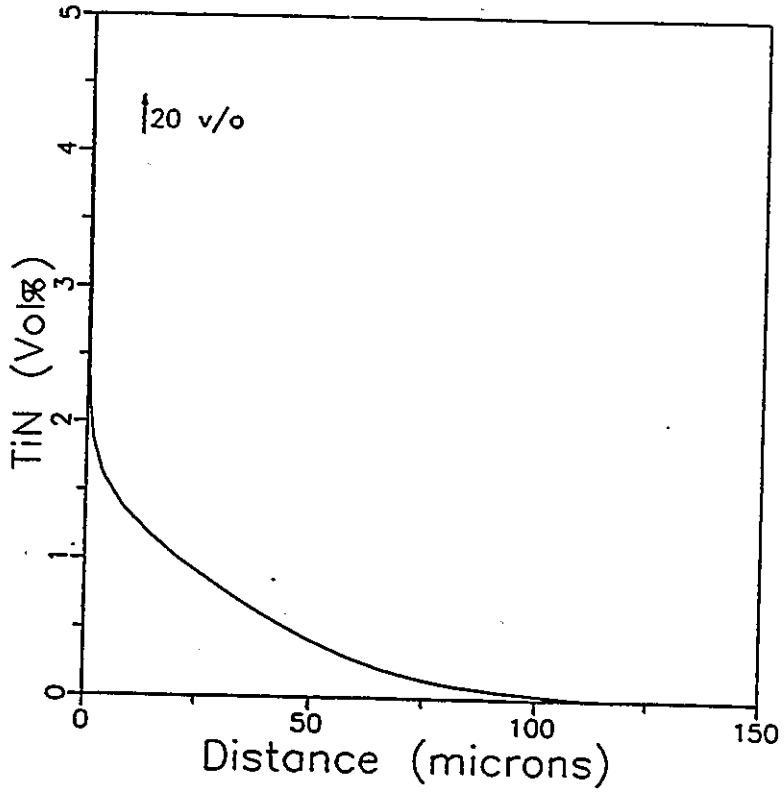

Figure 4.1.17: Calculated distribution of TiN particles in a 0.5 w/o Ti alloy nitrided 96 hours at 1020°C in 1 atmosphere nitrogen gas. The distribution and depth of precipitation bear a qualitative resemblance to Figure 4.1.10a. The surface concentration is calculated as 20 v/o.

The diffusion profile of a 0.5 w/o Ti alloy nitrided for 48 hours at a temperature of 1020°C in 1 atmosphere nitrogen is shown in Figure 4.1.18. The finite difference solution is shown by the solid line and is in good agreement with the experimental results. Wagner's solution (Equation 2.1.9) is also plotted as the dashed line. As discussed in Chapter 2.1.4 internal nitridation acts in such a way as to negatively distort this profile. The observed (Figure 4.1.14a) and calculated distribution of particles shown in Figure 4.1.19 are also in qualitative agreement.

The diffusion profiles for a series of Ni alloys ranging in composition from 0.5 w/o Ti to 5 w/o Ti nitrided at 900° C are shown in Figure 4.1.20. The diffusivity of Ti in Ni was determined to be 2.3×10^{-16} m^2/s at 900°C. All but the 0.5 w/o Ti alloy can be fitted with Wagner's solution (solid lines). The 0.5 w/o Ti alloy deviates from Wagner's solution due to internal nitridation. From this alloy a KD_C value of 2.8×10^{-18} m^2/s $[w/o]^2$ at 900° C was calculated. The dotted line represents the Finite Difference solution for these conditions. The distribution of particles for a 0.5 w/o Ti alloy is shown in Figure 4.1.21, in qualitative agreement with observations (Figure 4.1.14b).

Good agreement was found between the calculated diffusion profiles of alloys ranging from 4.5 w/o Ti alloy to 0.5 w/o Ti, nitrided 48 hours at a temperature of 1020°C in 0.25 atmospheres nitrogen (Figure 4.1.22) using the same data as the 1 atmosphere pressure experiments. We note that with reduced pressure of nitrogen gas the

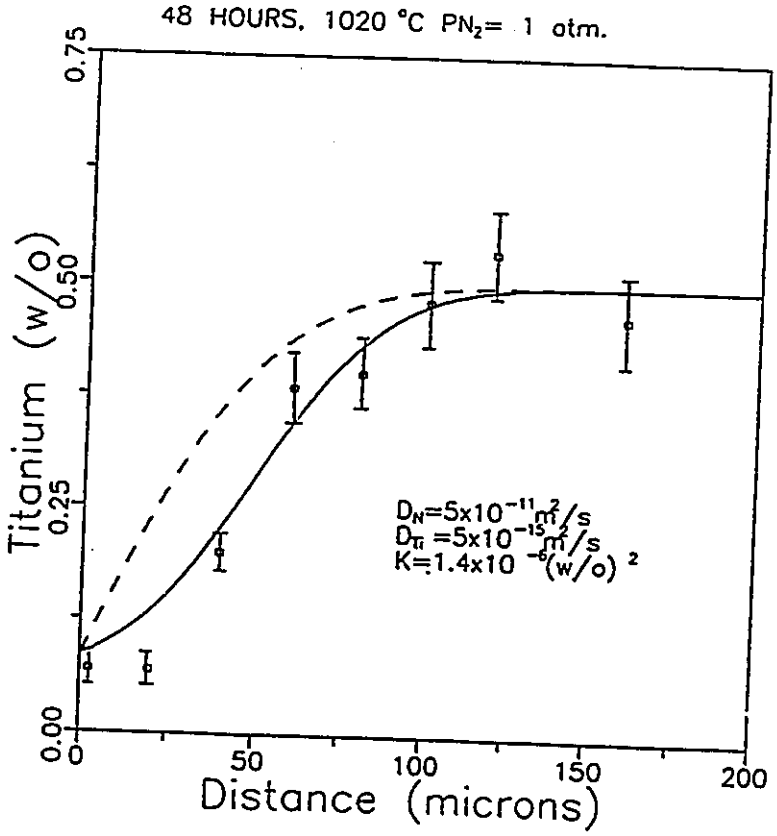

Figure 4.1.18: Measured profile of Ti in a 0.5 w/o Ti alloy nitrided 48 hours, 1020°C at 1 atmosphere nitrogen gas. The solid line represents the finite difference solution. The dashed line is from Equation 2.1.9 (no internal precipitates).

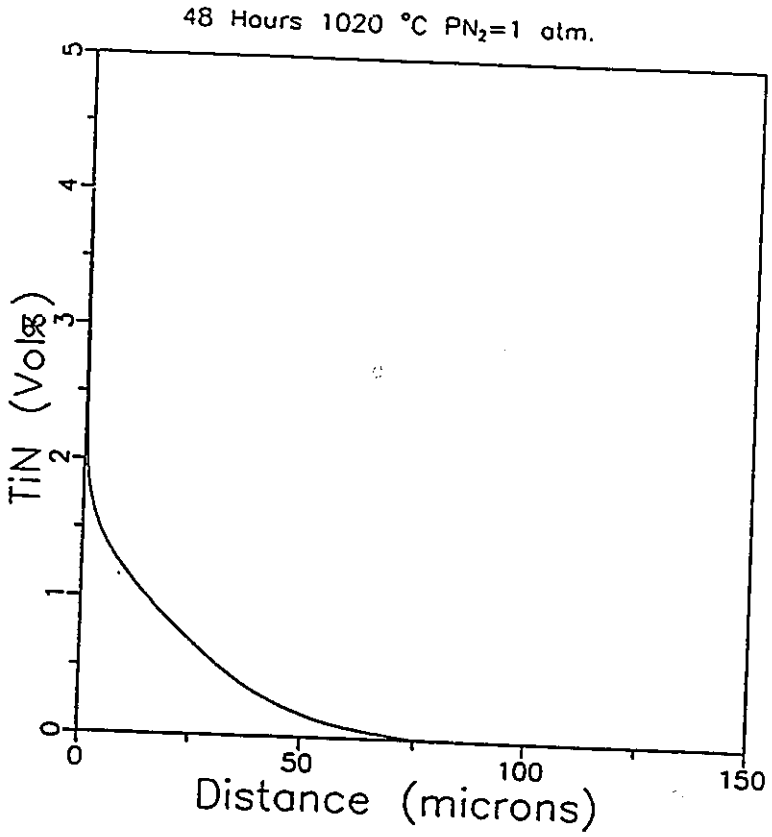

Figure 4.1.19: Calculated distribution of TiN particles in a 0.5 w/o Ti alloy nitrided 48 hours at 1020°C in 1 atmosphere nitrogen gas. The distribution and depth of precipitation bear a qualitative resemblance to Figure 4.1.14a.

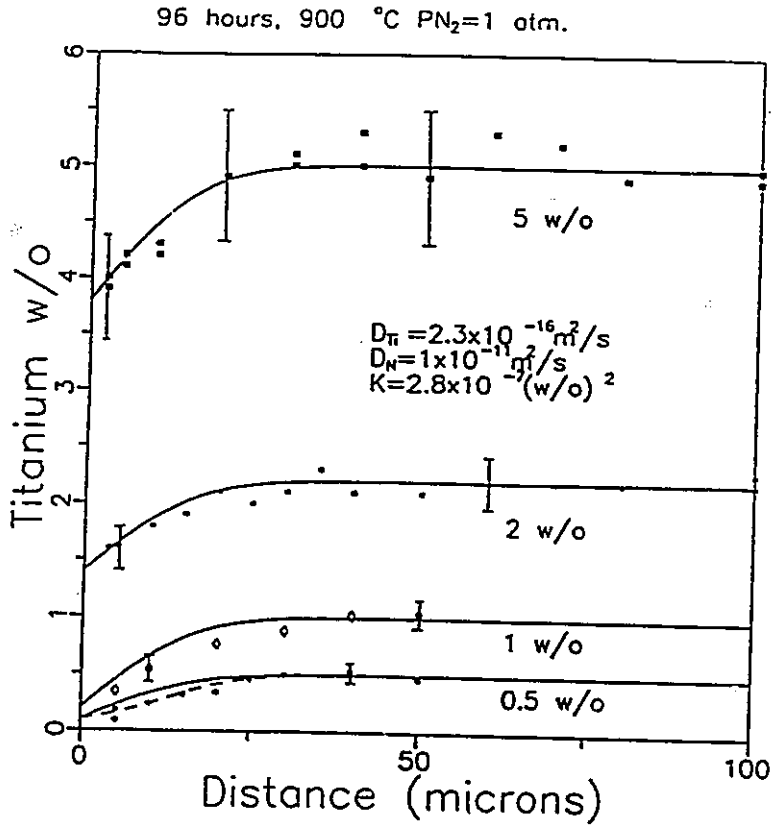

Figure 4.1.20: Measured and calculated profiles of Ni- Ti alloys ranging in composition from 0.5 w/o to 5 w/o Ti, nitrided 96 hours at 900°C in 1 atmosphere nitrogen gas. The diffusivity of Ti was determined to be 2.3 x 10^{-16} m^2/s from the highest Ti level.

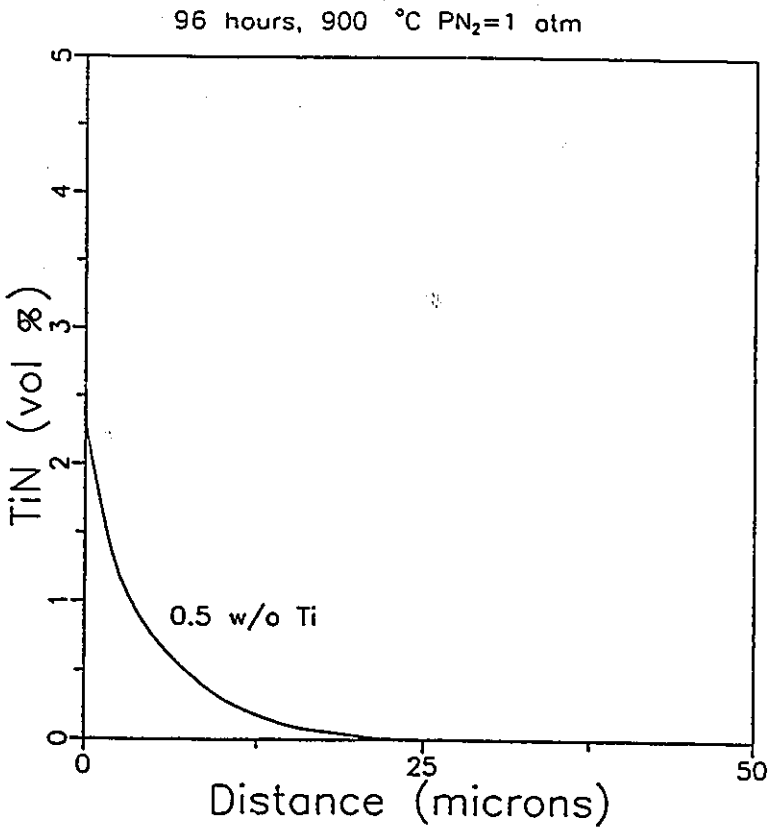

Figure 4.1.21: Calculated distribution of TiN particles in a 0.5 w/o Ti alloy nitrided 96 hours at 900°C in 1 atmosphere nitrogen gas. The distribution and depth of precipitation bear a qualitative resemblance to Figure 4.1.14b.

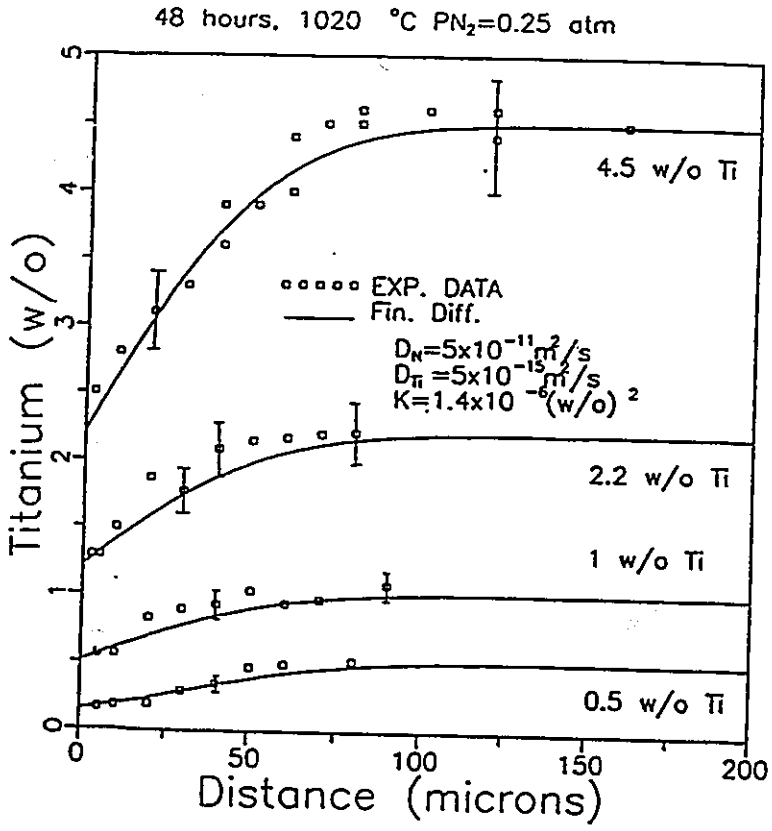

Figure 4.1.22: Measured and calculated profiles of Ni- Ti alloys ranging in composition from 0.5 w/o to 5 w/o Ti, nitrided 48 hours at 1020°C in 0.25 atmospheres nitrogen gas. The diffusivity data were accessed from Figures 4.1.14 and 4.1.15.

diffusivity of Ti in Ni remains at 5×10^{-15} m^2/s, indicating that metal solute diffusion is uneffected by the reduction in nitrogen partial pressure. The tendency is for higher interfacial concentrations of Ti at a reduced partial pressure of nitrogen. The calculated profile of TiN as a function of distance is shown in Figure 4.1.23, where it compares favourably with observations (Figure 4.1.14c).

The measured and calculated diffusion profiles for a 0.5 w/o Ti are shown in Figure 4.1.24 for an experiment performed at 800° C. The penetration profile was not very well developed and as a consequence there is a large experimental uncertainty in diffusivity determinations. An approximate value of 1×10^{-17} m^2/s was assigned for the diffusivity of Ti in Ni from the 5 w/o Ti alloy (not shown). A KD_C value of 1×10^{-19} m^2/s $[w/o]^2$ was assigned to the 0.5 w/o Ti alloy which again is acknowledged to be uncertain. A summary of the experimental data is shown in Table 4.1.1:

Table 4.1.1
Table of Kinetic/Thermodynamic Information of Ni-Ti-N alloys

Temperature (°C)	D_{Ti} (m^2/s)	KD_N ($[w/o]^2$ m^2/s)
800	1×10^{-17}	1×10^{-19}
900	2.3×10^{-16}	2.8×10^{-18}
1020	5×10^{-15}	7×10^{-17}

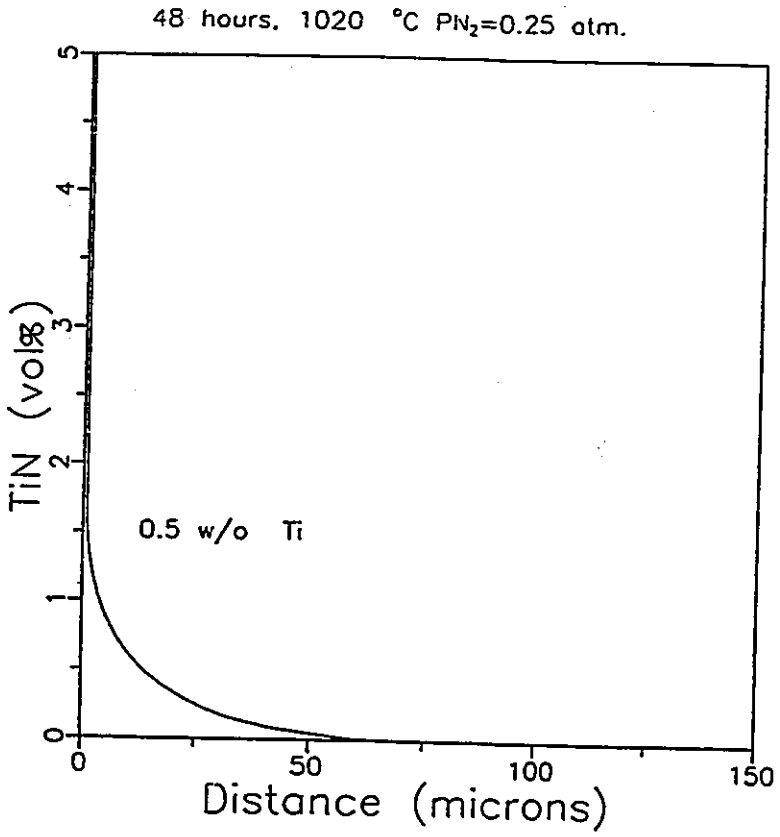

Figure 4.1.23: Calculated distribution of TiN particles in a 0.5 w/o Ti alloy nitrided 48 hours at 1020°C in 0.25 atmosphere nitrogen gas. The distribution and depth of precipitation bear a qualitative resemblance to Figure 4.1.14c.

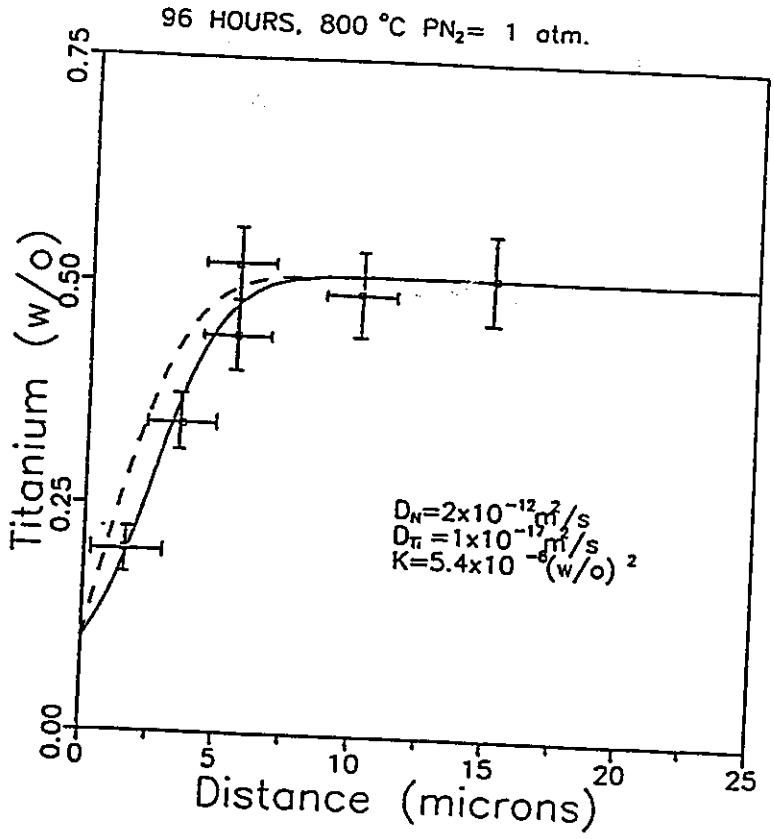

Figure 4.1.24: Calculated and measured diffusion profile for a 0.5 w/o Ti alloy nitrided at 800°C for 96 hours. A KD_C value of $1x\ 10^{-19}\ m^2/s\ [w/o]^2$ was assigned to this profile. The solid line is the finite difference solution, the dashed line is from Equation 2.1.9. No internal nitridation was observed in these alloys.

4.2: TEM OBSERVATIONS:

Introduction:

The chemical composition, crystal structure, morphology and the interfacial dislocation structure of the nitride phase found in the 0.1 w/o Ti alloys will be presented in this section. It was established that an fcc phase containing Ti and N, with a lattice parameter of 4.24 ± 0.02 Å was the only precipitated phase. This is consistent with TiN formation as established by X-ray diffraction measurements on the 5 w/o Ti alloys as outlined in the previous section. The nitride phase assumed a variety of shapes which could not always be reconciled with their orientation relationships. Five different orientation relationships will be shown. In only two of these were misfit compensating dislocations (ledges) observed. A detailed contrast study was made of one of these particles. The habit plane of the precipitated phase in the majority of cases was $\{100\}_{TiN}$.

4.2.1: Chemical Analysis Using TEM/STEM

Windowless EDX analysis indicated that once again Ti and N were the only chemical constituents of these particles. EELS analysis was also performed on these samples. An example from a particle in the alloy internally nitrided at 900°C is shown

in Figure 4.2.1a. An EELS analysis performed on a TiN standard is shown for comparison in Figure 4.2.1b. The two spectra are qualitatively the same despite the fact that they were not collected under identical conditions. In agreement with EDX analysis only Ti and N were present in these particles. Electron diffraction evidence for the existence of TiN was also gathered and will be shown in the subsequent sections of this chapter.

4.2.2: Type I: Cube on Cube Orientation Relationship : $(001)_{TiN} \| (001)_{Ni}$ with $[110]_{TiN} \| [110]_{Ni}$

An example of this orientation relationship, and the particle morphology usually associated with it is shown in Figure 4.2.2. Approximately forty percent of the particles had this orientation relationship. These particles were cuboidal in shape and primarily bounded by $\{100\}_{TiN}$ planes. Although all the interfaces in these samples were crystallographically equivalent, the length of each side of these particles were not always the same. For example the two sides in the present example differ in length by about 12%. An interesting feature of this sample was that the $(001)_{TiN}$ face is decorated with dislocations that appear to have been 'punched out' of the interface. Many of these dislocations have <110> line directions. A noteworthy example labelled 'A-A' in Figure 4.2.2, also has a loop associated with it. It appears that this dislocation had been emitted from the interface leaving behind a dislocation segment. These interfaces were generally very flat. A rare example of a step approximately 80 Å in height with an angle of

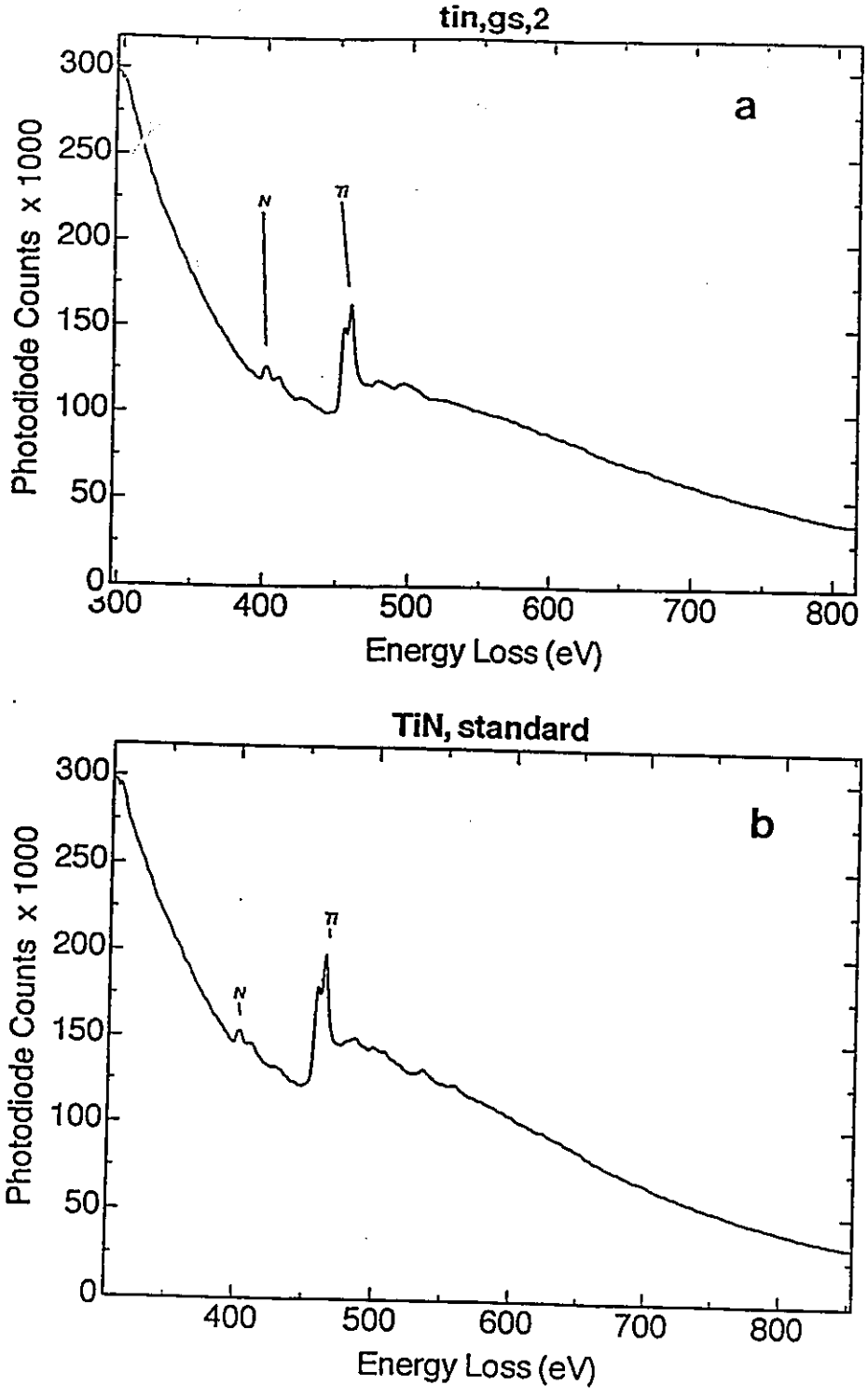

Figure 4.2.1: EELS analysis of a) an interior particle found in a 0.1 w/o Ti alloy nitrided 96 hrs in PN_2= 1atm, 900°C b) TiN standard.

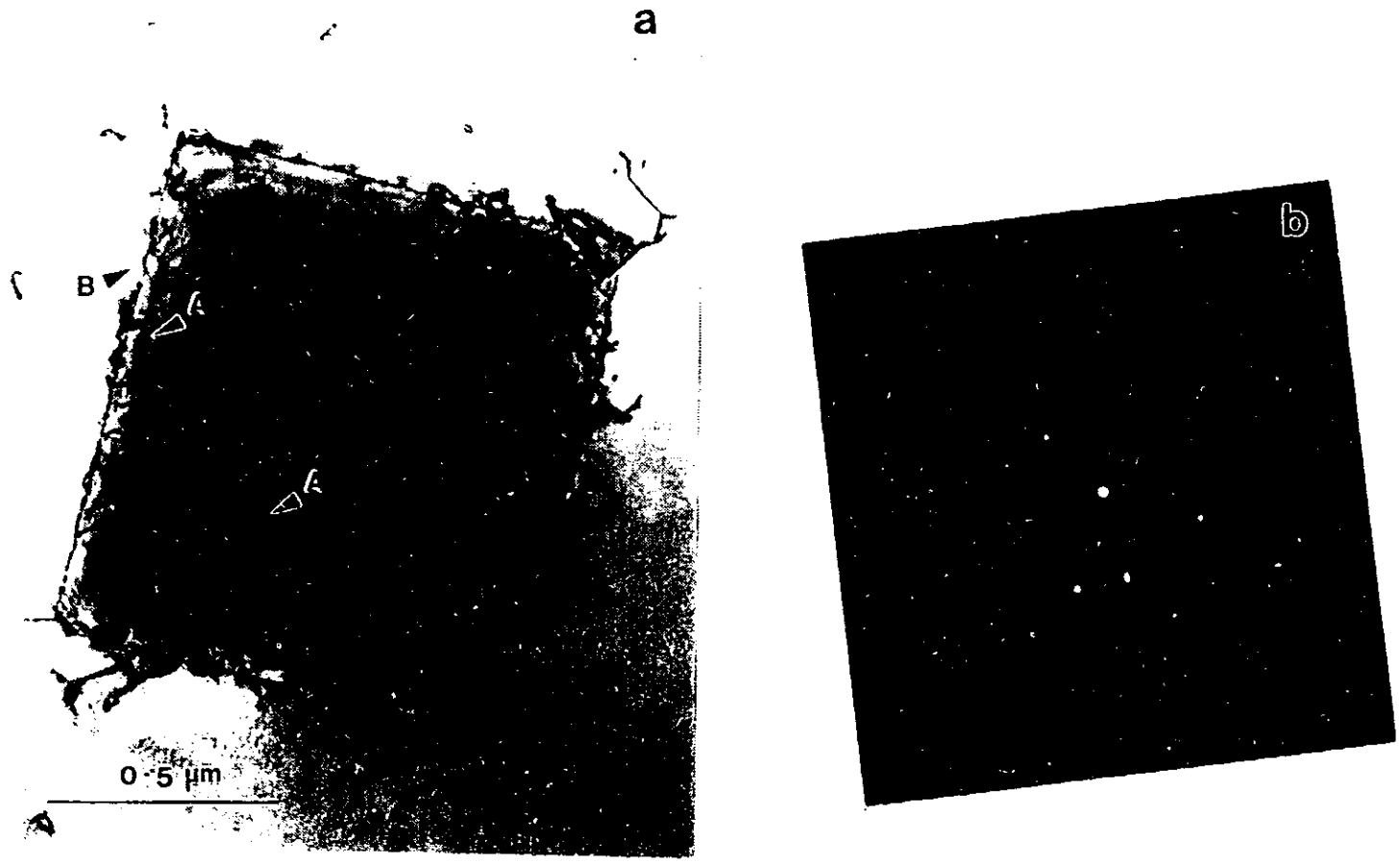

Figure 4.2.2: Example of a 'buried' particle with a 'cube- cube' orientation relationship: a) particle b) electron diffraction pattern. Bright Field [001]TiN‖[001]Ni.

approximately 45° to the interface is shown at 'B' in Figure 4.2.2. The diffraction pattern (Figure 4.2.2b) clearly shows that the particle has the same crystal structure as the nickel (fcc) phase. Measurement of the reciprocal lattice vectors showed the ratio of the lattice parameter of Ni to the particle to be 0.82±0.07 in fair agreement with that of a_{Ni}/a_{TiN}. An accurate means of determining the lattice parameter is to measure the length of the Kikuchi bands in the two phases. Measurement of the respective g_{800} bands yielded a value of 4.24±0.02 Å for the lattice parameter of the nitride phase. The extra (double diffraction) spots in the diffraction pattern should be noted.

Another example of a particle with a 'cube on cube' orientation relationship is presented in Figure 4.2.3, with its diffraction pattern. Note that the particle once again has sides that differ in length by about 12%. The sides of this particle were very flat with no visible ledges. Unlike the previous example this particle extends from the top to the bottom surface of the foil as noted by the absence of double diffraction spots in the diffraction pattern.

Although the majority of particles observed in this orientation relationship were dominated by $\{100\}_{TiN}$ facets other shapes were occasionally observed. To complete this section an example of a particle in a $[101]_{TiN}$ zone axis is depicted in Figure 4.2.4. This clearly shows a particle with a cube on cube orientation relationship with both {100}

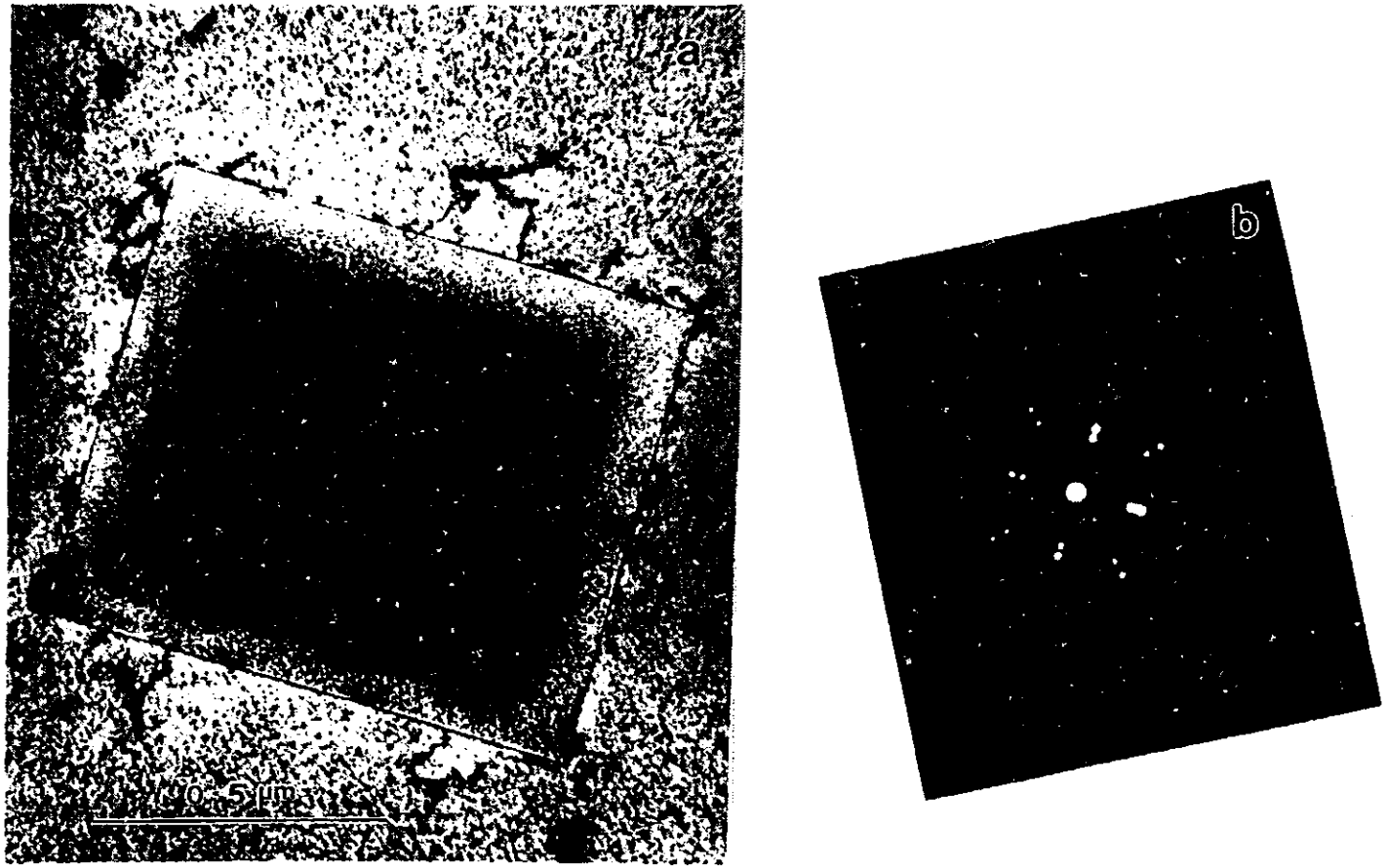

Figure 4.2.3: a) Example of a particle with a 'cube- cube' orientation relationship. b) diffraction pattern.

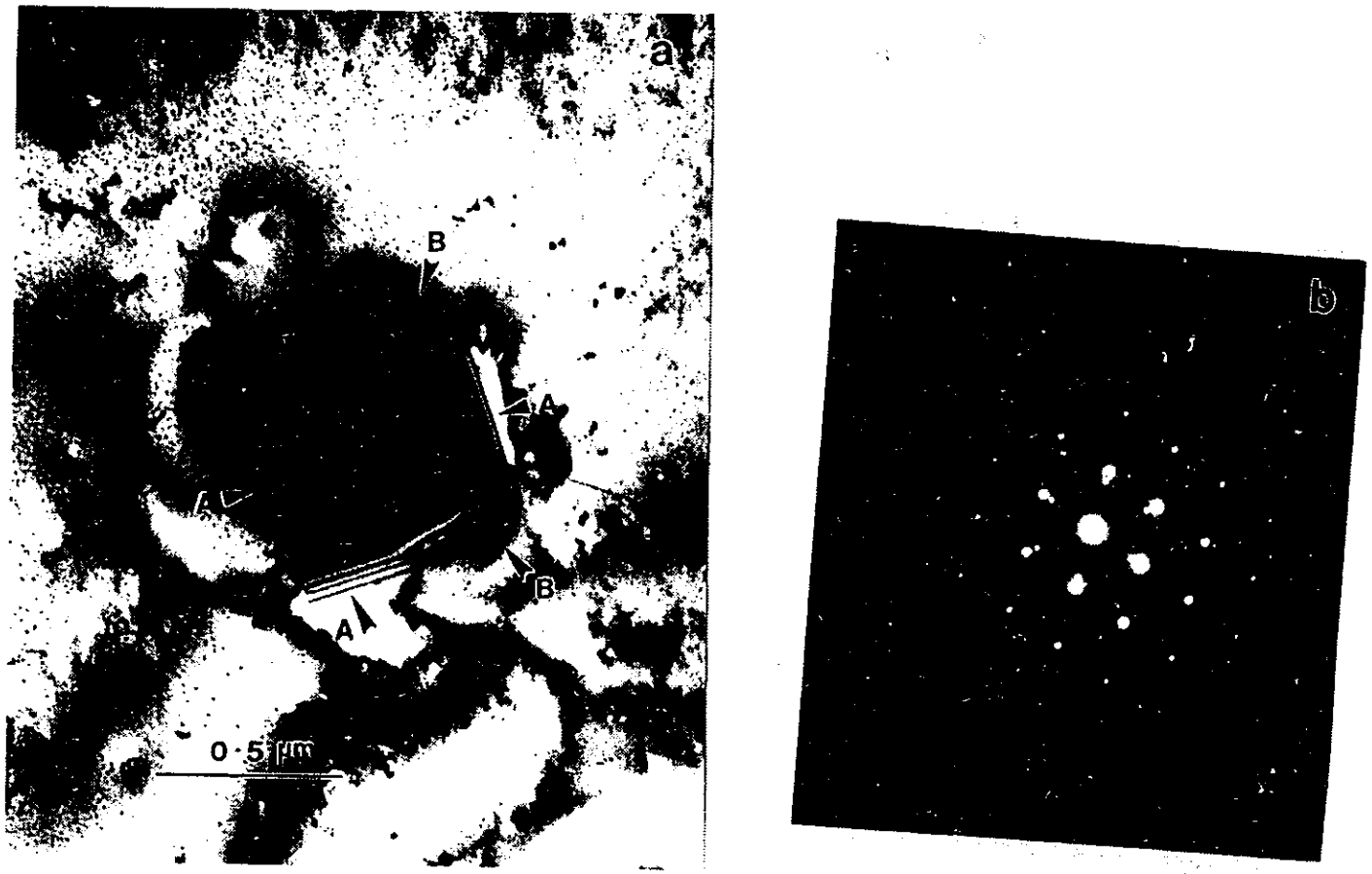

Figure 4.2.4: Example of a cube- cube orientation relationship with non - (200) facets. a) particle b) electron diffraction pattern. Bright field [101]TiN‖[101]Ni.

type facets (labelled 'A') as well as non- {100} type (labelled 'B').

4.2.3: Type II: $(\bar{1}11)_{Ni} \| (010)_{TiN}$ with $[211]_{Ni} \| [100]_{TiN}$

An example of a lath shaped particle of approximately 5 μm in length and 0.1 μm wide with this orientation relationship is shown in Figure 4.2.5. The long direction of the particle corresponds to $[100]_{TiN} \| [211]_{Ni}$ with the habit plane corresponding to $(010)_{TiN} \| (\bar{1}11)_{Ni}$. One end of the particle is bounded by a $\{100\}_{TiN}$ facet, while the other end has a 'wedged shaped' facet approximately indexed as (5 14 25). A higher magnification image of this end of the particle shows Moiré fringes with a spacing of approximately 50 Å, labelled 'M-M' in Figure 4.2.6a. The habit plane appears essentially flat, however, as noted in Figure 4.2.6b small step-like features less than 10Å in height may be observed at positions such as 'A'.

The requirements for imaging the interfacial dislocations were difficult to achieve in this present example. Dislocations were seen only in weak beam dark field conditions. Weak beam images of this particle (taken with g_{111}^{Ni}) are shown in Figure 4.2.7. Again the faceted end of the particle shows fringes with a spacing of approximately 50 Å (labelled M-M) in Figure 4.2.7a. Step- like features can be seen at

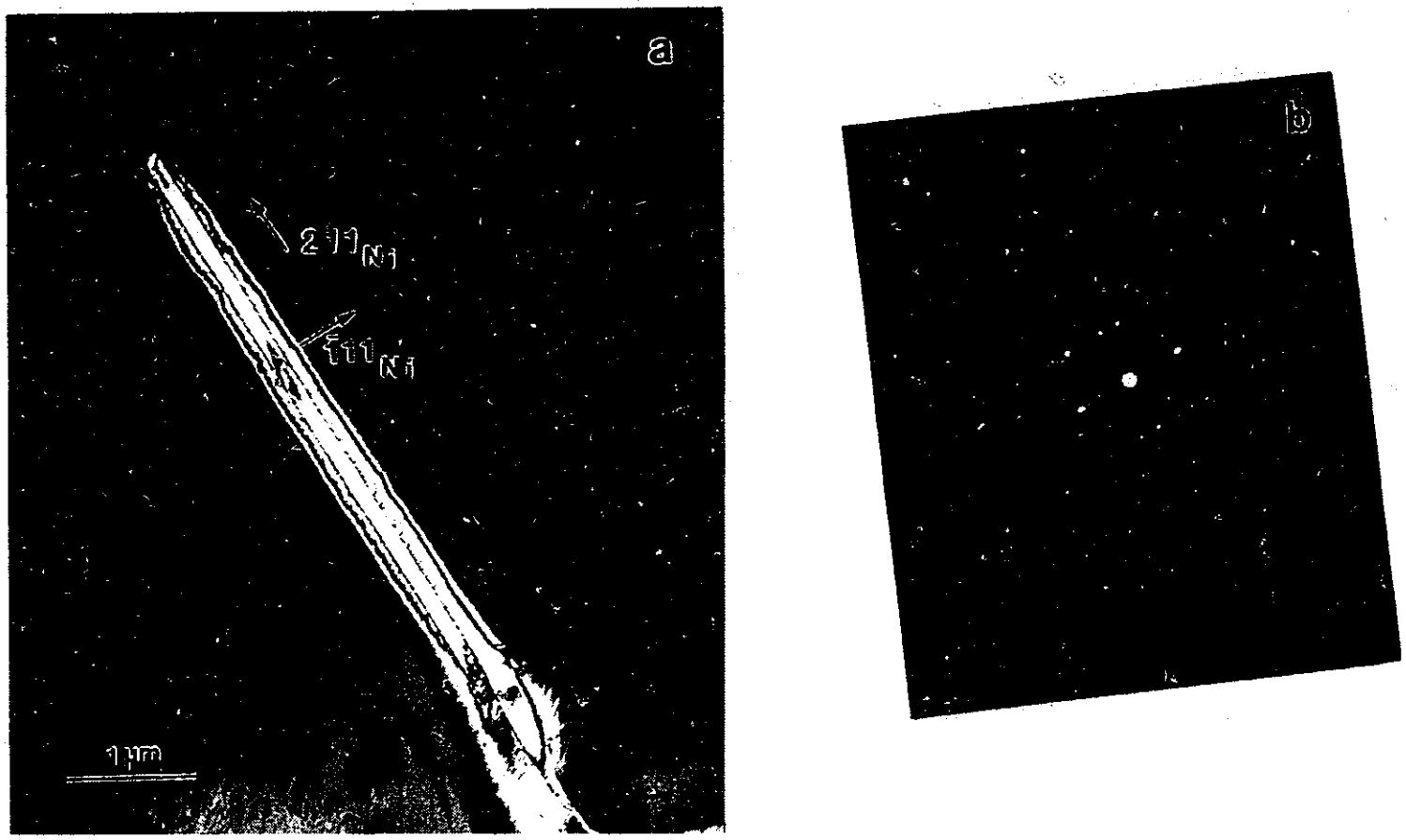

Figure 4.2.5: Example of a Type II orientation relationship a) particle b) electron diffraction pattern. Bright Field [001]TiN‖[0$\bar{1}$1]Ni.

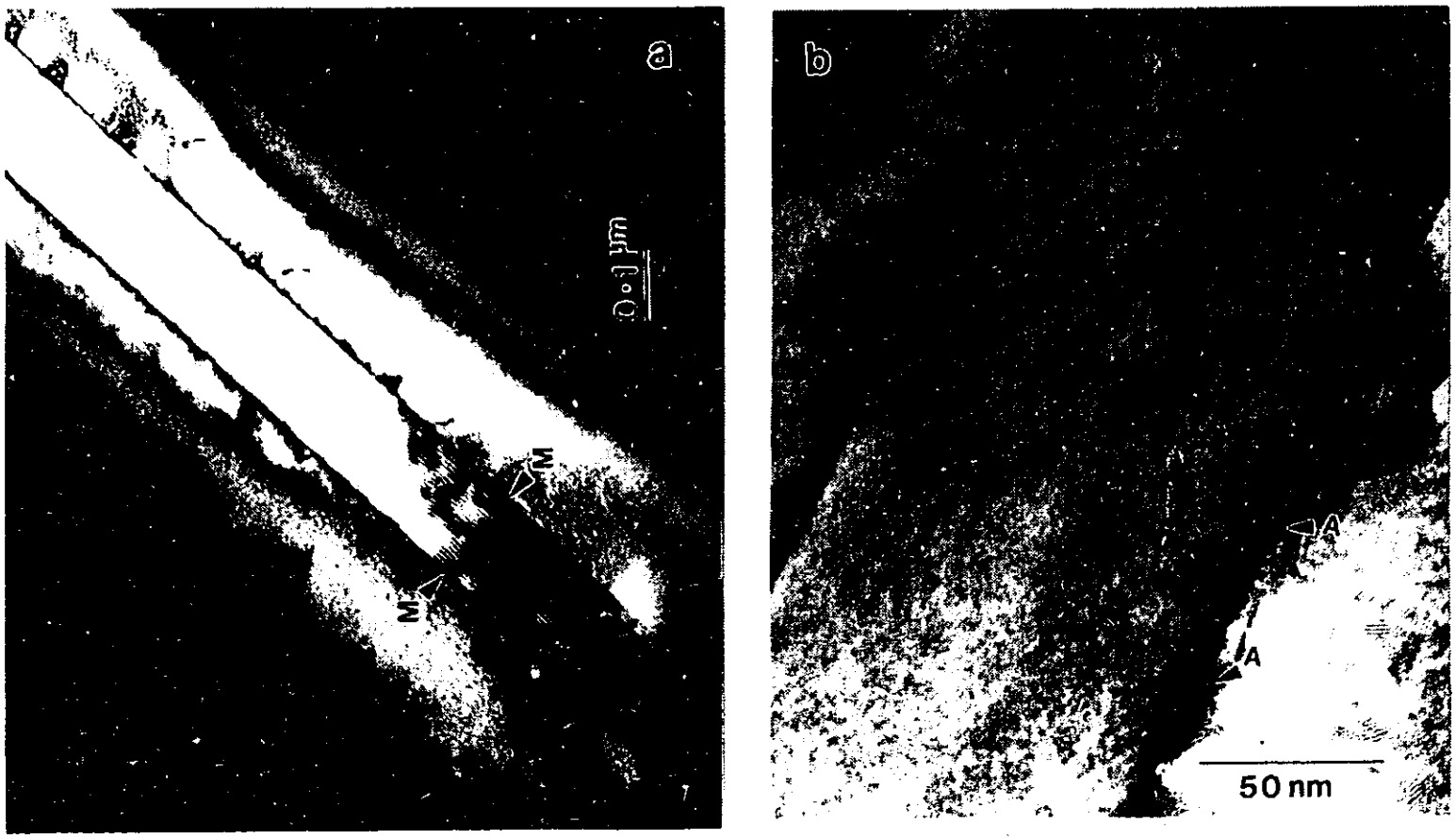

Figure 4.2.6: Showing higher magnification of a) faceted end of particle with Moiré fringes and b) the interface with fine step-like features

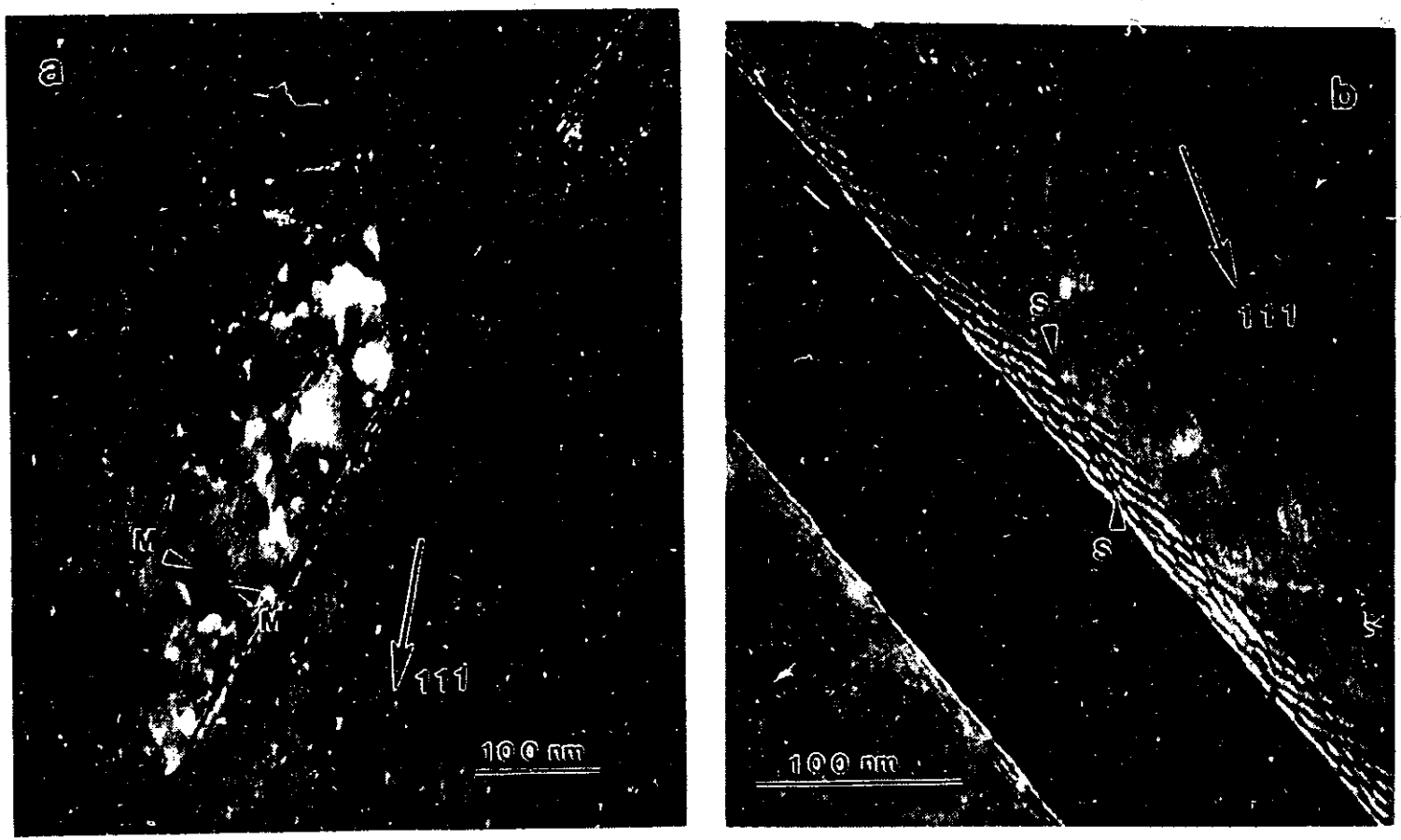

Figure 4.2.7: Weak beam dark field image of the dislocation configuration of the interface near the high index end facet and b) showing step- like feature near the (100) end facet. g_{111}^{Ni}, w = +1.9

areas such as 'S-S' in Figure 4.2.7b. Geometrical analysis showed that one set of dislocations has a line direction $[001]_{TiN}$ with a spacing of ≈120 Å. A second set perpendicular to the first, with a spacing of about 40 Å could be found in some areas (Figure 4.2.7).

4.2.4: Type III: [001]TiN ∥ $[\bar{1}\,\bar{2}\,1]$Ni (010)TiN ∥ $(7\bar{1}5)$Ni

This orientation relationship along with the cube on cube orientation relationship were the two most frequently observed. Three examples of particles with this orientation relationship will be shown. These provide examples of particles having different aspect ratios as well as interesting examples of dislocation contrast.

Case i- twist component: The morphology of this particle along with its diffraction pattern is shown in the edge-on position in Figure 4.2.8. The particle is lath shaped with the long direction corresponding to [100]TiN ∥ $[3\bar{4}\,5]$Ni with a (010)TiN ∥ $(7\bar{1}5)$Ni habit plane. A 'twist' component of the order of 0.9° was noted from the displacement of the Kikuchi patterns with respect to one another. The dimensions of the particle were 3.4 μm in length and 95 nm in width.

Unlike the particle in the previous example interfacial dislocations were visible both in bright field and in weak beam dark field. An example is shown in Figure

4.2.9 where dislocations on both sides of the particle could be imaged in bright field (w=0, Figure 4.2.9a). As in the previous example, under conditions of large w, only dislocations on one side of the particle could be imaged. This side was characteristically the side into which g pointed (Figure 4.2.9b). Reversing g at a fixed value of w>0 had the effect of reversing the side of the particle which displayed dislocation contrast. The top and bottom of the particle are marked by 'T' and 'B' respectively. This was determined both from tilting experiments as well as noting the change in black/white contrast of the dislocations indicated in the figure by 'BL' and 'WT'.

The structure of the interface is shown in a series of weak beam images in Figure 4.2.10. One set of dislocations is clearly evident in all the images, but another set of lines in weaker contrast can also be seen running parallel to a step- like feature at position 'S-S' in Figure 4.2.10a. Geometrical analysis utilizing these various images shows the 'strong' set of dislocations to have a line direction about 5° towards [001]TiN away from $[\bar{1}01]$TiN with a spacing of approximately 100 Å, while the step has a line direction close to [503].

Case ii- tilt component: The second example of a particle with this orientation relationship is shown in Figure 4.2.11. We note that the aspect ratio is different from the previous case, also as in the previous example the zone axes are not exactly parallel to one another; in this particular case, however, there is a 'tilt' component of 0.9° between

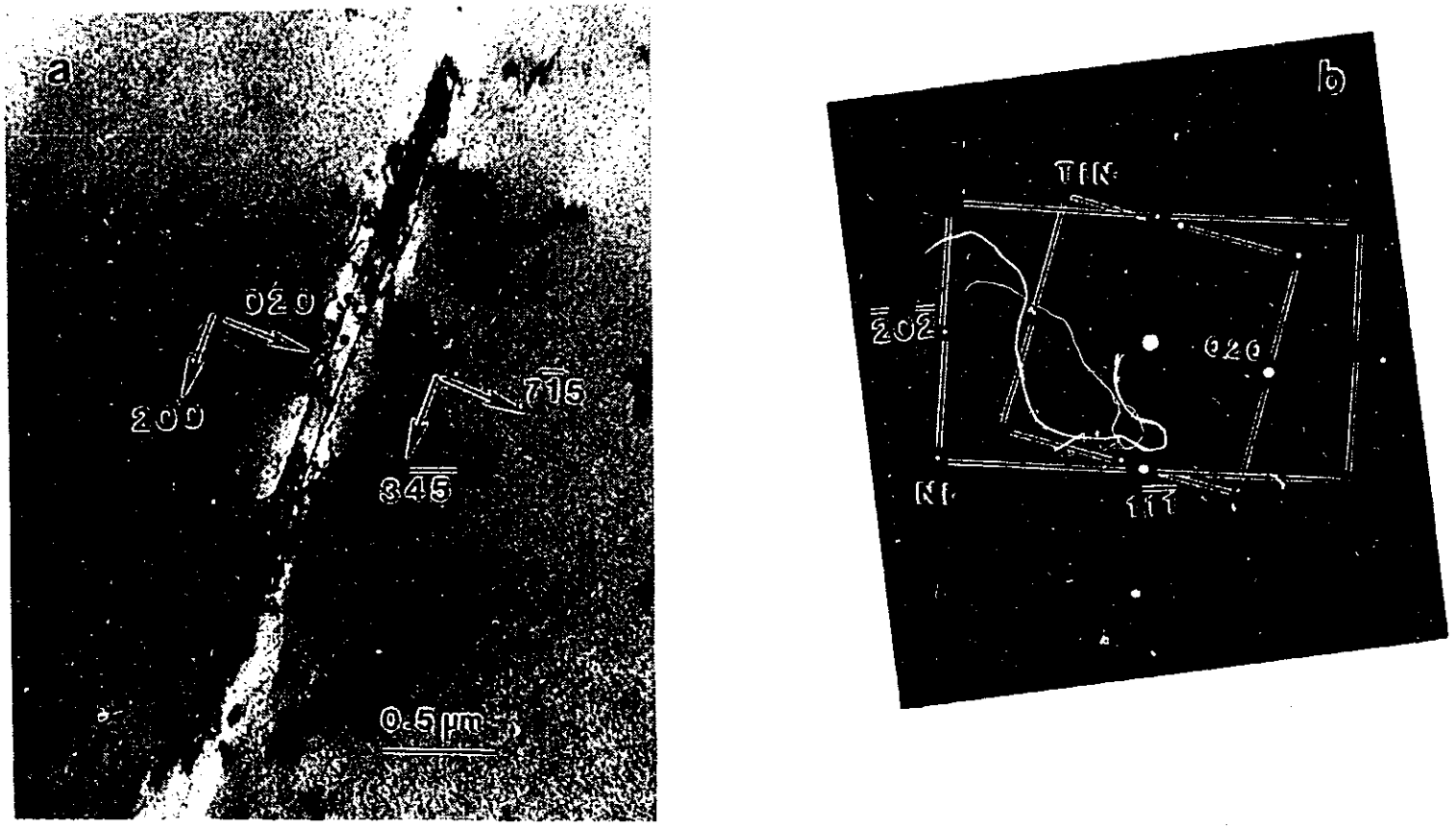

Figure 4.2.8: a) particle with a Type III- twist OR b) its diffraction pattern. Bright Field [001]TiN∥[$\bar{1}21$]Ni.

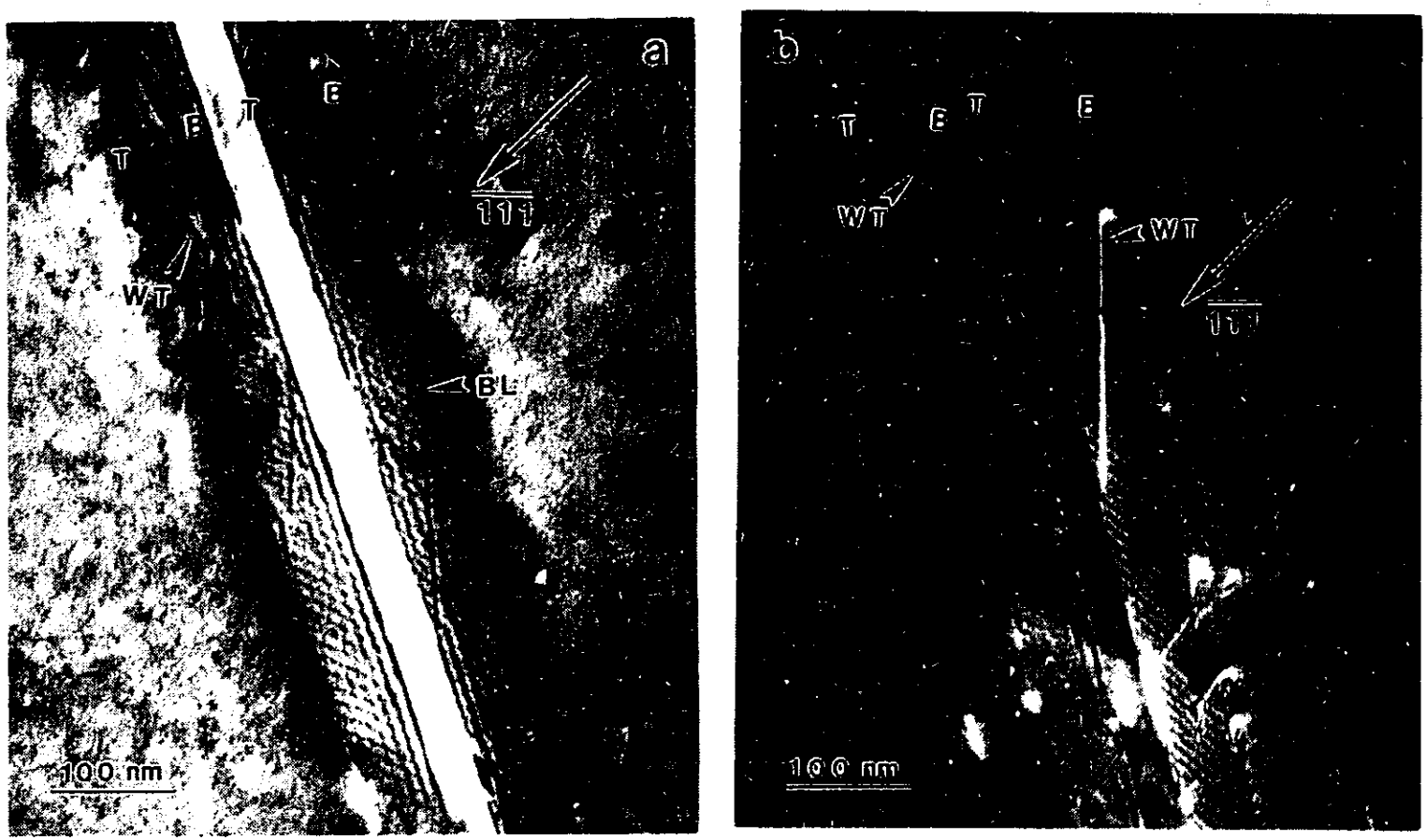

Figure 4.2.9: Showing effect of w on image $g_{\overline{111}}^{Ni}$ a) bright field w= 0 b) w=+ 1.9 'B' and 'T' refer to the top and bottom of the particle respectively. 'BL' and 'WT' refer to white and dark contrast respectively.

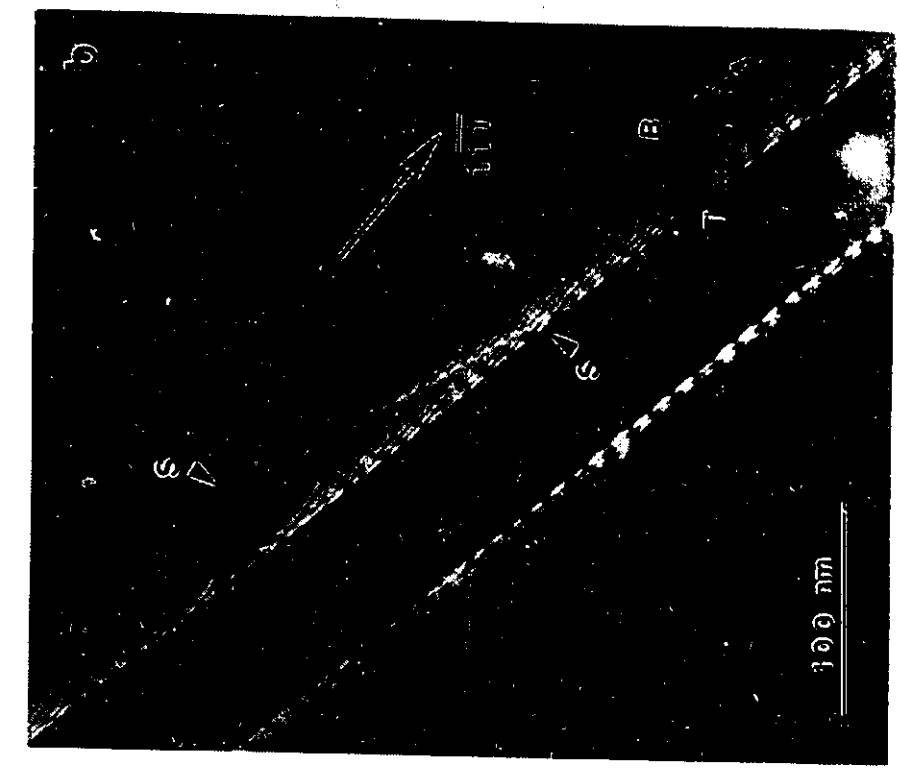
b
T
B
S
S
100 nm

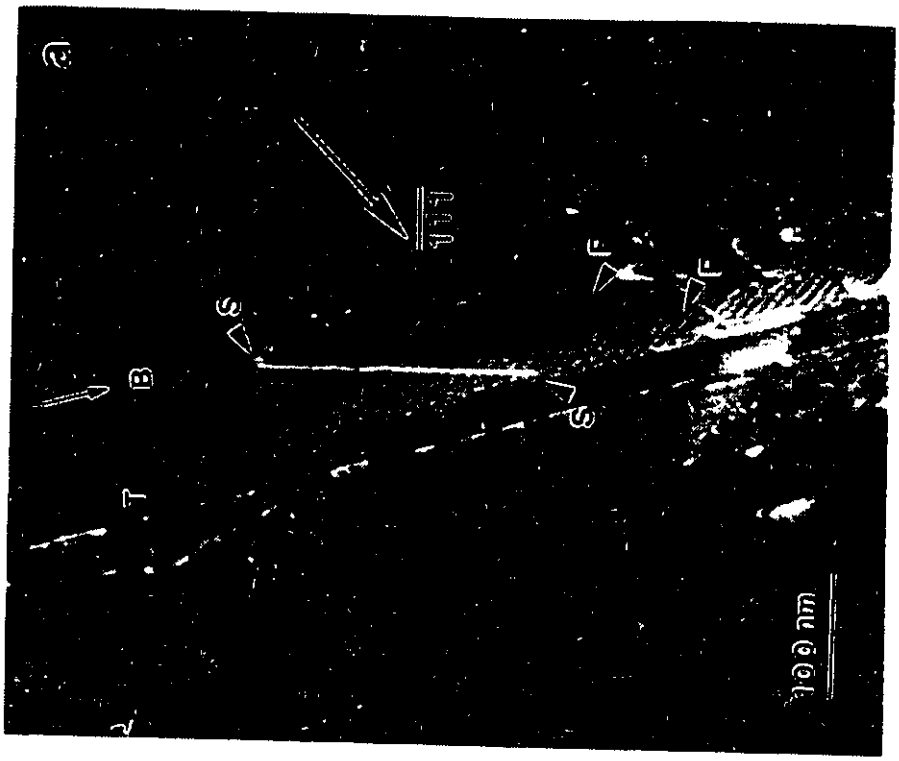
a
T
B
S
S
F
F
100 nm

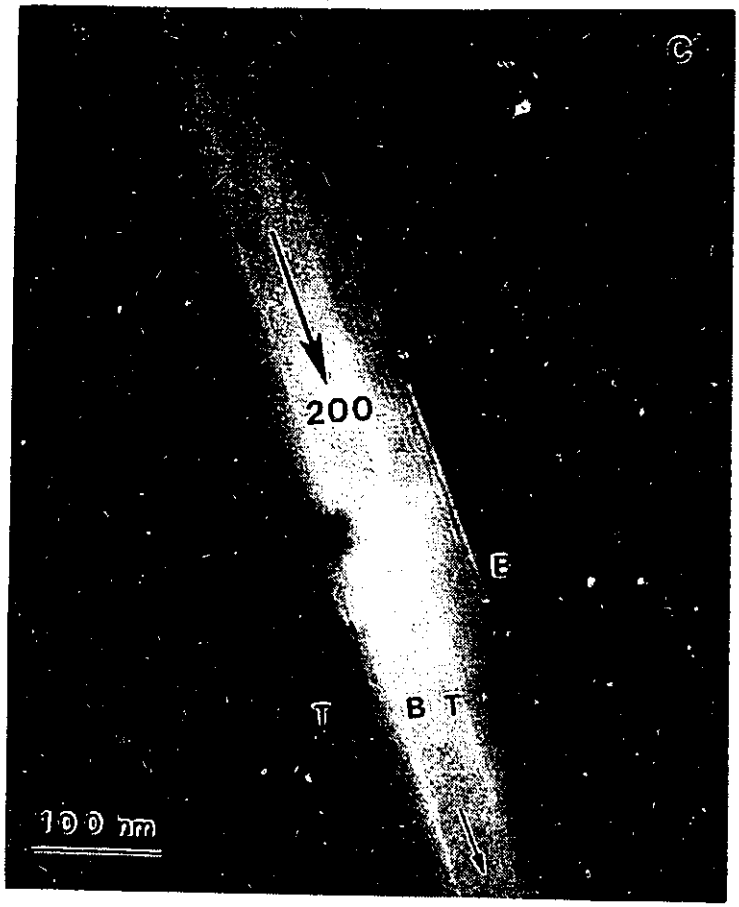

Figure 4.2.10: Weak Beam Dark Field Images of interfacial structure a) $g_{\overline{111}}^{Ni}$, w= +1.9 b) $g_{1\overline{11}}^{Ni}$, w= + 1.9 and c) g_{200}^{TiN}, w=+2.7

the two phases as noted by the displacement of the Kikuchi patterns. A facet is evident at one end of the particle with a $[3\bar{2}0]_{TiN}$ normal. The long direction of the particle is [100]TiN ‖ [[$3\bar{4}\bar{5}$]Ni with a (010)TiN ‖ ($7\bar{1}5$)Ni habit plane. The particle is 1.2 μm in length and 0.4 μm in width. The particle morphology is clearly shown in Figure 4.2.11b where a [012]TiN zone axis was used to obtain this image. The facet shows step-like features labelled 'S' in the figure, and the particle shape is terminated by (100)TiN facets indicated by the 'A' in the figure. It is noteworthy that in this case that there is some variability in the width of this particle. The convex nature of this interface may be seen clearly in a higher magnification image of the particle in an edge-on position oriented about 10° away from $[101]_{TiN}$ towards [001]TiN (Figure 4.2.12). Points such as 'S', about 15 nm in height, correspond to steps at the interface (Figure 4.2.12).

The structure of the interface was investigated using weak beam dark field and bright field microscopy including the so- called double two beam condition (Forwood and Clarebrough 1991). As in case i) under no conditions was an invisibility condition achieved. Weak beam images of this interface are shown in Figure 4.2.13. One set of dislocations is shown with a variable spacing between 100 Å and 160Å. Geometrical analysis of these dislocations shows that they are deviated 15° from [101] towards [001]. A comparison of this image to that of Figure 4.2.10c shows clearly that the line direction of these dislocations has changed by about 55° due to the small angular deviation in orientation relationship.

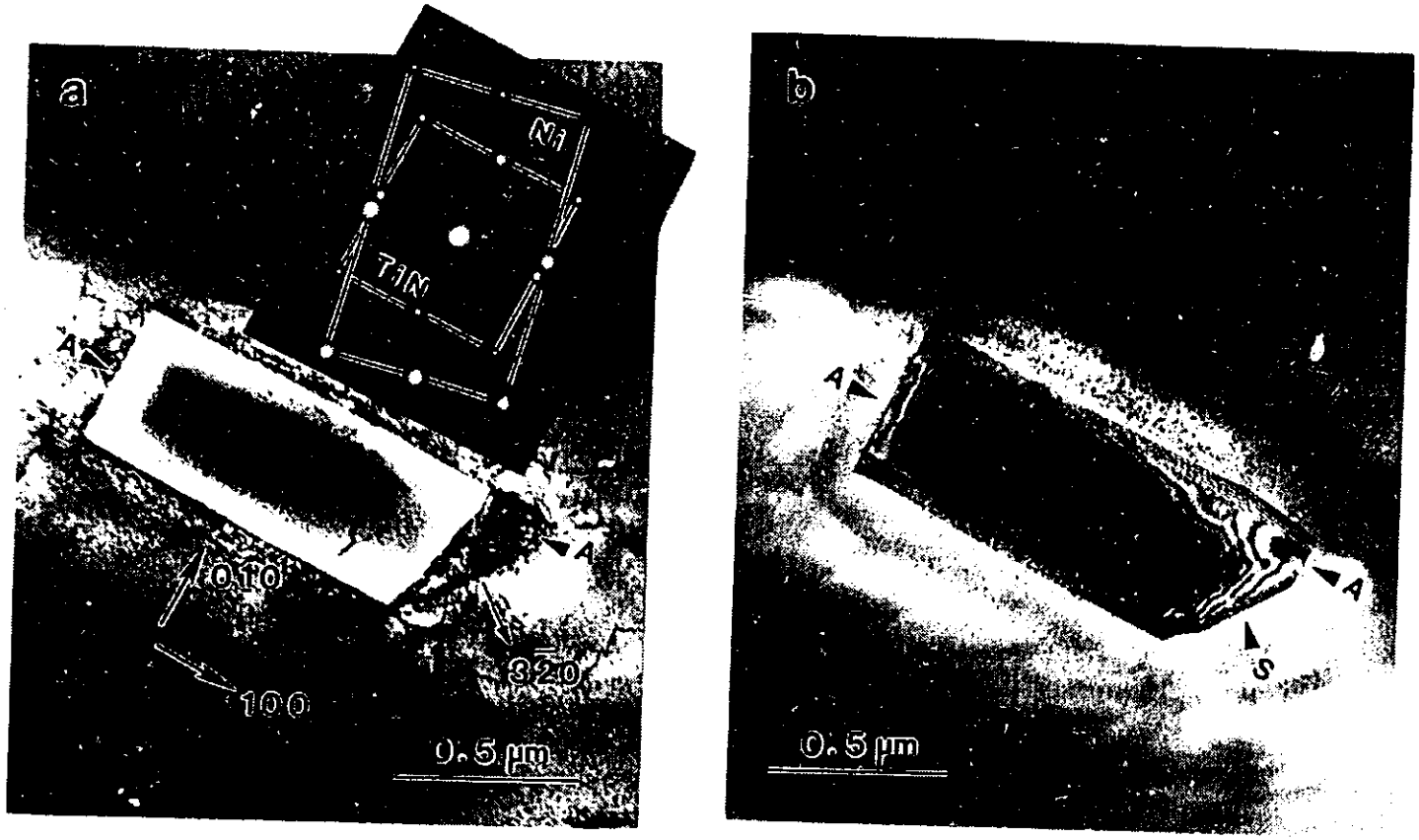

Figure 4.2.11: a) Example of a Type III- tilt OR: Bright Field [001]TiN≈‖[$\bar{1}\bar{2}$1]Ni b) [012]TiN zone axis

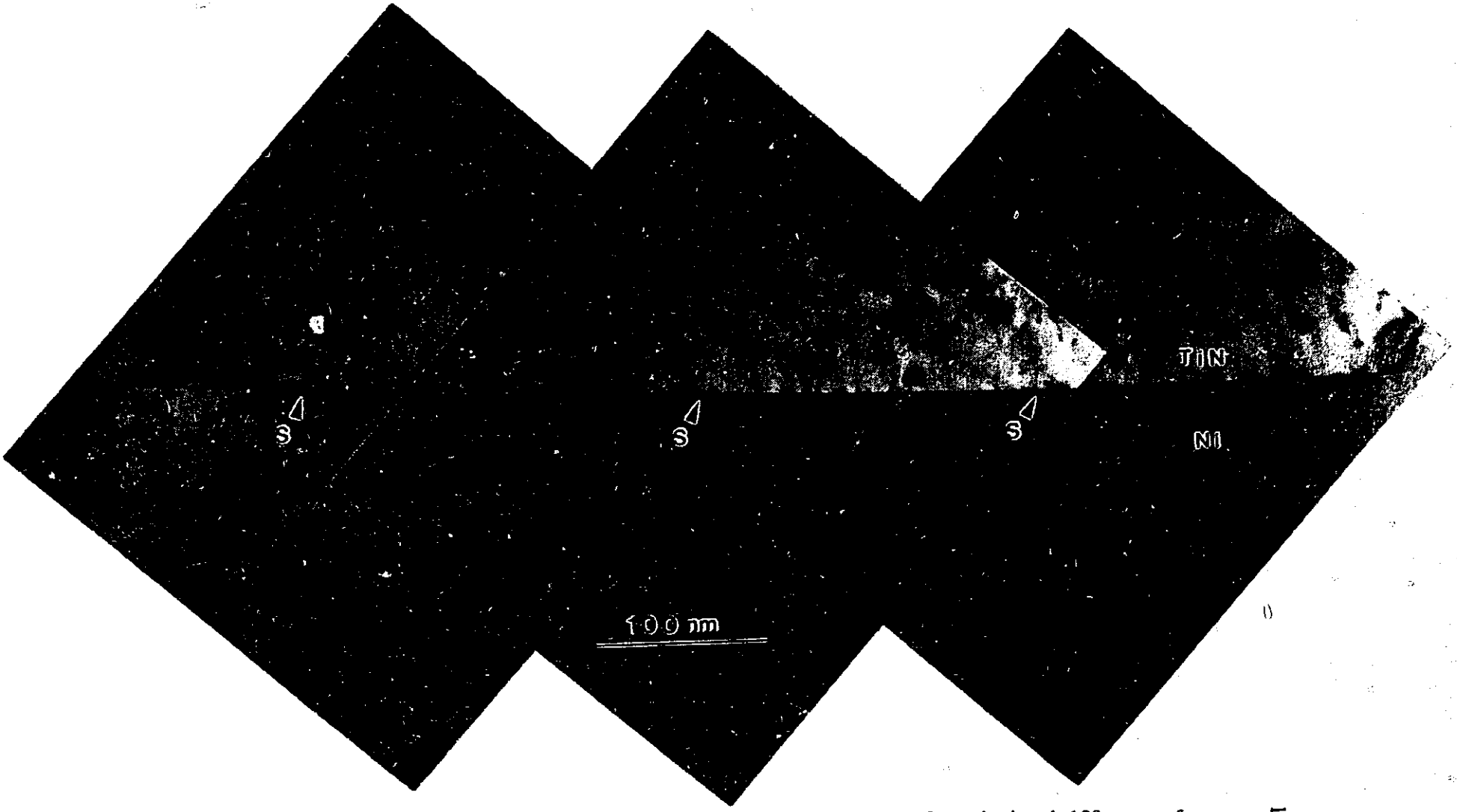

Figure 4.2.12: Higher magnification image of the interface deviated 10° away from [101]TiN towards [001]TiN. Step-like features may be observed at 'S'.

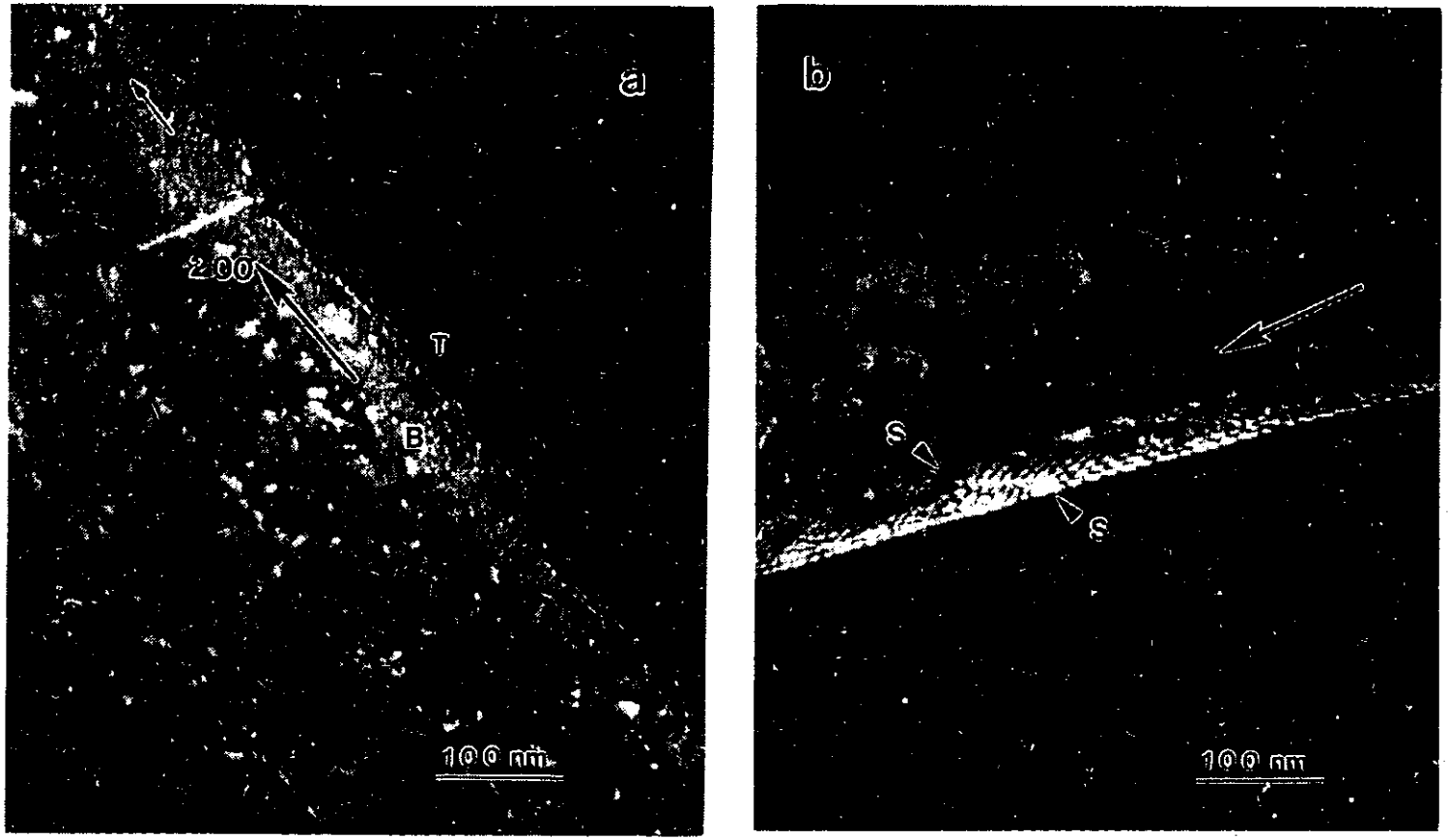

Figure 4.2.13: Weak Beam Dark Field of the interface a) g_{200}^{TiN}, w=+2.7 b) $g_{1\bar{1}1}^{Ni}$, w= +1.9:

case iii) - variant with $[010]_{TiN}$ normal: A type III OR variant was observed. This particle was indexed as (010)TiN ‖ (517)Ni with [001]TiN ‖ $[\overline{1}\,2\,1]$Ni and is viewed from a [010] zone axis in Figure 4.2.14 (i.e. normal to the previous examples which were viewed always close to [001]). This variant is crystallographically equivalent to the previous examples. The two ends of the particles are faceted and show clear dislocation contrast with a projected direction deviated 5° from $[10\overline{1}]$TiN towards [100] with a spacing of 94 Å. The projected spacing and orientation of these dislocations are close to what is observed for case (i). The facet was approximately indexed as $(101)_{Ni}$~‖ $(2\ 11\ \overline{1})_{TiN}$. The facets were parallel to one another as noted by the contrast study of Figure 4.2.15. The black/black (BL/BL) contrast of the defects at the interface both in dark and bright field indicate that effectively they lie at the 'top' of the Ni (i.e. at the bottom of the particle) while the black/white (BL/WT) contrast of the other facet in bright and dark field respectively indicates that the defects are at the "bottom" of the Ni foil (i.e. at the top of the TiN particle). A **g·b** analysis was performed on this particle utilizing both TiN and Ni reflections. Examples of the dislocation contrast from these various images are shown in Figures 4.2.16 to 4.2.19 and the results are summarized in Table 4.2.1. The misfit dislocations have a $[\overline{1}01]_{Ni}$ line direction which is approximately parallel to $[\overline{4}13]_{TiN}$. It may be recalled that the Type III- twist particle had a dislocation line close to $[\overline{1}01]_{TiN}$ which is almost parallel to $[31\overline{4}]_{Ni}$. The defects labelled as 'H' in the Figures 4.2.16 to 4.2.19 had a line direction close to $[\overline{2}12]_{Ni}$ approximately parallel to $[\overline{5}11]_{TiN}$.

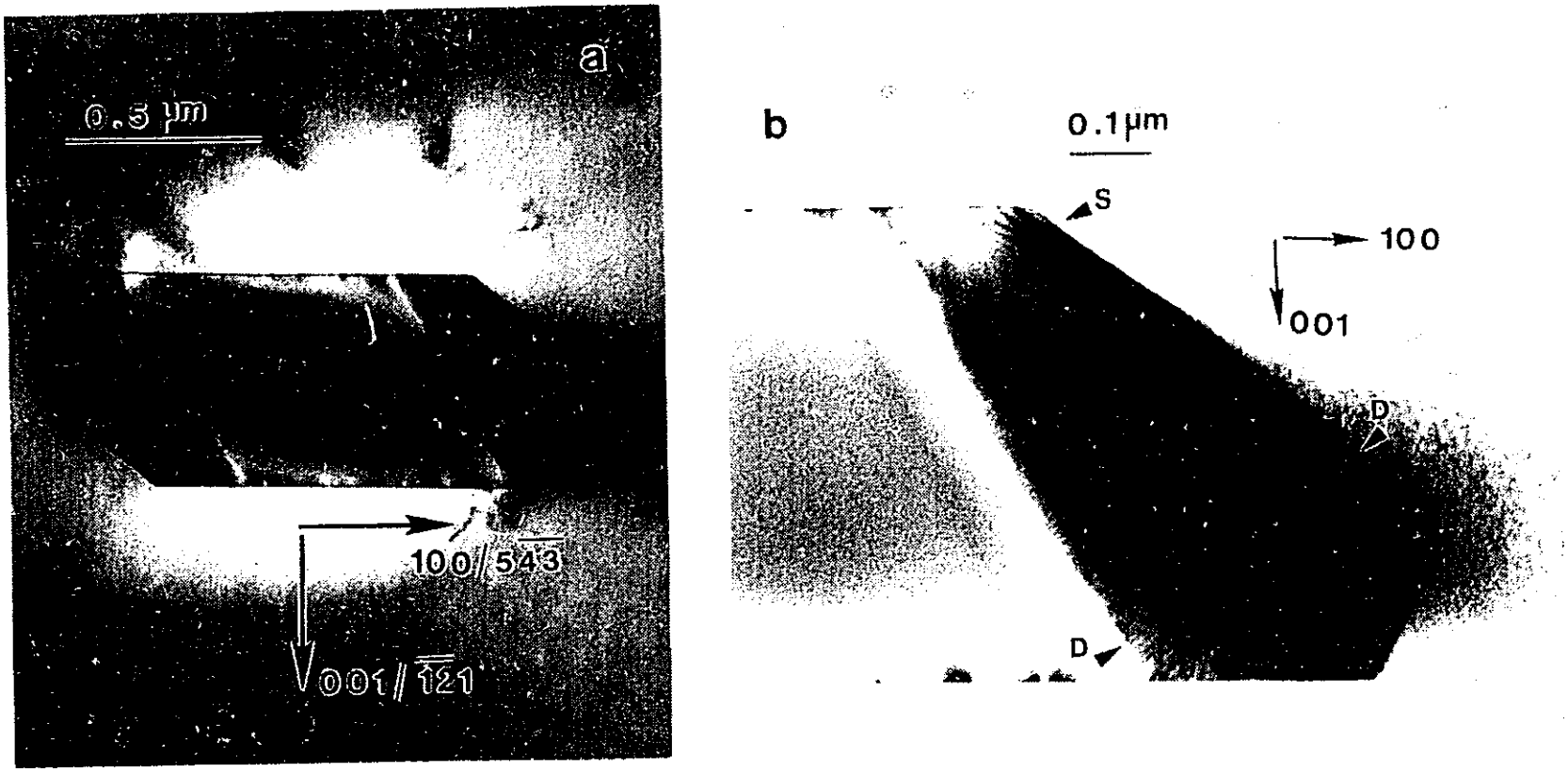

Figure 4.2.14: Particle with a Type II OR. The view is normal with respect to Figures 4.2.10 and 4.2.14 i.e. [010]TiN zone axis:

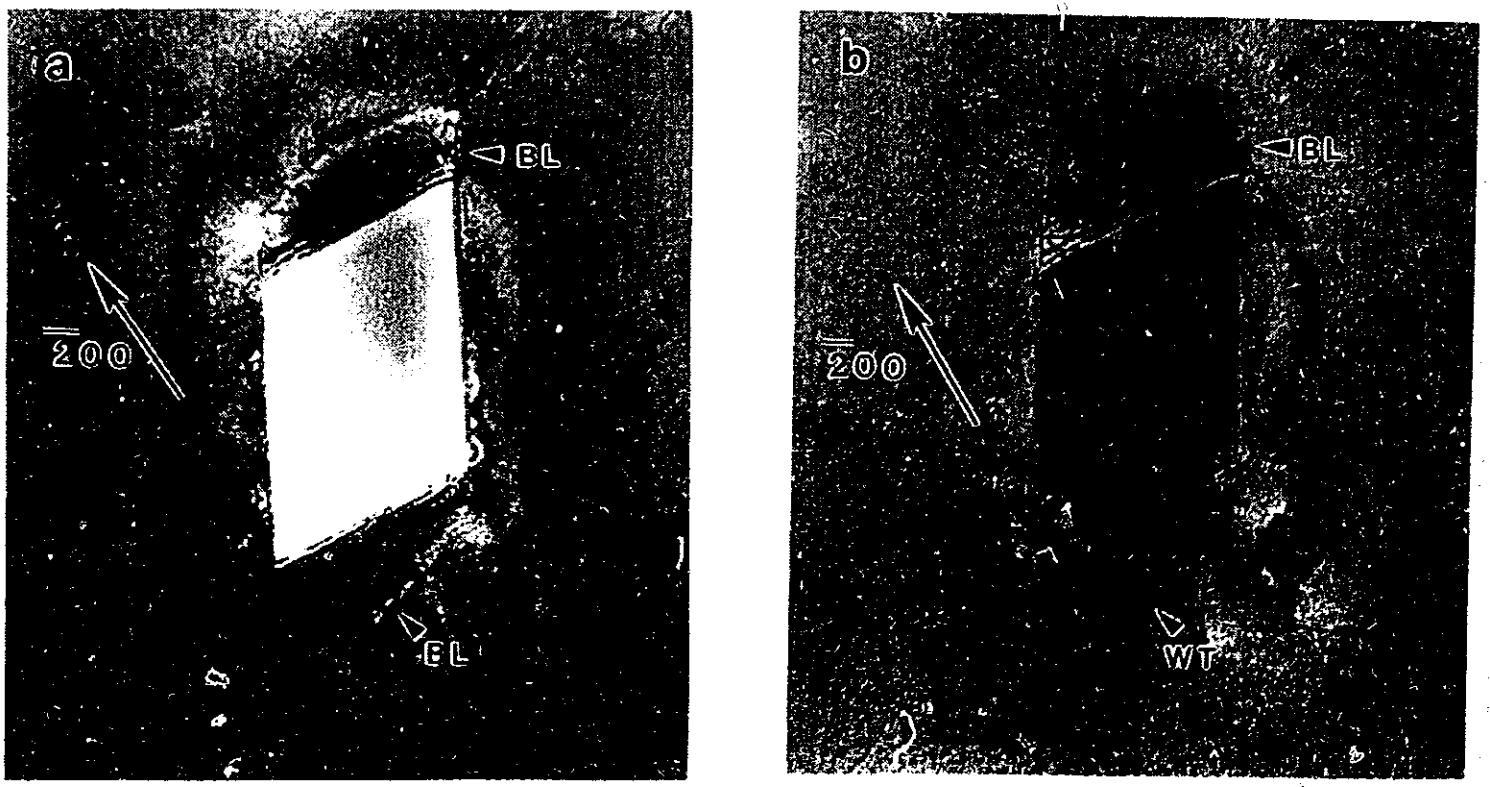

Figure 4.2.15: Example of black /white contrast variation between a) bright field and b) dark field.

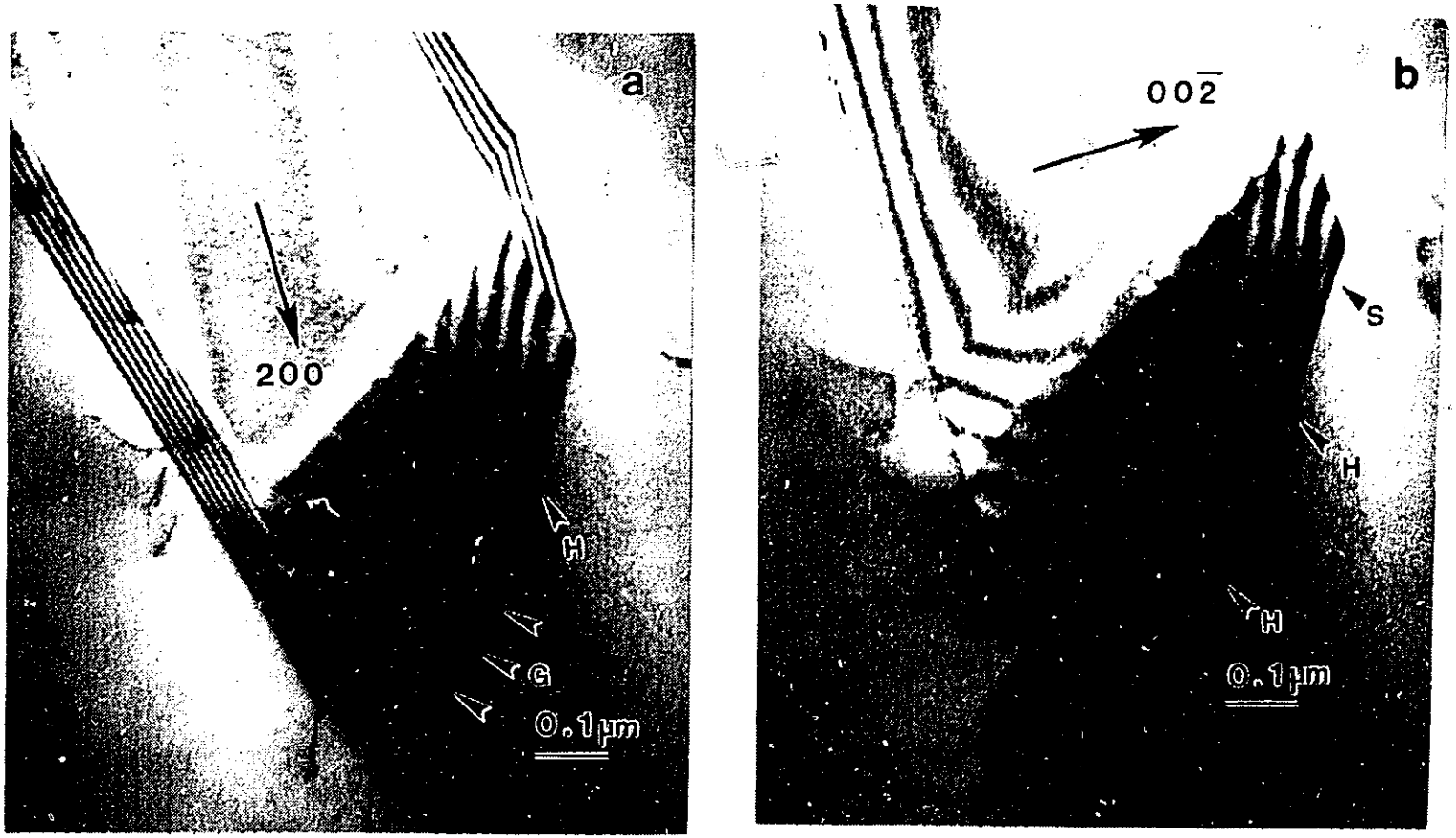

Figure 4.2.16: Bright field images of end facet a) g_{200}^{TiN} b) $g_{00\bar{2}}^{TiN}$

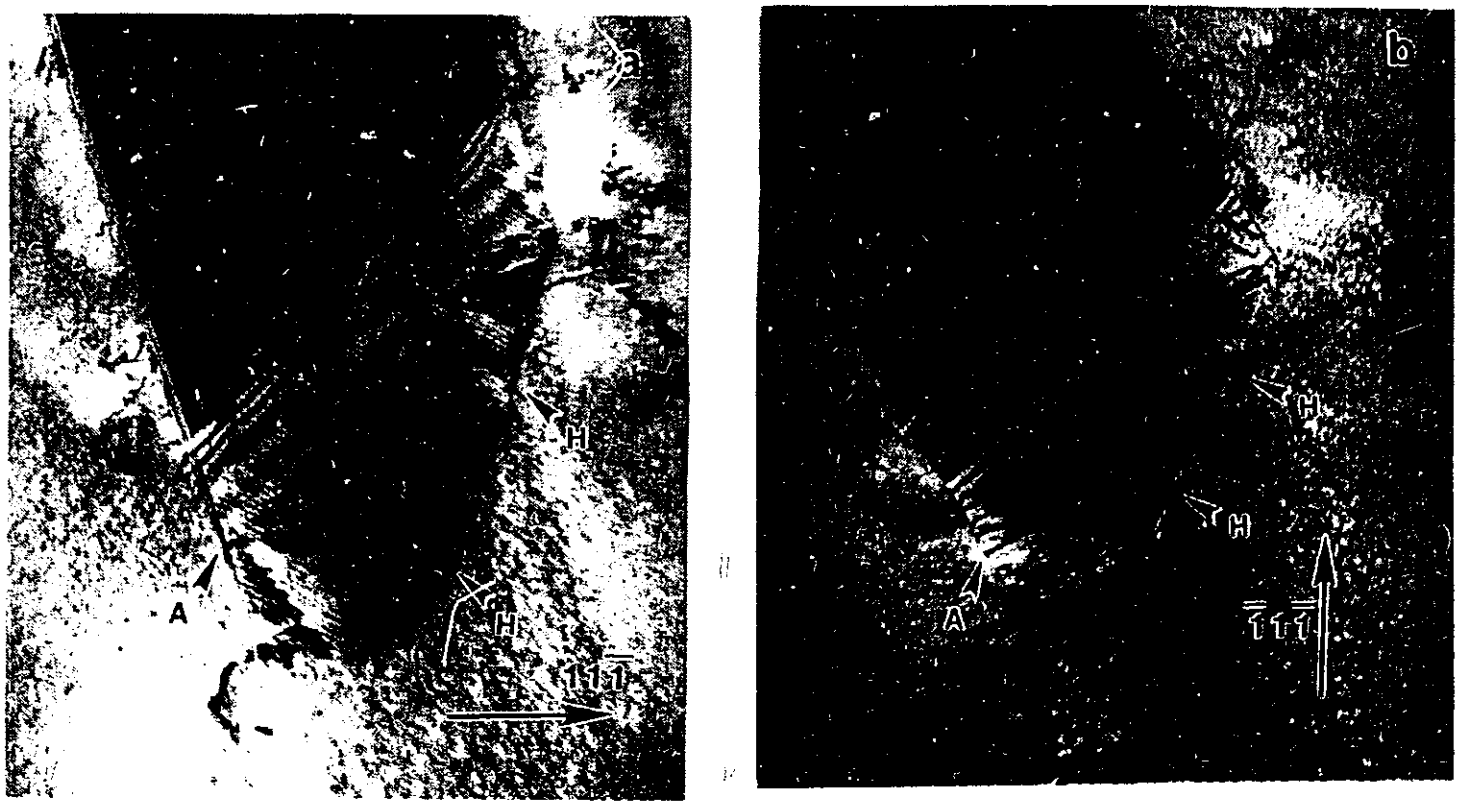

Figure 4.2.17: Dark field images using Ni reflections a) $g_{1\bar{1}\bar{1}}$ and b) $g_{\bar{1}\bar{1}\bar{1}}$

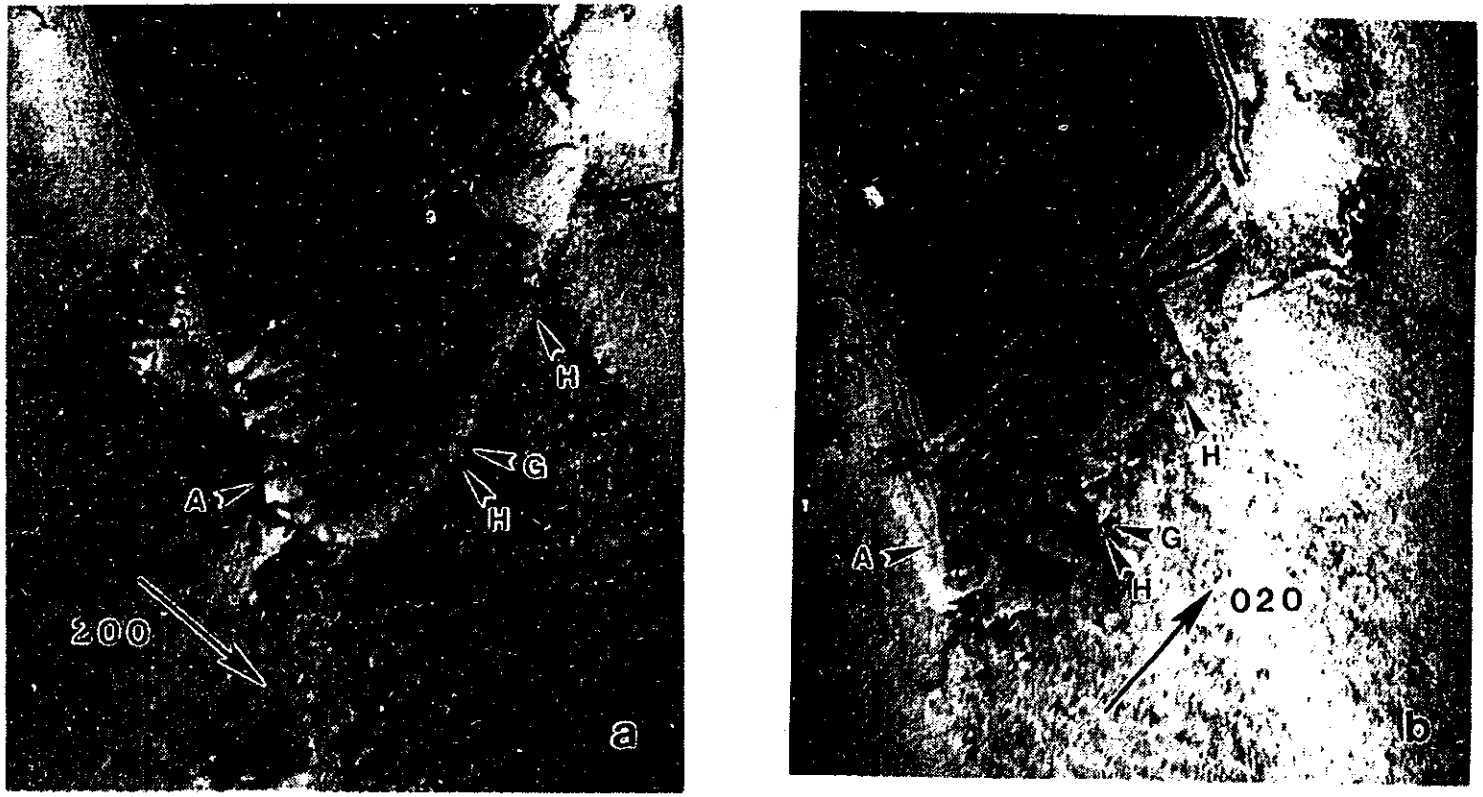

Figure 4.2.18: Dark field images using Ni reflections a) g_{200} and b) g_{020}

Figure 4.2.19: Dark field images using Ni reflections a) $g_{\bar{2}20}$ and b) g_{220}

Table 4.2.1
Summary of **g·b** analysis utilizing Ni reflections

g/b	$\frac{1}{3}[1\,\bar{1}\,1]$	$\frac{1}{2}[101]$	$\frac{1}{2}[10\bar{1}]$	$\frac{1}{2}[011]$	$\frac{1}{2}[01\bar{1}]$	$\frac{1}{2}[110]$	$\frac{1}{2}[1\,\bar{1}\,0]$	vis?
$11\bar{1}$	$\pm\frac{1}{3}$	0	±1	0	±1	±1	0	s.v
$\bar{1}1\bar{1}$	$\pm\frac{1}{3}$	±1	0	0	±1	0	±1	p.v
$\bar{2}20$	$\pm1\frac{1}{3}$	±1	±1	±1	±1	0	±1	v.
220	0	±1	±1	±1	±1	±1	0	n.v
200	$\pm\frac{2}{3}$	±1	±1	0	0	±1	±1	v.
020	$\pm\frac{2}{3}$	0	0	±1	±1	±1	±1	n.v

s.v= strongly visible, v= visible, p.v.= partially visible, w.v= weakly visible, n.v= not visible

Because there were several contradictions in the **g·b** analysis, no definite conclusion may be drawn as to the type of Burgers vector. The Burgers vector with the least number of contradictions, however, is $\mathbf{b}=\pm\frac{1}{2}[10\bar{1}]$Ni. A summary of the dislocation contrast and **g·b** results for the dislocations utilizing TiN reflections is shown in Table 4.2.2.

Table 4.2.2
Summary of **g·b** analysis utilizing TiN reflections

g/b	$\frac{1}{2}[100]$	$\frac{1}{2}[101]$	$\frac{1}{2}[10\bar{1}]$	$\frac{1}{2}[011]$	$\frac{1}{2}[0\bar{1}1]$	$\frac{1}{2}[110]$	$\frac{1}{2}[1\,\bar{1}\,0]$	vis?
200	±1	±1	±1	0	0	±1	±1	s.v
002	0	0	±1	±1	±1	0	0	n.v
$\bar{2}0\bar{2}$	±1	±1	0	±1	±1	±1	±1	n.v
$20\bar{2}$	±1	0	±1	±1	±1	±1	±1	w.v

Although there is insufficient information to form a definite conclusion, in this case the most likely Burgers vectors is **b**=±½[100]TiN. The dislocations labelled 'A' had a Burgers vector of a ½[101]Ni. It was not possible to determine the Burgers vectors of the defects labelled 'G' and 'H'.

4.2.5: Other Orientation Relationships:

In this section, the remaining two other observed orientation relationships are presented. The first of these (Type IV) is shown in Figure 4.2.20 for a particle viewed from a [101]TiN zone axis. A set of irregularly spaced dislocations may be observed in Figure 4.2.20b. A study of the selected area diffraction pattern (SADP) shows that [101]TiN $\|$ [101]Ni with (010)TiN $\|$ $(17\bar{1})$Ni. The particle dimensions are 2.8 μm in length and 0.1 μm in width.

The last example (TYPE V) is shown in Figure 4.2.21. In this case the particle is shown in the edge on position with [101]TiN $\|$ [211]Ni. The habit plane is (010)TiN $\|$ $(\bar{1}11)$Ni. The particle dimensions are 3 μm in length and 0.1 μm in width. A higher magnification image of one end of the particle shows Moiré Fringes with a spacing of approximately 50 Å (Figure 4.2.21c). No misfit compensating dislocation configurations were observed at particles having either of these orientation relationships.

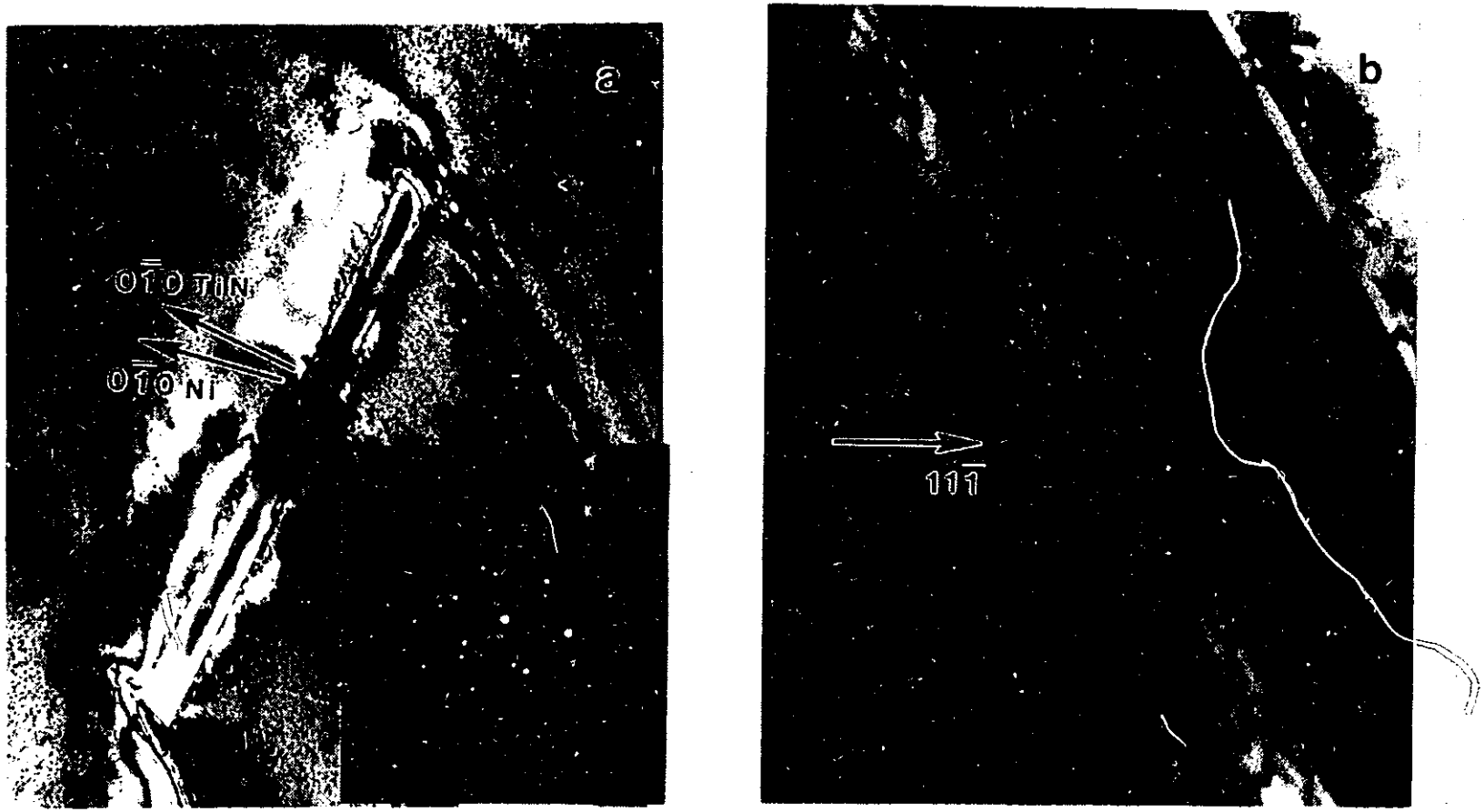

Figure 4.2.20: Example of particle with Type IV OR a) Bright Field [101]Ni‖[101]TiN and b) interface structure


b)

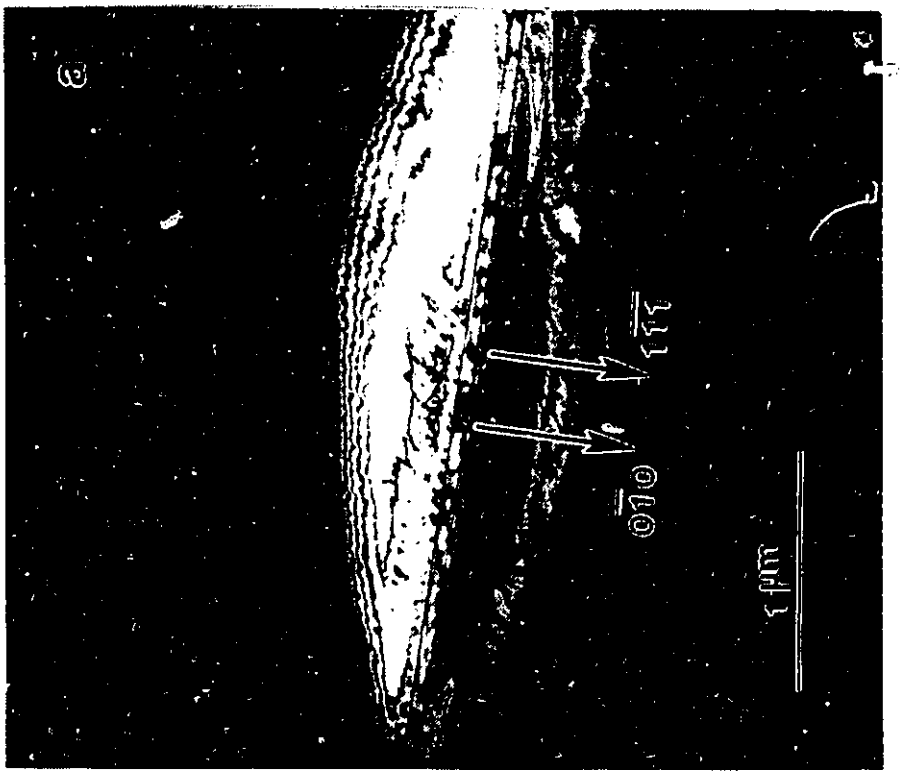
a)
c
$\overline{1}11$
$0\overline{1}0$
1 μm

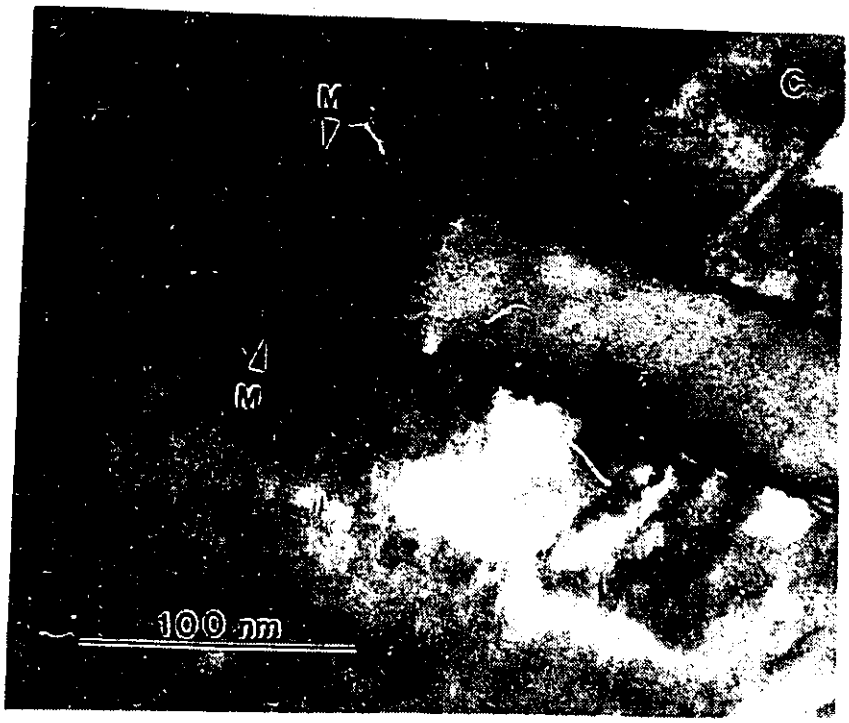

Figure 4.2.21: Example of a particle with a Type V OR a) bright field [110]TiN‖[211]Ni b) diffraction pattern and c) higher magnification of the interface showing Moirè fringes.

Chapter 5

Discussion of Experimental Results:

Introduction:

Chapter 5 is divided into two parts. Section 5.1 discusses the internal nitridation behaviour of Ni- Ti alloys. It seeks to further legitimize the theoretical developments presented in Section 2.1 by extracting individual K and D_C values from the literature and comparing them with the experimentally obtained KD_C products from Section 4.1. The second part, Section 5.2, analyzes the interfaces observed in Section 4.2 in terms of the various geometrical models presented in Section 2.2. Insights are therefore gained as to the applicability of these models in the interpretation of TiN/Ni interfaces.

5.1.1: Phase Identification:

The gold-like colour of the sample surfaces (Figure 4.1.1) is strongly indicative of TiN formation at all experimental temperatures. Chemical analysis via Auger,

spectroscopy, windowless EDX analysis, and EELS confirmed the presence of only Ti and N in the nitride. X-ray diffraction and lattice parameter measurements of the removed surface nitride film indicated that these TiN films were stoichiometric. No other Ti or Ni nitrides were detected. Thermodynamic calculations in Section 5.1.2 support this conclusion with respect to Ti_2N formation. The apparent tensile stress on these films cannot be reconciled with the difference in thermal expansion coefficient (Table 2.3.1) between Ni and TiN (which would lead to compressive stress in the TiN). The experimental scatter in the lattice parameter determinations is the most likely explanation for this discrepancy. The nitride particles observed with TEM from the 0.1 w/o Ti alloys were also TiN (Section 4.2). This is supported both by chemical analysis (EELS and EDX) as well as the lattice parameter measurement of 4.24±0.02 Å. In itself the experimental error in the lattice parameter measurement represents a rather large range of stoichiometry of TiN (Figure 2.3.2). Consideration of the diffusion paths on the ternary isotherm, however, would suggest that the nitrides found in the lower Ti alloys are also stoichiometric. The reason for this is that at the highest Ti levels the tie line composition between TiN_1 and the γ solid solution was approximately 2 w/o. The tie line composition for the 0.1 w/o Ti alloy was approximately 0.05 w/o Ti. For these alloys to be in equilibrium with a sub-stoichiometric nitride implies the unlikely circumstance that the tie lines of the higher and lower Ti alloys would cross. Values of KD_C were determined from experiment. It remains to be shown that these values are in reasonable accord with similar experimental systems. Given reliable thermodynamic data the solubility product

can be calculated.

5.1.2: Calculation of Thermodynamic Parameters:

The solubility of N in Ni is not known to any degree of certainty. Values of 1ppm to 5 ppm (atom basis) were assumed for the solubility between 800°C and 1020°C (Wriedt and Gonzalez 1961). The Gibbs free energy at infinite dilution is (at 1ppm N in Ni):

$$\tfrac{1}{2}N_{2(g)} \rightarrow [N]_{(Ni)} \qquad (5.1.1)$$

$$\Delta\overline{G}^{\infty} \sim +114.87\ T\ J/mol\ K$$

Chattopadhyay and Kleykamp (1983) estimate the relative partial excess Gibbs energy of titanium in nickel at infinite dilution as -165 ± 10 kJ/mol between 1100 and 1300 K.

$$Ti_{(s)} \rightarrow Ti_{(Ni)} \qquad (5.1.2)$$

$$\Delta\overline{G}^{\infty} \sim -165000\ J/mol\ (1100\text{-}1300K)$$

The free energy of formation of TiN and Ti_2N has been documented by Ohtani and Hillert (1990). For TiN:

$$Ti_{(s)} + \tfrac{1}{2}N_2 \rightarrow TiN_{(s)} \qquad (5.1.3)$$

$$\Delta G^{\circ} = -352710 + 145.853\ T - 7.65543 T \ln T$$

$$-0.00464\ T^2\ J/mol\ K$$

and for Ti_2N:

$$2Ti(s) + \tfrac{1}{2}N_2(g) \rightleftarrows Ti_2N \qquad (5.1.4)$$

$$\Delta G^{\circ} = -455840 + 135.997\ T$$

Subtracting Equations 5.1.1 and 5.1.2, from 5.1.3 yields for TiN:

$$Ti_{(Ni)} + N_{(Ni)} \rightarrow TiN \qquad (5.1.5)$$

$$\Delta \overline{G}^{\infty} = RT\ \ln \{[X_{Ti}][X_N]\}$$

$$\Delta \overline{G}^{\infty} = -187710 + 30.98\ T - 7.65543\ T \ln T$$

$$-0.00464\ T^2\ J/mol$$

Subtracting Equations 5.1.1 and 2x5.1.2, from 5.1.4 yields for Ti_2N:

$$2Ti_{(Ni)} + N_{(Ni)} \rightleftarrows Ti_2N \qquad (5.1.6)$$

$$\Delta \overline{G}^{\infty} = -125840 + 21\ T\ J/mole\ T$$

A summary of these values at the three experimental temperatures is presented in Table 5.1.1. These values show, in agreement with previous studies (Binder et. al. 1991) and the results of this work, that TiN is favoured over Ti_2N formation. This result is a consequence of the energy penalty in extracting two moles of Ti for every mole of N in the formation of Ti_2N.

Table 5.1.1
Summary of Gibbs Free Energy at Infinite Dilution

Temperature °C	$\Delta\overline{G}^{\infty}$ TiN J/(mole N)	$\Delta\overline{G}^{\infty}$ Ti_2N J/(mole N)
1020	-218572	- 98687
900	-214834	-101207
800	-217131	-103307

The solubility product $[X_{Ti}][X_N] = Ks$ becomes for a 1 ppm N solubility:

$$Ks=[X_{Ti}][X_N]= \exp\{-22576/T + 3.73 - 0.921\ \mathrm{InT} - 0.000558\ T\} \qquad (5.1.7)$$

Solubility products as weight percentages at the three temperatures of interest are presented in Table 5.1.2.

Table 5.1.2
Table of Solubility Product Data

Temperature/N sol. in Ni	1 ppm	5 ppm
1020°C	1.4×10^{-6} [w/o]^2	7×10^{-6} [w/o]^2
800°C	2.8×10^{-7} [w/o]^2	1.4×10^{-6} [w/o]^2
700°C	5.4×10^{-8} [w/o]^2	2.7×10^{-7} [w/o]^2

The attainment of a small solubility product is consistent with the stability of TiN. For example low values of solubility products have been noted in TiN precipitation in austenite (Wada and Pehkle 1978). The calculated solubility products should be regarded as a first time determination of these values in Ni.

5.1.3: Comparison of Interstitial Diffusivity Data in Ni and γ-Fe:

A range of diffusivities was calculated based on the results of Table 5.1.2 and the measured KD_C values of Table 4.1.1. These are presented in Figure 5.1.1 along with C and N diffusivities in Ni and γFe. Interstitial diffusivity data of γFe and Ni should be comparable due to the similarity of crystal structure, lattice parameter, melting temperature and position on the periodic table of these two elements. The data, of Figure 5.1.1, falls within a relatively narrow range for diffusivity data of less than an order of magnitude (Kirkaldy and Young 1987). Furthermore the upper bound for the diffusivity of N in Ni determined in this work is close to the lower bound suggested by Douglass (1991) for the N diffusivity in a Ni-30Cr alloy. Despite the uncertainties in the calculation of the solubility product K these results must be regarded as providing further validation of the theory presented in Section 2.1. As already noted the shapes of the predicted diffusion profiles were always of correct form with the transition point accurately accessed.

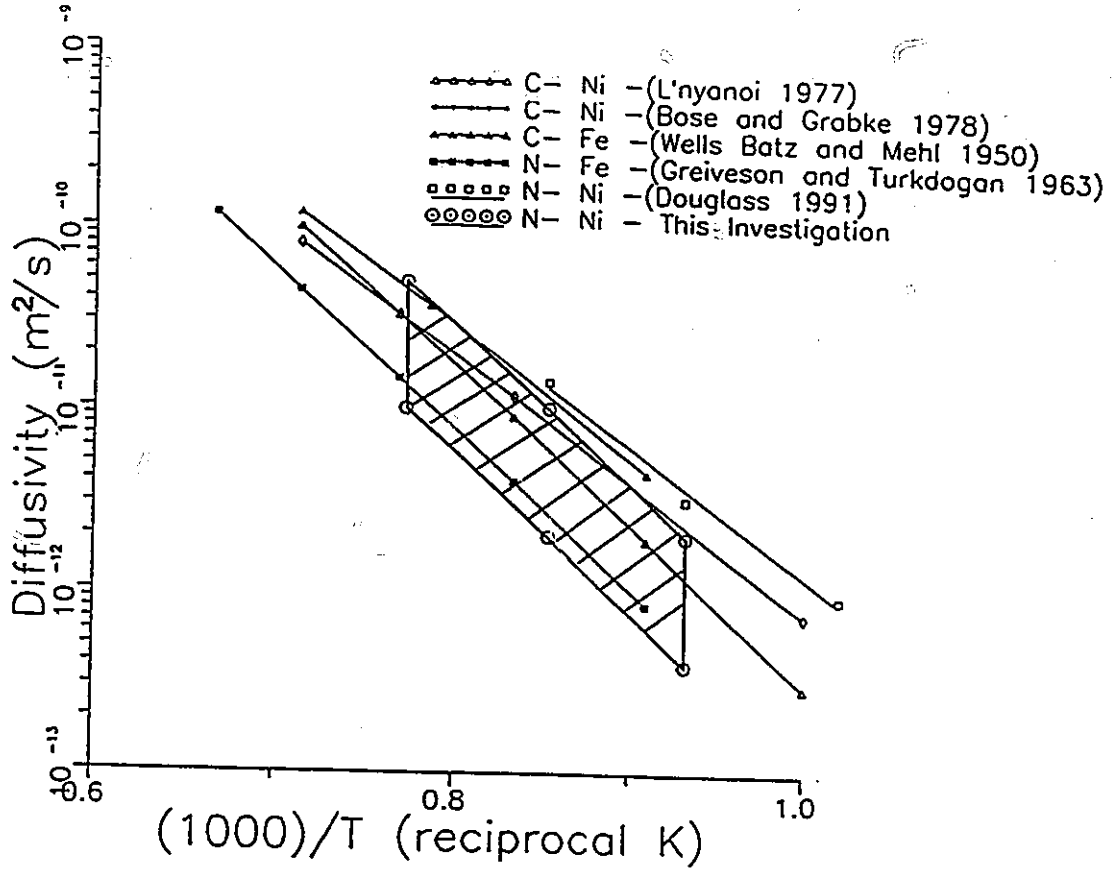

Figure 5.1.1: Comparison of the experimentally determined diffusivity of N in Ni to C and N diffusivities in Ni and γFe. Upper and lower bounds assume 1ppm and 5ppm solubility of N in Ni respectively.

This analysis can be used in a relatively straightforward manner to determine K or D_C in systems where one these values is known and the other is difficult to measure. This is particularly useful for systems of low solubility which present distinct experimental difficulty. This can be accomplished in two ways, by either determining the point of transition between external and internal oxidation and applying the transition criterion $(KD_C/D_B B_I^2) \leq 0.1$, or by evaluating KD_C numerically as was done in this work. The diffusivity of Ti in Ni was determined to be:

$$D_{Ti} = 0.0736 \exp(-320000/RT)\ m^2/s \quad \text{(between 1073 K and 1293 K)}$$

where are R is in J/mole-K. The values of the diffusivity of Ti in Ni were in reasonable accord with other substitutional alloys in Ni. The high activation energy (and high pre-exponential term) is a consequence of the narrow temperature range used to obtain this data. If a pre-exponential term of the order $1 \times 10^{-4}\ m^2/s$ is assumed (Brown and Ashby 1980) then the activation energy based on this experimental data becomes approximately -279 000 J/mol K or -66 000 cal/ mol K which is in good agreement with other substitutional diffusion activation energies (Brown and Ashby 1980)[1].

---

[1] Note added in proof: It has recently come to my attention that the diffusivity of Ti in Ni had been measured by Swalin and Martin (1956). They obtained:

$$D_{Ti} = 0.00008 \exp(-260000/RT)\ m^2/s \quad (1100°C - 1300°C)$$

Although the activation energies differ substantially the maximum error in the diffusivity is 30% between 900°C and 1020°C. This remarkably good agreement between the results of this work and Swalin and Martin's further supports the conclusions reached in this document.

R.A. Swalin and A. Martin (1956); *Trans. AIME* **206**, pp. 567-572

5.1.4. Surface Morphology and the Role of Vacancies:

In samples that had undergone internal nitridation there was an associated displacement of Ni to the surface (Figure 4.1.7). In some cases this was crystallographic in appearance (4.1.8) forming on discrete atomic planes and on coherent twin boundaries. This is in part supported by TEM studies where an association was noted in some cases between {111}Ni planes and TiN particles. Although the exact mechanism is unclear, it is generally accepted that excess volume changes associated with internal precipitation are the driving force for solvent removal. The local volume change associated with TiN precipitation has been calculated to be 13% in this system. The fact that Ni is characteristically on top of the TiN is consistent with a diffusive, vacancy driven process rather than plastic deformation. It has been suggested with other systems of this type that vacancies are required to alleviate the stress generated by these volume changes. For example this type of mechanism is thought to be operative in oxidation reactions where anion diffusion through the oxide is important (Evans 1995). In a number of studies of internal oxidation it has been suggested that removal of the solvent species can in some cases become rate limiting (Section 2.2). The modest volume changes associated with TiN precipitation as well as a low N solubility in Ni suggest that these effects are unimportant in this system. The excellent agreement between the predicted and measured diffusion profiles of Section 4.1 lend further credence to this assertion. The finite

difference method can however incorporate the role of vacancies to more fully test the effects of solvent removal. This is accomplished by rewriting Equation 5.1.3 to include the movement of vacancies as a rate limiting step:

$$Ti_{(Ni)} + N_{(Ni)} + \eta \text{ vacancy} \rightarrow TiN \qquad (5.1.8)$$

$$\eta = (\mu_{TiN} - \mu_{Ti})/\mu_{vac}$$

where μ represents the molar volume. In this way the assumption of strict nitrogen (or oxygen) diffusion controlled internal nitridation (oxidation) need not be made (Yi et. al. 1987, Park et. al. 1984).

The morphology and interfacial structure of the TiN particles will now be explored.

5.2: Interpretation of TEM Results:

Introduction:

This section is restricted to a geometrical interpretation of the observed orientation relationships (OR)s and the resulting dislocation structures. Primary and secondary O-lattice as well as 'plane matching' calculations were performed whenever appropriate. In certain instances the results of 'plane matching' theory and O-lattice theory were indistinguishable. Moiré pattern formation is clearly related to the O-lattice; whenever appropriate Moiré patterns of the interface were produced for comparison.

5.2.1: Particle Morphology Considerations:

The shapes of the TiN particles are probably governed not by capillarity effects but by the kinetics of growth. There is evidence from Section 4.2 to interpret the growth of TiN in Ni as due to the propagation of growth ledges on semi-coherent interfaces. As discussed in Section 5.1.4, this growth must require vacancies to accommodate the excess volume changes due to TiN precipitation. The role of vacancies is thought to be important in a number of other (excess volume) interstitial systems such as Pt-C and Mo-Hf-N (Westmacott and Dahmen 1986). TiN particles with large aspect ratios were usually associated with at least one high index TiN facet in the principal growth direction, suggesting that these high index facets are better able to accommodate the atomic rearrangements required for growth of TiN. The particle with the Type II orientation relationship is a good example (Figure 4.2.6). The aspect ratio of this particle was approximately 50:1. The growth direction was terminated by a high index (5 14 25) TiN rounded facet suggesting that steps at the tip could facilitate growth. The semi-coherent {010}TiN facets appear to be the least mobile without the intervention of growth steps. Evidence for the influence of growth steps on morphology is provided in Figure 4.2.11 and 4.2.12 by the particle with a Type III- tilt OR. A 3:1 aspect ratio was noted for this particle along with a convex shaped semi-coherent (010)TiN interface consisting of numerous steps. In comparison the particle with the Type III- twist OR, shown in

Figure 4.2.8, had nearly the identical orientation relationship but the aspect ratio was in this case 35:1 with a very flat (010)TiN interface. Clearly the number of growth steps and their propagation on (010)TiN may account for the differing aspect ratios of these two particles.

The morphology of the cube on cube particles (Type I OR) bounded by {010}TiN ‖ {010}Ni planes additionally suggests that diffusion influenced the morphology of these particles. Since all the interfaces of these particles were crystallographically equivalent, growth should have been equally probable on all faces. The sides of these cuboidal particles, however, rarely had the same dimensions as noted for example by Figure 4.2.2 and Figure 4.2.3. This is probably due to the directional nature of the solute, gas and vacancy diffusion profiles that occur during internal nitridation. Furthermore, the absence of high index TiN facets as well as a lack of observed growth ledges is consistent with the generally observed small aspect ratios of these particles.

Each of the orientation relationships will now be examined in detail, to determine if any points of commonality, exist between them.

5.2.2: Type I- Cube on Cube Orientation Relationship:

i) O-lattice Interpretation:

A schematic diagram of the interpenetrating atom positions is shown in Figure 5.2.1 for a cube on cube (001)TiN interface. A word of caution is in order in the interpretation of these schematic diagrams. These represent a hypothetical interpenetrated structure without space filling atoms (in the plane of the interface). Furthermore the O-Lattice relationships are established from these diagrams between like atoms as discussed in Section 2.2.5 (i.e. between Ni and Ti atoms in this case). This is a direct consequence of choosing Ti and Ni atoms as having a common origin. Exactly the same O-lattice is obtained if Ni and N were chosen as having a common coordinate origin. The O-lattice is a geometrical construction and does not depend on the types of atoms used to define the transformation **A**. The interface can be obtained by defining the interfacial plane then, allocating the atoms to their respective side of the interface. A mismatch of about 18% exists between the Ni lattice and the Ti sublattice as noted in Figure 5.2.1. The detailed O-lattice calculation is shown in Appendix II, using the orthonormal coordinate system defined by TiN (defined as lattice 1). The basis ½<110> vectors of each phase were used to establish the transformation matrix $\mathbf{A}=\mathbf{S}^{-1}_{TiN}\mathbf{S}_{Ni}$, (a pure contraction matrix in this case). The procedure has been outlined in detail in Sections 2.2.2 and 2.2.3. The columns of the O-lattice matrix are the basis vectors of the O-lattice. The result for the

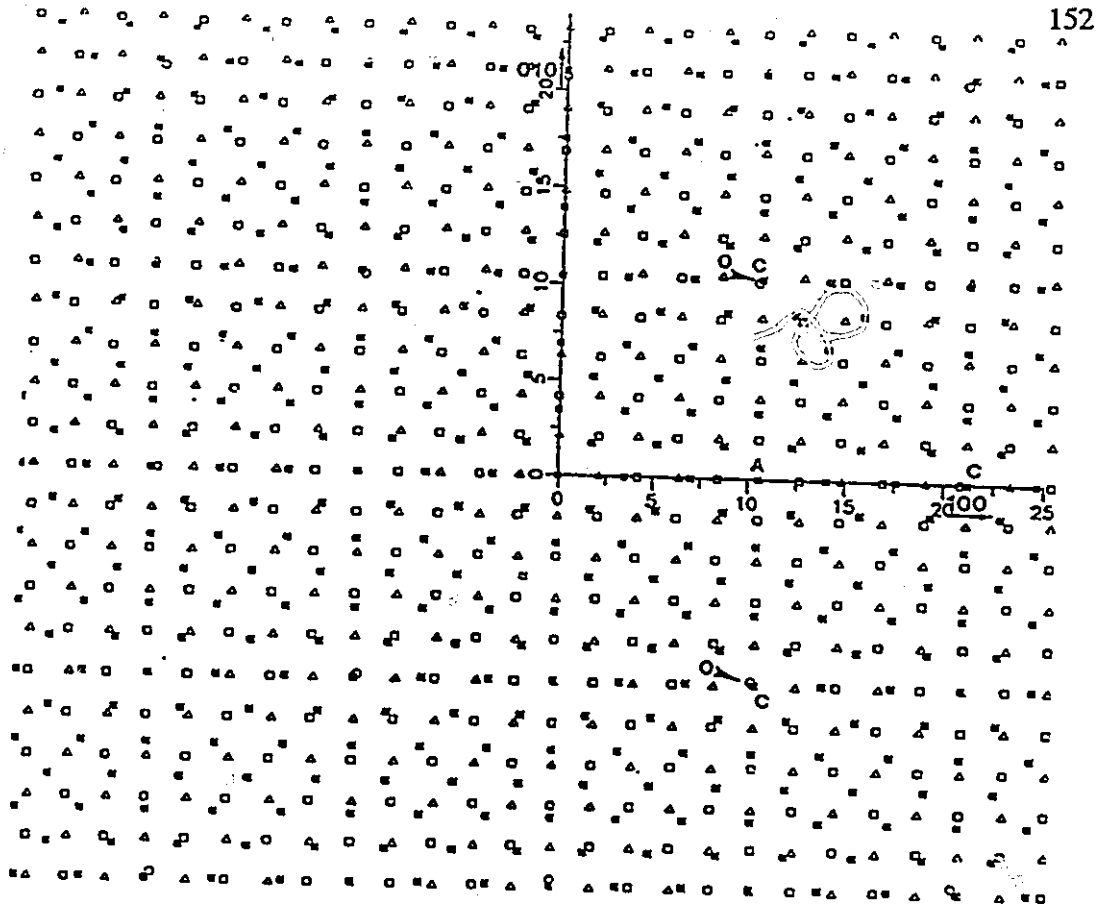

Figure 5.2.1: Schematic Diagram of atom positions of a cube - cube interface in the plane of the interface. Open squares represent Ti atom positions, open triangles are nitrogen atoms, and the closed squares represent the Ni atom positions. The points marked by 'O' and 'C' are the O-points and near CSL points respectively. The 'A' marks the anti-CSL point i.e. coincidence between Ni and N atoms.

O- lattice calculation (in Å) is:

$$X^{o}=\begin{vmatrix} -10.4 & -10.4 & -10.4 \\ -10.4 & 10.4 & 0 \\ 0 & 0 & -10.4 \end{vmatrix} \qquad (5.2.1)$$

These points are indicated in Figure 5.2.1 by the arrows. In this case the O- points also represent a near coincidence site lattice between the Ni lattice and the Ti sublattice. This is a 'special' boundary according to Bollman (1979), in that two independent Burgers vectors are contained in the interface. It is composed of two perpendicular sets of pure edge dislocations, spaced about 15 Å apart in the [110] and [$\bar{1}$10] directions. The small spacing of these dislocations would make them difficult to detect with conventional TEM. The dislocations in Figure 4.2.2 have the appearance of "punched out" dislocations and not primary (or secondary) dislocations. During cooling the thermal expansion mismatch between the particle and the matrix could provide sufficient strain to punch out these dislocations. The dislocation lines observed in Figure 4.2.2 could be a consequence of slip on the {111}Ni planes intersecting the boundary. Shieu and Sass (1990) in a HREM study, however, were able to detect two sets of misfit O-lattice dislocations for a cube on cube (100) NiO/Pt interface.

ii) CSL Theory

It may be recalled that when the primary O- lattice spacing becomes of the order of the unit cell it may be advantageous to consider the interface in terms of a near coincidence model. Secondary dislocations may then be required to accommodate deviations from exact coincidence. Inspection of Figure 5.2.1 also shows if N atoms are allowed to form the CSL, an 'anti-CSL' unit cell half the size of the CSL unit cell is produced. This point is indicated by the 'A' in Figure 5.2.1. The transformation matrix is established from the near CSL relationship between the Ni and the Ti sublattice as noted by the O-lattice calculation. The results of the secondary O-lattice calculation (in Angstroms) is shown below (the details of which are shown in Appendix III).

$$X^{sec}=\begin{vmatrix} -93 & -93 & -93 \\ -93 & 93 & 0 \\ 0 & 0 & -93 \end{vmatrix} \qquad (5.2.2)$$

It is worth reminding the reader that in this case the Burgers vectors of the dislocations are given by the DSC vectors which were determined to be the difference vectors between the Ni' lattice and the Ti sublattice as discussed in Section 2.2.3 with the result in Å (as column vectors):

$$DSC=\begin{vmatrix} 0.35 & 0.35 & 0.35 \\ 0.35 & -0.35 & 0 \\ 0 & 0 & 0.35 \end{vmatrix} \qquad (5.2.3)$$

A schematic diagram of the secondary dislocation configuration in the plane of the interface shows two sets of pure edge (<0.35 0.35 0> type) dislocations spaced 130 Å apart, Figure 5.2.2. The weak contrast associated with secondary dislocations could make them difficult to detect (Forwood and Clarebrough 1991). The growth step located at 'B' in Figure 4.2.2 is consistent with the secondary O- lattice calculation both in direction and spacing. Steps might be expected to terminate at primary or secondary 'O'-points (Bollman, 1979). It is important to note that the same result is obtained had the anti-CSL points been used to establish the transformation matrix A_{csl}.

The Σ notation is often used to describe CSL boundaries. Two planar Σ values (σ) are required for interphase boundaries, one with respect to the Ti sublattice and the other with respect to Ni. The σ values are 25, and 36 for σ_{Ti} and σ_{Ni} respectively. If the anti-CSL points were included in this analysis the σ values become 25 and 18 for σ_{TiN} and σ_{Ni} respectively. As noted in Section 2.2.4 σ values of well over 50 may still produce local minima in interfacial energy.

iii) Plane Matching Approximation:

There were several plane matching candidates for this orientation relationship. If the [110]Ni line direction is regarded as the trace which (111)Ni makes

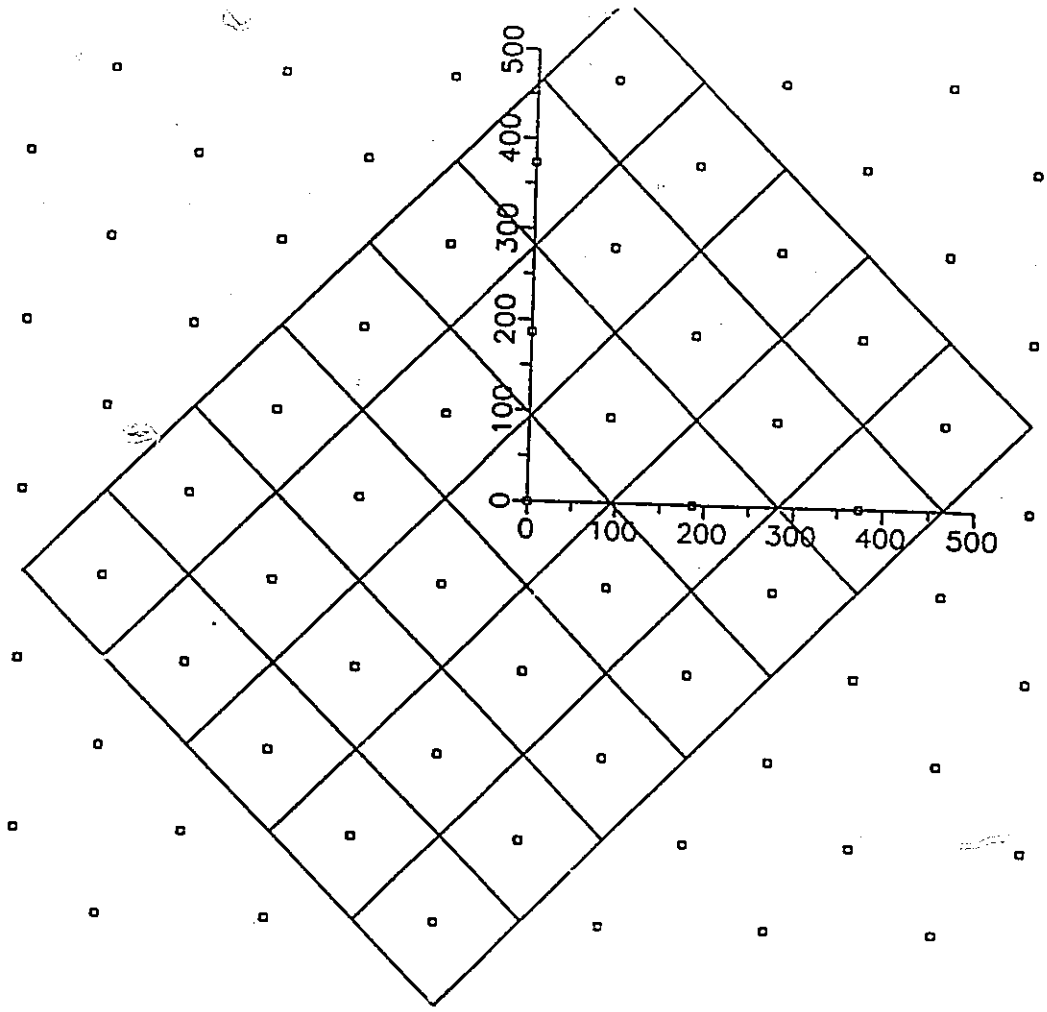

Figure 5.2.2: Secondary O- lattice for cube- cube interface.

with the interface a set of dislocations is predicted with a spacing of 7 Å in the [110] direction. However, if (100)Ni is matched with (100)TiN, a set of dislocations with a line direction of [010] and a 7 Å spacing would be produced. These results are significantly different from O-lattice theory where two sets of <110> dislocations are predicted 15Å apart. Dislocation spacings of this magnitude are difficult to detect due to the small strain fields associated with closely spaced dislocation cores. It was not possible from the experimental evidence to determine if either theory would be appropriate in this example. However as already noted, evidence for the existence of two sets of O-lattice misfit dislocations has been documented for cube-cube metal/ceramic systems elsewhere (Shieu and Sass 1990).

5.2.3: Type II- [100]TiN ‖ [211]Ni, (010)TiN ‖ ($\bar{1}$11)Ni:

This is the orientation relationship one might have expected on the basis of two close packed (low energy) planes meeting to form an interface (Wolf 1991). Furthermore this orientation relationship has also been observed in the Cu/MgO system produced from the internal reduction of (CuMg)O (Backhaus-Ricoult and Hagège 1992). The long direction of the particle corresponds to ½[211]Ni ‖ [100]TiN. It is terminated at one end by a (100) facet while the other end has a high index TiN facet as discussed in Section 5.2.1. The magnitudes of ½[211]Ni and [100]TiN differ by ~1.6%.

i) O-lattice interpretation:

The schematic diagram of the atom positions in the (011)Ni ‖ (001)TiN planes are shown in Figure 5.2.3 for this particle in an edge- on position. The Moiré fringes of Figure 4.2.7 are from $(\bar{1}11)$Ni parallel to (020)TiN, giving a theoretical line spacing of 49 Å, which is in good agreement with observations. The atom positions in the plane of the interface are shown in Figure 5.2.4. A Primary O-lattice calculation was performed with the transformation $\mathbf{A}=\mathbf{S}^{-1}_{\mathrm{Ni}}\mathbf{S}_{\mathrm{TiN}}$ being defined by the nearest neighbours around the origin of the two interpenetrating lattices. These points are identified as b1, b2, and T1 in Figures 5.2.4 and 5.2.3 respectively. In terms of crystal coordinates the structure matrix used to define the transformation with respect to Ti and Ni are (read as column vectors):

$$S_{TiN}=\frac{a_{TiN}}{2}\begin{vmatrix}1 & 1 & 1\\ 0 & 1 & 0\\ 1 & 0 & -1\end{vmatrix} \qquad (5.2.4)$$

The structure matrix for Ni used to define the transformation matrix is:

$$S_{Ni}=\frac{a_{Ni}}{2}\begin{vmatrix}1 & 0 & 1\\ 0 & 1 & 1\\ 1 & 1 & 0\end{vmatrix} \qquad (5.2.5)$$

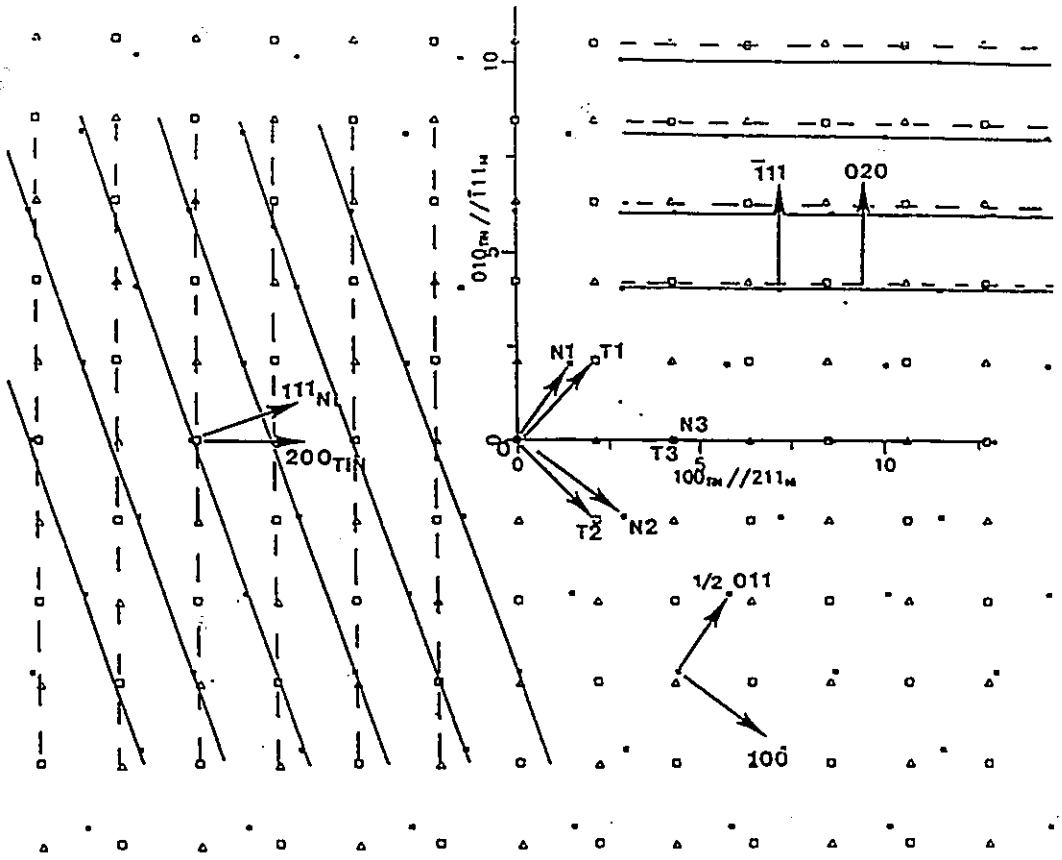

Figure 5.2.3: Schematic Diagram of the atom positions normal to the interface of a Type II OR viewed from [001]TiN‖[011]Ni.

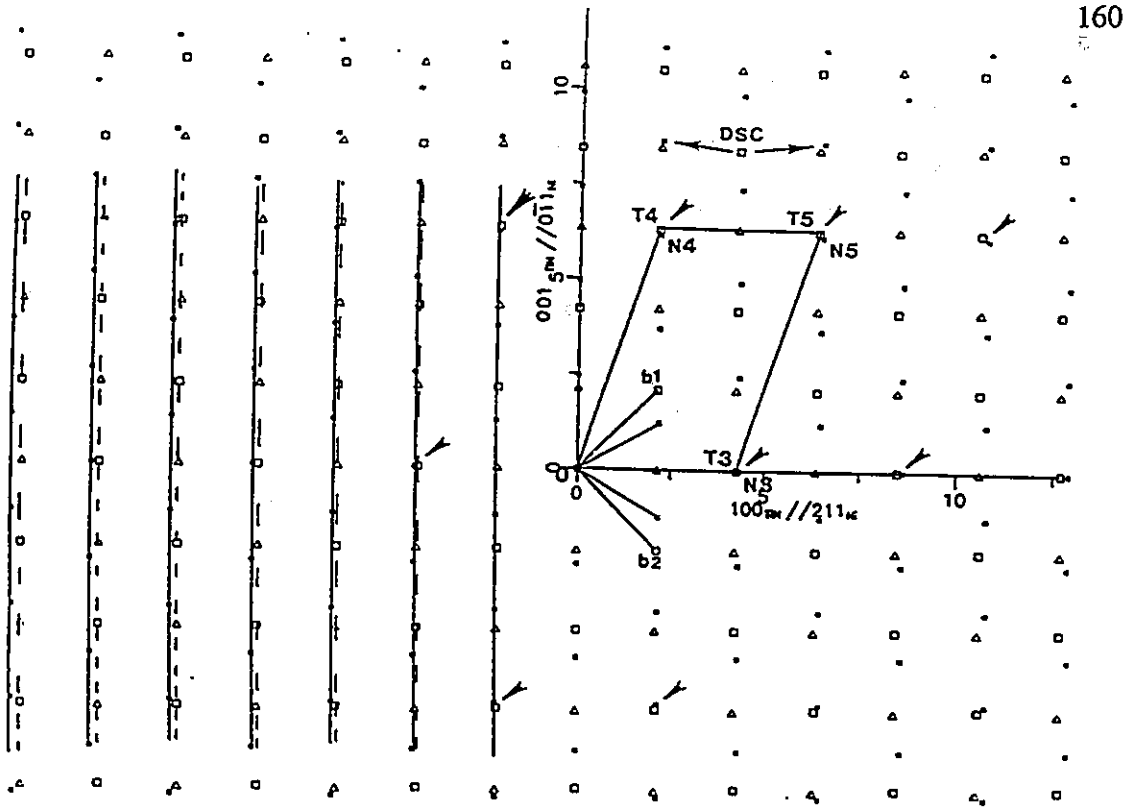

Figure 5.2.4: Schematic Diagram of the atom positions in the habit plane of a Type II OR $(\bar{1}11)Ni \| (010)TiN$.

The detailed calculation is presented in Appendix IV for the orthonormal coordinate system defined by TiN and taking Ni as lattice 1. The result for $\mathbf{X}^o$ is as follows (in Angstroms).

$$X^o = \begin{vmatrix} -128 & 906 & -128 \\ 0 & 49 & 0 \\ 3 & 0 & -3 \end{vmatrix} \qquad (5.2.6)$$

The O-lattice is a pseudo-hexagonal planar array on (010)TiN. The spacing between these 'O-lattice planes' is 49Å. This is the same spacing and direction as the Moiré fringes observed in Figures 4.2.6 and 4.2.7 complicating the interpretation of these features. The results are presented in graphical form in Figure 5.2.5 for (010)TiN. A vertical set of essentially [001]TiN dislocations is predicted spaced 128 Å apart which are composed of a/2[101]Ni and a/2[110]Ni Burgers vectors as noted in Figure 5.2.5. This gives this essentially vertical set a mixed dislocation character. A 'fine' set of a/2[011]Ni dislocations of pure edge character spaced 6Å apart is also predicted but even if such discrete features exist they would not be observable with conventional TEM.

ii) CSL interpretation:

A Secondary O-Lattice calculation was also performed utilizing the near CSL O-N3-N4-N5≈O-T3-T4-T5 of Figure 5.2.4 to attempt to ascertain the significance

(if any) of the second set of fringes with a [100]TiN line direction observed in Figure 4.2.7. The **DSC** vectors are shown in Figure 5.2.6 for the TiN and Ni' lattice as discussed in Section 2.2.3. In Figure 5.2.6 the plane of the interface is shown in exact coincidence along with the **DSC** lattice to the left of Figure 5.2.6. The **DSC** lattice vectors are multiples of the **DSC** vectors determined by Grimmer's (1974) reciprocity theorem from the diffraction pattern. They are also consistent with the **DSC** vectors of the (001)TiN plane, which are assumed to be the Burger's vectors of TiN. The detailed calculation is shown in Appendix V with the results presented below in the coordinate system defined by TiN.

$$DSC=\frac{a_{TiN}}{10}\begin{vmatrix}5 & 5 & 5\\ 5 & 0 & 0\\ 0 & 1 & -1\end{vmatrix} \qquad (5.2.7)$$

$$X^{sec}=\begin{vmatrix}-906 & 128 & 128\\ -49 & 0 & 0\\ 0 & -20 & 20\end{vmatrix} \qquad (5.2.8)$$

The results (Figure 5.2.7) show three sets of dislocations. The two sets with essentially a [001] line direction are spaced 128 Å apart and have $a_{TiN}/10$ [501] and $a_{TiN}/10$ [$50\bar{1}$] Burgers vectors (Figure 5.2.7). The set of dislocations with a line direction of [100] spaced 40 Å apart are pure edge in character with a $a_{TiN}/5$[0 0 1] Burgers vector. The finer set of fringes (Figure 4.2.7) are possibly this second set of dislocations.

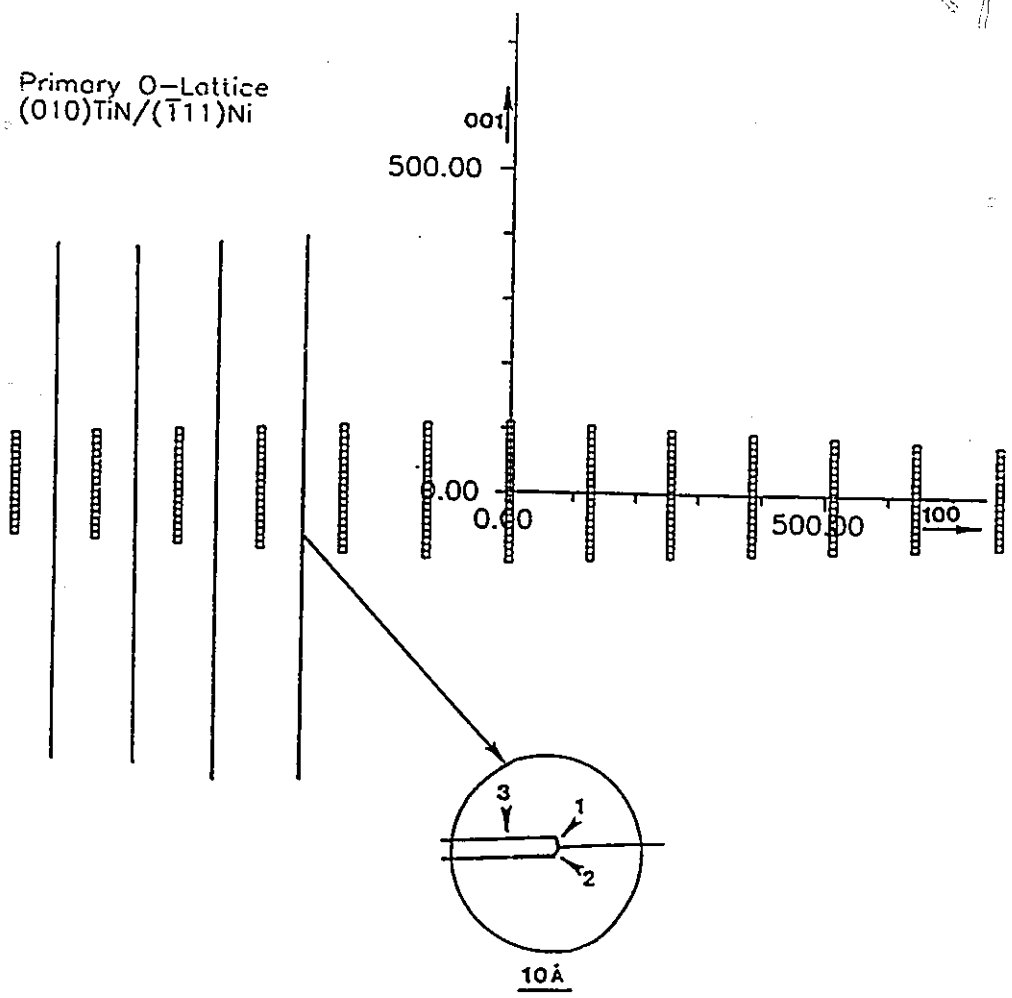

Figure 5.2.5: Results of O-lattice calculation of dislocation configuration in the plane of the interface. The spacing of the O-points in the [100]TiN direction is approximately 130Å. The inset shows the structure of the vertical and horizontal sets of dislocations. The Burgers vectors of the sets labeled 1,2,3 are b=½[110]Ni, b=½[101]Ni and b=½[011]Ni respectively.

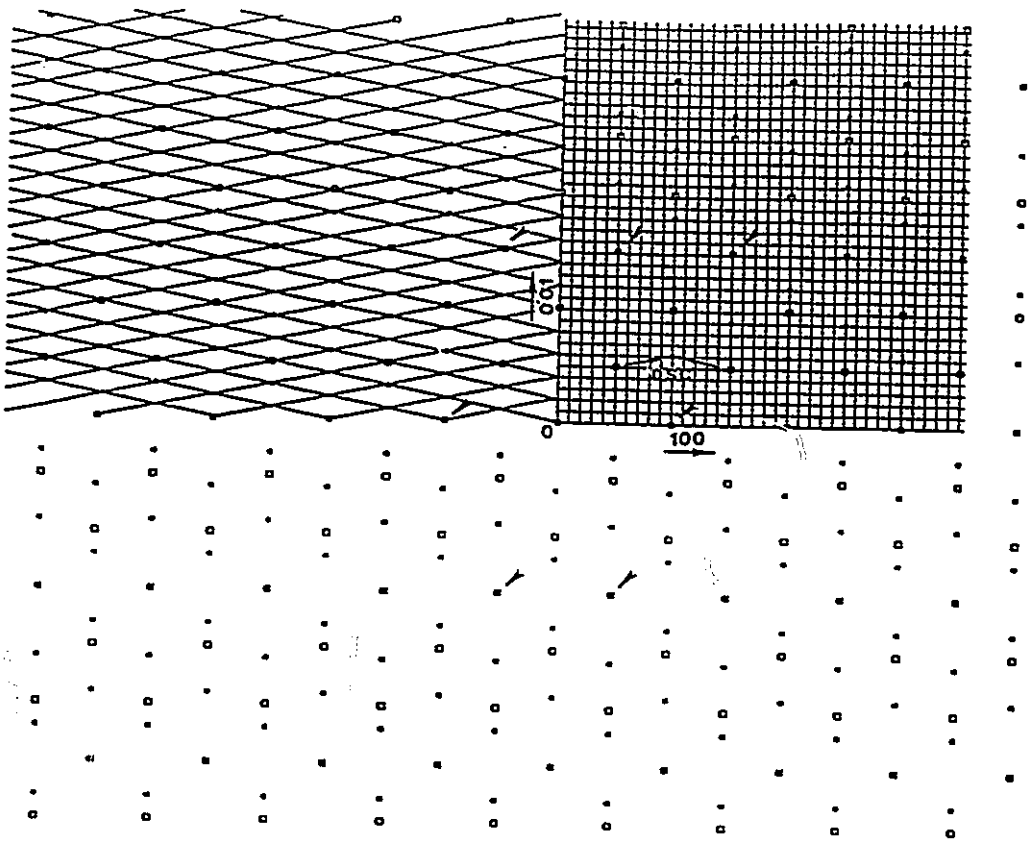

Figure 5.2.6: Schematic Diagram of atom positions in the interface, placed in exact coincidence with TiN as the reference lattice. The DSC vectors are indicated to the left of the diagram.

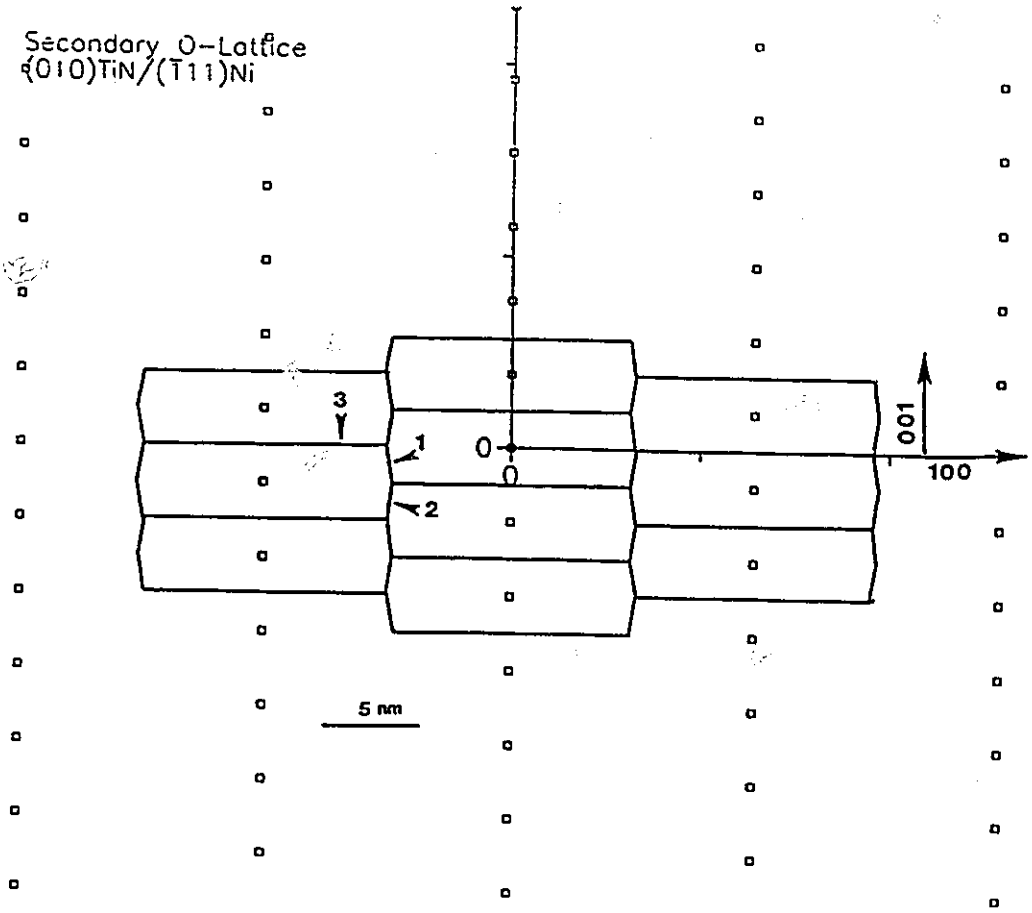

Figure 5.2.7: Results of Secondary O- lattice calculation and possible dislocation configuration in the plane of the interface the line segments labeled 1,2,3, have DSC vectors of b=1/10[50$\bar{1}$]TiN, b=1/10[501]TiN and b=1/10[002]TiN.

The planar σ values for the habit plane are 3, 6 and 5 for σ_{Ti}, σ_{TiN} and σ_{Ni} respectively. The inclusion of N atoms does not change the size of the CSL.

iii) Plane Matching Theory:

Plane matching theory would also predict a single set of [001] dislocations with a spacing of 128 Å based on the projected spacings of (200)TiN and (111)Ni on the boundary plane as shown in Figure 5.2.4 and 5.2.5. A Moiré pattern of a (010)TiN interface is shown in Figure 5.2.8. The agreement between this model and observations is good. As already noted the fringes observed on the (5 14 25)TiN end facet of Figure 4.2.6 and 4.2.7 are consistent with plane matching of (020)TiN and (111)Ni as well as with O-lattice theory. It is apparent, however, that the dislocations with the [001]TiN line direction are not visible once they encounter the high index end. This is consistent both with plane matching theory and O-lattice theory since the calculations show very finely spaced dislocations on this facet.

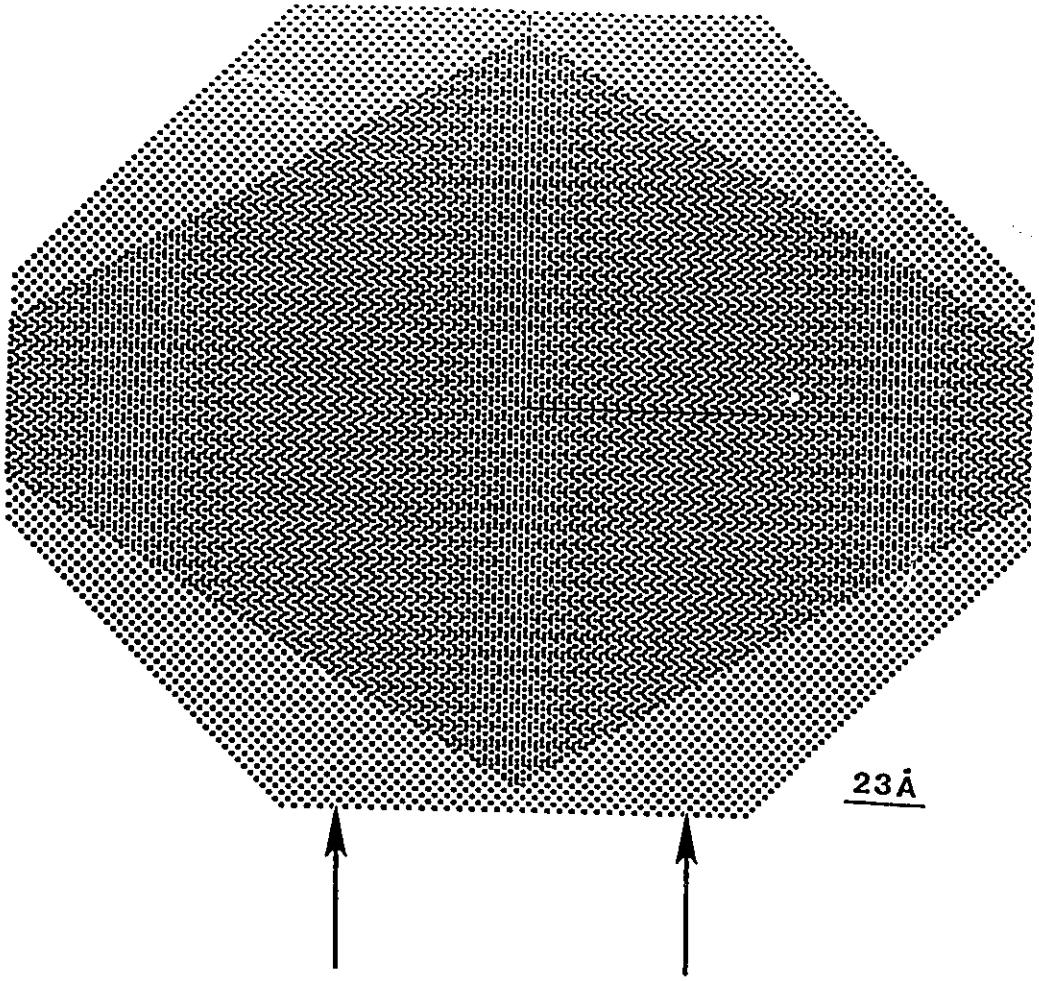

Figure 5.2.8: Moiré Pattern of atom positions in the plane of the interface. Compare with results of Figure 5.2.5.

5.2.4: Type III- [001]TiN ‖ [$\bar{1}\,\bar{2}$1]Ni (010)TiN ‖ (7$\bar{1}$5)Ni

This orientation relationship along with the cube on cube orientation relationship were the two most frequently observed. It is worthwhile beginning this discussion by first assuming that the orientation relationships were exact, then observe the sensitivity of the dislocation structures to slight rotations as noted in Section 4.2. This is accomplished by defining an appropriate rotation matrix **R** such that a new transformation matrix can be defined as:

$$\mathbf{A'=R\cdot A} \qquad (5.2.9)$$

The atom positions corresponding to the particle in the edge- on position and in the plane of the interface are shown in Figure 5.2.9 and 5.2.10 respectively. The transformation $\mathbf{A=S^{-1}_{Ni}S_{TiN}}$ is derived from the following nearest neighbours around the origin (taking Ni as lattice 1):

$$S_{Ti}=\frac{a_{TiN}}{2}\begin{vmatrix}0 & 1 & 0\\ 1 & 0 & -1\\ 1 & -1 & 1\end{vmatrix} \qquad (5.2.10)$$

and

$$S_{Ni}=\frac{a_{Ni}}{2}\begin{vmatrix}0 & 1 & -1\\ -1 & 0 & -1\\ 1 & -1 & 0\end{vmatrix} \qquad (5.2.11)$$

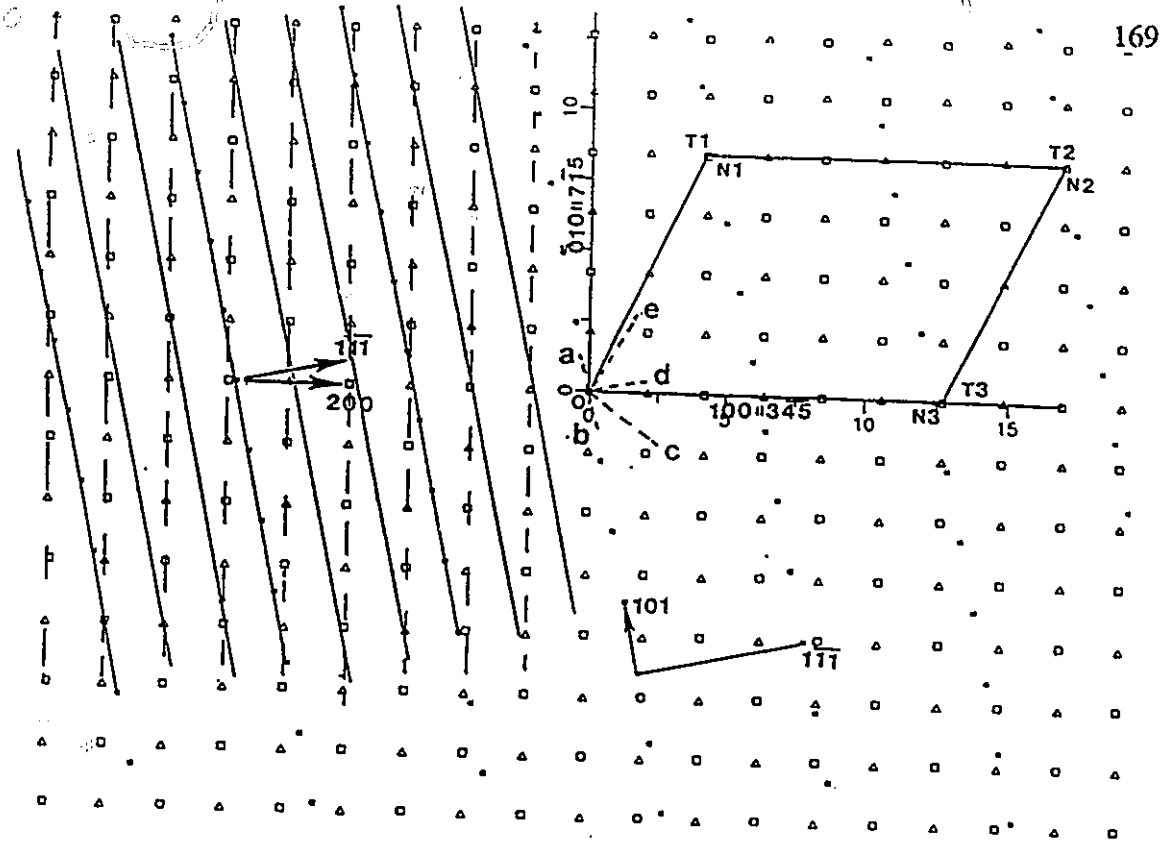

Figure 5.2.9: Schematic Diagram of the atom positions normal to the interface for a Type III OR viewed from $[\bar{1}21]$Ni‖[001]TiN. The out of plane Ni Burgers vectors are indicated by a,b,c,d,e where a=½$[0\bar{1}1]$Ni, b=½$[\bar{1}10]$Ni, c=½$[0\bar{1}\bar{1}]$Ni, d=½$[10\bar{1}]$Ni, e=½$[1\bar{1}0]$Ni.

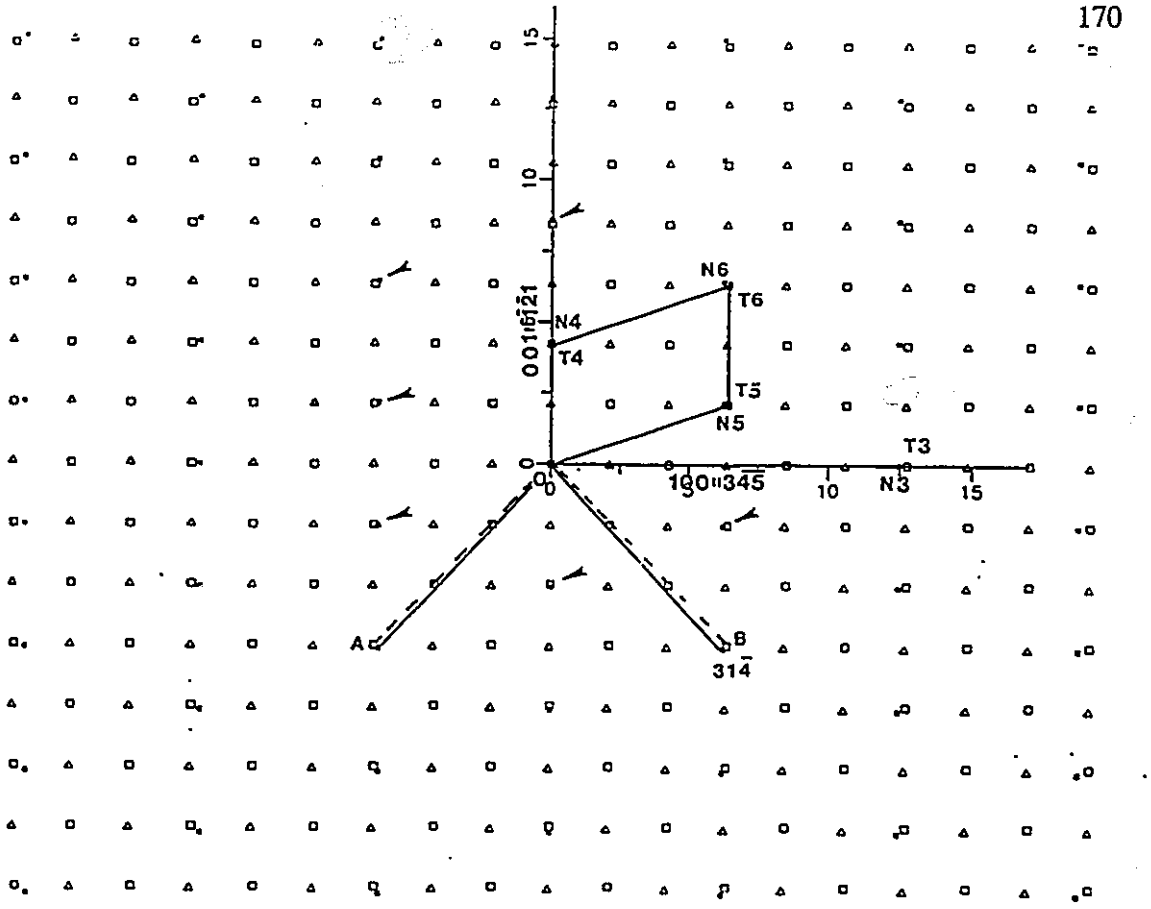

Figure 5.2.10: Schematic Diagram of atom positions in the plane of the interface for a Type III OR (010)TiN‖(7$\bar{1}$5)Ni.

The detailed calculation is shown in Appendix VI, in the orthonormal coordinate system defined by TiN. The result for $\mathbf{X}^o$ (in Å) is shown below.

$$X^o = \begin{vmatrix} -5 & 17 & 5 \\ \sim 0 & 8 & \sim 0 \\ -22 & -236 & -220 \end{vmatrix} \qquad (5.2.12)$$

This O-lattice is shown projected onto the (010)TiN plane in Figure 5.2.11. (The true O-lattice plane, which contains two independent O-lattice vectors, is rotated ~5° about [001]TiN- see appendix VI). The subsequent O-lattice planes are displaced by 8Å. The dislocation structure found on the O-lattice plane may be regarded as consisting of two sets of dislocations. One set with a 6Å spacing lacks physical significance and would not be observable with conventional electron microscopy. The second set of dislocations has a spacing of 50Å oriented 12° away from [001]TiN towards [101]TiN. The Burgers vectors of these dislocations is deduced to be $\frac{1}{2}[\overline{1}\,\overline{1}\,0]$Ni from theory (the Ni Burgers vectors are also given by Equation 5.2.10).

Case i) Twist Component:

Calculations were performed to ascertain the effect of the observed small twist or tilt components on the Primary O- Lattice. The effect of a +0.9° (Ni lattice) twist about [010] was first calculated. This rotation has the effect of aligning almost perfectly

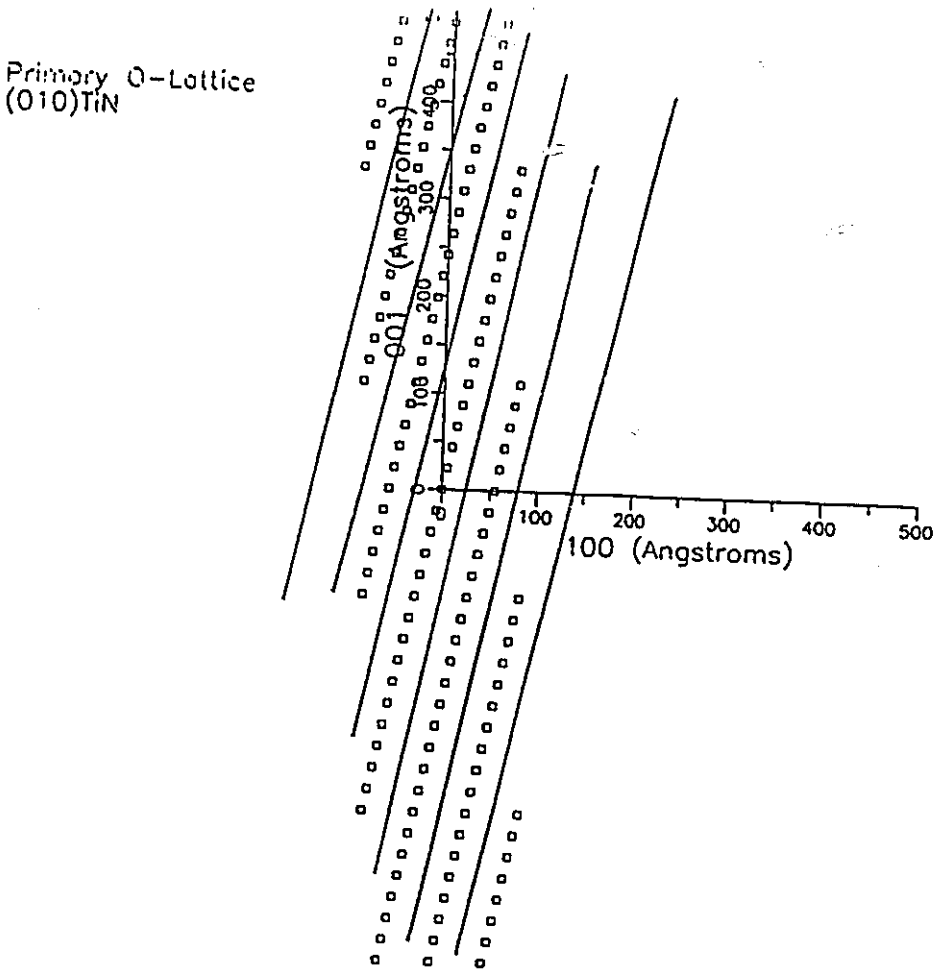

Figure 5.2.11: Results of Primary O-lattice calculation in the habit plane.

the $[31\bar{4}]$Ni and $[\bar{1}01]$TiN directions as shown in Figure 5.2.12, (these may be regarded as the traces of $(1\bar{1}1)$TiN and (111)Ni on (010)TiN). The atom spacings are 8.982 Å and 8.994 for $\frac{1}{2}[31\bar{4}]$Ni and $3/2[\bar{1}01]$TiN respectively (i.e. they differ by only ~0.1%). The result of the calculation of $\mathbf{X}^o$ values is shown below in Å, the details of which may be found in Appendix VII. This rotation also serves to make the O-lattice plane and (010)TiN coincide within experimental error.

$$X^o_{twist} = \begin{vmatrix} -7 & 0 & 10 \\ 0 & 0 & -8.5 \\ 10 & 140 & 125 \end{vmatrix} \qquad (5.2.13)$$

As noted by this result the dislocation spacing is very sensitive to slight twist rotations. These results are presented in Figure 5.2.13. Once again only one significant set of dislocations is predicted, spaced about 80Å apart. The predicted line direction of these dislocations is 7° away from $[\bar{1}01]$TiN towards [001]. These two results are in excellent agreement with observations. As with Type II, (assuming a Wigner-Seitz configuration), the dislocations are predicted to be composed of two segments with $\frac{1}{2}[10\bar{1}]$Ni and $\frac{1}{2}[1\bar{1}0]$ Burgers vectors. These Burgers vectors, however, do not agree with all the TEM observations since one of the TEM images which had a particularily strong image (Figure 4.2.10a) satisfied $\mathbf{g}\cdot\mathbf{b}=0$ (if $\mathbf{b}=\frac{1}{2}[10\bar{1}]$Ni). Furthermore, $\mathbf{b}=\frac{1}{2}[011]$Ni is the only (Ni) Burgers vector that would permit both of the dislocation images in Figure 4.2.10 to be in contrast. As noted in Section 4.2.3, no

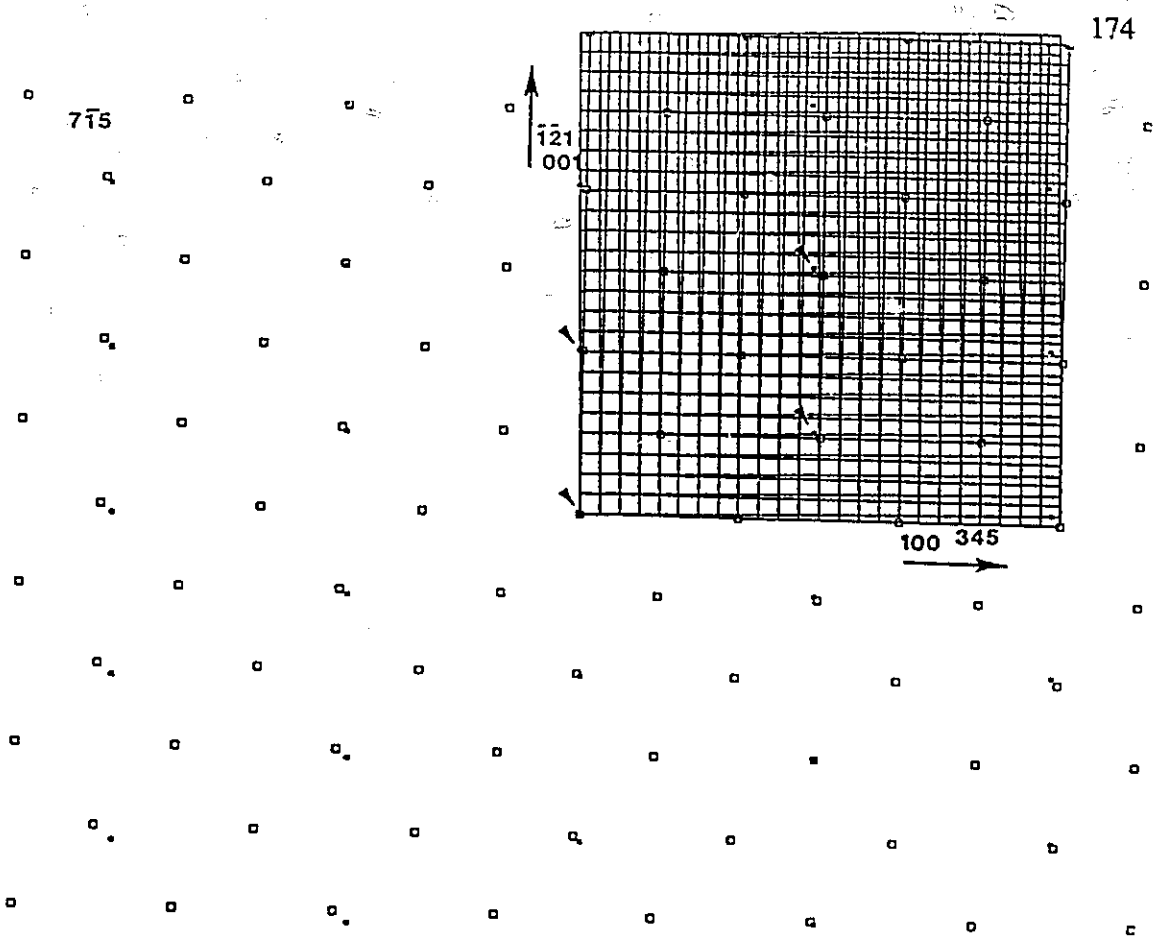

Figure 5.2.12: Showing Effect of 0.9° Twist on atom positions in the habit plane.

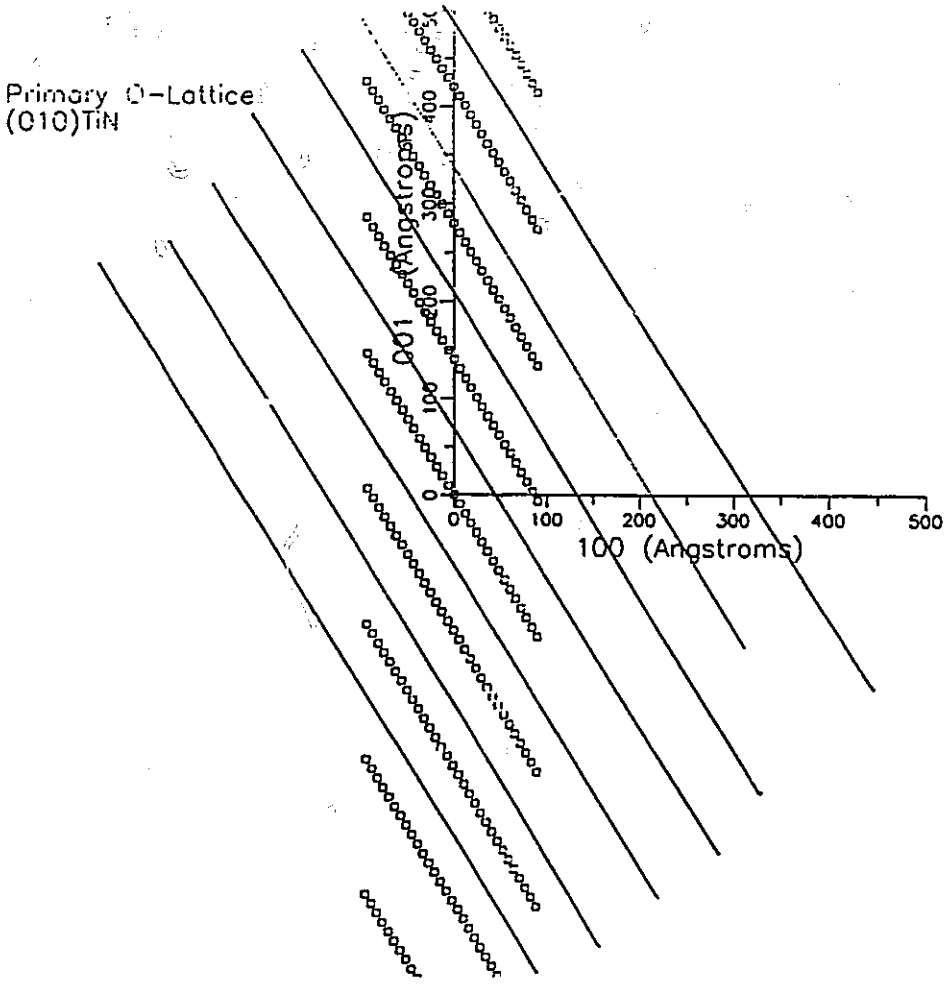

Figure 5.2.13: Showing Effect of 0.9° Twist on the Primary O-lattice in the habit plane. The Burgers vector are defined as 'd' in Figure 5.2.9.

invisibility condition for dislocations was achieved with these particles.

case ii) tilt component:

The effect of a -0.9° (Ni) rotation about [100] was ascertained as before. The details of the calculation are shown in Appendix VIII. The result for $\mathbf{X}^o$ is as follows and is shown in Figure 5.2.14 projected onto the (010) plane.

$$X^{o}_{tilt} = \begin{vmatrix} -6 & 11 & 0 \\ \sim 0 & 9 & \sim 0 \\ -13 & -141 & -127 \end{vmatrix} \qquad (5.2.14)$$

The primary O-lattice plane in this case is deviated by about 10° from (010)TiN (appendix VIII). This incidently agrees with observations which indicated that the particle with this OR had an interface which deviated from (010)TiN. Once again only one significant set of dislocations is predicted with a line direction about 20° from [001] towards [101]. Although the direction of these defects is close to what is observed, the spacing predicted by this calculation is about half of the observed spacing. The Burgers vector in this case is ½[$\overline{1}\,\overline{1}$0]Ni which makes these dislocations mostly edge in character. The observed highly stepped nature and irregular spacing of the dislocations of this interface might account for the differences between observation and calculation.

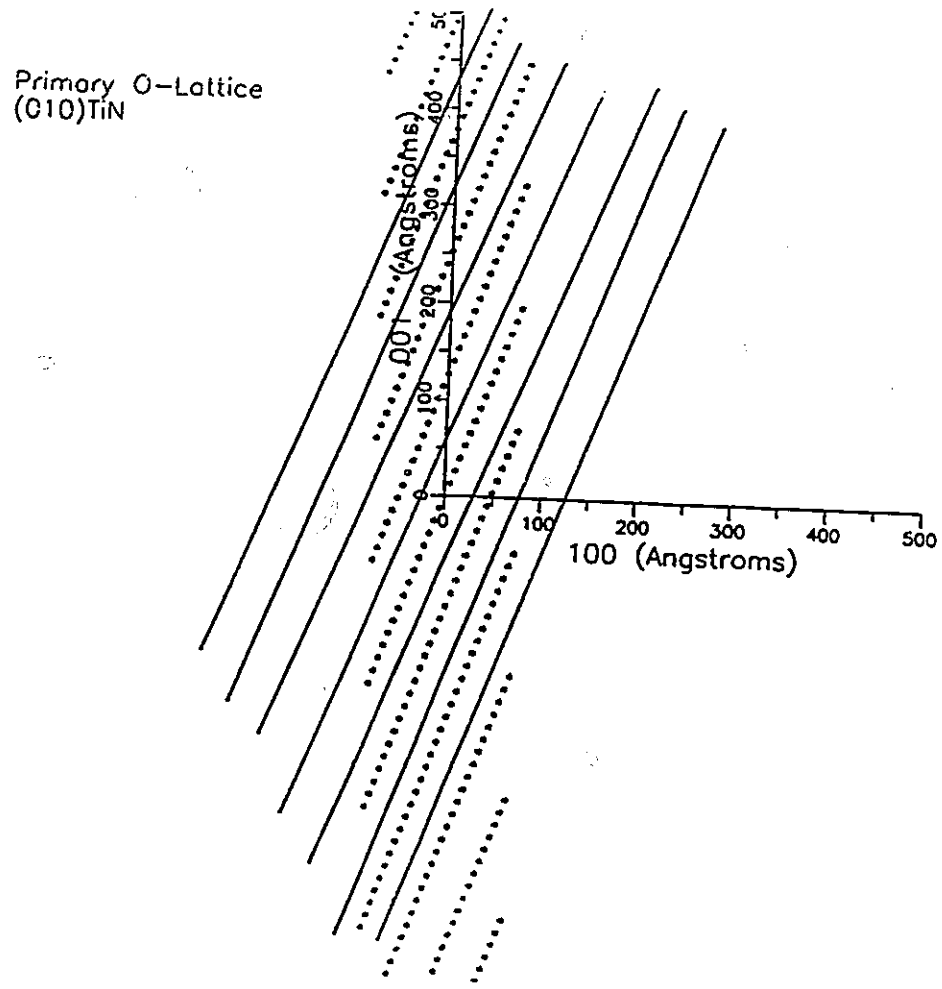

Figure 5.2.14: Showing the Effect of 0.9° Tilt on the Primary O- lattice in the habit plane in a Type III OR. The Burgers vectors are defined as 'e' in Figure 5.2.9.

case iii) -Type III- variant:

The particle with this variant was oriented in such a manner that a complete **g·b** analysis could be performed. The structure matrix (in crystal coordinates) is once again given by Equation 5.2.10 and 5.2.11 for TiN and Ni respectively. However the transformation matrix **A** is formulated in a different manner to account for the 23° rotation about [001]TiN of this variant in the coordinate system of TiN (Appendix IX). It was not possible to determine the precise orientation relationship with respect to twist or tilt components given the high index zone axis and the weak diffraction spots associated with it. The spacing and orientation of these dislocations are, however, consistent with case (i). The calculation was therefore conducted assuming a twist between +0.9° and +1.25° about [010]TiN. The predicted spacing and orientation of these dislocations are once again in excellent agreement with observations (Figure 4.2.15) as shown in Figure 5.2.15. The dislocation are assumed not to change their orientation or spacing substantially due to the inclined facet since the O-lattice points are closely spaced and nearly aligned in the [010]TiN direction. The Burgers vector of these dislocations was deduced from O-Lattice theory to be ½[10$\bar{1}$]Ni and ½[1$\bar{1}$0]. Although there is some (limited) agreement with the results in the **g·b** analysis of Section 4.2.3, it is by no means conclusive.

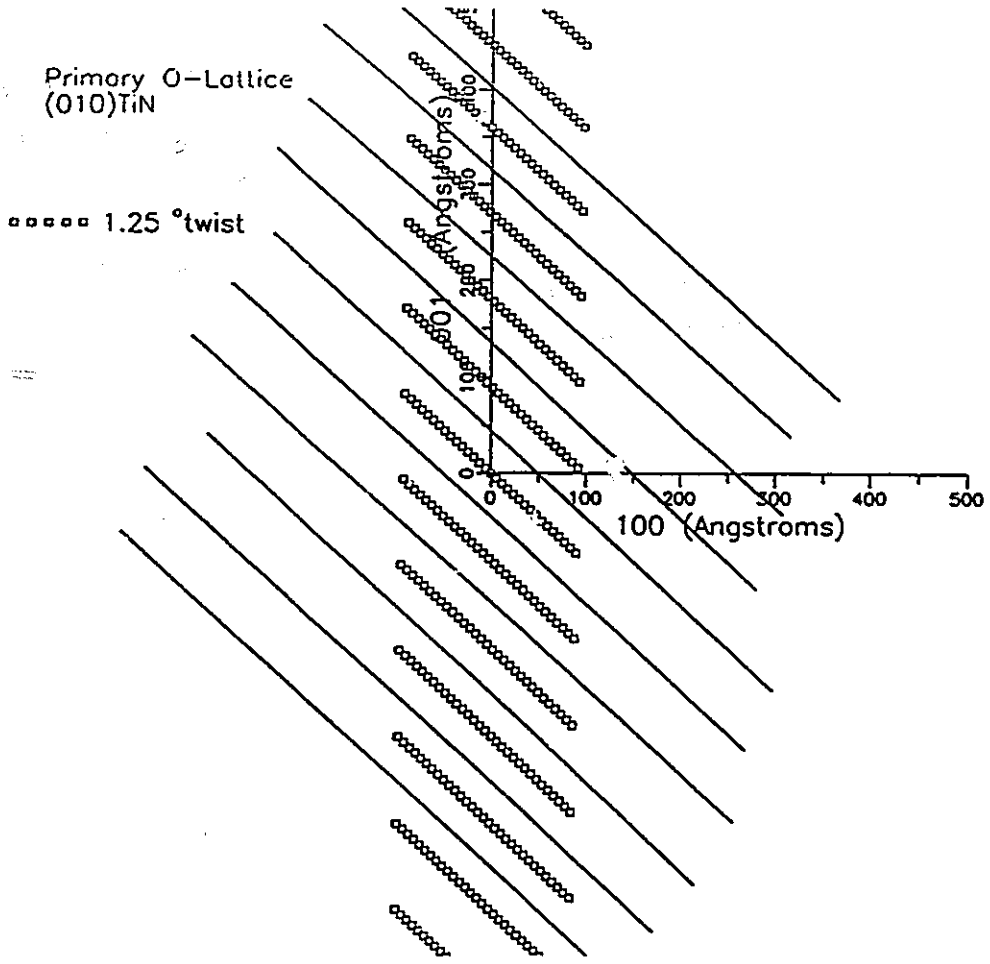

Figure 5.2.15: Showing the effect of 1.25° twist on the Primary O-lattice in the habit plane of a Type III OR.

iv) CSL Interpretation:

The atom positions are shown in Figure 5.2.10 for the atoms in the plane of the interface. A near CSL unit, O-N4-N5-N6≈O-T4-T5-T6, is shown with every Ni atom in the boundary coincident with a Ti atom. The size of the unit cell of this near CSL is exactly the same size as that found in the Type II orientation relationship. The σ values for the boundary plane are: 3,6 and 1 for σ_{Ti}, σ_{TiN} and σ_{Ni} respectively. The CSL unit cell does not change its size with the inclusion of the N atoms.

v) Plane Matching Interpretation:

As noted, the twist component had the effect of aligning almost perfectly the [31$\bar{1}$]Ni and [$\bar{1}$01]TiN directions indicating that plane matching of (111)Ni and (1$\bar{1}$1)TiN may be important. The results of the plane matching calculation, shown in Table 5.2.1, are in poor agreement with observations. This is because the traces of (111)Ni and (1$\bar{1}$1)TiN are almost perfectly aligned due to the twist component therefore the dislocation spacing is very large.

Table 5.2.1
Table of Plane Matching Results (111)Ni and (1$\bar{1}$1)TiN

Rotation	Spacing Å	Orientation
0°	168	7° away $[101]_{100}$
0.9° about [010]	1079	[100]

The (200)TiN planes were slightly mismatched across the interface with $(1\bar{1}\bar{1})$Ni (Figure 5.2.9). The results of this calculation are shown in Table 5.2.2 and are in better accord with observation. The twist rotation produces an almost identical result to that of O-lattice theory, with a slightly smaller spacing. The traces of the $(1\bar{1}\bar{1})$Ni planes are effectively 'twisted' in the habit plane by -0.2° by the 0.9°tilt component.

Table 5.2.2
Plane Matching Results $(1\bar{1}\bar{1})$Ni and (200)TiN

orientation	spacing Å	direction
0°	96	[001]
0.9° twist $[010]_{TiN}$	79	9° away from $[\bar{1}01]_{001}$
0.9° tilt $[100]_{TiN}$	96	9° away from $[001]_{101}$

The results of these calculations are in excellent accord with observations for both the twist and tilt orientations. While the results of O-lattice and plane matching theory differ with respect to the tilt orientation they are nearly identical with respect to the twist orientation. This shows once again that it is sometimes difficult to distinguish the results of plane matching theory from O-lattice theory without Burgers vector determinations. A $\frac{1}{3}[1\bar{1}\bar{1}]$Ni or $\frac{1}{2}$[100]TiN Burgers vector might be expected as a strict interpretation of a plane- matching dislocation. There was some support for a $\frac{1}{2}$[100]TiN Burgers vector from the **g·b** analysis of Section 4.2.3.

vi) Contrast Behaviour of Interfacial Dislocations:

The contrast behaviour of these interfacial dislocations was extremely sensitive to the diffracting conditions used. Weak beam dark field (and to a lesser extent dark field) provided the best operating conditions for imaging these defects. There were some inconsistencies in the **g·b** analysis, and in this regard the interpretation of these Burgers vectors as $\frac{1}{2}[10\bar{1}]$Ni should be viewed with caution. The most serious inconsistency, as already noted, is the strong image of Figure 4.2.10a under **g·b**=0 conditions, although the small edge component might account for the visibility of this image. As noted in the previous section, because both O-lattice theory and Plane Matching theory can make similar predictions, it is useful to have Burgers vector determinations in order that one theory may be distinguished from the other. The general unreliability of **g·b** analysis and the extreme sensitivity of the images to the diffraction conditions make this difficult. Some of these problems stem from the fact that these features are imaged essentially at the top or bottom of a TEM foil, where complicated Bloch wave oscillations can dramatically change the contrast of dislocations at these surfaces. The invisibility of dislocations on one side of the particle under conditions of $w>0$ is another complicating feature. This effect is not due to these dislocations acting as loops around the particle as might be expected. It may be recalled that the image of a dislocation loop can appear either inside or outside the actual loop depending on the sign of (**g·b**)s. Therefore the image might be visible on both sides of the particle or on

neither.

5.2.5: Other Orientations:

Two other orientation relationships were observed. They were put into this category because of the small number of observations (2 for Type IV and 1 for Type V) and their lack of visible misfit dislocation configurations.

a) Type IV: [101]TiN ‖ [101]Ni:(010)TiN ‖ (17$\bar{1}$)Ni

The atom positions normal to the habit plane are shown for this orientation relationship in Figure 5.2.16. The boundary plane is a (010)TiN ‖ (17$\bar{1}$)Ni. Once again (11$\bar{1}$)Ni planes are rotated in such a fashion as to suitably arrange themselves with (11$\bar{1}$)TiN such that their traces are well matched in the plane of the interface. This is exactly the situation that was observed with the Type III (twist) particle. An O-lattice calculation performed (not shown) also shows that the (010)TiN is a primary O-lattice plane. In this case the fine spacing of the O-points would make it difficult to observe any misfit dislocation configurations. The contrast features noted in Figure 4.2.20b are either growth steps or matrix dislocations intercepting the interface.A near CSL is observed in the habit plane as shown in Figure 5.2.17. The vector **E** shows the traces of (11$\bar{1}$)Ni planes. The σ values for this interface are 30, 60 and 12 for σ_{Ti}, σ_{TiN} and σ_{Ni} respectively.

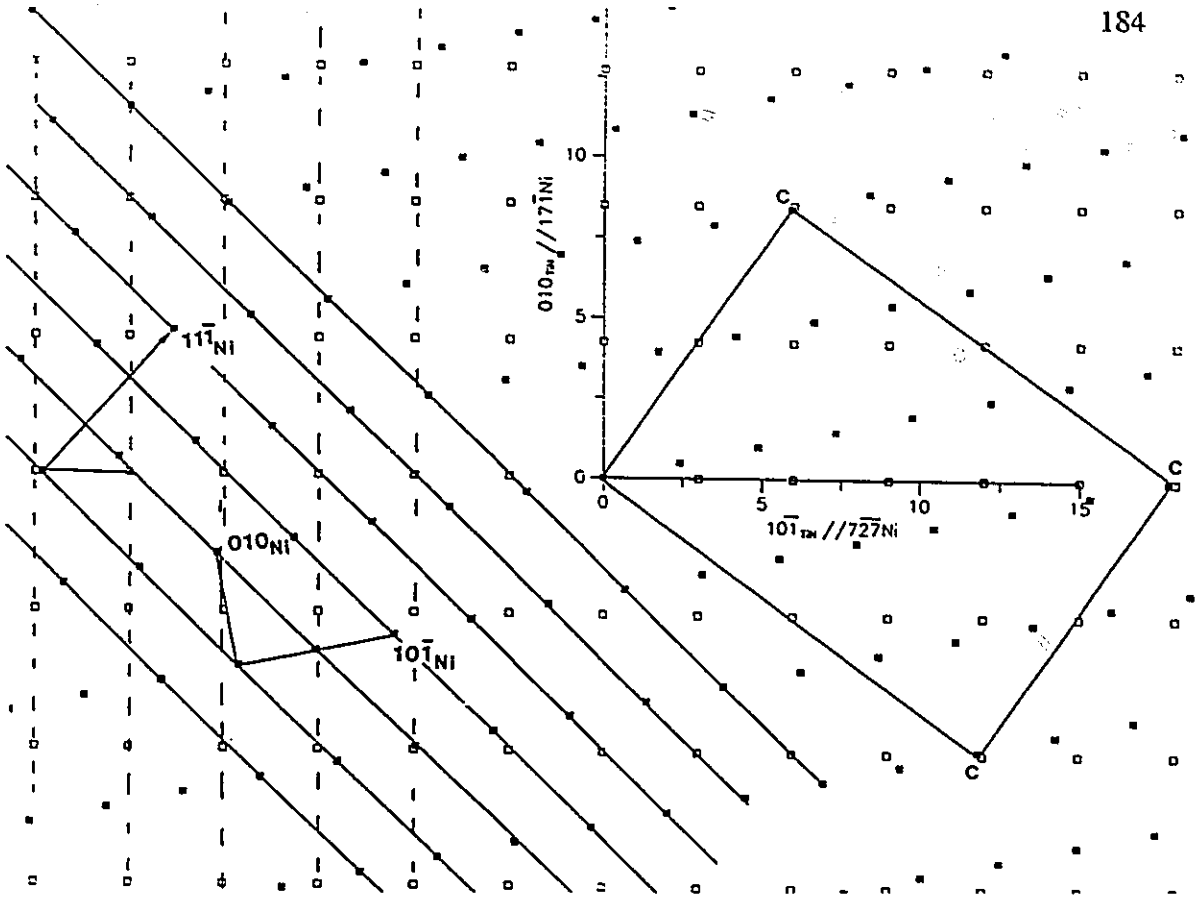

Figure 5.2.16: Schematic Diagram of the atom positions normal to the interface of a Type IV OR (101)TiN‖(101)Ni.

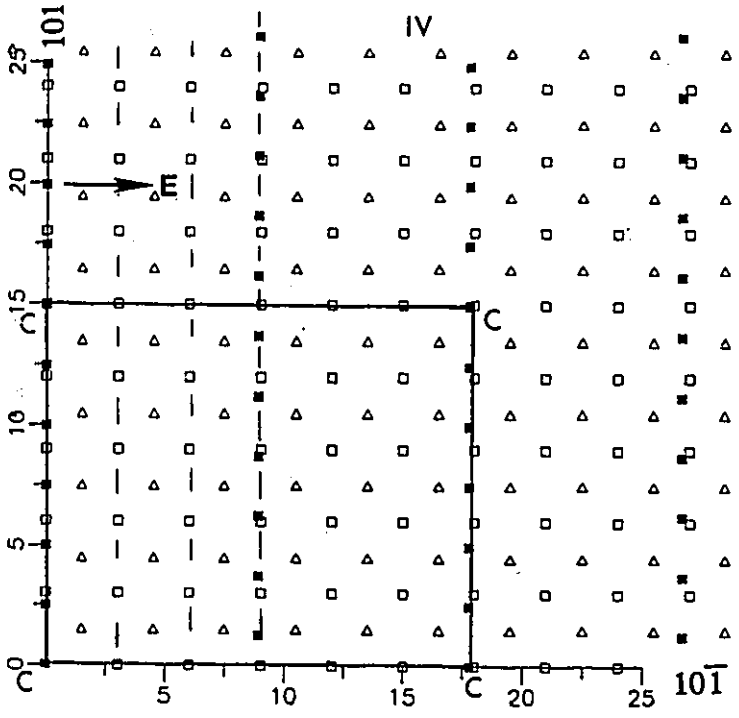

Figure 5.2.17: a) Schematic Diagram of atom positions in the plane of the interface of a Type IV OR (101)TiN‖(17$\bar{1}$)Ni.

b) Type V: [110]TiN ‖ [211] Ni:($\bar{1}$11)Ni ‖ (010)TiN

This orientation relationship is related to Type II, but with a rotation in the boundary plane of 45 degrees. A schematic diagram of the atom positions normal to the habit plane are shown in Figure 5.2.18. As noted ($\bar{1}$11)Ni and (010)TiN meet to form the interface as in the Type II OR. An O-lattice calculation (not shown) indicates that similar to the Type II OR, the (010)TiN habit plane is a primary O-plane.

A schematic diagram of the atom positions in the plane of the interface is shown in Figure 5.2.19. The lines indicated, show the mismatch of (10$\bar{1}$) planes of TiN with (01$\bar{1}$) Ni. The σ values for this interface are 15 ,30 and 24 for σ_{Ti}, σ_{TiN} and σ_{Ni} respectively.

5.3.1: Synthesis of Results:

There were several key observations made in Section 5.2. It is worthwhile reviewing these salient points:

1/ Although habit planes other than {010}TiN were found, the majority of particles had {010} TiN habit planes, indicating that this was an important factor in determining the habit and by implication the orientation relationships of the particles.

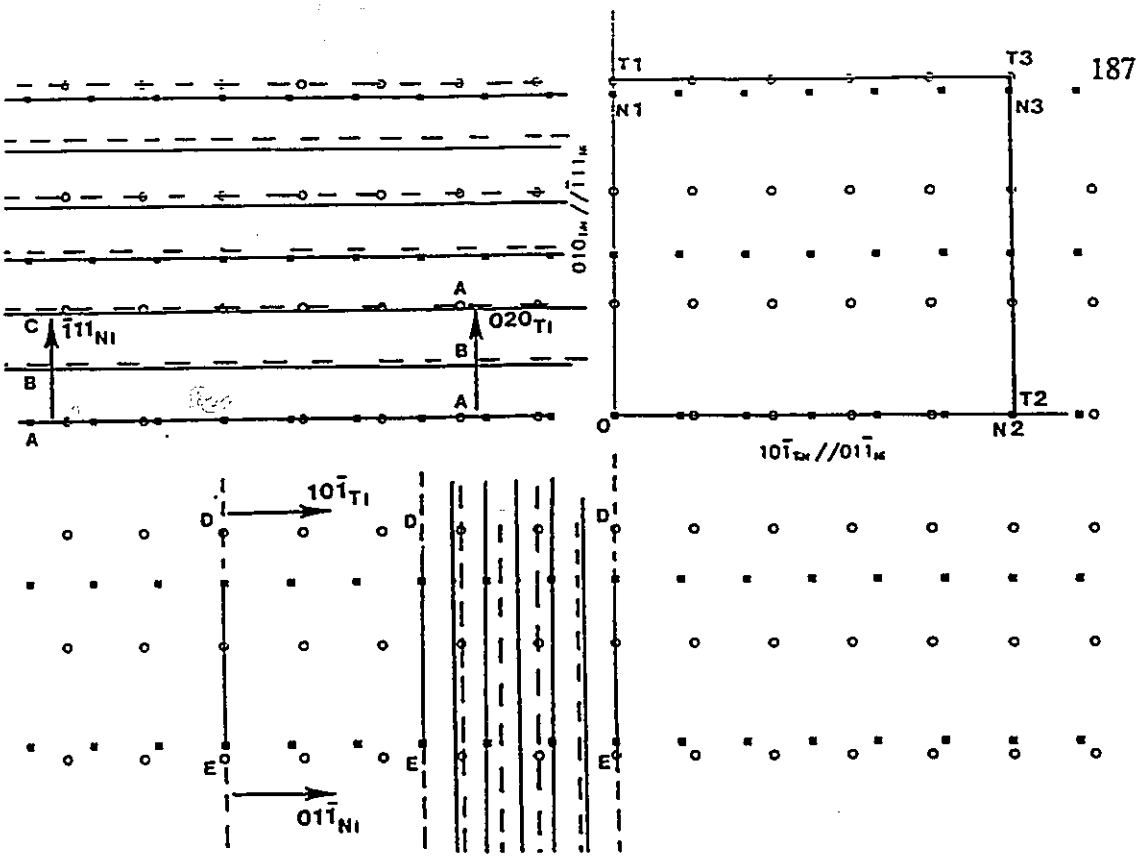

Figure 5.2.18: Schematic Diagram of the atom positions normal to the interface of a Type V OR (101)TiN‖(211)Ni.

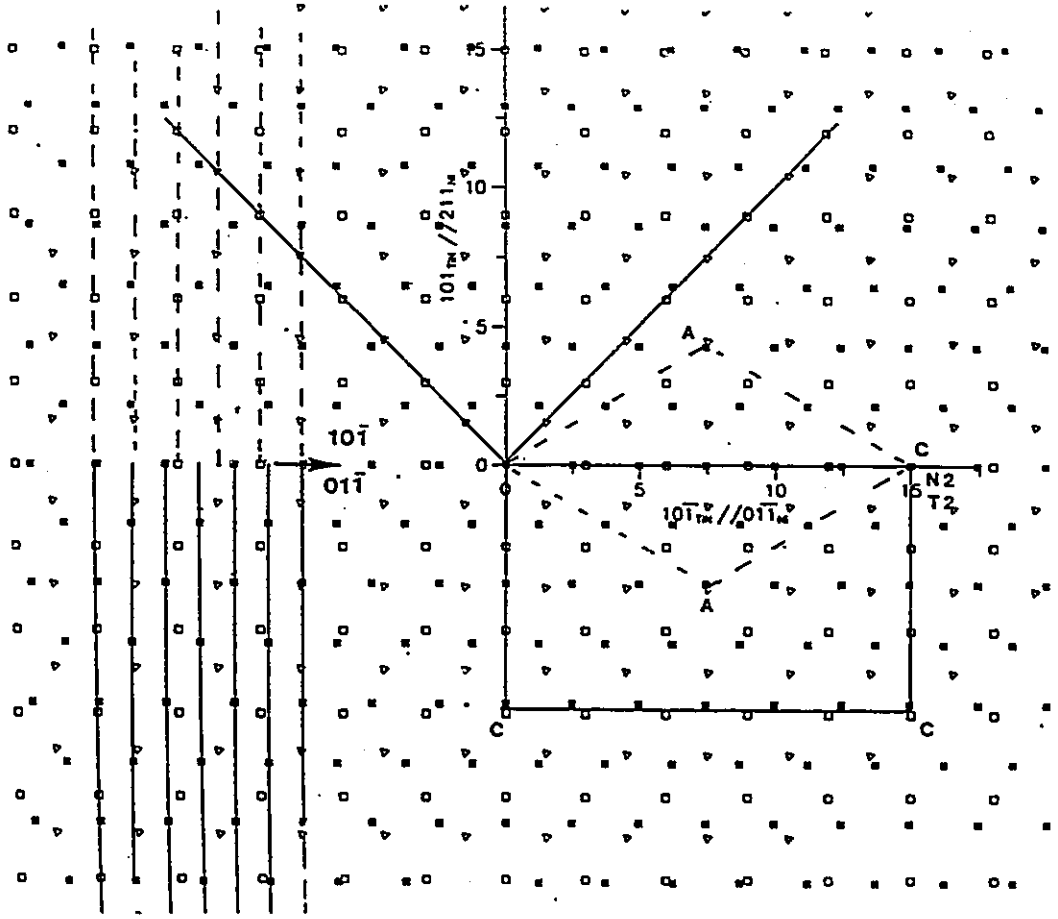

Figure 5.2.19: a) Schematic Diagram of atom positions in the plane of the interface of a Type V OR (111)Ni‖(010)TiN.

2/ All the particles studied had an association of low index planes ({111}Ni or {200}Ni and {200}TiN or {111}Ni), such that these planes were parallel to one another and to the habit plane, or that their traces were well matched in the plane of the interface. In the language of O-lattice theory this resulted in the primary O-plane (Zhang and Purdy 1993) becoming (0 1 0)TiN, as noted by O- lattice calculations.

3/ Misfit dislocations were observed at two of the ORs. O-lattice theory and Plane-Matching theory made similar predictions as to the dislocation spacing and direction in these cases, both predicting one predominant set of dislocations. In the case of plane matching theory the dislocations arise from the mismatch of {111}Ni and {100}TiN across the interface.

4/ All the particles had relatively small σ values (σ_{Ni}<20 with respect to TiN). These are shown (also normalized with respect to the Ni habit plane spacing) in Table 5.2.3 and Table 5.2.4. No correlation was found between σ values and the observed frequency of an orientation relationship.

Table 5.2.3
Table of Orientation Type Versus σ w.r.t. the Ti sub-lattice

Type	Plane (Ni)	σ_{Ti}	σ_{Ni}	σ_{Ni}/d_{hkl}	σ_{Ti}/d_{hkl}	freq.
I	(001)	25	36	20	14	0.4
II	$(\bar{1}11)$	3	5	2.5	1.5	0.05
III	$(7\bar{1}5)$	3	1	2.5	7.5	0.4
IV	$(17\bar{1})$	30	12	24	50	0.1
V	$(\bar{1}11)$	15	24	12	7.5	0.05

Table 5.2.4
Table of Orientation Type Versus σ w.r.t TiN

Type	Plane (Ni)	σ_{TiN}	σ_{Ni}	σ_{Ni}/d_{hkl}	σ_{Ti}/d_{hkl}	freq.
I	(001)	25	18	10	14	0.4
II	$(\bar{1}11)$	6	5	2.5	3	0.05
III	$(7\bar{1}5)$	6	1	2.5	15	0.4
IV	$(17\bar{1})$	60	12	24	120	0.1
V	$(\bar{1}11)$	15	12	6	7.5	0.05

The presence of {010}TiN habit planes in all the orientation relationships implies that this was the controlling factor in selecting low energy interfaces during nucleation. Cuboidal TiN particles bounded by {010} are almost always produced from the vapour and are also precipitated in both solid and molten steel. The surface energy of {010}TiN, like all of the rock salt structures, is the lowest and has been estimated by Hultman and co-workers (1989) to be ~1.1 J/m^2 for TiN. The surface energy of (011)TiN

by comparison was estimated in this same study as 1.6 J/m^2, while the surface energy of (111)TiN was considered extremely high as noted by the near absence of these facets during the void formation experiments in TiN of Hultman et. al. (1989).

The process of nucleation should select interfaces of the lowest interfacial energy γ. From homogeneous nucleation theory, the nucleation rate is known to depend exponentially on $-\gamma^3$ (Aaronson 1993). It is evident that due to the excess volume changes associated with the nucleation event a flux of vacancies are is required to alleviate the stresses generated by the volume mismatch between nucleus and matrix. It seems unlikely, however, since this stress is generated by volume mismatch, that it should depend on the orientation relationship, so that to a good first approximation the nucleation of TiN should be governed by capillarity considerations. In this regard the interfacial energy of the five orientation relationships bounded by {010}TiN cannot differ substantially since they were all found. The presence of fairly small near CSLs in all the observed ORs suggests that these play a role in selecting low energy interfaces. Some differences in interfacial energy must exist due to the abundance of Type I and Type III particles. However, no correlation was found between the frequency of observation of a particular OR and the size its corresponding planar CSL relationship. Therefore, an overly simplistic interpretation of the lowest energy interfaces corresponding to the lowest σ values cannot be substantiated. Sutton and Balluffi (1987) have similarly argued that geometrical criteria for low energy interfaces in metal- ceramic or ceramic-

ceramic systems are not very useful because electronic contributions to the interfacial energy in some cases tend to dominate. The results presented in this work tend to agree with this assessment. In summary it would appear that the minimization of the interfacial energy for the TiN/Ni system involves the selection of orientation relationships such that (0 1 0)TiN facets are primary O-lattice planes that contain a planar near CSL relationship.

The morphology of these particles is dictated by a number of factors many of which are poorly understood. Two points about the growth of these particles are, however, readily apparent. The first, is that there is experimental evidence to suggest that both growth ledges and high index facets facilitate the growth of TiN in Ni. The principal growth direction is often a high index facet while the semicoherent {010}TiN facets are the least mobile without the intervention of growth ledges. The growth ledges (presumably of dislocation character) are regarded as the sink for vacancies. This hypothesis is in part supported by research in other excess volume interstitial systems such as Pt-C and Mo-Hf-N (Westmacott and Dahem 1987) where a cooperative growth mechanism where-by vacancies are condensed to facilitate growth was noted. Finally, it was shown via the finite difference model that the nitridation behaviour of this system is well described without accounting for vacancy interactions with the particles. This stems from the high diffusivity of vacancies which can very quickly relieve the aforementioned stresses generated at these growing particles. The broader question as to what determines

the particle aspect ratios, and what decides the terminating habit of the growing particles cannot be addressed by this work. The answer may depend in a very complicated manner on the interfacial energy, the strain field around the particle, on the directional nature of the diffusion fields as well as on the proximity of sources and sinks for vacancies.

Chapter 6

SUMMARY AND CONCLUSIONS:

A study was conducted on the nitridation behaviour of dilute Ni-Ti alloys and on the orientation relationships and interfacial structures between TiN and Ni. The following is a summary of the main conclusions and contributions to science made in this work:

1: Beginning with the Fickian relationships first proposed by Kirkaldy (1969) to describe internal sulphidation and assuming a solubility product of the form K=BC, these equations were combined to yield for the metal solute:

$$\frac{\partial B}{\partial t}=[D_B+\frac{KD_C}{B^2}]\frac{\partial^2 B}{\partial x^2} \qquad (2.1.8)$$

This second order differential equation shows that the concentration profile of the metal solute, B, is dependent not only on the diffusivity of the metal, D_B, but also on the solubility product K and on the gas diffusivity D_C. Two limiting cases were identified from Equation 2.1.8. The first, which depends only the metal diffusivity, D_B, corresponds to Wagner's error function solution for the superficial oxidation of alloys dilute in B. The

second limiting case (D_B=0) corresponds to Wagner's oxygen controlled internal oxidation as proven analytically by Ohriner and Morral (1979). A criterion describing the transition from internal to external nitridation (oxidation) was deduced from Equation 2.1.8 as:

$$\frac{KD_C}{B_I^2 D_B} < 0.1$$

where B_I is the interfacial composition of the metal solute.

2: A finite difference algorithm was presented based on these ideas. A comprehensive test of this approach showed that it could generate the well known analytical solutions of Wagner's two limiting conditions. It was also shown that provided the solubility product K is small, Ohriner and Morral's (1979) analytical solution is valid even for an alloy not saturated in the gas phase (i.e. the composition need not be confined to the solvus of the ternary isotherm). As well as reproducing these analytical solutions, the model was successfully tested against the experimental work of Swisher (1968) and Kirkaldy (1969).

3: A detailed investigation was conducted on the concentration profiles of Ti in Ni as a consequence of either internal nitridation or superficial nitridation. It was found that the program always generated the correct shapes of the diffusion profiles as well the transition to external nitridation in the Ni-Ti-N system. Based on the measured interfacial

composition of the interface, first time determinations of both KD_N and D_{Ti} values were obtained between 800°C and 1020°C. The diffusivity of Ti in Ni is similar to other substitution solutes in Ni and can be expressed as:

$$D_{Ti}=0.0700 \exp(-320\ 000/RT)\ m^2/s \qquad (900°C - 1020°C)$$

A solubility product calculation of TiN in Ni showed values between 1.4×10^{-6} and 5×10^{-8} $[w/o]^2$ (between1020°C and 800°C respectively). Using this data, a diffusivity of N in Ni was obtained which compares favourably to other interstitial diffusivity data in Ni and γFe. The upper bound value for the diffusivity of N in dilute Ni-Ti alloys can be expressed as:

$$D_N= 0.0003 \exp(-170\ 000/RT)\ m^2/s \qquad (900°C-1020°C)$$

where R is in units of J/mole-K

4: Stoichiometric TiN was the only precipitated phase found between 800°C-1020°C in this work.

5: A first time investigation of the interfacial structure between TiN and Ni was conducted. It was determined that at least five different orientation relationships (OR)s exist between TiN and Ni.

6: The habit planes were dominated by {010}TiN indicating that this was an important factor in selecting the morphology and orientation relationships of these particles. This plane coincided both with a primary O-lattice plane and with a fairly small near CSL relationship. These factors probably all play a role in the selection of these orientation relationships and habit planes in the Ni/ TiN system.

7: In only two cases were misfit dislocations observed. In both these cases there was an association of {100}TiN and {111}Ni such that the traces of these planes were slighlty mismatched in the plane of the interface. Both O-lattice and plane matching theory made similar predictions as to the misfit dislocation configurations of Type II and Type III ORs. In both cases one predominant set of dislocations was predicted and observed.

Chapter 7

Recommendations for Future Work:

There remain a number of intriguing problems identified in this work that may warrant further study. These are:

1: The surface morphologies showed unique microstructure. The appearance of the Ni 'nodules' on twin boundaries remains largely unexplained. Related to this problem is the preferential appearance of (surface) Ni on the traces of {111}Ni planes particularly at low temperatures. An explanation of precipitation as related to the association of {111}Ni and {010}TiN planes was offered with limited experimental support. Both these issues may be resolved by careful (and difficult) sectioning experiments coupled with electron channelling experiments to determine the grain orientation.

2: The growth mechanism of TiN in Ni is also poorly understood. An in-situ TEM study of the dissolution of TiN in Ni would be an ideal experiment to determine the growth (dissolution) mechanisms of these particles. It is realized that given the stability of TiN this may not be possible. An alternative approach is to identify a TiN particle early in the growth process in a TEM foil. By conducting successive nitriding experiments on

this TEM foil, the morphological changes of the particle may then be followed.

3: It was suggested how the FD program could incorporate a vacancy role as a rate limiting step in the precipitation TiN. This is hypothesised in terms of ledges (and their associated risers) acting as a good vacancy sink at the interface of a growing particle so that the precipitation process is limited by available vacancies. Useful calculations could be performed of several hypothetical situations concerning starting alloy concentrations, gas solubilities, vacancy concentrations, diffusivities of the various species and mean distance of available sources of vacancies (other than the surface). This may resolve the issue of under which circumstances solvent removal as controlled by a vacancy flux may act as a rate limiting step to internal nitridation or oxidation.

4: The difficult problem remains to explain the appearance of the varied orientation relationships observed in this work, which defy geometrical categorization. Atomistic computer modelling of these interfaces might yield plausible explanations for this behaviour.

5: Computer simulation methods are also available which can simulate interfacial dislocations, provided that useful double two beam conditions can be obtained. In future work it would be advisable to perform computer simulations to unambiguously identify the Burgers vector of these dislocations.

6: A high resolution (lattice imaging) TEM study of the interfaces between TiN and Ni would also be extremely useful in identifying possible defect structures at such interfaces.

Chapter 8

References:

Aaronson, H.I. (1993) "Atomic Mechanisms of Diffusional Nucleation and Growth and Comparisons with their Counterparts in Shear Transformations", *Met. Trans. A*, **24A**, 241.

Backhaus-Ricoult, M. and Hagege, S. (1992) "Metal-Ceramic Interfaces in Internally Reduced Mg,Cu)O", *Acta Met. Mater.*, **40**, S267.

Balluffi, R.W. and Schober T. (1972), "On the Stucture of High Angle Grain Boundaries with Particular Reference to a Recent Plane Matching Approach", *Scripta Metall.* **6**,697

Balluffi, R.W., Brokman, A. and King, A.H. (1982) "CSL/DSC Lattice Model for General Crystal-Crystal Boundaries and their Line Defects", *Acta Met.*, **30**, 1453.

Bilby B.A. (1955), in Defects in Crystalline Solids, The Physical Society, London, 124

Binder, S., Lengauer, W. and Ettmayer, P. (1991) "The Ti-N-Ni System: Investigations Relevant for Cermet Sintering", *J. Alloys and Comp.*, **177**, 119.

Birchenall, C.E. (1971) "Oxidation of Alloys" in Oxidation of Metals and Alloys, American Society for Metals, Metals Park, Ohio, 177.

Bollmann, W. (1970) Crystal Defects and Crystalline Interfaces Springer-Verlag, New York.

Bollmann, W. (1974) "O-lattice Calculation of an FCC-BCC Interface", Phys. Stat. Sol. (a), **21**, 543

Bollmann, W. (1982) Crystal Lattices, Interfaces, Matrices, An Extension of Crystallography, Printed by the author, Imprimerie des Bergues, Geneva.

Bongartz, K., Schulten, R., Quadakkers, W.J. and Nickel, H. (1986) "A Finite Difference Model Describing Carburization in High-Temperature Alloys", *Corrosion*, **42**, 390.

Bonnet, R. and Durand, F (1975) "A General Analytical Method to Find a Basis for the DSC Lattice", *Scr. Metall.*, **9**, 935.

Brooks, H. (1952) "Theory of Internal Boundaries" in Metal Interfaces, ASM, Metal Park, Cleveland, Ohio

Bose, S.K. and Grabke, H.J. (1978) "Diffusion Coefficient of Carbon in Iron-Nickel Austenite in the Temperature Range 950-1100 °C", *Z. Metallkde*, **69**, 8.

Brown, A.M. and Ashby, M.F. (1980) "Correlations for Diffusion Constants", *Acta Met.*, **28**, 1085.

Buchmayr, B. and Kirkaldy, J.S. (1990) "Preferential Concentration and Depletion of Carbides After Annealing of Mismatched Alloy Weldments", Fundamentals and Applications of Ternary Diffusion, Pergamon, Oxford, 162.

Chan D.K., Jang H., and Seidman D.N. (1994) " Atomic Scale Studies of the Chemical and Structural Nature of Ag/CdO {222} Interfaces" presented at the ASM/TMS meeting in Rosemount, Illinois

Chattopadhyay, G. and Kleykamp, H. (1983) "Phase Equilibria and Thermodynamic Studies in the Titanium-Nickel and Titanium-Nickel-Oxygen Systems", *Z. Metallkde.*, **74**, 182.

Christ, H.J., Biermann, H., Rizzo, F.C. and Sockel, H.G. (1989) "Influence of the Solubility Product on the Concentration Profiles of Internal Oxidation", *Oxid. Met.*, **32**, 111.

Cliff, G. and Lorimer, G.W. (1975) "The Quantitative Analysis of Thin Specimens", *J. Microscopy*, **103**, 203.

Cullity, B.D. (1978), Elements of X-Ray Diffraction, Addison-Wesley, Reading Massachusetts, 356

Dalvi, A.D. and Coates, D.E. (1972) "A Review of the Diffusion Path Concept and Its Application to the High-Temperature Oxidation of Binary Alloys", *Oxid. Met.*, **5**, 113.

Darken L.S. (1948), *Trans. Met. Soc. AIME* **175**, 184

Darken L.S. (1961), *Trans. Am. Soc. Metals* **54**, 600

Douglass, D.L. (1991) "Anomalous Behavior During Internal Oxidation and Nitridation", *JOM*, **43**, 74.

Evans, H.E. (1995) "Stress Effects in High Temperature Oxidation of Metals", *Int. Mat. Rev.*, **40**, 1.

Fecht H.J. and Gleiter H. (1985), " A lock-in Model for the Atomic Structure of Interface Boundaries Between Metals and Ionic Crystals", *Acta. Metall.* **33** 4, 557

Fletcher N.H. (1971), "Crystal Interface Models-A Critical Survey" in Advances in Materials Research **5**, Wiley- Interscience, New York, Herbert Herman ed.,281

Forwood, C.T. and Clarebrough, L.M. (1989) "The Dislocation Structure of fcc-bcc Interfaces in a Cu-Fe Alloy", *Phil. Mag. B*, **59**, 637.

Forwood, C.T. and Clarebrough, L.M. (1991) Electron Microscopy of Interfaces in Metals and Alloys, Adam Higer, Bristol

Frank F.C. (1950), in Plastic Deformation of Crystalline Solids, Carnegie Institute of Technology, 150

Goldstein J.I., Williams D.B., Cliff G. (1981), "Quantitative X-Ray Analysis" in Scanning Electron Microscopy and X-Ray Microanalysis (Goldstein J.I., Newbury D.E, Echlin P., Joy D.C., Fiori C.E and Lifshin E. editors) Plenum Press, New York, 155

Grieveson, P. and Turkdogan, E.T. (1964) "Kinetics of Reaction of Gaseous Nitrogen with Iron Part I: Kinetics of Nitrogen Solution in Gamma Iron", *TMS-AIME*, **230**, 407.

Grimmer, H. (1974) "A reciprocity Relation Between the Coincidence Site Lattice and the DSC Lattice", *Scr. Met.*, **8**, 1221.

Guan, S.W. and Smeltzer, W.W. (1994) "Oxygen Solubility and a Criterion for the Transitioin from Internal to External Oxidation of Ternary Alloys", *Oxid. Met.*, **42**, 375.

Guan, S.W., Yi, H.C. and Smeltzer, W.W. (1994a) "Internal Oxidation of Ternary Alloys. Part I: Kinetics in the Absence of an External Scale", *Oxid. Met.*, **41**, 377.

Guan, S.W., Yi, H.C. and Smeltzer, W.W. (1994b) "Internal Oxidation of Ternary Alloys. Part II: Kinetics in the Presence of an External Scale", *Oxid. Met.*, **41**, 389.

Guruswamy, S., Park, S.M., Hirth, J.P. and Rapp, R.A. (1986) "Internal Oxidation of Ag-In Alloys: Stress Relief and the Influence of Imposed Strain", *Oxid. Met.*, **26**, 77.

Hoshino A. and Ataki R. (1970), *Tetsu to Hague* **56** 2, 252

Hirsch, P., Howie, A., Nicholson, R., Pashley, D.W. and Whelan, M.J. (1977) Electron Microscopy of Thin Crystals, Krieger Publishing Company, Malabar, Florida.

Hultman, L., Sundgren, J.E. and Greene, J.E. (1989) "Formation of Polyhedral N_2 Bubbles During Reactive Sputter Deposition of Epitaxial TiN(100) Films", *J. Appl. Phys.*, **66**, 536..

Jang, H., Seidman, D.N. and Merkle, K.L. (1993) "The Chemical Composition of a Metal/Ceramic Interface on an Atomic Scale" The Cu/MgO {111} Interface", *Interface Sci.*, **1**, 61.

Kirkaldy, J.S. (1957), Can. J. Phys., **22**, 751

Kirkaldy, J.S. and Brown, L.C. (1963) "Diffusion Behaviour in Ternary, Multiphase Systems", *Can. Met. Quart.*, **2**, 89.

Kirkaldy, J.S. and Purdy G.R. (1968) Can. J. Phys., **47**, 865

Kirkaldy, J.S. (1969) "On the Theory of Internal Oxidation and Sulphation of Alloys", *Can. Met. Quart.*, **8**, 35.

Kirkaldy, J.S. (1971) " Ternary Diffusion and its Relationship to Oxidation and Sulphidation", in Oxidation of Metals and Alloys, American Society for Metals, Metals Park, Ohio.

Kirkaldy, J.S. and Young D.J. (1987), Diffusion in the Condensed State, The Institute of Metals, London

Kirkwood, D.H., Atasoy, O.E. and Keown, S.R. (1974) "The Structure of Nitrided and Annealed Iron-Titanium Alloys", *Metal Sci.*, **8**, 49.

Laflamme, G.R. and Morral, J.E. (1978) "Limiting Cases of Subscale Formation", *Acta Met.*, **26**, 1791.

L'nyanoi, V.N. (1977) "Study of the Diffusion of Carbon in Solid Solutions by High-Temperature Vacuum-Metallography", *Fiz. Khim. Obrabot. Mater.*, **3**, 104.

Lu, P. and Cosandey, F. (1992) "Dislocation Structures at Cu-MgO and Pd-MgO Interfaces", *Acta Met. Mater.*, **40**, S259.

Mackert, J.R., Ringle, R.D. Jr. andd Fairhurst, C.W. (1983) "High-Temperature Behavior of a Pd-Ag Alloy for Porcelain", *J. Dent. Res.*, **62**, 1229.

Mykura, H., Bansai, P.S. and Lewis, M.H. (1980) "Coincidence-Site-Lattice Relations for MgO-CdO Interfaces", *Phil. Mag. A*, **42**, 225.

Mitra, R., Cjiou, W.A., Fine, M.E. and Weertman, J.R. (1993) "Interfaces in As-Extruded XD Al/TiC and Al/TiB_2 Metal Matrix Composites", *J. Mater. Res.*, **8**, 2380.

Moll, S.H. and Oglivie, R.E. (1959) , *TMS-AIME*, **215**, 613.

Ohno, H., Kanzawa, Y., Kawashima, I. and Shiokawa, N (1983) "Structure of High-Temperature Oxidation Zones of Gold Alloys for Metal-Porcelain Bonding Containing Small Amounts of In and Sn", *J. Dent. Res.*, **62**, 774.

Ohriner, E.K. and Morral, J.E. (1979) "Precipitate Distribution in Subscales", *Scr. Met.*, **13**, 7.

Otani, H. and Hillert, M (1990) "A Thermodynamic Assessment of the Ti-N System", *CALPHAD*, **14**, 289.

Otsuki, A. and Mizuno, *Proc. Symp. on Grain Boundary Structure and Related Phenomena. Trans Japan Inst. Metals Suppl.*, **27**, 789

Portnoi, K.I., Mukaseev, A.A., Gribkov, V.N. and Levinskii, Y.V (1968)"Modulus of Normal Elasticity of Porosity-Free Titanium and Zirconium Nitrides", *Poroshkovaya Metallurgiya*, **5(65)**, 87.

Press, W.H., Teukolsky, S.A., Vetterling, W.T. and Flannery, B.P. (1992) Numerical Recipes in Fortran The Art of Scientific Computing, Cambridge University Press, Cambridge, 838.

Pumphrey, P.H. (1972) "A Plane Matching Theory of High Angle Grain Boundary Structure", *Scr. Met.*, **6**, 107.

Rapp, R.A. (1961) "The Transition form Internal to External Oxidation and the Formation of Interruption Bands in Silver-Indium Alloys", *Acta Met.*, **9**, 730.

Rapp, R.A. (1965) "Kinetics, Microstructures and Mechanism of Internal Oxidation- Its Effect and Prevention in High Tempearture Alloy Oxidation", *Corrosion*, **21**, 382.

Read W.T. and Shockley W. (1950), *Phys. Rev.* **78**, 275

Shieu, F.S. and Sass, L. (1990) "Experimental and Theoretical Studies of the Dislocation Structure of NiO-Pt Interfaces", *Acta Met. Mater.*, **38**, 1653.

Silcock, J.M. (1978) "Rates of Nitriding and Nitride Composition in Austenitic Steels Containing Titanium", *Metal Sci.*, **12**, 561.

Stott, F.H. (1992) "Developments in Understanding the Mechanisms of Growth of Protective Scales on High-Temperature Alloys", *Mat. Char.*, **28**, 311.

Sutton, A.P. and Balluffi, R.W. (1987) "On Geometric Criteria for Low Interfacial Energy", *Acta Met.*, **35**, 2177.

Swisher, J.H. (1968) "Sulfur Solubility and Internal Sulfidation of Iron-Titanium Alloys", *TMS-AIME*, **242**, 2433.

Swisher, J.H. (1971) "Internal Oxidation", in Oxidation of Metals and Alloys, American Society for Metals, Metals Park, Ohio.

Unthank, D.C., Driver, J.H. and Kack, K.H. (1974) "Nitride Hardening of an Austenitic Stainless Steel Containing Titanium", *Metal Sci.*, **8**, 209.

Van der Merwe J.H. (1950), *Proc. Phys. Soc. (London)* **A63**, 616

Van der Merwe (1963), "Crystal Interfaces, Part I. Semi-Infinite Crystals" *J. Appl. Phys.* **34** 1, 117

Wada, H. and Pehlke, R.D. (1985) "Nitrogen Solubility and Nitride Formation in Austenitic Fe-Ti Alloys", *Met. Trans. B*, **16B**, 815.

Wagner, C. (1952) "Theoretical Analysis of the Diffusion Processes Determining the Oxidation Rate of Alloys", *J. Electrochem. Soc.*, **99**, 369.

Wagner, C. (1956) "Oxidation of Alloys Involving Noble Metals", *J. Electrochem. Soc.*, **103**, 571.

Wagner, C. (1959) "Realionstypen bei der Oxydation von Legierungen ", *Z. Elektrochem.*, **63**, 772.

Wagner, C. (1965) "Passivity and Inhibition During the Oxidation of Metals at Elevated Temperatures", *Corr. Sci.*, **5**, 751.

Wagner, C. (1968) "Internal Oxidation of Cu-Pd and Cu-Pt Alloys", *Corr. Sci.*, **8**, 889.

Wells, C., Batz, W. and Mehl, R.F. (1950) , *TMS-AIME*, **188**, 553.

Westmacott, .H. and Dahmen, U. (1986) "Recent TEM Studies of Precipitate Growth Mechanisms", *Reveu Phys. Appl.*, **21**, 757.

Wriedt, H.A. and Gonzalez, O.D. (1961) "The Solubility of Nitrogen in Solid Iron-Nickel Alloys Near 1000 °C", *TMS-AIME*, **221**, 532.

Wriedt, H.A. (1985) "The N-Ni (Nitrogen-Nickel) System", *Bull. Alloy Phase Diagr.*, **6**, 558.

Wriedt, H.A. and Murray, J.L. (1987) "The N-Ti (Nitrogen-Titanium) System", *Bull. Alloy Phase Diagrams*, **8**, 378.

Wolf D. (1985),"On the Relationship Between Symetrical Tilt, Twist, 'Special' and 'Favored' Grain Boundaries", J. de Physique Colloque, **C4** (4), C4-197

Yi, H.C., Guan, S.W., Smeltzer, W.W. and Petric, A. (1994) "Internal Oxidation of Ni-Al and Ni-Al-Si Alloys at the Dissociation Pressure of NiO", *Acta Met. Mater.*, **42**, 981.

Zou, H. and Kirkaldy, J.S. (1990) "Multicomponent Diffusion Theory Applied to Carbonitride Precipitate Growth in Pentenary Microalloyed Steels", Fundamentals and Applications of Ternary Diffusion, Pergamon, Oxford, 184.

Zhang, W.Z. and Purdy, G.R. (1993), *Phil. Mag.*, **68**, #2, 279-290

Appendix I
A Finite Difference Computer Algorithm for Internal Precipitation of a BC Phase

```
      PROGRAM TINS
$DEBUG
C*************************************************************************
C     THIS PROGRAM WILL USE A FINITE DIFFERENCE APPROACH                  *
C     TO SOLVE FICK'S SECOND LAW                                          *
C     USED TO ANALYSIS ANY DATA WITH BC AS A PRODUCT                      *
C     IT INCLUDES CROSS EFFECTS 'HRO' THE WAGNER INTERACTION EFFECT       *
C*************************************************************************
      REAL*8 CO,DEX,DET,C,AL1,B,AL2,D,E,T1,T2,T,K,F,DEC,V,W
      REAL*8 P,RT,Z1,Z2,VF,ALC,ALD
      INTEGER PS
      DIMENSION C(-2:700)
      DIMENSION B(-2:700)
      DIMENSION D(-2:700)
      DIMENSION E(-2:700)
      DIMENSION F(-2:700)
      OPEN (13,FILE='DIFF.DAT')
      OPEN (15,FILE='SOL.DAT')
C*************************************************************************
C                  VARIABLE NAMES                                         *
C    CS=SURFACE CONCENTRATION OF GAS (MOLES/CM3)                          *
C    CO=ORIGINAL METAL ALLOY COMPOSITION MOLES/CM3)                       *
C    T1,T2=THERMAL DIFFUSIVITY OF GAS, METAL SPECIES                      *
C    DEX,DET= INCREMENTS OF POSITION, TIME                                *
C    T=NUMBER OF TIME INTERVALS I.E. TIME=T*DET                           *
C    VF=MOLAR VOLUME OF BC PHASE                                          *
C    W=WAGNER INTERACTION COEFFICIENT                                     *
C    PS=DEPTH OF SAMPLE I.E. LENGTH=PS*DEX                                *
C*************************************************************************
      READ (13,*) CS,CO,T1,T2,DEX,DET,K,T,VF,W,PS
      AL1=T1*DET/(DEX*DEX)
      AL2=T2*DET/(DEX*DEX)
      ALC=AL1*W*(CS*0.5/0.151618399)
      ALD=AL2*W*(CO*0.5/0.151618399)
      IF (2*AL1.GE.1.OR.2*AL2.GE.1.OR.2*ALC.GE.1) THEN
      PRINT*,'UNSTABLE USE SMALLER TIME INCREMENT'
      GOTO 100
      END IF
C*************************************************************************
C     PREPARE THE INITIAL BOUNDARY CONDITIONS                             *
C     STEP 1: DELTA TIME=0                                                *
C     THE DIMENSION ARRAY C(J) IS CONCENTRATION,J=POSITION                *
C*************************************************************************
      DO 11 J=0,1
          C(J-1)=CS
          B(J-1)=CS
          IF(CS*CO.GT.K) THEN
          D(J-1)=K/CS
          E(J-1)=K/CS
          F(J-1)=CO-K/CS
            ELSE
          D(J-1)=CO
          E(J-1)=CO
          F(J-1)=0
          END IF
 11   CONTINUE
      DO 15 J=1,PS+2
          C(J)=0
          B(J)=0
          D(J)=CO
```

```
            E(J)=CO
            F(J)=0
   15   CONTINUE
        DO 19 N=1,T
            DO 37 J=1,PS
            IF(F(J-1)/VF.GE.1) THEN
            PRINT*,'COMPLETE SURFACE COVERING'
            GOTO 100
            END IF
            V=1-(F(J)/VF)
            C(J)=AL1*V*(B(J+1)-2*B(J)+B(J-1))+B(J)
     +          +ALC*V*(D(J+1)-2*D(J)+D(J-1))
C*************************************************************************************
C           THIS PART OF THE PROGRAM DEALS WITH THE "SINK" TERMS                     *
C*************************************************************************************
            IF(C(J)*D(J).GT.K) THEN
              P=D(J)-C(J)
              RT=DSQRT(P*P+4*K)
              Z1=0.5*(P-RT)
              Z2=0.5*(P+RT)
              IF (Z1.GT.0.AND.D(J).GT.Z1) THEN
                 F(J)=F(J)+D(J)-Z1
                 D(J)=Z1
                 C(J)=K/D(J)
              END IF
              IF (Z2.GT.0.AND.D(J).GT.Z2) THEN
                 F(J)=F(J)+D(J)-Z2
                 D(J)=Z2
                 C(J)=K/D(J)
              END IF
              IF (Z1.LT.0.AND.Z2.LT.0) THEN
                 PRINT*,'NO POSITIVE ROOTS'
                 GOTO 100
              END IF
            END IF
   37       CONTINUE
            DO 21 J=1,PS
            IF(J-1.EQ.0)THEN
C*************************************************************************************
C           DEC IS THE CHANGE OF CONCENTRATION ENTERING THE SURFACE                  *
C           SINCE IT IS THE SURFACE THERE ARE NO EXIT TERMS                          *
C*************************************************************************************
            DEC=AL2*V*(D(J)-D(J-1))+ALD*V*(C(J+1)-2*C(J)+C(J-1))
            F(0)=F(0)+DEC
            END IF
            E(J)=AL2*V*D(J+1)+(1-2*V*AL2)*D(J)+AL2*V*D(J-1)
     +          +ALD*V*(C(J+1)-2*C(J)+C(J-1))
   21   CONTINUE
        DO 78 J=1,PS
        B(J)=C(J)
        D(J)=E(J)
   78   CONTINUE
   19   CONTINUE
  100   CONTINUE
        TLT=0
        TLN=0
        DO 23 J=0,PS
        X=J*DEX*10000
        WRITE (15,801)X,C(J),D(J),F(J),F(J)*100/VF
        TLT=(CO-D(J))*DEX+TLT
        TLN=F(J)*DEX+TLN
   23   CONTINUE
        WRITE (15,803)DET*N/3600
  801   FORMAT (F8.2,E16.6,E16.6,E16.6,E16.6)
  803   FORMAT ('TIME=',F10.2,2X,'HOURS')
C       WRITES THE TOTAL MOLES OF TI CONSUMED AND TIN CREATED
        WRITE (15,805)TLT,TLN
  805   FORMAT ('TI CONSUMED =',E16.6,3X,'TIN CREATED =',E16.6)
        CLOSE(UNIT=13)
        CLOSE(UNIT=15)
        END
```

```
 THE STRUCTURE MATRIX 1 IS
    2.12000000     2.12000000     2.12000000
    2.12000000    -2.12000000      .00000000
     .00000000      .00000000     2.12000000
 THE STRUCTURE MATRIX 2 IS
    1.76180000     1.76180000     1.76180000
    1.76180000    -1.76180000      .00000000
     .00000000      .00000000     1.76180000
 THE DSC VECTORS ARE:
    2.12000000     2.12000000     2.12000000
    2.12000000    -2.12000000      .00000000
     .00000000      .00000000     2.12000000
 THE TRANSFORMATION MATRIX A IS
     .83103774      .00000000      .00000000
     .00000000      .83103774      .00000000
     .00000000      .00000000      .83103774
 THE DETERMINANT OF A IS
     .573934E+00
 THE INVERSE OF THE A MATRIX IS
    1.20331479      .00000000      .00000000
     .00000000     1.20331479      .00000000
     .00000000      .00000000     1.20331479
 THE DETERMINANT OF A INVERSE IS
     .174236E+01
 THE T MATRIX IS
    -.20331479      .00000000      .00000000
     .00000000     -.20331479      .00000000
     .00000000      .00000000     -.20331479
 THE DETERMINANT OF THE T MATRIX IS
    -.840440E-02
 THE T INVERSE MATRIX IS
   -4.91848130      .00000000      .00000000
     .00000000    -4.91848130      .00000000
     .00000000      .00000000    -4.91848130
 THE DETERMINANT OF T INVERSE IS
    -.118985E+03
 THE O-LATTICE IS
 -10.42718035   -10.42718035   -10.42718035
 -10.42718035    10.42718035      .00000000
    .00000000      .00000000   -10.42718035
 THE DETERMINANT FOR THE O-LATTICE IS
     .226741E+04
```

Appendix III
Secondary O- Lattice Calculation of Type I OR

```
THE STRUCTURE MATRIX 1 IS
  10.60000000   10.60000000   10.60000000
  10.60000000  -10.60000000     .00000000
    .00000000     .00000000   10.60000000
THE STRUCTURE MATRIX 2 IS
  10.56000000   10.56000000   10.56000000
  10.56000000  -10.56000000     .00000000
    .00000000     .00000000   10.56000000
THE DSC VECTORS ARE:
    .35333333     .35333333     .35333333
    .35333333    -.35333333     .00000000
    .00000000     .00000000     .35333333
THE TRANSFORMATION MATRIX A IS
    .99622642     .00000000     .00000000
    .00000000     .99622642     .00000000
    .00000000     .00000000     .99622642
THE DETERMINANT OF A IS
    .988722E+00
THE INVERSE OF THE A MATRIX IS
   1.00378788     .00000000     .00000000
    .00000000    1.00378788     .00000000
    .00000000     .00000000    1.00378788
THE DETERMINANT OF A INVERSE IS
    .101141E+01
THE T MATRIX IS
   -.00378788     .00000000     .00000000
    .00000000    -.00378788     .00000000
    .00000000     .00000000    -.00378788
THE DETERMINANT OF THE T MATRIX IS
   -.543486E-07
THE T INVERSE MATRIX IS
-264.00000000     .00000000     .00000000
    .00000000 -264.00000000     .00000000
    .00000000     .00000000 -264.00000000
THE DETERMINANT OF T INVERSE IS
   -.183997E+08
THE O-LATTICE IS
 -93.27999912  -93.27999912  -93.27999912
 -93.27999912   93.27999912     .00000000
    .00000000     .00000000  -93.27999912
THE DETERMINANT FOR THE O-LATTICE IS
    .162329E+07
```

Appendix IV
Primary O- Lattice Calculation of Type II OR

```
THE STRUCTURE MATRIX 1 IS
   2.15555510     1.43703435     2.15555510
    .00000000     2.03225973      .00000000
   1.24450794      .00000000    -1.24450794
THE STRUCTURE MATRIX 2 IS
   2.12000000     2.12000000     2.12000000
    .00000000     2.12000000      .00000000
   2.12000000      .00000000    -2.12000000
THE DSC VECTORS ARE:
   2.15555510     1.43703435     2.15555510
    .00000000     2.03225973      .00000000
   1.24450794      .00000000    -1.24450794
THE TRANSFORMATION MATRIX A IS
    .98350536      .34772574      .00000000
    .00000000     1.04317375      .00000000
    .00000000      .00000000     1.70348451
THE DETERMINANT OF A IS
    .174772E+01
THE INVERSE OF THE A MATRIX IS
   1.01677127     -.33892488      .00000000
    .00000000      .95861308      .00000000
    .00000000      .00000000      .58703205
THE DETERMINANT OF A INVERSE IS
    .572174E+00
THE T MATRIX IS
   -.01677127      .33892488      .00000000
    .00000000      .04138692      .00000000
    .00000000      .00000000      .41296795
THE DETERMINANT OF THE T MATRIX IS
   -.286646E-03
THE T INVERSE MATRIX IS
 -59.62576899  488.28607517      .00000000
    .00000000   24.16222334      .00000000
    .00000000      .00000000     2.42149540
THE DETERMINANT OF T INVERSE IS
   -.348863E+04
THE O-LATTICE IS
-128.52663025  906.63984910 -128.52663025
    .00000000   49.10391349      .00000000
   3.01357026      .00000000    -3.01357026
THE DETERMINANT FOR THE O-LATTICE IS
    .380383E+05
```

Appendix V
Secondary O- Lattice Calculation of Type II OR

```
THE STRUCTURE MATRIX 1 IS
   2.12000000    2.12000000    4.24000000
   2.12000000     .00000000     .00000000
    .00000000    6.36000000     .00000000
THE STRUCTURE MATRIX 2 IS
   1.43701661    2.15555097    4.31110195
   2.03227295     .00000000     .00000000
    .00000000    6.22253968     .00000000
THE DSC VECTORS ARE:
   2.12000000    2.12000000    2.12000000
   2.12000000     .00000000     .00000000
    .00000000     .42400000    -.42400000
THE TRANSFORMATION MATRIX A IS
   1.01676933    -.33893130     .00000000
    .00000000     .95861932     .00000000
    .00000000     .00000000     .97838674
THE DETERMINANT OF A IS
    .953628E+00
THE INVERSE OF THE A MATRIX IS
    .98350724     .34773073     .00000000
    .00000000    1.04316696     .00000000
    .00000000     .00000000    1.02209071
THE DETERMINANT OF A INVERSE IS
    .104863E+01
THE T MATRIX IS
    .01649276    -.34773073     .00000000
    .00000000    -.04316696     .00000000
    .00000000     .00000000    -.02209071
THE DETERMINANT OF THE T MATRIX IS
    .157273E-04
THE T INVERSE MATRIX IS
  60.63268321 -488.42553095    -.00000065
    .00000000  -23.16586391     .00000000
    .00000000     .00000000  -45.26789618
THE DETERMINANT OF T INVERSE IS
    .635837E+05
THE O-LATTICE IS
-906.92083721  128.54128812  128.54128867
 -49.11163149     .00000000     .00000000
    .00000000  -19.19358798   19.19358798
THE DETERMINANT FOR THE O-LATTICE IS
    .242333E+06
```

Appendix VI
Primary O- Lattice Calculation of Type III OR

```
 THE STRUCTURE MATRIX 1 IS
    -.24916000     1.99325000      .24916000
    1.22061000      .40687000    -1.22061000
    2.15776000    -1.43850000     2.15776000
 THE STRUCTURE MATRIX 2 IS
     .00000000     2.12000000      .00000000
    2.12000000      .00000000    -2.12000000
    2.12000000    -2.12000000     2.12000000
 THE DSC VECTORS ARE:
    -.24916000     1.99325000      .24916000
    1.22061000      .40687000    -1.22061000
    2.15776000    -1.43850000     2.15776000
 THE TRANSFORMATION MATRIX A IS
    1.02104542      .20842339      .00000000
    -.34034847     1.66736204      .00000000
    -.34035163     -.06947511      .98250037
 THE DETERMINANT OF A IS
     .174236E+01
 THE INVERSE OF THE A MATRIX IS
     .94021226     -.11752830      .00000000
     .19191981      .57575943      .00000000
     .33927358      .00000000     1.01781132
 THE DETERMINANT OF A INVERSE IS
     .573936E+00
 THE T MATRIX IS
     .05978774      .11752830      .00000000
    -.19191981      .42424057      .00000000
    -.33927358      .00000000     -.01781132
 THE DETERMINANT OF THE T MATRIX IS
    -.853525E-03
 THE T INVERSE MATRIX IS
    8.85302779    -2.45257386      .00000000
    4.00497161     1.24764704      .00000000
-168.63423653    46.71711535   -56.14406780
 THE DETERMINANT OF T INVERSE IS
    -.117161E+04
 THE O-LATTICE IS
   -5.19945659    16.64841892     5.19945659
     .52501173     8.49053982     -.52501173
 -22.10513919  -236.35915772  -220.18570827
 THE DETERMINANT FOR THE O-LATTICE IS
     .128140E+05
```

```
THE ROTATION MATRIX IS
     .99987388      .00000000      .01588183
     .00000000     1.00000000      .00000000
    -.01588183      .00000000      .99987388
THE ROTATION AXIS IS
  .00000000  1.00000000   .00000000
THE ROTATION ANGLE IS
     .910000E+00
THE TRANSFORMATION MATRIX A IS
    1.01551123      .20729371      .01560390
    -.34034847     1.66736204      .00000000
    -.35652477     -.07277649      .98237645
THE DETERMINANT OF A IS
     .174236E+01
THE INVERSE OF THE A MATRIX IS
     .94009368     -.11752830     -.01493229
     .19189561      .57575943     -.00304804
     .35539550      .00000000     1.01229467


 DETERMINANT OF A INVERSE IS
   .573936E+00
E T MATRIX IS
   .05990632      .11752830      .01493229
  -.19189561      .42424057      .00304804
  -.35539550      .00000000     -.01229467
E DETERMINANT OF THE T MATRIX IS
   .153433E-02
E T INVERSE MATRIX IS
-3.39946871      .94176233    -3.89529331
-2.24368839     2.97872714    -1.98656359
98.26667666   -27.22303468    31.26312982
E DETERMINANT OF T INVERSE IS
   .651752E+03
E O-LATTICE IS
-6.40857194     -.78943674   -10.40164423
 -.09162593     -.40260544    -8.48142899
 9.74549749   139.82180489   125.17116452
E DETERMINANT FOR THE O-LATTICE IS
 -.712825E+04
```

```
THE ROTATION MATRIX IS
   1.00000000      .00000000      .00000000
    .00000000      .99987388      .01588183
    .00000000    -.01588183       .99987388
THE ROTATION AXIS IS
 1.00000000    .00000000    .00000000
THE ROTATION ANGLE IS
   -.910000E+00
THE TRANSFORMATION MATRIX A IS
   1.02104542      .20842339      .00000000
   -.34571095     1.66604835      .01560390
   -.33490334     -.09594710      .98237645
THE DETERMINANT OF A IS
    .174236E+01
THE INVERSE OF THE A MATRIX IS
    .94021226     -.11751348      .00186656
    .19191981      .57568682     -.00914411
    .33927358      .01616471     1.01768295
THE DETERMINANT OF A INVERSE IS
    .573936E+00
THE T MATRIX IS
    .05978774      .11751348     -.00186656
   -.19191981      .42431318      .00914411
   -.33927358     -.01616471     -.01768295
THE DETERMINANT OF THE T MATRIX IS
   -.147763E-02
THE T INVERSE MATRIX IS
   4.97776734    -1.42671565    -1.26321524
   4.39627350     1.14406168      .12755233
 -99.52465082    26.32781916   -32.43159535
THE DETERMINANT OF T INVERSE IS
   -.676760E+03
THE O-LATTICE IS
  -5.70743922    11.15858208      .25600858
    .57630494     9.04487250     -.02585030
 -13.04603784  -141.01266054  -126.91316053
THE DETERMINANT FOR THE O-LATTICE IS
    .740176E+04
```

Appendix IX

Primary O- Lattice Calculation of Type III OR- variant (1.25° twist about [010])

```
 THE STRUCTURE MATRIX 1 IS
     .24916000     1.99325000     -.24916000
    1.22061000     -.40687000    -1.22061000
    2.15776000    -1.43850000     2.15776000
 THE STRUCTURE MATRIX 2 IS
     .00000000     2.12000000      .00000000
    2.12000000      .00000000    -2.12000000
    2.12000000    -2.12000000     2.12000000
 THE DSC VECTORS ARE:
     .24916000     1.99325000     -.24916000
    1.22061000     -.40687000    -1.22061000
    2.15776000    -1.43850000     2.15776000
 THE TRANSFORMATION MATRIX A IS
    1.02104542     -.20842339      .00000000
     .34034847     1.66736204      .00000000
    -.34035163      .06947511      .98250037
 THE DETERMINANT OF A IS
     .174236E+01
 THE ROTATION MATRIX IS
     .99976203      .00000000      .02181489
     .00000000     1.00000000      .00000000
    -.02181489      .00000000      .99976203
 THE ROTATION AXIS IS
   .00000000  1.00000000   .00000000
 THE ROTATION ANGLE IS
     .125000E+01
 THE TRANSFORMATION MATRIX A IS
    1.01337770     -.20685820      .02143313
     .34034847     1.66736204      .00000000
    -.36254462      .07400531      .98226656
 THE DETERMINANT OF A IS
     .174236E+01
 THE INVERSE OF THE A MATRIX IS
     .93998852      .11752830     -.02051062
    -.19187414      .57575943      .00418671
     .36139628      .00000000     1.01016789
```

```
THE DETERMINANT OF A INVERSE IS
    .573936E+00
THE T MATRIX IS
    .06001148    -.11752830     .02051062
    .19187414     .42424057    -.00418671
   -.36139628     .00000000    -.01016789
THE DETERMINANT OF THE T MATRIX IS
    .247868E-02
THE T INVERSE MATRIX IS
  -1.74029467    -.48211768   -3.31199746
   1.39752496    2.74431261    1.68908810
  61.85508818   17.13585182   19.36915947
THE DETERMINANT OF T INVERSE IS
    .403441E+03
THE O-LATTICE IS
  -8.16858511    1.49162522   -6.12440615
   7.34258947    -.76071508    -.05329600
  78.12200341   88.45805457    5.46599168
THE DETERMINANT FOR THE O-LATTICE IS
   -.441246E+04
```